

https://dspace.org/

Synthesis and characterisation of metal selenide nanocrystals for use in electronic devices

Airo, Mildred Awuor

2017

http://hdl.handle.net/10539/23606

Airo, Mildred Awuor (2017) Synthesis and characterisation of metal selenide nanocrystals for use in electronic devices, University of the Witwatersrand, Johannesburg, <http://hdl.handle.net/10539/23606>

Downloaded from a DSpace repository. https://dspace.org/

SYNTHESIS AND CHARACTERIZATION OF METAL SELENIDE NANOCRYSTALS FOR USE IN ELECTRONIC DEVICES

BY

Mildred Awuor Airo (700083)

BSc (Hons)

A THESIS SUBMITTED IN FULFILMENT OF THE REQUIREMENTS

FOR THE DEGREE OF

DOCTOR OF PHILOSOPHY IN THE SCHOOL OF CHEMISTRY

FACULTY OF SCIENCE

UNIVERSITY OF WITWATERSRAND

Advisors

Prof. Nosipho Moloto

Prof. Justice M. Moloto



Declaration

I declare that the work reported herein is my own, independent work submitted at the School of Chemistry, University of the Witwatersrand, Johannesburg. And that this work has not been submitted for any degree or examination in any other institution of higher learning.

Name: Mildred Awuor Airo

Date: 26/05/2017 Signature: 

Abstract

Advancements in nanotechnology and nanosystems promise to extend limits of sustainable development and environment remediation in an attempt to address some of the world most challenging problems. Specifically, nanotechnology has played an important role in the design, synthesis, and characterization of various new and novel functional nanomaterials possessing extremely unique properties. For example, low dimensional nanostructures such as semiconductor nanocrystals with well controlled sizes, shapes, porosities, crystalline phases, and structures have been prepared via various synthetic methods. In addition these semiconductor nanocrystals have attracted research attention because of their fundamental role in the comprehension of the quantum size effect and great potential applications to save resources and improve the environment.

Tremendous studies have established that morphological, optical, catalytic and electronic properties of semiconductor nanocrystals can be manipulated during synthesis by simply varying the growth parameters. Herein we establish the effect of different synthetic methods and several growth parameters on the properties of the as-synthesized semiconducting metal selenides nanocrystals (Ni_xSe_y and In_xSe_y) including structural, optical, electronic and catalytic properties. For example, reducing coordinating solvent oleylamine was seen to favour a particular morphologies and stoichiometries despite the duration of synthesis. In the case of In_xSe_y nanocrystals, oleylamine favoured indium monoselenide (InSe) nanosheet formation while addition of 1-DDT as a co-surfactant to oleylamine produces In_2Se_3 nanowires. For Ni_xSe_y nanocrystals, TOP as a co-surfactant to different ligands favoured the formation Ni_3Se_2 with different shapes including dots, plates, rods and wires in different solvents. Other parameters studied included the reaction time and temperature.

Besides the properties, we probe the potential applications of these materials in dye sensitized solar cells as counter electrodes as well in chemical sensor as the sensing material. Ni_xSe_y nanocrystals were employed as CE in DSSCs in an attempt to replace the noble expensive platinum conventionally used as CE in most DSSCs. It was established that different stoichiometry played a significant role in the catalytic reduction of I_3^-. Thus, different photovoltaic performance parameters were obtained with $NiSe_2$ giving a higher PCE of 1.5 % followed Ni_3Se_4 then Ni_3Se_2. These values were however very low compared to the ones reported in literature, something that was attributed to low electron mobility, enhanced recombination and reduced catalytic performance as a result of poor device assembly and the organic ligand layer encapsulating the nanocrystal.

In another scenerio, indium monoselenide nanocrystals were employed in chemiresistive sensors to detect the presence of a number of VOCs including formaldehyde, methanol, chloroform and acetone in the ambient. Indeed despite the well-known electrical, optical and structural properties previously reported in literature, metal selenides such as CdSe, PbSe and ZnSe among others present lack of investigation for gas sensing. The experimental results showed that different morphologies of InSe nanostructures interacted differently to the analyte gas suggesting difference in the electronic properties of different morphologies. The InSe nanoparticle based sensors gave a good response to HCHO and MeOH fumes and were more selective to HCHO fumes than chloroform and acetone. While those fabricated using the InSe nanosheets though responding well to HCHO recovered half way when exposed back in air and resulted in relatively high noise to signal ratio when exposed to MeOH. The operating temperature range for the InSe sensor devices were determined to be near room temperature. The sensors response was observed to decrease with increasing temperature from 30 °C to 90 °C. Evident from the results,

the surface capping molecule (oleylamine) employed to stabilize the nanostructures during synthesis was responsible for the poor sensing abilities of the nanostructures.

Acknowledgement

First and foremost, I would like to express my deepest gratitude to God almighty for this far He has brought me; for the good health and wellbeing I needed to complete this project and for maintaining my sanity through this challenging yet most interesting journey of my life and career.

Though the cover page of this thesis only bears my name, I am by no means its sole contributor. Rather a number of individuals and organizations are behind the success of this piece of work that deserves to be acknowledged and appreciated. Most important of all, I show extensive gratitude to all my academic supervisors Prof Nosipho Moloto and Prof Justice Makwena Moloto for their enthusiasm, guidance and unrelenting support throughout this project. More specifically, I am forever indebted to Prof Nosipho Moloto for being more than a supervisor. She played the role of my big sister and my mother and was constantly there for me beyond my project. Through my three surgeries she has been a great pillar via her immense understanding and patience and the big heart. She is my number one role model in almost all sectors of life, from family to research world. She has taught me everything I know today in terms of material chemistry and nanotechnology. In other words she has persistently gone beyond her duties to fire fight my worries, concerns and anxieties and has worked to instill great confidence in myself and my work.

Secondly, my gratitude goes to all the individuals and groups who contributed immensely to this work, either directly or indirectly. I thank Dr. Pierre Kalenga for his guidance and mentorship in most parts of this project; Mr. Tumelo Phaahlamohlaka, for his continuous assistance with the BET measurements and always helping out with the replacement of gas cylinders and gas regulators. My Honours students Ian and Somandla helped me improve on my supervision skills

and their challenging questions helped me to grow in the research world. CATOMAT group and my group members; Lerato Machogo, Rudo Sithole, Siziwe Gqoba, Stefan Govindraju plus the new members of the group and the vacation students. Through the progress meetings and lab meetings, your critics towards my results added a lot of value this work. Dr. Emily Aradi, we laughed together, cried together and pushed science together. You are my sister from another mother.

With immense pleasure, I record my deep sense of gratitude to Prof. Neil Coville for having confidence in me and his recommendation as well support during the admission process. His input and guidance during my research has been quite helpful.

Special thanks go to my host during my visit to Brazil, Prof. Hummelgen Ivo for the warm welcome, unrelenting support, guidance, care and understanding beyond the laboratory work. In addition, my thanks go to Mr Rafael Rodrigues who helped me carry out the sensing experiments and taught me the analysis of the results. In connection to this, I would like to sincerely thank the entire GOOD group and Michelle (Prof. Ivo's wife) for their support as well as their warm welcome. A special thanks also to Marcia Greenshield for her attention being my tour guide throughout the visit and for welcoming me to her family.

My deepest gratitude goes to my family members and my in-laws for their constant prayers especially my mum and dad for always believing in me; and Wuon oluoch for his abundant words of wisdom. My little sisters Chris, Quinter (Q-Q), and Cindy; my brothers Wlado, Tony and Feddy who made my holidays memorable, enjoyable and fun whenever I had a break from work and I am so grateful to you all. Last, but certainly not least, I must acknowledge with tremendous and deep thanks my beloved husband, Francis. He has been my supervisor, my co-

supervisor, my co-author, my colleague, my competitor, my confidant, my pillar, my nurse, my doctor, my empire and basically my entire world. Through his unconditional love, patience, support and unwavering belief in me, I've been able to complete this long journey. For the first two years of this project, he remained wifeless in Kenya without complaining in the name of allowing me go after my dream. After joining me in 2014, he has patiently endured many, many long hours alone while I ran my experiments, prepared my presentations and worked on my thesis. At the same time, he has also given me so many happy and beautiful memories throughout this journey. We have laughed and cried, travelled and played, built and settled, and planned and discussed our work and lives. Francis reminded me about my strengths whenever I felt weak and weary. I could not have completed this journey without you my love and I am forever indebted to you.

Special thanks go to Organization of Women in Science in Developing Countries (OWSD) and NRF-South Africa for their generous, timely funding that always enabled me pay my fees as well up-keep. In particular OWSD for the seminars, workshops and the travel mobility grant help me improve on my paper writing skills and the scope of my research.

Finally, appreciation also goes to Wits, School chemistry XRD unit and Wits MMU units for giving me the opportunity to undertake my research as well providing required facilities and expertise.

Dedication

This work is a special dedication to number one role, my beloved mum, Angelina Nyakodongo; my best companion and beloved husband, Francis Otieno and to my entire family members.

List of publications

1. N. Moloto, M.J. Moloto, M.Kalenga, S. Govindraju, M. Airo. "Synthesis and characterization of MnS and MnSe nanoparticles: morphology, optical and magnetic properties." J. Optical Materials. 2014.

2. Mubiayi P. Kalenga, Stefan Govindraju, Mildred Airo, Makwena J. Moloto, Lucky M. Sikhwivhilu, and Nosipho Moloto. "Fabrication of a schottky device using CuSe nanoparticles: colloidal versus microwave digestive synthesis." J. of Nanoscience and Nanotechnology. 2014.

3. Mildred A.Airo, Siziwe Gqoba, Mubiayi P. Kalenga Stefan Govindraju, Makwena J. Moloto, Nosipho Moloto. "Synthesis and characterization of indium monoselenide nanoparticles: a proposed pseudo top-down mechanism." J. of Crystal Growth. 2014.

4. Govindraj S., Kalenga, M. P., Airo M., Moloto M.J.; Sikhwivhilu, L. M.; Moloto N. "Size quantization in Cu2Se nanocrystals." J. of Optical Materials. 2014.

5. Francis Otieno, Mildred Awuor Airo, Kamalakannan Ranganathan, Daniel Wamwangi, Annealed silver islands for enhanced optical absorption in organic solar cells, Thin Film Solids, 2015.

6. Mildred A. Airo, Rafael Rodrigues, Siziwe Gqoba, N. Ntholeng, Francis Otieno, Makwena J. Moloto, Márcia W. C. C. Greenshields, Ivo A. Hümmelgen, Nosipho Moloto, "colloidal inse nanostructures: effect of morphology on their chemical sensitivity to methanol and formaldehyde fumes," Sensors and Actuators B, 2016.

7. Mildred A. Airo, Siziwe Gqoba, Francis Otieno, Makwena J. Moloto, Nosipho Moloto, "Structural modification and band-gap crossover in indium selenide nanosheets, RSC Advances, (2016).

8. Rafael Rodrigues, Mildred A. Airo, Siziwe Gqoba, Noshipho Moloto, Márcia W. C. C. Greenshields, Messai A. Mamo, Neil J. Coville, Alfred R. M. de Oliveira, Ivo A. Hümmelgena, "Chemical Sensors Based on Large Surface Area Nanoparticles for Aldehydes and Alcohols Detection and Distinction Using Generalized Tristimulus Analysis, " ACS sensors, 2016. Under review.

9. Otieno F, Mutuma B, Airo M, Kamalakannan R, Rudolph E, Neil C, Wamwangi D, "enhancement of organic photovoltaic device performance via P3HT:PCBM solution heat treatment. Thin Solid Films, 2017.

10. N. Ntholeng, B. Mojela, S. Gqoba, M. Airo, S. Govindraju, M. J. Moloto, J. Van Wyk and N. Moloto, "Colloidal synthesis of pure $CuInTe_2$ crystallites based on the HSAB theory," New J. Chem, 2016.

11. S. Gqoba, M. Airo, N. Ntholeng, L. Machogo, R. Sithole, M.J. Moloto, J. Van Wyk, N. Moloto, Evolution of In_2S_3 nanoplates with time, Materials Today: Proceedings (2015), in press.

12. Francis Otieno, Mildred Airo, Kamalakannan Ranganathan, Daniel Wamwangi, Enhancing light absorption and lifetime stability of organic solar cells using pentacene encapsulation, The Proceedings of the 60th Annual Conference of the South African Institute of Physics (SAIP2015).

13. Mildred Airo, Francis Otieno, Makwena Moloto, Nosipho Moloto, Colloidal synthesis of nickel selenide series for their application as counter electrodes in dye sensitized solar cells, RSC advances. TO BE SUBMITTED

Research visits

1. Visiting researcher at the Federal University of Parana, Brazil (09/2014-12/2014) through the OWSD research visit/conference support fund: Visited Prof. Ivo A. Hümmelgen's lab and conducted research on chemical sensor application of colloidal semiconductor nanocrystals. More specifically, InSe nanosheets were used to fabricate chemical sensors which were used to test presence of volatile organic compounds including formaldehyde, methanol, chloroform and acetone fumes.

2. Attended the forth international school for materials for energy and sustainability in Colorado, USA from 13/07 – 21/07 2015. The school's aim was to present the art and the future perspectives for materials as they can be applied to energy generation and storage for sustainable energy technologies. I resented a poster describing the synthesis of InSe nanoparticles and their application on photovoltaics.

Presentations

1. Oral presentation at the India Brazil South Africa (IBSA) summit held St. George's hotel on the 30/05/2013.
2. Poster presentation at Inorgarnic conference held on 30/06/2013 - 4/07/ 2013 in Durban.
3. Oral presentation at Catalysis Organometallics and materials' (CATOMAT) seminar held at Chemistry department, University of the Witwatersrand on the 16/08/2013.
4. Oral presentation at 5th Annual Gauteng's Nanosciences Young Researcher's Symposium (NYRS) held on the 08/11/2013 in CSIR Pretoria.
5. Oral presentation to South Africa national research fund (NRF) at Chemistry department, University of Witwatersrand held on the 21/05/2014.
6. Oral presentation at the 5th International Conference on Nanoscience and Nanotechnology in Africa held at Vaal University of Technology from 30/02/2014 - 02/04/2014.
7. Oral presentation at the OWSD regional scientific writing workshop held at the CSIR Pretoria from the 18/08/2014– 22/08/2014.
8. Oral Presentation to Good group seminar meeting at Universidade federal do Parana held on the 19/09/2014.
9. Oral Presentation to Good group seminar meeting at Universidade federal do Parana held on the 13/12/2014.
10. Oral presentation at Catalysis Organometallics and materials' (CATOMAT) seminar held at Chemistry department, University of the Witwatersrand on the 20/02/2015.

11. Oral presentation at the fourth International school for materials for energy and sustainability (ISMES IV) held at Colorado school of mines, USA from 13/07/2015-21/07/2015.
12. Oral presentation at Vaal University of technology – Wits seminar held University of the Witwatersrand on the 11/09/2015.
13. Oral presentation at Catalysis Organometallics and materials' (CATOMAT) seminar held at Chemistry department, University of the Witwatersrand on the 02/10/2015.
14. Oral presentation at the 6th International Conference on Nanoscience and Nanotechnology in Africa held at University of South Africa held on the 04/04/2016.
15. Oral presentation at the 64th South Africa Institute of Physics (SAIP) conference held on the 04/07/2016 at the University of Cape Town.

Table of Contents

Declaration i
Abstract ii
Acknowledgement v
Dedication viii
List of publications ix
Research visits xii
Presentations xiii
List of figures xix
List of Schemes xxv
List of tables xxvi
List of symbols and abbreviations xxvii
Thesis synopsis xxx
Chapter 1 : Background and rational 1
1.1 Background 1
1.2 Problem statement 3
1.3 Motivation 4
1.4 Aims and objectives 4
Chapter 2 : Introduction to colloidal semiconductor nanocrystals. 7
2.1 Introduction 7
2.2 Properties of semiconductor nanocrystals 12
2.2.1 Electronic structure of semiconductor nanocrystals 12
2.2.2 Optical transitions in semiconductor nanocrystals 17
2.3 Synthesis of metal selenide semiconductor nanocrystals 30
2.3.1 Mechanism of nanocrystal growth 30
2.3.2 Shape evolution mechanism/growth and shape control 35
2.4 Synthetic methods of semiconductor metal selenide nanocrystals 43
2.4.1 Hydrothermal/Solvothermal methods 44
2.4.2 Hot injection methods 46
2.4.3 Non-injection method (direct heating method) 47

2.4.4 Liquid exfoliation 48
2.5 Application of metal selenides nanocrystals (semiconductor nanocrystals) to chemical sensors 49
2.5.1 Mechanism and Principles of chemical sensors 53
2.6 Application of semiconductor nanocrystals to dye sensitized solar cells 64
2.6.1 Structure and operating principle of a dye sensitized solar cell 65
2.6.2 Characterization of parameters 72
Chapter 3 : Synthesis and characterization of indium selenide nanocrystals 105
3.1 Background 105
3.2 Properties of different polymorphs of indium selenide 106
3.2.1 Indium (III) selenide, In_2Se_3 107
3.2.2 Tetraindium triselenide, In_4Se_3 108
3.2.3 Indium monoselenide, InSe 109
3.2.4 In_6Se_7 110
3.3 Synthetic methods to make of indium selenide 110
3.4 Experimental 113
3.4.1 Chemicals and materials 113
3.4.2 Synthesis of indium monoselenide nanocrystals using the non-hot injection method 113
3.4.3. Synthesis of In_2Se_3 nanocrystals using a non – hot injection method 114
3.5 Characterization techniques 114
3.5.1 Optical characterization 114
3.5.2 Structural characterization 115
3.6 Results and discussions 115
3.6.1 Interdependency of time and precursor concentration: their effect on the properties of the nanocrystals 115
3.6.2 Formation mechanism of InSe nanosheets 141
3.6.3 Formation pathway of InSe nanoparticles 143
3.7 Effect of ligand variation and time on the properties on In_xSe_y (incomplete) 146
3.7.1 50 % OLA and 50 % 1-DDT 146
3.7.2 80 % OLA and 20 % 1-DDT 148
3.8 Mechanism of formation of InSe phase and In_2Se_3 phase 154

3.9 Conclusions 156
Chapter 4 : Applications of indium selenide nanocrystal in chemical sensors for detection of volatile organic compounds. 165
4.1 Background 165
4.1.1 Definition and sources of VOCs 165
4.1.2 Importance of formaldehyde detection 165
4.1.3 Use of nanostructures to improve the performance of chemical sensors 167
4.1 Experimental procedures 169
4.1.1 Chemicals and materials 169
4.2.2 Device fabrication and characterization 169
4.3 Results and Discussions 171
4.3.1 Formaldehyde and methanol sensing properties of InSe nanostructures 173
4.3.2 InSe nanoparticle based sensors 174
4.3.3 Temperature studies for nanoparticles based sensors during the detection of formaldehyde and methanol 178
4.3.4 Response of nanoparticles based sensor to other VOCs for selectivity study 180
4.3.5 Formaldehyde and methanol sensing properties of InSe nanosheets 181
4.3.6 Temperature studies for nanosheets based sensors during the detection of formaldehyde and methanol 183
4.3.7 Response of nanosheets based sensor to other VOCs for selectivity study 184
4.3.8 Comparison of the activity of nanoparticles and nanosheets devices on detection of formaldehyde; difference in the shape of the curves. 185
4.4 Conclusions 188
Chapter 5 : Synthesis and characterization of nickel selenide nanocrystals 193
5.1 Background 193
5.2 Experimental 195
5.2.1 Chemicals and materials 195
5.2.2 Synthesis of nickel selenide nanostructures 195
5.2.3 Characterization techniques 197
5.3 Results and Discussion 198
5.3.1 Synthesis of Ni_3Se_2 nanostructures via hot injection in HDA (with TOP) 199
5.3.2 Synthesis of Ni_3Se_2 nanostructures in OLA 210

5.3.3 Synthesis of nickel selenide nanostructures via direct heating method (without TOP) 219
5.3.4 Effect of different coordinating solvents on the structural properties of nickel selenide nanoparticles 229
5.4 Conclusions 234
Chapter 6 : Application of Nickel Selenide nanocrystals as counter electrodes in dye sensitized solar cells (DSSCs). 238
6.1 Background 238
6.2 Experimental procedures 240
6.2.1 Chemicals and materials 240
6.3 Fabrication and assembly of the DSSC device 240
6.3.1 Cleaning of the substrates 240
6.3.2 Preparation of TiO_2 paste 240
6.3.3 Fabrication of the photoanode 241
6.3.4 Preparation of the counter electrode 241
6.3.5 Device assembly 242
6.4 Characterization techniques 243
6.4.1 Structural characterization 243
6.4.2 BET measurements 244
6.4.3 Photovoltaic measurements 244
6.5 Results and Discussion 244
6.6 Conclusion 256
Chapter 7 : Conclusion and Future work. 263
7.1 Conclusion 263
7.2 Future work 265
Appendix 267

List of figures

Figure 2-1: Schematic correlation diagram relating cluster states to the bulk crystal states [5, 7]. 9

Figure 2-2: Density of electron states for various dimensionalities showing the process of energy bands splitting from bulk system to a quantum confined system, QD. For d = 1, 2, 3, the density of states obeys $\rho(E)\alpha E^{\frac{d}{2}-1}$. For a quasi-zero dimensional system, the density of states is described by a set of δ-functions [13, 17]..... 10

Figure 2-3: (a) is a schematic diagram of the three lowest discrete energy levels of electron, and hole, in a semiconductor nanocrystal quantum dot with the corresponding wave functions are represented by the dashed lines. Allowed optical transitions are given by the arrows. (b) Assignment of the excitonic peaks observed in the absorption spectrum of colloidal CdTe quantum dots associated with the three optical transitions [82, 83]. 21

Figure 2-4: Schematic representation of the mixing between different valence subbands of CdSe nanocrystals as a result of quantum confinement. The arrows indicate allowed interband optical transitions; (b) is the linear absorption spectrum of CdSe with average rad radius of 4.1 nm showing the positions of the four well-resolved transitions that involve either 1S or 1P electron states [85, 86]. 22

Figure 2-5: Shows the cascade intraband relaxation steps [18]. 24

Figure 2-6: Schematic illustration of exciton recombination pathways in semiconductors with (1) radiative recombination, (2) defect assisted radiative recombination and 3) non-radiative recombination [82, 83]. 26

Figure 2-7: Calculated band structures of (a) bulk MoS_2, (b) quadrilayer MoS_2, (c) bilayer MoS_2, and (d) monolayer MoS_2 [109]. 29

Figure 2-8: Change in free energy during the formation of a spherical crystal nucleus. ΔGv gives the volume excess free energy, ΔGs the surface excess free energy, and ΔGTOT is the free energy change. ΔGc indicates the activation energy for nucleation [82]. 33

Figure 2-9: Two-dimensional representation of end-member growth mechanisms: (upper) growth of large crystals at the expense of small crystals and (lower) growth by assembly. 35

Figure 2-10: Simple energy landscape illustrating the choice between the thermodynamically and kinetically controlled products..... 37

Figure 2-11: The lowest energy structure of a nanocrystal can vary, depending on the relative stability of its facets. 38

Figure 2-12: Schematic illustration of the influence of the monomer fluxes on the shape of a colloidal NC. (a) high monomer flux, (b) low monomer flux, (c) very low monomer flux [144]. 42

Figure 2-13: Schematic illustration of the classification of chemical sensors. 55

Figure 2-14: Diagram illustrating the electronic structure of a semiconductor for an n-type semiconductor with band gap, Eg, bulk Fermi level, E_f, surface Fermi level, E_{fs}, and surface potential, ϕs. The near-surface electric field, the depletion region, is shaded, and the filled electronic levels are speckled [210]. 57

Figure 2-15: Shows a three-dimensional view of the crystallite of gas-sensitive material after adsorption of oxygen [227]. 60

Figure 2-16: Defined regions of the general response curve [24]. 61

Figure 2-17: Classification of the electrolytes used in dye-sensitized solar cells. IL stands for ionic liquids, HTM for hole transport material and PE is polymer electrode [241]. 67

Figure 2-18: Operating principle of dye-sensitized solar cells [241]. 71

Figure 2-19: The J-V characteristics of solar cell in the dark and under illumination [289]..... 73

Figure 2-20: Equivalent circuit used to represent interfaces in solar cell [251, 297]. 76

Figure 3-1: Binary phase diagram of indium selenide as adopted from Han et al. [8]. 106

Figure 3-2: Crystal structures of In_2Se_3 stochiometry as adopted from ref [8]. 108

Figure 3-3: Crystal structure model of In_4Se_3 [8]. 109

Figure 3-4: Crystal structure models of (a) β-InSe and (b) γ-InSe [8]..... 110

Figure 3-5: XRD patterns of InSe nanoparticles synthesized at temperature of 200 ºC with a mole ratio of 1:1 ($InCl_3$:Se) after: (a) 8 min which gave the InSe layers, (b) 10 min, (c) 30 min and (d) 60 min. 117

Figure 3-6 Multiple TEM images of InSe samples synthesized at temperature of 200 ºC with a mole ratio of 1:1 ($InCl_3$:Se) after (a-c) 8 min, (d-f) 10 min (g-i) 30 min and (j-k) 60 min. (l) show the particle size distribution of the nanoparticles. 119

Figure 3-7: HRTEM images of the nanosheets synthesized in 10 min and the nanoparticles synthesized in 60 min (insets are the FFT images of the corresponding HRTEM images). 121

Figure 3-8: EDS spectra of the nanosheets synthesized in (a) 10 min and the nanoparticles synthesized in (b) 60 min. 122

Figure 3-9: Absorption spectra for InSe nanoparticles synthesized at 200 ºC with a mole ratio of 1:1 after (a) 8 min, (b) 10 min, (c) 30 min and 60 min. 124

Figure 3-10: Photoluminescence spectra of InSe synthesized at a temperature of 200 ºC and a mole ratio of 1:1 after (a) 10 min (b) 30 min and (c) 60 min. 125

Figure 3-11: The band structure of InSe with the bulk band gap and electronic transitions. 126

Figure 3-12: XRD spectra of InSe nanocrystals from 1:2 mole ratio ($InCl_3$:Se) a) 10 min and b) 60 min. The peaks marked with (*) are indexed to In_2Se_3..... 128

Figure 3-13: TEM images of InSe nanocrystals from 1:2 mole ratio (inCl_3:Se) a) 10 min, b) 30 min and c) 60 min. 129

Figure 3-14: UV-vis spectra of InSe nanocrystals from 1:2 mole ratio ($InCl_3$:Se) (a) 10 min, (b) 30 min and (c) 60 min. 130

Figure 3-15: XRD patterns of InSe nanosheets synthesized at temperature of 200 ºC with a mole ratio of 2:1 ($InCl_3$:Se) after: (a) 8 min, (b) 30 min and (c) 60 min. 131

Figure 3-16: Multiple TEM images of InSe samples synthesized at temperature of 200 ºC with a mole ratio of 2:1 ($InCl_3$:Se) after (a) 8 min, (b) 30 min and (c) 60 min. 133

Figure 3-17: Absorption spectra for InSe nanosheets synthesized at 200 ºC with a mole ratio of 2:1 after (a) 8 min (b) 30 min and (c) 60 min. 135

Figure 3-18: Photoluminescence spectra of InSe synthesized at a temperature of 200 ºC and a mole ratio of 2:1 after (a) 8 min (b) 30 min and (c) 60 min. 135

Figure 3-19: XRD patterns of InSe nanosheets synthesized at temperature of 200 ºC with a mole ratio of 3:1 ($InCl_3$:Se) after: (a) 8 min and (b) 30 min. 137

Figure 3-20: Multiple TEM images of InSe samples synthesized at temperature of 200 ºC with a mole ratio of 3:1 ($InCl_3$:Se) after (a-c) 8 min, (d-f) 30 min and (g-i) 60 min. 139

Figure 3-21: Absorption spectra for InSe nanosheets synthesized at 200 ºC with a mole ratio of 3:1 after (a) 8 min (b) 30 min..... 140

Figure 3-22: Photoluminescence spectra of InSe synthesized at a temperature of 200 ºC and a mole ratio of 3:1 after (a) 8 min and (b) 30 min. 141

Figure 3-23: XRD pattern of In_2Se_3 nanosheets synthesized at temperature of 200 ºC with a mole ratio of 1:1 ($InCl_3$:Se) after 30 min 50 % OLA and 1-DDT. 147

Figure 3-24: TEM images of In_2Se_3 samples synthesized at temperature of 200 ºC with a mole ratio of 1:1 ($InCl_3$:Se) for 30 min..... 148

Figure 3-25: XRD patterns of InSe nanoparticles synthesized at temperature of 200 ºC with a mole ratio of 1:1 (InCl3:Se) after: (a) 10 min which gave the InSe layers, (b) 30 min and (c) 60 min. 149

Figure 3-26: Multiple TEM images of In_2Se_3 samples synthesized at temperature of 200 ºC with a mole ratio of 1:1 ($InCl_3$:Se) after (a) 15 min, (b) 30 min and (c) 60 min 50 % OLA/1-DDT. 150

Figure 3-27: EDS spectra of the nanocables and nanowires synthesized in 80 % OLA+ 20 % 1-DDT at 200° C for (a) 15 min and (b) 30 min respectively. 151

Figure 3-28: Absorption spectra of the samples obtained at (a) 15 min, (b) 30 min and (c) 60 min. 153

Figure 3-29: PL spectra of the In_2Se_3 nanocrystals produced in 80 % OLA + 20 % 1-DDT at 200 C for (a) 15 min, (b) 30 min and (c) 60 min. 153

Figure 3-30: Schematic representation of (a) reduction process In^{+3} to In^{+2} and Se to Se^{-2} when 100 % oleylamine was used and (b) the stabilization process of In^{+3} ions by both 2 ml and 5 ml of 1-DDT introduced in the reaction mixture. 155

Figure 4-1: TEM images of InSe (a) nanoparticle and (b) nanosheets used in the device fabrication while (c) is the film of the nanoparticles and (d) is the film of the nanosheets based sensors. 171

Figure 4-2: Graphs of (a) conductance and (b) capacitance verses frequency for the nanoparticles based sensors while c) is the conductance and d) the capacitance verses frequency for the nanosheets based sensors used to determine the working frequency. 173

Figure 4-3: The dynamic response recovery curves of InSe nanoparticle based sensors when exposed to 15 ml of (x) methanol and y) formaldehyde at room temperature. 175

Figure 4-4: Repeatability curves for the nanoparticle based sensors when exposed to (a) methanol and b) formaldehyde fumes. 176

Figure 4-5: a) is the nanoparticle sensor response to different concentration of formaldehyde fumes and b) is the sensitivity curve of the same sensor. 176

Figure 4-6: Response curve for nanoparticle based sensor when exposed to formaldehyde fumes for longer duration to ascertain the possibility of the sensor reaching saturation point. 178

Figure 4-7: Response verses temperature curves when the nanoparticle based sensor was exposed to different concentration of (a) formaldehyde and b) methanol fumes. 179

Figure 4-8: Sensitivity curves of the nanoparticle based sensors when exposed to different concentration. 181

Figure 4-9: Dynamic response curves for nanosheets based sensors when exposed to a) methanol and b) formaldehyde fumes. 182

Figure 4-10: a) Response curve for nanosheet based sensors when exposed in different concentration of formaldehyde and b) is the sensor's sensitivity profile. 183

Figure 4-11: Response verses temperature curves when the nanosheets based sensor was exposed to different concentration of (a) formaldehyde and b) methanol fumes. 184

Figure 4-12: Sensitivity profiles of the nanosheets based sensors when exposed to a) acetone and b) chloroform fumes. 185

Figure 4-13: Gas response curves of a) nanoparticle b) nanosheet based sensors when exposed to 15 µL formaldehyde gas. 187

Figure 4-14: Gas response verses frequency curves of a) nanoparticles and b) nanosheets based sensors when exposed to methanol and formaldehyde. 188

Figure 5-1: Schematic illustrations of the commonly observed crystal structures of a) $NiSe_2$, b) $Ni_{1-x}Se$ and c) Ni_3Se_2. 194

Figure 5-2: XRD pattern of Ni_3Se_2 synthesized in HDA at 180 °C after (a) 10 min, (b) 30 min (c) 60 min and (d) is the XRD pattern for pure HDA. 200

Figure 5-3: TEM images of Ni_3Se_2 synthesized in HDA at 180 °C after (a) 10 min, (c) 30 min and (e) 60 min. The particles sizes demonstrated Ostwald ripening process. 202

Figure 5-4: Absorption spectra of quantum dots synthesized at 180 °C in HDA for (a) 10 min, (b) 30 min and c) 60 min. 204

Figure 5-5: The emission spectra of quantum dots synthesized in HDA at 180 °C at (a) 10 min, (b) 30 min and (c) 60 min. 205

Figure 5-6: XRD pattern of Ni_3Se_2 synthesized in HDA at 200 °C after (a) 10 min, b) 30 min and c) 60 min. 206

Figure 5-7: TEM micrographs of Ni_3Se_2 nanocrystals obtained at (a) and (b) 10 min, (c) and (d) 30 min, (e) and (f) 60 min in HDA at 200 °C. 207

Figure 5-8: Absorption spectra of the Ni_3Se_2 synthesized at 200° C at (a) 10 min, (b) 30 min and (c) 60 min in HDA. 209

Figure 5-9: Emission spectra of the Ni_3Se_2 synthesized at 200° C at (a) 10 min, (b) 30 min and (c) 60 min in HDA. 210

Figure 5-10: XRD patterns for Ni_3Se_2 fabricated in OLA at 200 °C for (a) 10 min and (b) 30 min. 212

Figure 5-11: TEM images of Ni_3Se_2 synthesized in OLA at 200 °C after (a) 10 min and (b) 30 min. 213

Figure 5-12: Absorption spectra of Ni_3Se_2 synthesized in OLA at 200 °C after (a) 10 min and (b) 30 min. 214

Figure 5-13: Emission spectra of Ni_3Se_2 synthesized in OLA at 200 °C after (a) 10 min and (b) 30 min. 214

Figure 5-14: : XRD spectra of Ni_3Se_2 synthesized in OLA at 220° C for (a) 10 min and (b) 30 min. 215

Figure 5-15: TEM images of Ni_3Se_2 synthesized in OLA at 220 °C after a) 10 min and b) 30 min. 216

Figure 5-16: The absorption spectra of the Ni_3Se_2 fabricated in OLA at 220 °C for (a) 10 min and (b) 30 min. 217

Figure 5-17: The emission spectra of the Ni_3Se_2 fabricated in OLA at 220 °C for a) 10 min and b) 30 min. 218

Figure 5-18: XRD patterns of nickel selenide nanoparticles synthesized at mole ratio (Ni/Se) 1:1 for 30 min at a) 180° C and b) 200° C. The matched indices are for the monoclinic Ni_3Se_4 while the (*) represent the cubic $NiSe_2$ peaks. 220

Figure 5-19: SEM micrographs of nanoparticles synthesized at mole ratio 1:1 for 30 min 180 °C with (b) being the higher showing the nanoparticles at higher magnification than a) and 200 °C with (d) representing the nanoparticles at higher magnification than (c). 221

Figure 5-20: Absorption spectra of nanoparticles synthesized at mole ratio 1:1 for 30 min at (a) 180° C and (b) 200° C. 222

Figure 5-21: Emission spectra of nanoparticles synthesized at mole ratio 1:1 for 30 min at (a) 180° C and (b) 200° C. 223

Figure 5-22: XRD patterns of $NiSe_2$ obtained at mole ratio 1:2 after 30 min showing phase evolution from orthorhombic $NiSe_2$ to thermodynamically stable cubic $NiSe_2$ at (a) 180 °C, (b) 200 °C and c) 220 °C. 225

Figure 5-23: (a) and (b) are the SEM images of the $NiSe_2$ nanoparticles fabricated at 180 °C and 200 °C respectively while (c) are the TEM images of the particles fabricated at 220 °C. All these were obtained at a mole ratio 1:2 for a period of 30 min. 226

Figure 5-24: Absorption spectra of $NiSe_2$ nanoparticles obtained in a mole ratio 1:2 at reaction temperatures (a) 180 °C, (b) 200 °C and (c) 220 °C for duration of 30 min in oleylamine as the coordinating solvent. 228

Figure 5-25: Emission spectra of $NiSe_2$ nanoparticles obtained in a mole ratio 1:2 at reaction temperatures (a) 180 °C, (b) 200 °C and (c) 220 °C for duration of 30 min in OLA as the coordinating solvent. 229

Figure 5-26: The XRD patterns of nanoparticles synthesized at 200 °C for 30 min in different solvents. In (a), spectra w, x, y and z represent nanoparticles obtained in; ODA/TOP, HDA/TOP, OLA/TOP and OLA/OA respectively. (b) Spectra w, x, y and z are obtained from nanoparticles synthesized in; ODA, HDA, OA and OLA respectively. The (*) in spectrum w are associated with impurities in the sample while the (#) in spectrum are ascribed to NiSe phase within the sample. Spectrum x in both (a) and (b) have the same indices as they were matched using the same card numbers. 231

Figure 5-27: (a) TEM image of nanoparticles obtained in HDA/TOP; (b) TEM images of products obtained in ODA/TOP while (c) is the SEM image of same; (d) is the TEM image of NPs in OLA/TOP; (e) TEM images of NPs synthesized in HAD; (f) SEM image of NPs in OLA; (g) TEM image of NPs in OA; (h) TEM image of NPs in ODA and (i) SEM image of NPs in OLA/OA. 233

Figure 6-1: XRD patterns showing the stoichiometries of nickel selenide nanostructures used for the device fabrication; (a) Ni_3Se_2, (b) Ni_3Se_4 and (c) $NiSe_2$. The peaks marked (*) represent planes for both orthorhombic and cubic $NiSe_2$ phase and (#) presenting the planes for the cubic phase. 245

Figure 6-2: J-V characteristics curves of untreated Ni_3Se_4 and Ni_3Se_2 nanocrystals; (a) is the log curve of current density showing the dark current (represented by [x]) and current generated under illumination (represented by [y]) while (b) is the J-V curves showing the quality of the FF. 247

Figure 6-3: SEM images (a) Ni_3Se_2, (b) Ni_3Se_4 and (c) $NiSe_2$ respectively. 249

Figure 6-4: Photocurrent density-voltage characteristics of DSSCs with Ni_xSe_y-Pt and Pt CEs at AM1.5G illumination (100 mW cm^{-2}). 250

Figure 6-5: An image showing the cracked TiO_2 surface after exposing it air for 10 min. 252

Figure 6-6: (a) Current-voltage characteristics of the reference Pt device and (b) Log-log curve of the dark current-voltage characteristic of the Pt device. 255

List of Schemes

Scheme 3-1: Formation pathway of InSe nanosheets 143

Scheme 3-2: Schematic illustration of the proposed growth mechanism for the InSe nanoparticles with the images based on TEM images obtained in the course of the 60 min synthesis. 145

Scheme 4-1: Sealable chamber for dynamic measurements rotating the cap 180° to expose the sensor from (a) ambient air to (b) the environment containing the VOC. 170

Scheme 5-1: Schematic representation of the reaction procedure followed for the hot injection method..... 196

Scheme 5-2: Illustration of the synthetic procedure followed in the direct heating/non-hot injection method..... 197

Scheme 6-1: Schematic illustration of the assembled DSSC device. 243

List of tables

Table 3-1: A summary of the results generated from UV – vis and the emission profiles..... 126

Table 3-2: A summary of the UV-vis and the emission profile results 136

Table 3-3: A summary of the UV-vis and the emission profiles 141

Table 4-1: Shows the sensitivity of the InSe nanostructured devices to the presence of different volatile organic compounds. 180

Table 6-1: Summary of the BET surface area of different stoichiometries of different nickel selenide nanostructures used in the fabrication of the counter electrodes. 246

Table 6-2: Photovoltaic performance parameters of DSSCs with Ni_xSe_y-Pt and Pt CEs measured at AM1.5G illumination (100 mW cm^{-2}). 250

Table 6-3: A summary of photovoltaic performance parameters of various Ni-Se CE from literature. 253

List of symbols and abbreviations

BET - Bruanauer–Emmett–Teller

CdSe - Cadmium selenide

CdTe - Cadmium telluride

CE - Counter electrode

CuInSe - Copper indium gallium selenide

D-A - Donor-Acceptor

DDT - Dichlorodiphenyltrichloroethane

DSSCs - Dye-sensitized solar cell

ECS - Energy conversion and storage devices

EDS - Energy-dispersive X-ray spectroscopy

*E*g - Energy gap

ENIG - Electroless Nickel Immersion Gold

FF - Fill factor

FFT - Fast Fourier transform

FTO - Fluorine doped tin oxide

HCHO - Formaldehyde

HDA - Hexadecylamine

HER - Hydrogen evolution reaction

HOMO - Highest occupied molecular orbital.

HRTEM - High resolution transmission electron microscopy

HTMs - Hole transport materials

IDLH - Immediately dangerous to life or health

InSe - Indium selenide

IPCE - The incident photon-to-electrical (power) conversion efficiency

ISMES IV - International School for Materials for Energy and Sustainability

ITO - Indium doped tin oxide

Jsc - Short circuit current density

LUMO - Lowest unoccupied molecular orbital

MBE - Molecular beam epitaxy

MeOH - Methanol

MOCVD - Metal-organic chemical vapour deposition

MoS_2 - Molybdenum disulphide

NCs - Nanocrystals

NIOSH - National Institute for Occupational Safety and Health

NRF - National research foundation

NYRS - National nanotechnology young researcher's symposium

OA - Oleic acid

ODA - Octadecylamine

OER - Oxygen evolution reaction

OLA - Oleylamine

OWSD - Organization for Women in Science for the Developing World

PbSe - Lead sulphide

PCE - Power conversion efficiency.

PL - Photoluminescence

Pt - Platinum

QDs - Quantum dots

QFL - Quasi-Fermi level

QSLs - Quantum-size levels

RCT - Charge transfer resistance

RGO - Reduced graphene oxide

R_s - Series resistance

R_{sh} - Shunt resistance

SAIP - South African Institute of Physics

SDOS - Surface density of states

SEM - Scanning electron microscope

SMO - Semiconductor metal oxide

TEM - Transmission electron microscope

TiO_2 - Titanium dioxide

TMSs - Transition-metal selenides

TOP - Tri-n-octylphosphine

TOPO - Tri-n-octylphosphine oxide

UV-VIS - Ultraviolet-visible spectrophotometry

VOCs - Volatile organic compounds

WHO - World Health Organization

ZnO - Zinc oxide

Thesis synopsis

Chapter one entails a brief background on the importance of nanomaterials and nanosystems towards the realization of possible solutions to the global sustainability challenges. In addition, the chapter synopsis, the aims, objectives and motivation for the project are also presented herein.

Chapter two introduces the main building block of this research – the colloidal semiconductor nanocrystals and their electronic components. The chapter begins with an introduction on the concept of semiconductor nanocrystals tackling quantum dots and low dimension semiconductor nanocrystals. A short description on the properties of semiconducting nanocrystals that make them suitable for application in solar cells and chemical sensors are also included with emphasis on metal selenide nanocrystals. Different synthetic methods to prepare colloidal nanostructures are then described. This chapter also focusses on the basic concepts of solar energy conversion using photovoltaics and application of semiconductor nanocrystals in solar cells. Attention is fixed on dye sensitized solar cells and the working principle of a DSSC is discussed herein. Also included in this chapter are the basic concepts and the working principles of chemical sensors with emphasis of the application of semiconductor nanocrystals in chemicals sensors.

Chapter three focusses on colloidal synthesis and characterization of indium selenide nanocrystals. The chapter begins with an introduction to indium selenide series describing the characteristics of different polymorphs of the In – Se system followed by different synthetic methods employed in literature to obtain different forms and phases of In_xSe_y. Next, the effects of growth conditions such as time, concentration of the precursors, and type of ligand on the formation via direct heating method and the properties of In-Se nanostructures are presented in

this chapter. The effect of achieving nearly monolayer InSe nanosheets and its effect on the band structure of the semiconductor is also mentioned herein.

Chapter four focusses on the use of indium selenide nanostructures as the sensing material in conductiometric/chemiresistive sensors for the detection of volatile organic compounds (VOCs). The chapter commences with a brief definition of VOCs and their various sources; then attention is narrowed to the detection of formaldehyde. The experimental results on the sensing ability of InSe nanoparticles and nanosheets are presented in this chapter. The result of conductance and capacitance variation when the sensors were exposed to methanol, formaldehyde, chloroform and acetone are discussed herein. The chapter demonstrates the use of two distinctly different sizes and shapes of InSe NCs in order to illustrate the difference in the electronic properties of the nanostructures as a result of shapes and sizes and their different interaction with the analyte gas.

Chapter five describes the various synthetic methods including hot injection method and the direct heating method employed to synthesize nickel selenide nanostructure series together with the characterization techniques used. The chapter begins with a brief introduction on the different polymorphs of the nickel selenide series and the various methods that have been employed in literature to obtain them. Next the experimental results presented in this chapter demonstrates the significant impacts the growth conditions such as time, reaction temperature, concentration of precursor, method of synthesis and the type of ligand have on the properties of the final products. The chapter also examines the effect of mixed ligands on the resulting properties of nickel selenide, more specifically the effect of TOP when used hand in hand with other coordinating solvents, and the results are discussed herein.

Chapter six explores the utilization of different stoichiometries of nickel selenide series as counter electrodes in DSSCs with the aim of finding an alternative to expensive platinum. The chapter begins with a short introduction on the urgency to find alternative sources of energy with a few examples of renewable sources of energy. Then it describes the use of transition metal chalcogenides as major components in several energy conversions and storage devices with main focus on nickel selenide nanostructures. A few reports from the literature on the use of nickel selenide as counter electrodes in DSSCs are also presented in this chapter. Further on, the chapter demonstrates both the catalytic and electronic properties of the as-prepared nickel selenide nanoparticles. Different stoichiometries are incorporated into the DSSCs as counter electrodes after which the results from their *I-V* characteristic curves are presented.

Chapter 7 presents a general summary and conclusion of the work presented in this thesis. The chapter highlights the successes of the projects, together with some recommendations for further investigations.

Chapter 1 : Background and rational

1.1 Background

Great potential in improving the quality and sustainability of life has been exhibited by materials approaching the nanoscale dimension [1]. Current research developments in nanotechnology and nanoscience are aimed at achieving and/or improving the sustainable developments, virtually in all industrial sectors including health care, telecommunication technologies (electronics), energy and transport, agri-food and water purification. Among the global challenges that greatly influences these developments are energy and environmental sustainability [2].

Energy shortage has become a major concern. Currently the increasing world population which is expected to double by the middle of the 21st century and the massive growth in the economic development surges the global demand for energy. These consequently have created immense shortage in the energy sector, and so, much pressure on the existing energy resources. It is also noteworthy that fossil fuels, which are a major source of energy, are also dwindling fast. Therefore, in the light of preceding explanations, we can point out the fact that energy is one of the main factors that must be considered in discussions of sustainable development in terms of its sustainable supply. Ongoing research has pointed out that one solution to the impending energy shortage is to make more use of renewable energy sources such as solar energy. Solar energy can be converted to more usable forms by using technologies such as photovoltaics. Further, studies have indicated that there is still a huge gap between our present use of solar energy and its potentials thus posing a grand challenge in energy research.

Environment remediation especially air quality has become a worldwide concern. Among the pollutants considered during air quality control are volatile organic compounds (VOCs).

VOCs are important class of compounds but have adverse effects on human health at high concentrations. In addition atmospheric VOCs play a critical role as precursors of ozone, photochemical smog and can form secondary organic aerosols. The present over reliance on fossil fuels for energy not only has a major impact on the environment through land and the surrounding water bodies' degradation; but are also major sources of VOCs in the atmosphere. For instance combustion of fossil fuels in power plants and in vehicles and evaporative emissions from cars releases a number of VOC gases in the air. In addition, VOCs especially aromatic organic compounds are also among the most important ambient carcinogens. For example benzene is a known carcinogen and exposure to high ambient concentrations represents a considerable health risk, while toluene is toxic for the central nervous system. [2] Several methods have been used to detect these VOCs in the ambient. However, research indicates that there is still a challenge to develop sensors/detectors that are sensitive at low concentrations and selective; sensors that are durable and can operate at low temperatures.

In light of the above observations, advancement in nanotechnology promises to contribute to resource saving via improvement in renewable energy sources, reduced consumption of materials and improving the environment. Specifically nanomaterials and nanosystems offer platforms that can provide efficient, cost-effective, and environmentally acceptable solutions to the global sustainability challenges facing society [3]. Recent progress in the synthesis of nanomaterials and fundamental understanding of their properties has led to significant advances in the integration of these nanomaterials into many applications such as optoelectronic devices for clean energy generation, storage, utilization, waste heat recovery and environmental purification (detoxification and disinfection) [4]. However, there is still great need to find a workable balance between the surging needs for clean and reliable sources of energy, public safety and the preservation of the natural environment. From a

science perspective the challenge is to design a new generation of novel materials that can wisely produce and wisely consume energy and detect the cleanliness of the environment [2, 3, 5, 6]. Leading experts around the world have highlighted the latest findings on a wide range of methods to fabricate different nanostructures including semiconductor nanocrystals with their different applications. In addition to these findings, this thesis is devoted to the colloidal synthesis and characterization of novel semiconducting metal selenide nanostructures with controlled sizes, shapes, crystalline phases and structures for their utilization in energy conversion and environmental purification through the establishment of solar cells and chemical sensors respectively.

1.2 Problem statement

Solar energy and in particular solar cell technology is seen as a best alternative for energy generation for electrification. There are three generations of solar cells. The first and second generation type of solar cells are currently commercially available in the market, however they are expensive as a result of the high manufacturing cost of the technology involved in processing them. DSSCs which fall under the third generation solar cells widely use platinum, a noble metal, to fabricate efficient counter electrode (CEs) due to its high conductivity and electro-catalytic activities. Nevertheless, the high cost, limited resources, and corrosion by iodine species in the electrolyte solution seriously restricts the large-scale application of Pt-based CEs in DSSCs. Therefore, economic, stable, and effective non-Pt catalysts should be exploited to fabricate novel CEs.

In terms of environmental monitoring, gas detection using semiconductor metal oxide as their detection portion has had considerable impact to date. However, the need to operate at higher temperatures often limits this type of detection. In addition the available gas sensors in the market are quite expensive and they have a reduced sensitivity, selectivity and reversibility in

specified temperature conditions. Therefore, the capability of producing inexpensive sensors that can quickly identify the analyte even at low concentrations and can operate at low temperatures is of great essence.

1.3 Motivation

Nanostructured materials unlike their bulk counter parts are solution processable and thus present the possibility to produce low cost devices. In addition, they have excellent optical, electronic and catalytic properties and their sizes can be manipulated to obtain the desired band gaps to cater for the entire solar spectrum. Similarly, their catalytic activities can also be enhanced by manipulating their shapes and sizes during synthesis, and thus present a suitable property to be employed as CEs in DSSCs. Besides, their nano-size, nanostructured materials have large surface area to volume ratio make them ideal candidates for sensing purposes since the sensing mechanism relies on the interaction between the surface atoms of the material and the environment. Particularly for metal selenides and sulfides, their bandgaps are relatively low compared to their metal oxide counterparts. This means that the activation of intrinsic reactions occur at lower working temperatures, and only a minor energy supply is necessary during their sensing process. Also, the absence of oxygen in the crystal lattice of these chalcogenides may lead to a different catalytic mechanism on the surface reaction with respect to the metal oxides which dominate the chemo–resistive sensor based arena.

1.4 Aims and objectives

Generally, this work focusses on the colloidal synthesis of metal selenide (MSe; M=Ni, In) nanostructures with properties that can be exploited in both photovoltaics and sensing technologies. A detailed understanding on the role of the growth conditions such as time of synthesis, concentration of precursors, temperature of reaction and coordinating solvent on the properties of the final product is of great interest. Similarly, another point of concern is the effect of shapes, sizes and phase structure variation on the electronic and catalytic

properties of the as-prepared nanocrystals through (a) investigating their catalytic activities in DSSCs as counter electrodes and (b) experimental identification of the interaction of the semiconductors with the analyte during sensing.

To achieve the above mentioned aims, the following objectives were identified:

- Colloidal synthesis of In_xSe_y and Ni_xSe_y nanocrystals using the hot injection method and the direct heating method.
- To investigate the effect of different growth conditions including time of synthesis, coordinating solvents (ODA, OLA, OA, TOP, 1-DDT), temperature of reaction and concentration of precursors on the structural, optical, electronic and catalytic properties of the as-prepared nanostructures.
- Characterization of In_xSe_y and Ni_xSe_y nanocrystals via a number of techniques such as SEM, TEM, HRTEM, UV-VIS, PL among others.
- To fabricate solar cell and gas sensor devices based on the nanocrystals.
- To characterize/measure the performance of the fabricated devices.

References

[1] A. Vaseashta, Nanomaterials nexus in environmental, human health, and sustainability, in: Silicon versus carbon, Springer, 2009, pp. 105-118.

[2] A. Kelarakis, Functional nanomaterials for energy and sustainability, Advanced Materials Letters, 5 (2014) 236-241.

[3] M.S. Diallo, N.A. Fromer, M.S. Jhon, Nanotechnology for sustainable development: retrospective and outlook, Journal of Nanoparticle Research, 15 (2013) 1-16.

[4] A. Tuantranont, Applications of Nanomaterials in Sensors and Diagnostics, Springer Ser. Chem. Sens. Biosens, 14 (2013).

[5] T. Masciangioli, W.-X. Zhang, Peer reviewed: environmental technologies at the nanoscale, Environmental Science & Technology, 37 (2003) 102A-108A.

[6] D. Rickerby, M. Morrison, Nanotechnology and the environment: A European perspective, Science and Technology of Advanced Materials, 8 (2007) 19-24.

Chapter 2 : Introduction to colloidal semiconductor nanocrystals.

2.1 Introduction

The global semiconductor industry is a multi-billion dollar sector and forms the foundation of countless other industries including electronics, telecommunication, healthcare, energy and transport, agri-food, water purification and environmental monitoring. The modern microelectronics industry requirements of miniaturization, low power, efficient conversion and fast operation make it absolutely clear that the next generation of electronic devices will use the physics of low dimensional semiconductor structures often referred to as nanocrystals [1, 2]. Semiconductor nanocrystals exhibit fascinating and unique properties compared to their bulk materials due to confinement of their carriers to specific volume, which is at comparable or smaller in size to its Bohr radius [3, 4]. Bulk semiconductors are characterized by their band structures (direct or indirect) and their band gap energy (*E*g), which is the minimum energy required to excite an electron from the ground state valence energy band into the vacant conduction energy band. Upon absorption of a photon of energy greater than Eg, an exciton is created. An exciton, usually defined as an electron – hole pair bound together by a small binding energy is characterized by a finite size within the crystal defined by the Bohr exciton diameter. If one dimension of semiconductor nanocrystal is smaller than the Bohr exciton radius of the material (which normally ranges from 1 nm to 100 nm depending on the material) the band structure will be modified such that the charge carriers become spatially confined. In addition the continuous energy bands of the bulk semiconductor will be split into discrete energy levels like molecules as demonstrated in Fig. 2-1 [4-12]. Elementary excitation of nanocrystals will therefore experience quantum confinement resulting in finite motion along the confinement axis that is in either one (quantum wires e.g nanorods, nanowires and nanofibers), two (quantum well e.g nanodisks) or three (quasi-zero-dimensional system, quantum dot) dimensions. Consequently, a gradual

reduction in the density of state is experienced when transitioning from bulk system to a quantum confined state; this is illustrated in Fig. 2-2 [7, 13-16]. For the one and two dimensional quantum confined nanostructures, the density of electron and holes can be expressed according to equation 2-1 where *d* is the number of dimensions and E, the energy measured from the bottom of the conduction band for the electrons and the top of the valence band for the holes [17, 18].

$$\rho(E)\alpha E^{\frac{d}{2}-1} \quad \text{d=1, 2, 3.} \quad \ldots\ldots\ldots\ldots\ldots\ldots\ldots\ldots\ldots\ldots\ldots\ldots \quad (2\text{-}1)$$

Based on this equation, a three dimensional system will have continuous energy levels as a result of a smooth square-root function of energy. In one and two dimensional structures where $d = 1$ and $d = 2$, the density of states are no longer continuous and number of discrete energy levels appear due to the quantum confinement effect according to equation 2-2, where *l* is the size along the confinement direction [17].

$$E_n = \frac{\pi^2\hbar^2}{2m_{e,h}l^2}n^2 \quad \text{n=1, 2 , 3}\ldots\ldots\ldots\ldots\ldots\ldots\ldots\ldots\ldots\ldots\ldots\ldots \quad (2\text{-}2)$$

Equation 2-2 can be modified to equation 2-3 to give the direction in which the exciton formed inside different dimensions would move. For example, in a 1D, the exciton would have motion along the z axis and very limited motion along x- and y-axis. For 2D, the motion would be restricted in either two planes [17].

$$E(k) = E_n + \hbar^2\frac{(k_x^2 + k_y^2)}{2m_{e,h}} \quad \ldots\ldots\ldots\ldots\ldots\ldots\ldots\ldots\ldots\ldots\ldots\ldots \quad (2\text{-}3)$$

Quantum dots whose $d = 0$ experiences a slightly different scenario as their structures are zero dimensional. They are characterized by a discrete δ-function-like density of states with finite motion of quasiparticles in all directions, and a finite number of atoms and of elementary excitations within the same quantum dot [17]. Therefore, semiconductor

nanocrystals are tiny crystalline particles that exhibit size dependent electron and optical properties as a result of possible manipulation of the size of the exciton. With typical dimensions in the range of 1-100 nm, these nanocrystals bridge the gap between bulk crystals properties and the quantum confinement regime, thus enabling the exploitation of the useful properties of crystalline materials. In addition to the unique optical and electronic properties, there is a substantial increase in the fraction of surface atoms which in turn have increasing surface effects on other characteristics of materials such as phase transitions, phase transition temperatures, conductivity and electron affinity. Subsequently these also become shape and size dependent and are always referred to as the "size effect".

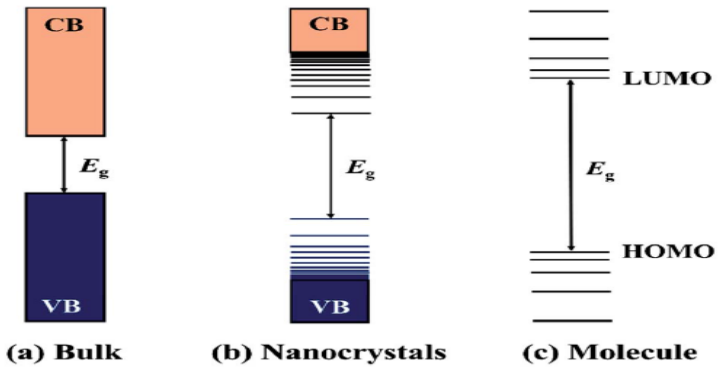

Figure 2-1: Schematic correlation diagram relating cluster states to the bulk crystal states [5, 7].

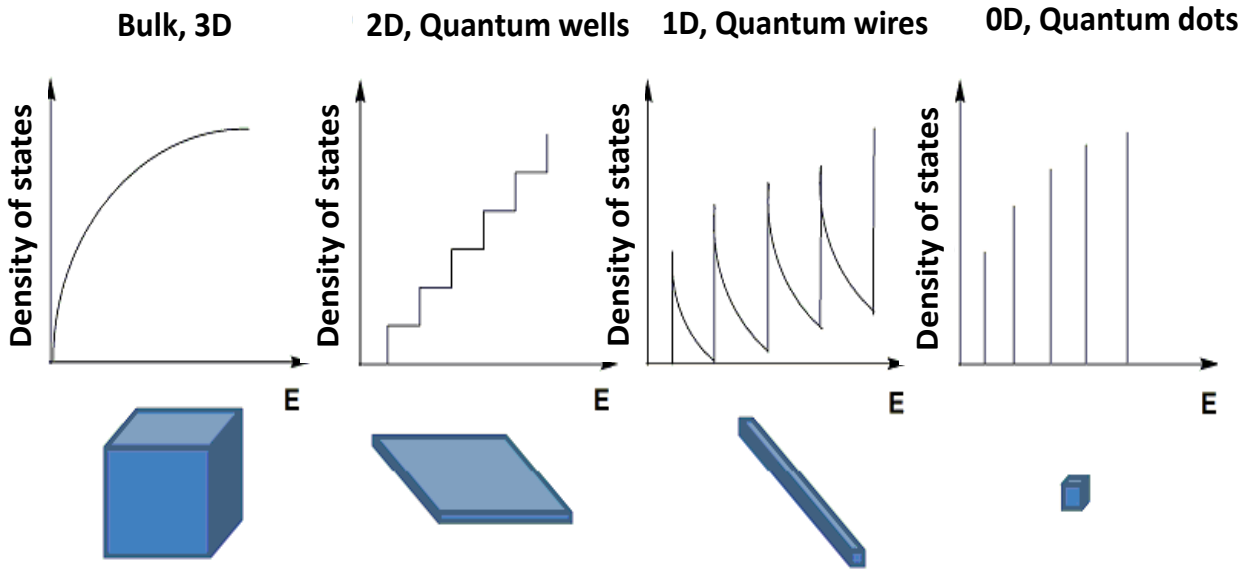

Figure 2-2: Density of electron states for various dimensionalities showing the process of energy bands splitting from bulk system to a quantum confined system, QD. For d = 1, 2, 3, the density of states obeys $\rho(E)\alpha E^{\frac{d}{2}-1}$. For a quasi-zero dimensional system, the density of states is described by a set of δ-functions [13, 17].

1980s marked the genesis of nanocrystals when they were discovered embedded in glass matrices containing semiconductor crystallite pigments [5, 11, 19-21]. Since then tremendous advances have been made on the syntheses of semiconductor nanocrystals with emphasis on size control in order to determine the extent of quantum confinement. In the current research, nanocrystals are often fabricated as colloids suspended in solution or as epitaxial structures grown on solid crystalline substrates. Epitaxial technologies (e.g. molecular beam epitaxy and metalorganic chemical vapour deposition) have been used to reproducibly prepare nanocrystals with a wide range of shapes and sizes in regular patterns which can then be directly incorporated into optoelectronic devices. However, solution phase techniques have provided flexible chemical processing with exceptional control over sizes and dimensionality/shape [11]. By controlling their dimensionality and finite sizes during synthesis, novel electro-optical, magnetic and structural properties are achieved to suit a

particular design of application [22]. For example, the 1-D semiconductor nanocrystals (nanorod and nanowires) have noticeably different optical properties in comparison to their quantum dot counter-parts [23-25]. For instance, the magnetic dipole moment tend to occur along the axis of the magnetic nanocrystals as the easy axis, which is desirable property for magnetic information storage [26]. The catalytic properties of various types of colloidal nanocrystals have also been suspected to be dependent on their shape [27]. The shape evolution of colloidal nanocrystals can also be employed as a sensitive probe for studying crystallization processes [28, 29]. Such studies have benefited and will continue to benefit the development of synthetic chemistry for colloidal nanocrystals with a desired shape control and applications.

Among all types of colloidal semiconductor nanocrystals, metal selenides are the most pursued due to their importance in both fundamental and technological applications [30-32]. In the area of fundamental nanoscience, metal selenide nanocrystals have acted as models towards the realization of high quality nanocrystals with well controlled size, shape and surface passivation thus leading to the systematic elucidation of size-dependent scaling laws and processes involved in quantum confined systems [33]. Similarly in the area of technological applications, metal selenide nanocrystals have considerable usage as major building blocks especially in low band gap semiconductors, photovoltaics, IR detection applications (biomedical diagnosis) and light emitting diodes[33-41]. For example, CdSe nanocrystals due to their reproducibility, monodispersity and tunable optical properties in the quantum confinement size regime (quantum dots) have been regarded as prototypes for most semiconductor nanocrystals after their first synthesis by Bawendi's group in 1993 [25, 42-45]. ZnSe based nanocrystals with or without dopants play an essential role in developing transition metal semiconductor nanocrystals as substitutes for cadmium based fluorescent nanocrystals in order to eliminate the toxic component [46-48]. In addition, transition metal

doped ZnSe nanocrystals including Mn^{2+} and Co^{2+} doped ZnSe cores have been explored for spin based electronics due to their magneto–electronic properties [49, 50]. Recently, metal selenide nanocrystals have been intensively investigated as promising thermal electric materials [51-53]. In the field of solar cells, metal selenides including binary (e.g. PbSe) and complex selenides (e.g. CuInSe) are also being actively investigated as active/absorbing layers in photovoltaics [30, 54-56]. Simultaneously transition metal selenides such as nickel selenides, cobalt selenides, $MoSe_2$, WSe_2 and $TaSe_2$ among others have exhibited excellent catalytic activities thus are currently considered as potential replacement to the expensive platinum counter electrode in dye sensitized solar cells [57-60].

2.2 Properties of semiconductor nanocrystals

2.2.1 Electronic structure of semiconductor nanocrystals

Doing more with less is the mantra for the current era. One of the directions considerable in achieving this slogan is the drive towards miniaturization in the next generation electronic devices. Subsequently, understanding the changes in the electronic structure of semiconductor nanocrystals, which are the hope of miniaturized devices, as their dimensions become smaller is a prime motivation to study properties of semiconductors at nanoscale. One of the defining features of semiconductor nanocrystals is tuneable band gap, a property that has been tremendously investigated via optical spectroscopy and theoretical frameworks. The colour of light emitted by the semiconductor nanocrystal is determined by the width of the gap like in the case of numerous quantum dots of group II-VI semiconductors such as CdSe, CdS and ZnSe [10, 61-71]. Nanocrystalline materials which conserve the electronic wave function are called direct band gap materials while indirect band gap materials are those where the lowest electronic transition between valence band and conduction band is forbidden and they have very small absorption coefficients. Upon absorption of a photon, an electron is promoted from the valence band to the conduction band thereby creating an

electron- hole pair. As discussed earlier, a decrease in the size of the semiconductor nanocrystal such that it is comparable to or smaller than the natural length scale of the electron-hole pair, result in the carriers being confined by the boundaries of the nanocrystals dimensions. This occurrence often referred to as "quantum-size effect," leads to atom-like optical behaviour in nanocrystals as the bulk bands become quantized as depicted in Fig. 2-1

When nanocrystals are small compared to the exciton Bohr radius, their electronic wave functions experience three-dimensional quantum confinement. This results in the formation quasiparticles due to the dot boundary. Consequently, both linear and nonlinear optical properties of small semiconductor nanocrystals arise as a result of transitions between electron and hole quantum-size levels (QSLs). As a result, in a spherical nanocrystal (quantum dot) surrounded by an infinite potential barrier, the energy of the electron and hole quantum-size levels, characterized by angular momentum quantum number *l*, can be written in parabolic approximation as expressed in equation 2-4 [4, 73, 74];

$$E_{l,n}^{e,h} = \frac{\hbar^2 \phi_{l,n}^2}{2m_{e,h}a^2} \quad \text{..... (2-4)}$$

where $m_{e,h}$ is the electron and hole effective mass respectively, a is the crystal radius, $\Phi_{l,n}$ is the *n*th root of the spherical Bessel function of the order *l* j_l._$\Phi_{l,n}$=0 . The four lowest roots have values corresponding to $\Phi_{0,0} = \pi$, $\Phi_{1,0} = \sim 4.49$, $\Phi_{2,0} = 5.76$ and $\Phi_{0,1}$ = respectively. Based on equation 4, it is evident that the total energy of the optical band edge transitions will increase with a decrease in the size of the nanocrystal; as a result of quantized size levels of the electron and the hole. For example, model CdSe nanocrystals have been used to confirm this characteristic such that its energy can be tuned to cut across almost the whole optical spectrum. That is, their band gap energies can be tuned from 1.8 eV, the bulk value, all the way to 3.0 eV simply by changing the size of the CdSe nanocrystal [42]. In bulk semiconductors, optically created exciton experiences a coulomb attraction between the

electron and the hole. Similarly, nanocrystals also experience coulombic attraction which basically depends on the confinement regime. Subsequently it is important to take into account this interaction because both particles (electrons and holes) are confined in the same crystal volume. The Coulomb energy of the electron and hole interaction, which is added as an energy correction is on the order of;

$$Ry^* = \frac{e^2}{2\kappa a} \quad \text{.....} \quad (2\text{-}5)$$

where $\dot{k}$ is the dielectric constant of the semiconductor. According to equation 2-4 and 2-5, the confinement energy of each carrier increases with decreasing size as $1/a^2$ and the Coulomb energy grows only as $1/a$. In sufficiently small nanocrystals, the energy correction to the quantization energies of electrons and holes becomes small and reduces transition energies by only a relatively small close to negligible amount. On the other hand, in large nanocrystals, the Coulomb interaction is more important than the quantization energies of the electrons and holes, thus has to be considered [65, 74].

To reveal the principle quantum confinement effect within a framework, theoretical analysis shows that the optical properties of nanocrystals strongly depend on the ratio of the nanocrystal radius, *a*, to the Bohr radius of the bulk exciton given by this relation;

$$a_B = \frac{\hbar^2 \kappa}{\mu e^2} \quad \text{.....} \quad (2\text{-}6)$$

where μ is the exciton reduced mass (2-6, 2-8). Consequently in the analysis of experimental data, one needs to consider three different regimes: $a \gg a_B$, $a \sim a_B$ and $a \ll a_B$.

2.2.1.1 *Weak Confinement Regime*

The weak confinement regime corresponds to the case when the nanocrystal radius, *a*, is small but still a few times larger than the exciton Bohr radius, a_B, i.e. when $a \gg a_B$. In this case, the only quantization occurring is that of the exciton centre-of-mass motion since the binding energy of an exciton, E_{ex}, is larger than the quantization energy of both the electrons and holes. The energy of an exciton in the weak confinement case is then expressed in the form;

$$\hbar\omega = E_g - E_{ex} + \frac{\hbar^2\pi^2}{2Ma^2} \quad \ldots\ldots\ldots\ldots\ldots\ldots\ldots\ldots\ldots\ldots \text{(2-7)}$$

where E_g is the band gap energy of the semiconductor material, $M = m_e + m_h$ is the exciton translation mass and π is the root value at $\Phi_{0,0}$ of the Bessel function. The binding energy of the exciton is given by;

$$E_{ex} = Ry^* / n^2 \quad \ldots\ldots\ldots\ldots\ldots\ldots\ldots\ldots\ldots\ldots\ldots\ldots \text{(2-8)}$$

Where Ry* is the Rydberg constant and n describes the internal excitonic states arising from the coulomb electron-hole interactions [17, 19, 61, 65, 74-76]. The weak confinement regime can be realized in large enough crystals. For instance investigations on CuCl nanocrystals whose excitonic Bohr radius is 7 Å showed that all the investigated samples experienced weak quantum confinement [77].

2.2.1.2 *Intermediate Confinement Regime*

An intermediate region may occur in a semiconductor when the nanocrystal radius 'a' is smaller than the Bohr radius of the electron a_e and the hole a_h, i.e. $a_e > a > a_h$, such that very different values for the electron and the hole effective masses are obtained. In this case, one of the particles is strongly confined while the other is not. For instance, the hole moves in the

average potential of the much faster electron and is localized at the center of the nanocrystal. The region of the hole motion around the crystal center in this case is much smaller than the nanocrystal radius and the size dependence of the exciton ground state can then be described as the behaviour of a donor localized at the nanocrystal centre. The excitation spectrum of such a donor-like exciton can be described as an oscillation of the hole about the crystal centre and has been observed in moderate size CdS and CuBr nanocrystals [65, 74, 78, 79].

2.2.1.3 Strong Confinement Regime

Strong confinement limit corresponds to the condition, $a \ll a_B$ implying that the confined electron and hole have no bound state thus corresponding to the hydrogenlike exciton, and the zero-point kinetic energy of electron and hole due to confinement expressed by equations 4 is considerably larger than the *Ry** value. Therefore the optical spectra can be considered as the spectra of transitions between electron and hole quantized size levels. In this case, the uncorrelated motion of an electron and a hole may be considered as the first approximation, and the Coulomb interaction may be ignored. Employing the rules dictating the interband transitions between quantum size levels of parabolic conduction and valence band, transition are allowed only between levels with same quantum numbers. Consequently, absorption spectra can be obtained via this expression [4, 17, 74];

$$\hbar\omega_{\nu} = E_g + E_{\nu}^{h}(a) + E_{\nu}^{e}(a) - 1.8\frac{e^2}{ka} \quad \text{..... (2-9)}$$

in which the term proportional to e^2/ka describes the effective Coulomb electron-hole interaction. Comparing this term with the exciton Rydberg energy, $e^2/2ka$ in a strong confinement regime, $a \ll a_B$, it is clear that the Coulomb interaction becomes very negligible in small quantum dots. In addition, the Coulomb term contribution to the ground-state energy

is even greater than in the bulk crystals. This is a principal difference of quantum dots as compared with crystal, quantum well, and quantum wire, where the Coulomb energy of a free electron-hole pair is zero. Therefore, an elementary excitation in a quantum dot can be classified as an exciton with a notation "exciton in quantum dot [17].

2.2.2 Optical transitions in semiconductor nanocrystals

2.2.2.1 Absorption

In a semiconductor, an electron can be promoted from the valence band to the conduction band as a result of absorption of a photon with energy equal to or greater than the fundamental band gap energy as portrayed in Fig. 2-4. Effects of quantization of the band gap energy in nanocrystal system with respect to the nanocrystal size are defined by equations (2-4) and (2-9). Primarily the equations present increasing band gap energy as a result of decreasing size scaling as $1/a^2$ if the coulomb interaction is negligible. Secondly, there is emergence of discrete energy bands of both the conduction band and the valence band. These phenomena are schematically illustrated in Fig. 2-5a. Experimentally, the quantum confinement effects in nanocrystals can be determined via analysis of their optical absorption spectra; where a decrease in size of the nanocrystal would result in most cases result in a blue-shift of the absorption onset to higher energies [80]. The possibility to resolve the absorption spectra is attributed to energy spacing between the discrete levels of the envelope function functions with different quantum numbers which is in the order of hundreds of meV. This is depicted in Fig. 2-5b, showing the absorption spectra of CdTe QDs of different sizes. The lowest energy optical transition can be assigned to the 1S(h) to 1S(e)-level (h denotes the hole and e the electron), the second transition to the 1P(h) to 1P(e) level, and so on.

During analysis of the absorption spectrum, a relatively sharp absorption feature near the onset of absorption usually corresponds to the excitonic peak defining the lowest excited state exhibiting large oscillator strength. The position of the excitonic peak is also dependent on the size of the nanocrystal thus its features such as form and width are a description of the size distribution, shape and type of stoichiometry of the nanocrystals. For instance, polydispersed samples are characterized by a shoulder in the absorption spectrum at the position of the excitonic transition while less pronounced absorption features in shorter wavelength range correspond to excited states of higher energy [81]. In addition, absorption spectra may show multiple peaks corresponding to the optical transitions between the electronic levels in the nanocrystal. With this regard, discrete energy levels of electron and holes in a semiconductor nanocrystal are sequentially labelled as S, P, D and so forth. Therefore after considering the parity-allowed transitions, the optical electronic transitions possibly observed in a nanocrystal (NC) spectrum are 1S(h)-1S(e), 1P(h)-1P(e), 1D(h)-1D(e) and so on as shown in Fig. 2-6 [82].

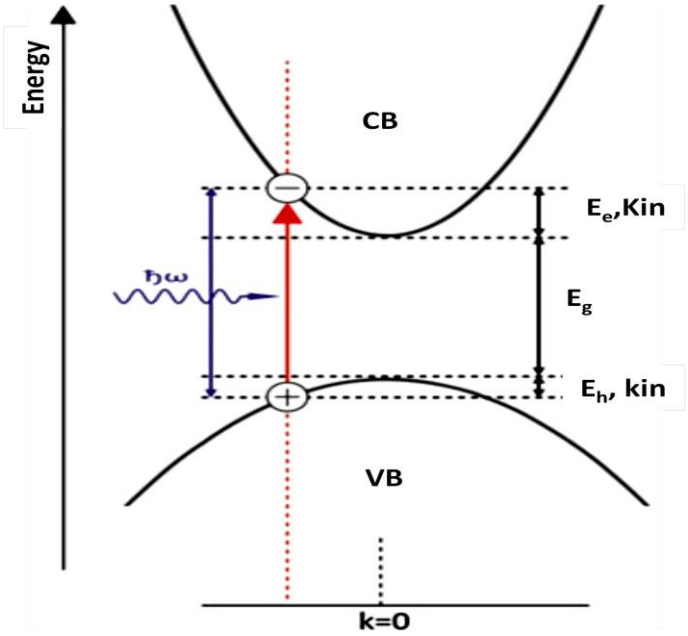

Figure 2-4: Schematic representation of the promotion of an electron from the valence band to the conduction band in a direct band gap semiconductor as result of the absorption of a photon [82, 83].

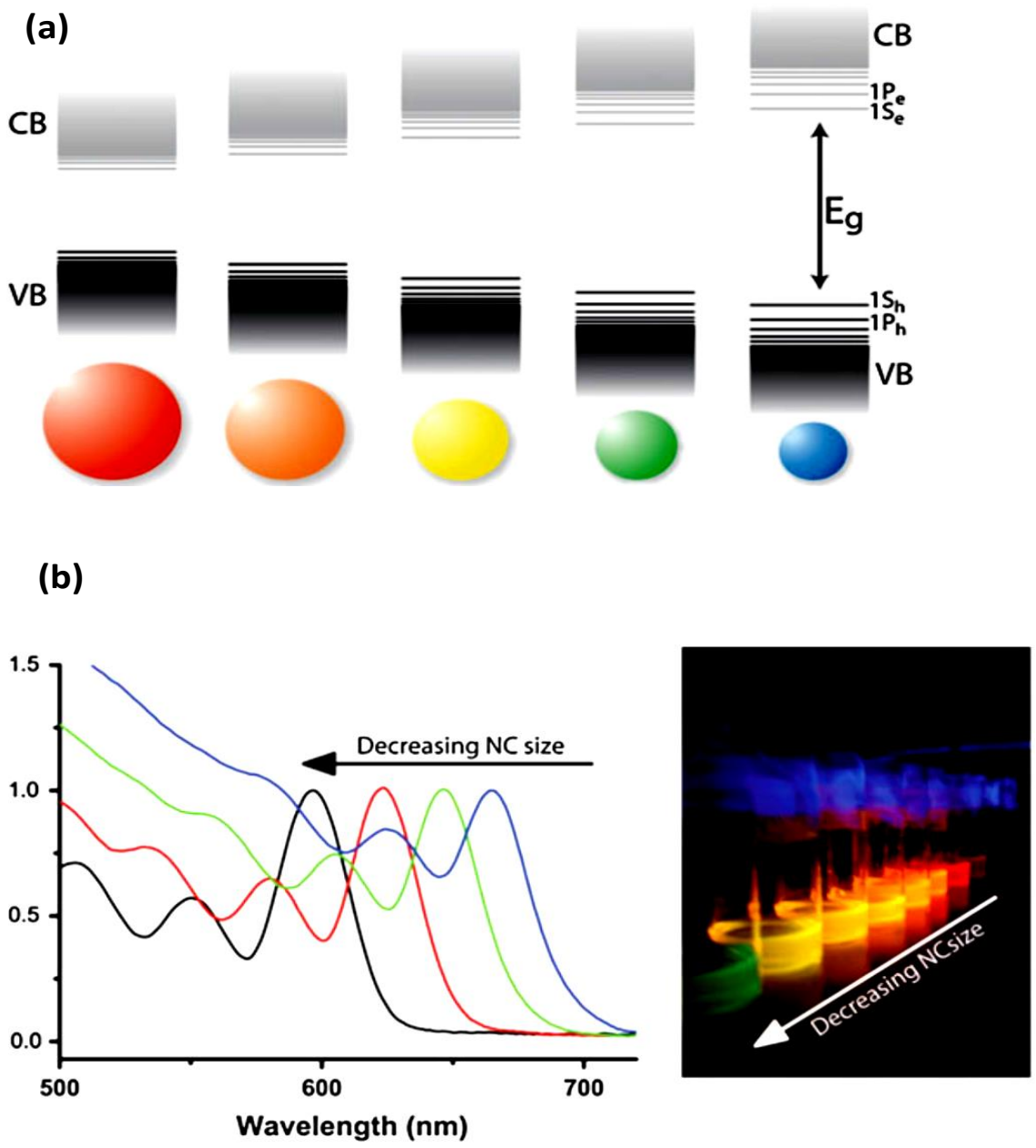

Figure 2-5: Schematic representation of the quantum confinement effects with: (a) showing the emergence of the discrete energy levels as the nanocrystal size reduces thereby an increase in the bandgap energies, (b) showing the absorption spectra (on the left) of colloidal suspensions of CdTe quantum dots of different sizes while the right side are the Photograph of vials containing colloidal suspensions of CdTe QDs of different sizes under UV excitation [82-84].

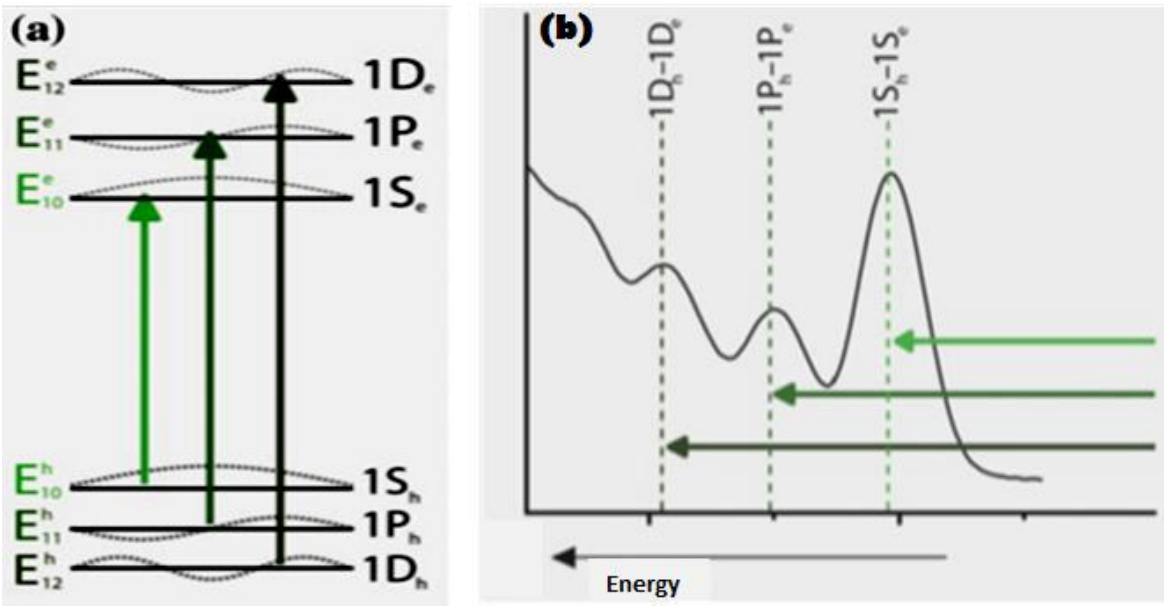

Figure 2-3: (a) is a schematic diagram of the three lowest discrete energy levels of electron, and hole, in a semiconductor nanocrystal quantum dot with the corresponding wave functions are represented by the dashed lines. Allowed optical transitions are given by the arrows. (b) Assignment of the excitonic peaks observed in the absorption spectrum of colloidal CdTe quantum dots associated with the three optical transitions [82, 83].

In the case of CdSe nanocrystals, quantum confinement leads to mixing between different valence subbands, which produces a more complex structure of hole quantized states. Taking into account the mixing between heavy, light, and spin-orbit split-off valence subbands, Ekimov and the group established via calculations the size dependent hole energies in CdSe NCs. Their results showed that the three lowest hole states are $1S_{3/2}$, $1P_{3/2}$ and $2S_{3/2}$ as depicted in Fig. 2-7(a). [85, 86]. The optical transitions that involved these states are well resolved in linear absorption spectra of good quality colloidal CdSe NCs resulting in several excitonic peaks as presented in Fig. 2-7(b).

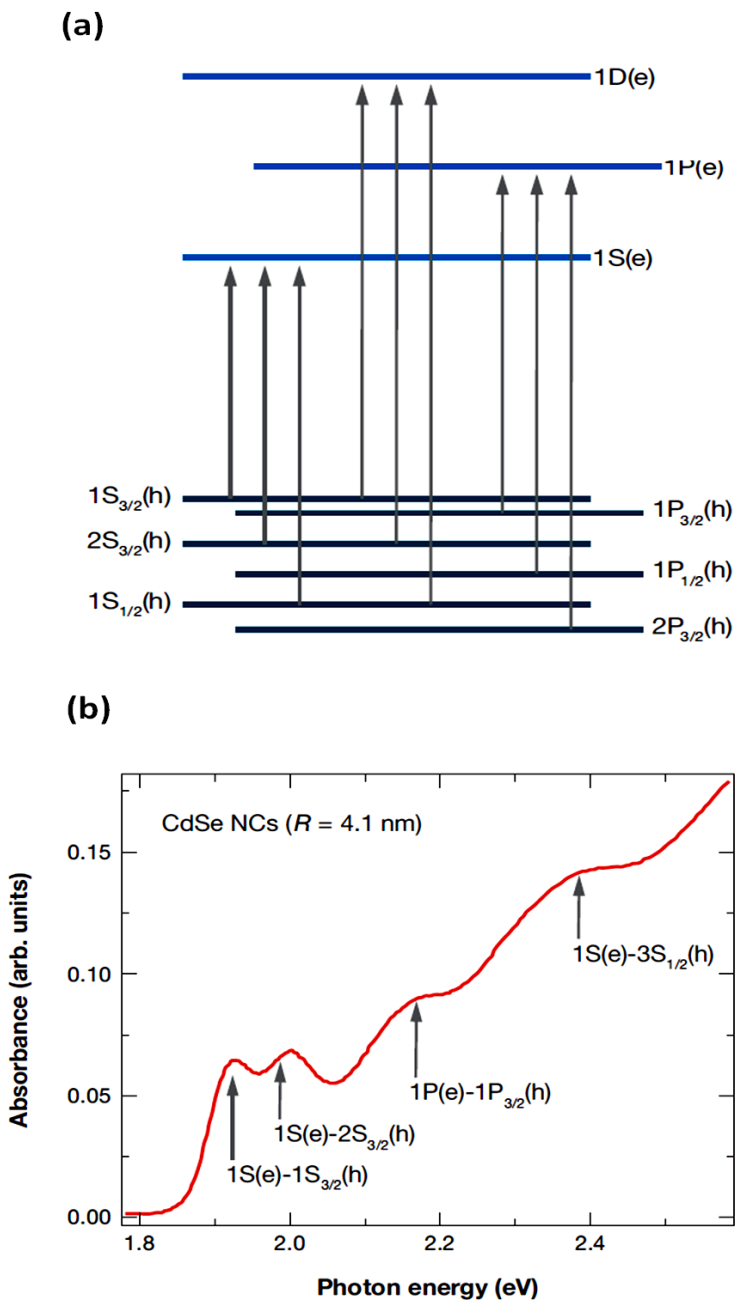

Figure 2-4: Schematic representation of the mixing between different valence subbands of CdSe nanocrystals as a result of quantum confinement. The arrows indicate allowed interband optical transitions; (b) is the linear absorption spectrum of CdSe with average rad radius of 4.1 nm showing the positions of the four well-resolved transitions that involve either 1S or 1P electron states [85, 86].

2.2.2.2 Luminescence properties

Photoluminescence spectroscopy, which is divided into fluorescence and phosphorescence, is a vital technique for examination of the size distribution and quality of semiconductor nanocrystals. The duration in which an electron remain in the excited state which happens to be longer in phosphorescence brings the differences between fluorescence and phosphorescence, otherwise the two process occur in a similar manner [18, 72]. Typically, when a semiconductor nanocrystal absorbs a photon with sufficiently larger energy than the band gap, a hot exciton is formed. The electron and the hole created then occupy the excited states above 1S in the discrete bands of the conduction and the valence band. In the event that a hot exciton is created, the very first process experienced is the exciton relaxation where the electron and the hole will quickly relax (<1 ps) to their ground states (the 1Se1Sh exciton) by means of a cascade of intraband non-radiative relaxation steps, through which their excess energy is dissipated as heat [85]. This phenomenon is depicted in Fig. 2-8. These intra-band transitions do not produce any radiations and are not controlled by the optical selection rules. Therefore they can take place very fast, either by coupling with phonons (i.e., lattice or ligand vibrations) of suitable energy, or by Auger scattering processes through which the excess energy of one carrier (e.g., the electron) is transferred to the other (e.g., the hole) [83, 85, 87].

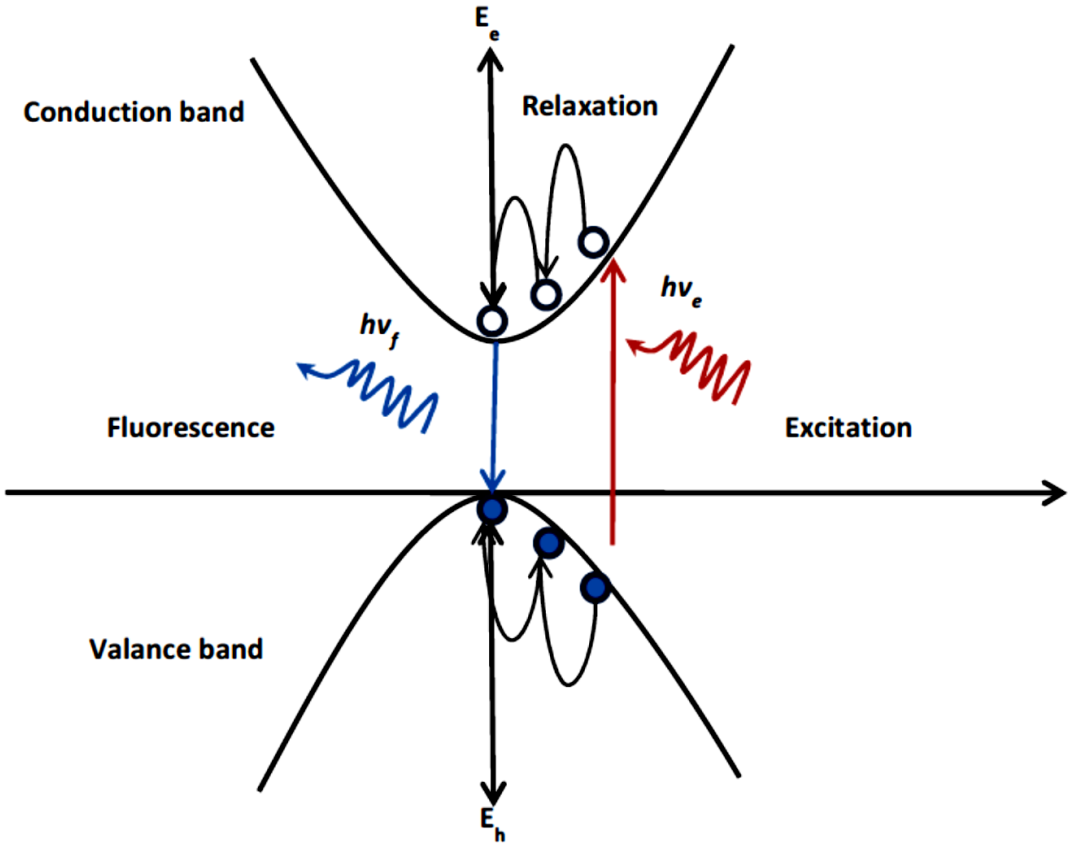

Figure 2-5: Shows the cascade intraband relaxation steps [18].

The second process is the electron-hole recombination which takes place after the exciton has reached its ground state (i.e, lowest energy 1Sh-1Se exciton) resulting in a further relaxation. During this process the excited electron returns to the valence band and the exciton energy is released either radiatively which results in photoluminescence or non-radiatively as described in Fig 2-9. Photoluminescence (PL) is the emission of a photon due to exciton relation via radiative recombination. A well-defined emission peak in a PL spectrum centred at energy position close to the absorption transition with the lowest energy corresponds to the direct recombination of the exciton. This implies that the emitted photons have energies corresponding to the band gap of the nanocrystals and as such present the same size dependence as the absorption transitions. Similarly the PL peak width defining the Stoke shift

(full width at half maximum) is determined by the size and shape dispersion of the measured nanocrystal population. This is exhibited in Fig. 2-5 where the emission colours are manipulated by just changing the size of the nanocrystal.

Radiative recombination can also occur after one (or both) charge carriers are trapped in a defect or surface state. The resulting emission is known as defect PL or trap PL, and is characterized by a very broad emission band at lower energies than the band gap which is typically very inefficient with photoluminescence quantum yields below 5 % [82, 84]. Trapping of the charge carriers in defect or surface states or impurities can also result in non-radiative recombination, through which the exciton energy is fully dissipated as heat in the crystal lattice. Trapping leads to strong carrier localization, which decreases the overlap between the electron and hole wave functions, thereby making the radiative recombination less likely and facilitating non-radiative relaxation; thereby presenting a case where non-radiative decay channels are always competing with the radiative ones on the surface of the nanocrystal [82, 83]. Tremendous theoretical and experimental investigations studies have established that the surface of the nanocrystal is the most important source of trap states. As the nanocrystal size becomes smaller, the surface atoms have fewer neighbours than their interior counterparts, and therefore possess unsatisfied chemical bonds (dangling bonds), ion vacancies, disorder due to adsorbed impurities, or uncommon oxidation states, which give rise to high density mid-gap states acting as electron and hole states (surface states) [12, 83]. Surface defects (e.g., vacancies) give rise to even more strongly localized energy states, which can very effectively trap the electron or hole. For these reasons, it is essential to control the surface quality of semiconductor NCs and eliminate dangling bonds, a process known as surface passivation. This can be achieved by coating with a wider band gap material which confines the carriers to the materials core or by coating the surface with suitable organic ligands [25, 83, 84, 88-91]. The choice of passivating agent could improve

the size-dependent band edge state luminescence efficiency, while promoting the solubility and the processibility of the nanoparticles [72].

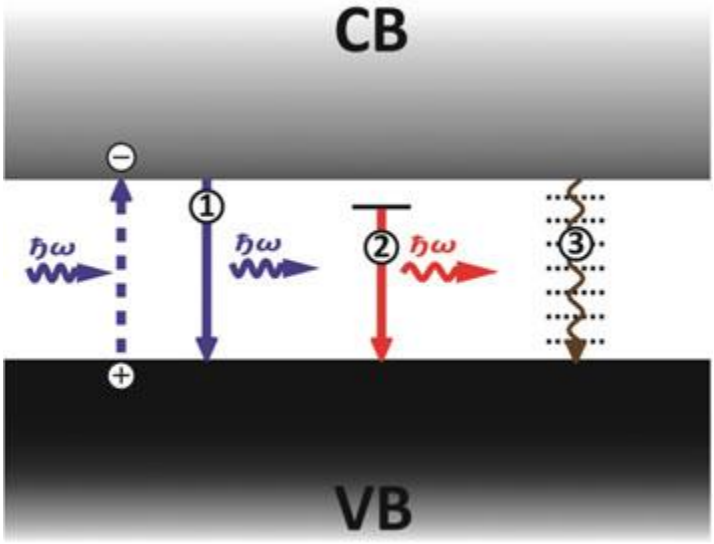

Figure 2-6: Schematic illustration of exciton recombination pathways in semiconductors with (1) radiative recombination, (2) defect assisted radiative recombination and 3) non-radiative recombination [82, 83].

Energy transfer is another possible non-radiative relaxation pathway for the semiconductor nanocrystals. It is experienced only when the distance between the nanocrystals is sufficiently small to allow strong dipolar interactions. In this scenario, energy transfer can occur from a donor nanocrystal to acceptor nanocrystal upon satisfying the resonance condition, which states that the donor level and the acceptor level should have the same energy. The energy transfer rate is determined by the strength of the donor-acceptor (D-A) interaction, which strongly increases with decreasing D-A distances [83].

2.2.2.3 Anomalous bandgap cross-over in ultrathin monolayers

Anomalous quantum Hall effects and massless Dirac fermions observed in monolayer graphene has catapulted advances in the fabrication of ultrathin layered transition metal chalcogenide and group III-VI metal chalcogenides [92-94]. Transformation of the bulk semiconductor down to a single monolayer has not only resulted in quantum confinement but also in modification of the band structure. For the transition metal chalcogenides, this is attributed to the interactions of the d-electrons which have led to a band gap crossover unlike the other sp-bonded semiconductor metal chalcogenides [94]. The benefits associated with this crossover include enhancement of the photoluminescence (PL) quantum yield resulting in an increase in the intensity of emitted light and the possibility to control the spin and valley degrees of freedom which is good for valley Hall effect [95-101].

Indirect to direct band gap crossover was first observed in MoS_2 when it was thinned from the bulk (with an indirect band gap) to a monolayer system which transitioned to acquire a direct band gap [102]. Kin et al. and Splendiani et al. demonstrated the quantum confinement in layered d-electron materials which resulted in the emergence of photoluminescence in ultrathin layer of MoS_2, something that is absent in the bulk material. The PL increased with decreasing layer thickness with monolayer giving the strongest luminescence [94, 102]. Theoretical calculations by Splendiani of the band structure of the bulk MoS_2 and the ultrathin layers of various thicknesses displayed in Fig. 2-10 showed that the direct excitonic transition energy at the Brillouin zone K point hardly changed with layer thickness. This is contrary to the indirect band gap which increases monotonically as the number of the layers decreases. Monolayer MoS_2 transforms into a two dimensional direct band gap semiconductor as a consequence of the high indirect transition energy it experiences. With the increase of the indirect bandgap in thinner MoS_2, the intra-band relaxation rate from the excitonic states decreases and the photoluminescence becomes stronger. In the case of

monolayer MoS_2, a qualitative change into a direct bandgap semiconductor renders *k*relax = 0, leading to a dramatic jump of luminescence that is only limited by the defect trapping rate *k*defect. This unusual optical behaviour in monolayer is attributed to the fact that the d-electron orbitals that form the conduction bands and the valence bands have different spatial distribution thus resulting in electronic states with different wave vector. There are more reports on these peculiar yet extraordinary PL properties of MoS_2 monolayers [102, 103]. Also, the indirect-to-direct bandgap crossover in monolayers has been found to be a common property of all the semiconducting transition metal dichalcogenides that have been investigated so far, including WS_2,WSe_2, $MoTe_2$ and $MoSe_2$ [103-106]: the only difference between all these materials is of a quantitative nature, i.e., the magnitude of the band gap, of the exciton binding energy, spin-orbit splitting.

Contrary to the indirect-to-direct bandgap crossover observed in the transition metal dichalcogenides, some polymorphs of layered group III-VI semiconducting compounds such as GaSe and InSe have demonstrated a possible direct-to-indirect bandgap crossover when number of layers are decreased. Though still a subject of debate, there are a few studies pointing towards this possibility. For example, Mudd et al. [107] demonstrated that the near band edge photoluminescence (PL) peak and the absorption induced photoconductivity of thinner InSe flakes experienced a strong blue shift to higher energies with decreasing thickness. This was consistent with 2D quantum confinement of photo-excited carriers by atomically flat interfaces. They also observed a quenching of the PL signals in the thinnest flakes (thickness less the 6 nm) as opposed to the enhancement of the PL signal seen in the MoS_2 monolayers and the other TMDs as discussed above. Since the bulk InSe has a direct bandgap, this observation points towards direct-to indirect bandgap crossover. Similarly, Hu et al. [108] observed a slight blue shift in the PL emission peak with a decrease in the number of layers in comparison to the bulk GaSe. This blue shift was a suggestion that the band

structure of the GaSe was undergoing modification with decreasing thickness. InSe nanosheets synthesized via colloidal route also portrayed a blue shift in the position of their PL peaks compared to their bulk [109]. More discussion on this is presented in chapter 3 of this thesis.

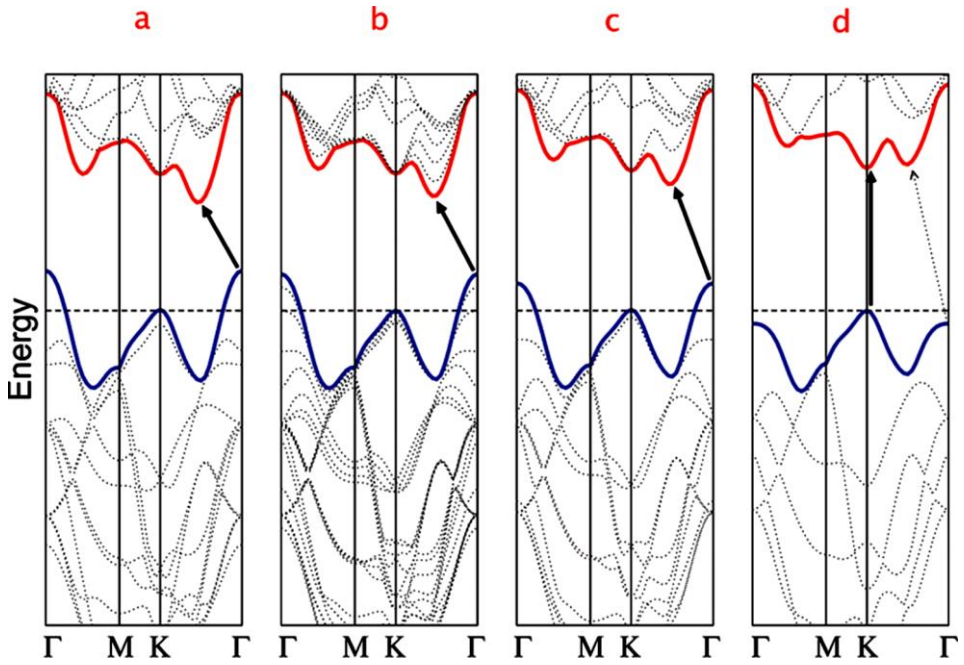

Figure 2-7: Calculated band structures of (a) bulk MoS_2, (b) quadrilayer MoS_2, (c) bilayer MoS_2, and (d) monolayer MoS_2 [109].

The solid arrows indicate the lowest energy transitions. Bulk MoS_2 is characterized by an indirect bandgap. The direct excitonic transitions occur at high energies at K point. With reduced layer thickness, the indirect bandgap becomes larger, while the direct excitonic transition barely changes. For monolayer MoS_2 in d, it becomes a direct bandgap semiconductor. This dramatic change of electronic structure in monolayer MoS_2 can explain the observed jump in monolayer photoluminescence efficiency.

2.3 Synthesis of metal selenide semiconductor nanocrystals

2.3.1 Mechanism of nanocrystal growth

Solution phase techniques, which involve precipitation of solid phase from homogenous solution, have been demonstrated as one of the most effective approaches for controlled synthesis of nanocrystals with various shapes and sizes. Similarly, these routes may provide models for understanding the precipitation and growth of nanophase materials in the environment [110-114]. In view of these situations, it is highly desirable to resolve and understand the process and parameters controlling the precipitation in order to improve the engineering of nanoparticles with desired properties. Two essential ingredients are necessary to explain formation of uniform nanocrystals by direct precipitation. The first is to establish the identity and to control the kinetics of the generation of the solute species that are involved in the solid phase formation (precursors of precipitation). The second is to explain all stages leading from the initial nucleation to growth process into final particles [110, 115]. Specifically for nucleation to take place a critical supersaturation of the particle-forming in the solution is fundamental so that only one burst nuclei occurs; otherwise subsequent nucleation will result in a broad size distribution. By definition, when the solute concentration becomes higher than the solubility limit of the solvent, then the solution is said to be supersaturated. Subsequently the degree of supersaturation is the ratio between the actual solute activity in the reaction medium and the solute solubility under the reaction conditions (temperature, solvent composition, etc.) [82]. Supersaturation is obtained during synthesis by increasing of the monomer concentration by addition of solute via injection of precursors or increase of temperature, by sudden decrease in temperatures to decrease solubility of the solute, by evaporation of the solvent, by a temperature gradient (particularly in hydrothermal growth) or by super-cooling [18, 116-118]. Therefore the whole complex

process of nanocrystal formation via precipitation is divided into two elementary steps of nucleation and growth stages, free from secondary nucleation and coagulation.

2.3.1.1 Nucleation

In general, nucleation which can occur either homogeneously or heterogeneously produces stable nuclei that are able to grow and become product particles. Heterogeneous nucleation occurs on a pre-existing surface, nuclei, ion, dust, particle or a substrate [12, 119, 120]. On the contrary, in homogeneous nucleation the solute molecules combine to produce nuclei as a result of thermodynamic concentration fluctuations in the absence of a solid interface or pre-existing surface. According to classical nucleation theory, monomer precursors can combine to form small unstable clusters of increasing free energy called embryos. For a spherical nucleus in a supersaturated solution, the overall free energy change, ΔG, is the sum of the free energy due to the formation of a new volume, ΔG_v, and the free energy due to the new surface created, ΔG_s, as expressed in equation 10 [18, 82, 110, 121-124]:

$$\Delta G = \Delta G_v + \Delta G_s = -\frac{4}{V}\pi r^3 k_B T In(S) + 4\pi r^2 \gamma \quad \ldots\ldots\ldots\ldots\ldots\ldots\ldots\ldots \text{(2-10)}$$

Where V is the molecular volume of the precipitated species, r is the radius of the nuclei, k_B is the Boltzmann constant, T is the reaction temperature, S is the saturation ratio and γ is the surface free energy per unit surface area. Stable nuclei size (critical size) is defined by the critical radius, r_c such that critical nuclei have equal chance to decompose to reactants or to grow to mature nanocrystals. ΔGv is negative due to the energy freed when chemical bonds are formed in the crystal nucleus while ΔGs is positive due to the fact that the nanocrystal surface atoms have unsaturated bonds. Due to the opposite signs of ΔGv and ΔGs and their different size dependencies (r^3 and r^2 respectively), ΔG will reach a maximum for nuclei with

critical radius (r_c) then start to decrease with increasing radius as presented in Fig. 2-11. This maximum free energy is the activation energy for nucleation and it happens when S>1 at a critical size r_c. This implies that nuclei with radius smaller than r_c will re-dissolve while nuclei larger than r_c will experience a further decrease in free energy thus forming stable nuclei that grow into particles. The radius r_c of the critical nuclei given by equation 2-11 demonstrate that a higher reaction temperature or a higher saturation ratio leads to a smaller critical radius. Subsequently, the nucleation rate increases with increasing temperature and degree of supersaturation. Therefore larger nucleation rates lead to a larger concentration of smaller NCs, while slower nucleation results in a smaller concentration of larger NCs [18, 82, 121-124].

$$r_c = \frac{2V\gamma}{3k_B T \ln(S)} \quad \text{..... (2-11)}$$

Stable nuclei from the solution continue to grow via molecular addition (monomer addition). This relieves the supersaturation step which then leads to the concentration dropping to critical level. In this case nucleation stops and the particles continue to grow by molecular addition until the equilibrium concentration of the precipitated species is reached. The subsequent stage is referred to as the size focussing regime where smaller nanocrystals will grow faster than larger nanocrystal because the driving force is greater in smaller nanocrystals. Careful control of the nucleation process results in a narrow size distribution of the nanocrystals.

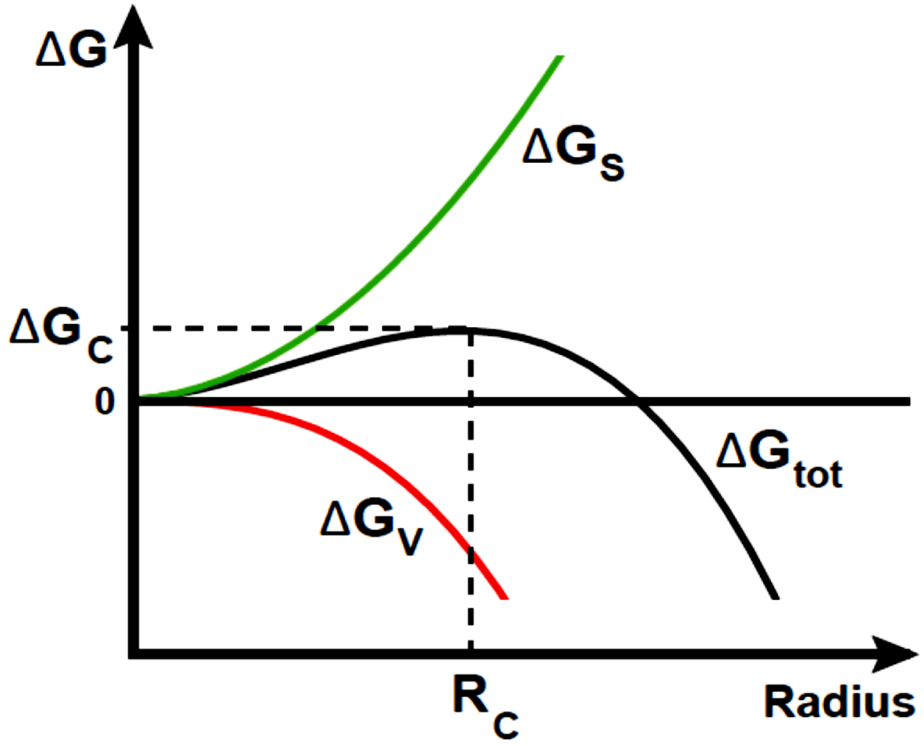

Figure 2-8: Change in free energy during the formation of a spherical crystal nucleus. ΔGv gives the volume excess free energy, ΔGs the surface excess free energy, and ΔGTOT is the free energy change. ΔGc indicates the activation energy for nucleation [82].

2.3.1.2. Growth

Once nucleation is completed and the critical cluster size is reached, particles will begin to grow from dissolved species. Subsequent growth occurs by two primary mechanisms namely coarsening (also known as Ostwald ripening) and/or aggregation. Growth by either mechanism causes a decrease in surface energy, making an increase in particle size energetically favourable [72, 125]. The coarsening process (Ostwald ripening) involves the growth of larger particles at the expense of smaller particles by way of diffusion of molecular scale species through the growth medium. Because the chemical potential of a particle

increases with decreasing particle size, the equilibrium solute concentration near a small particle is higher than near a large particle, as described by the Gibbs-Thompson as presented in equation 2-12 [111]:

$$S = S_0 \exp(^{2\sigma V_m}/_{RTr*}) \quad \ldots\ldots\ldots\ldots\ldots\ldots\ldots\ldots\ldots \quad (2\text{-}12)$$

where S is the solubility of the particle as a function of its radius, S_0 is the solubility of the (flat surface) solid with infinite dimensions, σ is the specific surface energy (solid-liquid interfacial energy), V_m is the molar volume of the solid phase, R is the gas constant, r* is the particle radius and T is the absolute temperature. Based on this, the resulting concentration gradients lead to the transport of solute from small particles to larger particles. This mechanism tends towards isotropic growth thus generating particles with almost spherical shapes. However, it may result in the formation of faceted particles if it occurs near equilibrium and there is sufficient difference in the surface energies of different crystallographic faces [125, 126].

Low solubility of certain inorganic compounds, even at nanoscale, the growth of nanocrystals in colloidal dispersion, the formation of nanostructures with complex shapes and the presence of defects such as dislocations (such as edge and screw dislocations) and planar defects (such as in stress-free) suggested other possible growth mechanisms for nanocrystals via colloidal route [126]. Further investigations have identified alternative crystal growth processes by aggregation called oriented attachment. This mechanism is based on the spontaneous self-organization of adjacent nanocrystals resulting in growth by coalescence of solid particles that share a common crystallographic orientation; producing particle assemblies built from randomly oriented to highly oriented nanoparticles. Nanocrystal growth via the orientation attachment mechanism generally leads to the formation of anisotropic nanocrystals and particles of irregular shapes as well as provides a route for incorporation of defects in

nanocrystals as a result of epitaxial aggregation [115, 127-134]. Primary particles may aggregate in an oriented fashion to produce a larger single crystal, or they may aggregate randomly and reorient, recrystallize, or undergo phase transformations to produce larger single crystals. One of the characteristics of the oriented attachment mechanism is the presence of a solid–solid interface between the nanocrystals, indicating that the growth process begins only after contact is established between particles, as schematically illustrated in Fig. 2-12.

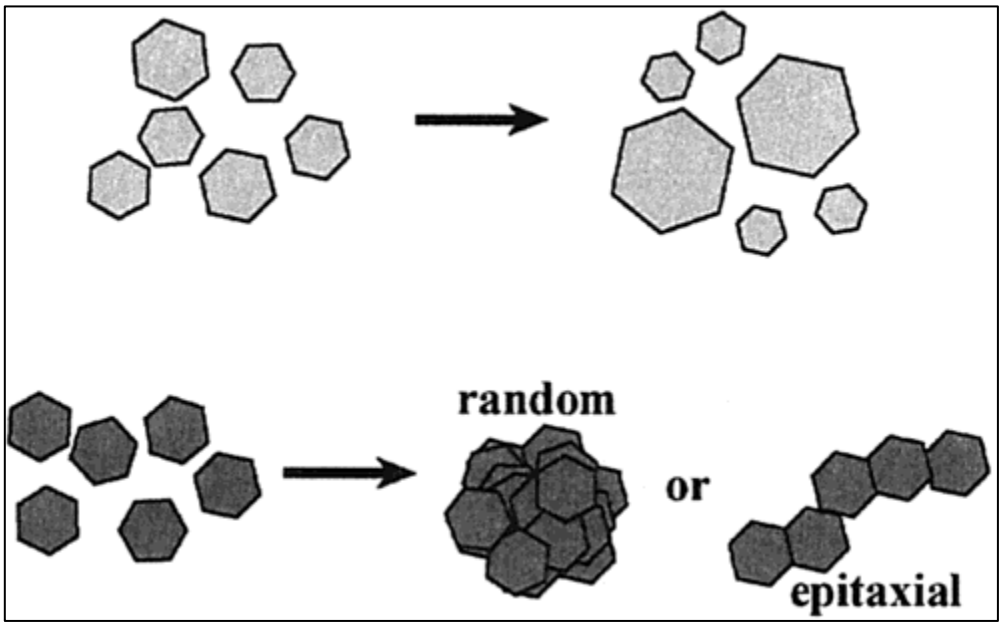

Figure 2-9: Two-dimensional representation of end-member growth mechanisms: (upper) growth of large crystals at the expense of small crystals and (lower) growth by assembly.

2.3.2 Shape evolution mechanism/growth and shape control

Synthesis of high quality semiconductor nanocrystals in the quantum confined size regime has recently reached a new horizon leading to the availability of zero-dimensional (e.g., cubes, stars, pyramids), one-dimensional (e.g., nanowires, nanorods), two-dimensional (e.g.,

platelets, nanodisks, nanosheets), and even more complex nanostructures (e.g., multipods, matchsticks, nanoflowers, and dumbbells) [82]. The majority of the investigations on the shape-controlled synthesis of nanocrystals have established that the most crucial factor determining the shape of the nanocrystals is the crystallographic phase of the initial seed (nuclei) formed during nucleation processes. The resulting seed may have a number of crystallographic phases; however the most favoured one will dominate depending on whether the reaction is thermodynamically controlled or kinetically controlled or a delicate balance between the two. Fig. 2-13 shows the potential energy landscape of the competitive reactions where C is the thermodynamically favoured product, that is, the product formed is the most stable and D is the kinetically favoured one implying that the pathway leading to it has the lowest energy barrier (the energy cost at the transition state). The rate constant is exponentially dependent on the activation energy E_a (eq.2-14). Thus the reaction corresponding to the red pathway is significantly faster and leads to D as the main product. On the other hand, if equilibrium is established, the molecules will experience different product states multiple times and eventually accumulate at the most stable state. The equilibrium constant is exponentially dependent on the driving force ΔG^0 (eq.2-13) thus making C the main product [135].

$$K = e^{-\frac{\Delta G^0}{RT}} \quad \ldots\ldots\ldots\ldots\ldots\ldots\ldots\ldots\ldots\ldots\ldots\ldots \text{(2-13)}$$

$$k_1 = Ae^{-\frac{Ea}{RT}} \quad \ldots\ldots\ldots\ldots\ldots\ldots\ldots\ldots\ldots\ldots\ldots\ldots\ldots \text{(2-14)}$$

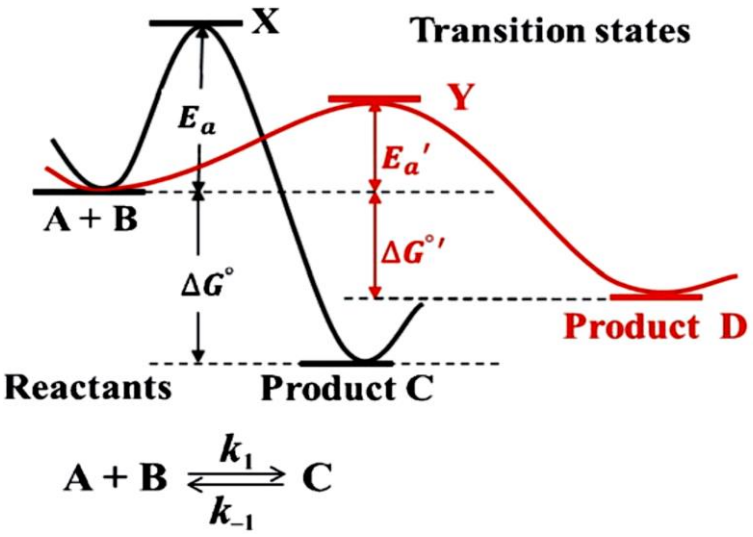

Figure 2-10: Simple energy landscape illustrating the choice between the thermodynamically and kinetically controlled products.

Under a thermodynamic growth regime, the explanation for the shape of the nanocrystal is based on its stability compared to the other alternative shapes. To evaluate the stability of NPs, one needs to compare the different end states (e.g. cube/ cuboid), the choice of facets, and the sharpness or roundedness of the edges and corners [135]. If all of the facets of a nanocrystal are equally favored, then a spherical shape would be preferred because it has the lowest S/V ratio (Fig. 2-14). At the other extreme, a polyhedron with sharp edges and corners will be preferred if only one type of facet is favored, for example, octahedra with (111) facets, cubes with (100) facets, etc. Most nanocrystals lie in between these two extremes, with a range of surface energies for the different types of facets. When the difference in the stability of the facets is reduced, more than one type of facet will appear and the resulting polyhedron should gradually appear rounder, with truncated edges and corners. The system seeks to minimize the total surface energy, that is, the sum of the facet area weighted by their respective surface energy [Eq. 2-15] [135].

$$\Delta G = \sum \gamma_i A_i \quad \text{..... (2-15)}$$

Here, *G* is the surface energy of a given facet and A is its area. In most cases, isotropic growth of nanocrystals is preferred under thermodynamic controlled regime that is characterized by sufficient supply of thermal energy and a low flux of monomer. Consequently, when synthesizing the thermodynamically controlled product, one should increase the reaction temperature and allow sufficient time so that the reaction can approach equilibrium. To increase the yield, the conditions can be selected to destabilize the starting material and /or stabilize the product.

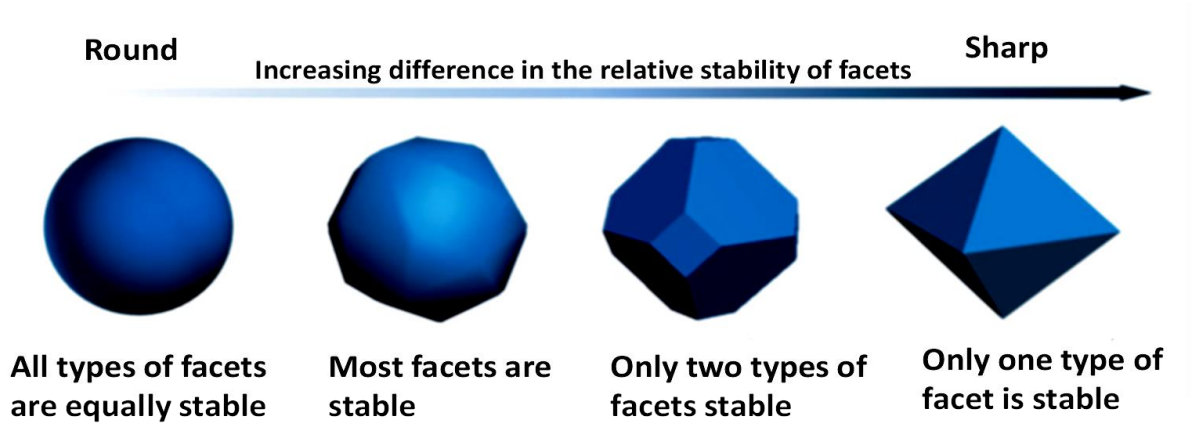

Figure 2-11: The lowest energy structure of a nanocrystal can vary, depending on the relative stability of its facets.

Unlike thermodynamic arguments that focus on the relative stability of a facet, kinetic controlled reactions are based on the relative growth rate. They occur under conditions that are far from equilibrium including high monomer concentration (high flux of monomer) and faster growth. In addition, to stabilize a metastable form, the growth is usually quenched while the growth rates are still significant. Kinetically, it has been proposed that the formation of a favoured stable facet is as a result the rapid growth at the unstable facets [136, 137]. This means that atoms newly added to unstable facet can form better bonding interactions than those added to a stable facet. According equation 2-14 the growth rate of a

crystal facet depends exponentially on the surface free energy (activation energy) [31, 135], therefore at higher growth rate, unstable facets with higher energy will grow faster than low energy facets. Bordered by the stable facets, the filling of the unstable facets reduces and eventually eliminates their area thus leading to nanocrystals with only stable facets thereby yielding high aspect ratio shapes which are highly anisotropic towards a specific direction. To increase the yield, one should lower the temperature just enough for the reaction to proceed and isolate the products as soon as it is finished, so that the competitive reverse reactions can be suppressed [82, 135].

Thermodynamically and kinetically controlled scenarios are drastically different with distinctive consequences and controlling methods. In experiments, mechanisms described in the next section have been used to determine the thermodynamic driving force and of the kinetic barrier during the synthesis in order to control nanocrystals shape evolution:

2.3.2.1 Equilibrium shape controlled.

The most widely cited classical model for shape control of crystals is given by the Gibbs–Curie–Wulff theorem which predicts that the shape of a crystal is determined by the relative specific surface free energy of individual crystallographic facet of the crystal [121, 138]. Wulff construction is a thermodynamic concept. Therefore, it considers the equilibrium shape of nanocrystal such that the final crystal shape is determined in a way that the total free energy of the system is minimized. Basically the stability of the facets can be evaluated on the basis of the bonding interactions within the facets, which depend on the surface packing efficiency; implying that availability of atoms with stronger bonds on the a facet makes the facet more stable. In the case of a colloidal NC, the free energies of the facets may be modified by ligands bound to the NC surface. This further extends the number of possible

equilibrium shapes for colloidal NCs. For example, the observation of nanocrystals adopting rounder shapes is sometimes associated with the removal of the ligand or a reduction of its concentration. This reduces the difference in the stability between the facets, thus leading to less sharp edges and corners, in other words, a more isotropic shape. Also, this model assumes that the binding between the ligand and the nanocrystal surface is sufficiently strong to thermodynamically drive the system towards a particular shape and even size [82, 135, 139, 140].

2.3.2.2 Effects of ligand and shape control

Ligands play very significant role in colloidal synthesis of nanocrystals. Via their binding processes on the nanocrystal surface and being part of the monomer in solution, they can govern both the kinetics and thermodynamics of shape evolution by controlling the crystal growth rate and the stability of facets [135, 141]. The binding strength of the ligand on the surface of the nanocrystal is dependent on the chemical bonding at the anchoring point and the ligand-ligand packing interactions [142]. The bulkiness of the ligands and their arrangement influences their packing thus the effective ligand-ligand interactions which, in case there is a crowded patch, can hinder dissociation of the neighbouring ligand. Specifically, ligands dynamically adsorb and detach from the surface of the nanocrystals. Therefore, faster ligand dynamics will result in a quick dissociation (short residence time) of the ligand from the surface of the nanocrystal thus making it more accessible to monomer [143]. As a result, the presence of ligands and the fact that some ligands may bind more strongly to certain facets limit access of the monomer (growth materials) to those specific facets thereby increasing their activation energy which in turn reduces their growth rate (kinetics) [31]. This leads to anisotropic growth of the other facets with low affinity for the

ligand. In other words, choosing to use a facet specific ligand/surfactant can result in variation in the relative growth rates of different facets thus leading to the formation of anisotropic shapes by promoting inequivalent growth. Interacting both with the solvent and with the crystal surface, the ligand layer also modulates the thermodynamic stability of the facets, thereby influencing the end states of the nanocrystal growth [82, 135].

2.3.2.3 Monomer concentration/fluxes and shape

Existing monomers in the reaction medium play a key role in the determination and evolution of the shapes of the resulting nanocrystals. Different monomer concentrations have been established to result in different shapes. For example, the required monomer concentration in the reaction solution increases in the following order: dots, rice grains, rods and then branched structures [29]. Monomer diffusion rate which increases with temperature and monomer activity defines what is known as monomer flux. High monomer fluxes favour kinetic control and anisotropic growth (1D growth), while low fluxes favour thermodynamic control and lead to isotropic growth (3D growth). Monomer fluxes that are too low to sustain growth, but are still sufficiently high to prevent NC dissolution, lead to a process called internal ripening. Material is then transported from high-energy facets to low-energy facets, causing the NC aspect ratio to slowly decrease towards a roughly isotropic shape. In other words, by further increasing the remaining monomer concentration in the solution, dot shaped nanocrystals can be converted to an elongated shape as depicted in Fig. 2.15, while those elongated shapes will evolve to a dot-shape if the remaining monomer concentration is not high enough. Even lower monomer fluxes will lead to Ostwald ripening [82, 144].

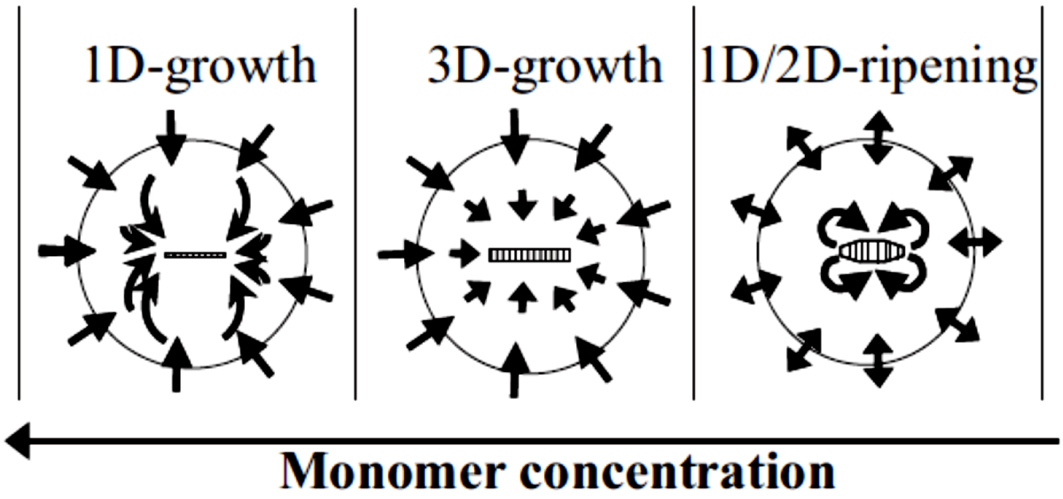

Figure 2-12: Schematic illustration of the influence of the monomer fluxes on the shape of a colloidal NC. (a) high monomer flux, (b) low monomer flux, (c) very low monomer flux [144].

2.3.2.4 Monomer incorporation rates and shape

This model can be treated as a simple extension of the free energy criterion for deciding the shape of crystals. Under kinetic control the growth rates are usually determined by the reaction rates between the incoming monomers and the surface sites. Consequently, differences between the free energy of the various crystallographic facets of the NC become significant. High energy facets can incorporate monomers at faster rates thereby leading to anisotropic growth. This process becomes relevant for growth at relatively low temperatures, that is, where reaction rates become slower than diffusion rates; or at high monomer concentrations where monomer diffusion rates are so high that the reaction rates become discriminatory [82, 84, 120].

2.3.2.5 Crystal structure and shape

The crystalline phase of the NC seed also influences the final shape of the NC, since this will expose different crystallographic facets to the growth medium. Non-centrosymmetric crystal

structures, such as wurtzite, are inherently polar and tend to grow anisotropically, easily yielding rods and multipods under kinetically controlled growth conditions. In contrast, centrosymmetric crystal structures, such as zinc blende, tend to grow isotropically [82]. In addition, the intrinsic symmetry with multiple equivalent facets known to exist in most lattices can break in the presence of a defect within the lattice. Therefor the preferred growth at the defect sites will induce anisotropic growth during the crystal growth. For example if there is a stacking fault between the crystal planes such as (111) or (100) etc., the growth along the fault plane at the edges would be more favourable than the deposition perpendicular to the plane, thereby resulting to platelike nanocrystals [145]. On the other hand, if a nucleus has a fivefold twinning defect, it can grow into a NW because longitudinal growth is preferred [146]. Essentially, the inability of the twinned domains to fill the space leads to bond stretching and defects (i.e. the induced strain), which restrict the lateral growth of the NWs [135]. Similarly, the presence of a screw dislocation on a facet would greatly favor deposition of the material thereon, thus making its growth many times faster than the other seemingly equivalent facets. Thus, the unidirectional growth leads to highly anisotropic NWs or nanotubes [147].

2.4 Synthetic methods of semiconductor metal selenide nanocrystals

To date, a number of synthetic techniques have been used to produce a variety of semiconductor nanocrystals. So far, solution-phase synthetic route, which can be divided into aqueous based, organic based and aqueous-organic based approaches, have been demonstrated as effective routes for controlled synthesis of nanocrystals with various shapes and sizes [5]. Chemical precipitation and hydrothermal methods are examples of aqueous based methods [6-9, 148-151]. They involve the use of environmentally friendly and biocompatible solvents. Non-aqueous methods employ high boiling organic solvents which

allow for the kinetic manipulation of the nucleation and growth process with the help of organic ligands in order to control the properties of the nanocrystals. Examples include the hot-injection method, non-hot injection (heating) method and solvothermal methods using an autoclave [42, 152-154]. Finally, in aqueous-organic approach reactants are dissolved in separate phases and solid nanocrystals are formed at the interface between aqueous and organic media [155-157]. Solution-phase syntheses of semiconductor nanocrystals have exhibited other advantages, the most notable of which are the ease of chemical processabilty, scability and production of nanocrystals in high yield. For the purpose of synthetic methods used in this project, this section summarizes the techniques that have possibly resulted in the preparation of metal selenide nanocrystals with controllable size, shape, composition and phase structures.

2.4.1 Hydrothermal/Solvothermal methods

Hydrothermal synthesis of crystals involves the use water as a solvent in a sealed reaction container (autoclave) at temperatures above 100 °C (above the boiling point) though below the supercritical temperature of water. If other solvents including polar or nonpolar solvents are used in the sealed reaction vessel and temperature above the boiling point of the solvent, then the method is called solvothermal synthesis. Currently solvothermal methods have been modified such that syntheses are done in organic solvents. Under the above mentioned conditions, a self-generated pressure (autogenous pressure) is developed within the vessel. In addition, the specific physico-chemical properties of the solvents in these conditions can, in particular, markedly improve the diffusion of chemical species from the material precursors. The use of water has been vastly investigated, specifically because at high temperature and elevated pressure, fundamental properties of water differ from those at ambient conditions. For example, the viscosity of water decreases with increasing temperature, and thus it has

been proposed that the mobility of dissolved ions and molecules is higher under hydrothermal conditions than at ambient pressure and temperature. Similarly, the dielectric constant of water is affected by temperature and pressure, and is considerably reduced above the critical point; this can have major implications on the solubility and reactivity of solid reagents under reaction conditions. The pressure within the sealed reaction vessel has been found to not only increase with increasing temperature but also to be dependent on other experimental factors such as percentage fill of the vessel and any dissolved salt [158-162]. The above cited changes experienced by the solvent/water provide more parameters to produce different high-quality nanoparticles and nanotubes, which are not possible at low temperatures. During the synthesis of nanocrystals, parameters such as choice of solvent, solvent pressure, temperature, reaction time, and the respective precursor-product system can be tuned to maintain a high simultaneous nucleation rate and good size distribution. Enormous numbers of nanoparticles more specifically metal selenide nanocrystals, have been produced via hydrothermal/solvothermal conditions. Tan et al. [163] reported on a greener solvothermal synthesis of pure single phase γ-In_2Se_3 with hierarchical flowerlike microspheres assembled by nanosheets. After 20 hrs at 220 °C, they obtained γ-In_2Se_3 structures in an environmentally friendly ethanol system in which $InCl_3.4H_2O$ was reacted with Se powder in the presence of biodegradable ascorbic acid (used as both reducing and a capping agent). The authors demonstrated that the addition of ascorbic acid and the high molar ratio of In/Se source lead the pre-formed solid spheres to convert into flowerlike microspheres based on the Ostwald ripening process. Yuan et al. [164] through simple control of Ni/Se ratio of raw materials and reaction temperature managed to produce a series of nickel selenides including cubic $NiSe_2$, orthorhombic $NiSe_2$ and hexagonal $Ni_{1-x}Se$ where the value of x was adjusted based on the reaction temperature which was between 180-260 °C. They also established that different solvents namely oleylamine and octadecylamine played a role in the phase

transformation and morphologies of the nickel selenides. Sobhani et al. [165, 166] prepared NiSe and $NiSe_2$ nanostructures in aqueous solution of hydrazine as a reductant and CTAB as a surfactant via hydrothermal methods. In one of their findings, they established that the molar concentration between $NiCl_2.6H_2O$ and $SeCl_4$ and the reaction temperature played important roles in controlling the morphology, composition and the structure of the products.

2.4.2 Hot injection methods

In order to achieve a burst nucleation that will subsequently lead to a narrow size distribution, this approach often involves rapid precursor injection into solvents at high temperatures. This is then followed by a reduction on the reaction temperature (upon injection) in order to separate the nucleation and the nanocrystals growth stages. The size distribution and the shape control of nanocrystals are highly correlated to the kinetics of nucleation and growth processes. Therefore during this preparation method, it is important to control reaction parameters such as the reaction temperature and time, the injection temperature, the reactivity and concentration of the precursors, the type of solvent/surfactant and pH among others. These parameters are known to control the kinetics of the reaction system. During the process, post-treatments such as rapid quenching of the reaction and size-selective precipitation are often conducted after the hot-injection in order to improve the size distribution of nanocrystals prepared. This is then followed by the addition of the solvent to a cooled solution, thereby increasing the barriers to flocculation. The solid nanocrystals were then separated from decomposition by-products in the centrifuge, and then the solids were dissolved in a solvent (e.g toluene) followed by centrifugation to dispose the by-products resulting in organic solvent-capped nanocrystals. Since its discovery in 1993 by Murray et al, hot-injection method has evolved such that high quality colloidal nanocrystals are obtained from relatively less toxic precursors and organic ligands. This injection-based synthesis has

led to the preparation of nearly all types of high-quality metal–selenide nanocrystals among others ranging from II-VI (e.g., CdS and CdSe) and III-V (e.g., InP and InAs) to IV-VI (e.g., PbS and PbSe) and III-VI (e.g., InSe) semiconductors [42, 167-175]. In this project, this method has been used to obtain nickel selenide nanostructures as discussed in details in chapter 5.

2.4.3 Non-injection method (direct heating method)

Another approach that has been employed towards the synthesis of nanocrystals is the non-injection synthesis (NIS). It is based on the concept of controlling the thermodynamics and the kinetics in the nanocrystal nucleation stage. Typically in non-injection methods, the separation of the nucleation and the growth is realized by slowly heating up the solution together with the precursors in one pot to a desired working temperature [33]. Tremendous investigations have indicated that high quality colloidal nanocrystals are produced at relatively high temperature (>200 °C). This factor creates a major challenge for controlling the shape and size distribution through a non-injection because such a synthesis involves a period of increasing temperature over a broad range (e.g., from room temperature to over 200 °C). If the reactivity of a precursor is too high, this broad change of temperature often leads to concurrent nucleation and growth of nanocrystals in the synthesis, which results in products with poor monodispersity. However, if the precursors are too stable, a very small number of nuclei may form, which leads to uncontrollable particle growth. Therefore the precursors should meet the requirement that they have negligible reactivity at a low temperature, but significant reactivity at elevated temperatures [5, 176]. After attaining the desired temperature, a burst nucleation will occur followed by the growth of nanocrystals, which is similar to the process in hot-injection methods. Compared to the hot-injection method, non-injection methods are far simpler without the injection step, this provides an

alternative way to obtain high-quality CS-NCs at relatively low temperatures, that is environmentally friendly and suited to scale-up; thus suitable for industrial process of high quality colloidal nanocrystals. This method has been applied to produce a number of high quality nanocrystals including CdSe, CdTe, PbSe, Ag_2S, Cu_2S, PbS, Ni_3S_4, CdS, ZnS, $CuInS_2$ and Cu_2ZnSnS_4 just to mention a few [33, 176-179]. In this project, it has mainly been used for the fabrication of InSe nanostructures [109, 180].

2.4.4 Liquid exfoliation

Like carbon graphene, layered metal chalcogenides can also be exfoliated either physically/mechanically or in solution to utilize their full potential [181-183]. Liquid phase exfoliation typically involves the sonication of commercial bulk metal chalcogenide crystals in a number of common solvents sorted on the basis of different surface tensions in order to obtain mono- and few layer nanosheets. The sheets are then purified using centrifugation and decanting the supernatant. This method is insensitive to air and water thus, can potentially be scaled up to give large quantities of exfoliated materials. The exfoliated products exhibited enhanced optical properties in solvents with surface tension close to γ-40 mJ/m^2; a phenomenon that can be explained using the Hansen solubility parameter theory [184]. According to this theory, successful solvents for the exfoliation are the one with dispersive, polar, and H-bonding components of the cohesive energy density within certain well-defined ranges. This can be concluded that those solvents which minimize the energy of exfoliation can be successfully used to obtained single sheets [184]. Specifically, the different optical properties showed by the single sheets have been attributed to modification of the band structure of the semiconductors at monolayer level. A very general solution-based exfoliation method has been reported by Coleman and co-workers [185] for almost all kinds of layered metal chalcogenides. According to this method, layered compounds such as MoS_2, WS_2,

$MoSe_2$, $MoTe_2$, $TaSe_2$, $NbSe_2$, $NiTe_2$, BN, and Bi_2Te_3 can be successfully dispersed and exfoliated in most of the common solvents and can be deposited as individual flakes or films [184].

2.5 Application of metal selenides nanocrystals (semiconductor nanocrystals) to chemical sensors

Chemical sensors have been reported as low cost alternatives using simple device architecture for monitoring, identification and detection of different chemical vapours, odorants and pollutants in many industries including; medical for diagnosis, food industry for quality control production, safety and security, transport, bioprocess control, petro-chemical and agriculture among other industrial processes. In addition, they are used in environmental monitoring to enhance personal, public and industrial safety both indoor and outdoor thus providing a serene place to live in [186-189]. In order to satisfy an expanding demand for novel applications, chemical sensors are under continuous evolution. Apart from the specific requirements of the applications, many other parameters have to be taken into account such as high sensitivity selectivity, reversibility in favourable temperature conditions; both in simple matrices and mixed samples/complex matrix setup. From the operative point of view, among other characteristics, they need to be compact (portable), safe and the manufacturing costs need to be low.

So far research in sensing materials, ranging from the well-known nanostructured metal-oxide semiconductors to conductive polymers or organic-inorganic hybrids has allowed production of highly performing devices [190-192]. This is attributed to their high surface area to volume ratio at nanoscale which favours the adsorption of gases on the sensor due to increased interaction between the analytes and the sensing part. More specifically detection using semiconductor metal oxides as their detection portion has considerable impact to date

owing to their advantages of their robust nature, less sensitivity to moisture and temperature influence, simple electronic interface, quick response and recovery time [193-195]. It is noteworthy that the good performance of the sensors based metal oxides nanostructures depends crucially on their dimensions, morphologies, compositions and surface activities. However, these type of sensors need to operate at higher temperatures ranging between 150° C -350 °C, thus often limiting their detection capability. In addition the available gas sensors in the market are quite expensive and have reduced sensitivity with respect to low concentration, selectivity, reversibility in specified temperature conditions and long term stability. Various techniques such as employing different forms of oxides, use of catalysts and other additives or ion implantation, use of masks and filters have been applied to improve the sensitivity, selectivity and temperature programming of the sensors. However a lack of consistency in the sensor properties has been a major problem associated with various techniques used for the fabrication of the sensor [196, 197]. The gas-sensing devices based on organic materials, such as polypyrrol, polyaniline, and metaphthalocyanines, have been shown gas sensitivity at room temperature, but their long response time due to the orderly structure limits their usage [198]. More recently, carbon nanotubes have been employed as an active material in semiconductor gas sensors due to their very large surface area and their exceptional electronic properties [199]. However, the strong sp^2 bonding in a near perfect hexagonal network in pristine carbon nanotubes is chemically inactive thereby preventing the formation of chemical bonds with the analyte molecule [200]. Other promising building blocks for optical chemical sensor devices are the luminescent semiconducting quantum dots. Photoluminescence properties of QDs have been shown to strongly depend on their surface environment. The suited PL properties include broad absorption band, size tuneable spectral emission, higher photostability, enhanced dipole moments of the QDs during contact with polar solvents and emission lifetime ranging between several hundreds of picosecond and

tens of nanosecond [201]. In the last ten years, authors reported the sensitivity of colloidal QDs embedded into polymeric matrix, sol-gel materials or dispersed in Al_2O_3 nanopore array [202-208]. These reports display sensitivity of quantum dots towards some commonly used solvents like methanol, ethanol, chloroform and acetone [207]. In addition selective detection has been achieved for colloidal QDs by means of chemical functionalization as reported by many authors [205, 206, 208, 209]. The sensitivity of QDs to environmental vapour depends on the interaction between the adsorbed organic species and the surface atoms [210]. This is a general property of the interaction between organics and semiconductor surfaces. Thanks to the high effective area available for the interaction with the solvent vapour, a higher PL sensitivity is expected for nanostructure compared to bulk surfaces and thin films [211-213].

In the search for novel sensing materials, the chemoresistive properties of non-metal oxides semiconducting metal chalcogenides are currently under investigations though still very poorly researched. Investigations on the physical and chemical properties of metal sulfide and selenide nanostructures have presented them as potentially good candidates in chemoresistive gas sensing field [214]. For example, the electro-optical properties which are also dependent on the size and shape and structure of the nanocrystals can be tuned during their solution processing. During fabrication, these nanostructures are known to have enhanced density of structural imperfections, a property that can be utilized in sensing technology. Also the absence of oxygen in the crystal lattice of these chalcogenides may lead to a different catalytic mechanism on the surface reaction with respect to the metal oxides which dominate the chemoresistive sensor based. In addition the absence of the oxygen may solve the constant drift of the signal suffered by metal oxides and ascribed to the in/out diffusion of oxygen vacancies, which alter the doping levels [214]. By using these materials, an improvement from the energy consumption point of view is expected as their band gaps are lower compared to their metal oxide counterparts. This means that the activation of intrinsic

reactions occur at lower at lower working temperatures, then minor energy supply is necessary [214].

So far, metal sulfides have been mainly studied as the sensing part or in combination with metal oxides in order to modify the sensing activity of the latter. Giberti et al. [215] built a conductometric CdS-based gas sensor by screen-printing the CdS powder on alumina substrate. They established that depending on the working temperature, the as-prepared devices could be efficiently employed to selectively detect alcohols in a complex mixture. In another report, Giberti et al. [216] fabricated conductometric gas sensors based on thick-films of SnS_2 nanorods then tested the sensors for various gases in both dry and wet conditions. The sensors showed the best results at an operating temperature of 300 °C. They also demonstrated that the devices had very good selectivity towards acetone and acetaldehyde at concentrations ranging 1–10 ppm, in both dry and wet conditions. Simultaneous presence of acetone and acetaldehyde in wet conditions resulted in almost the same response of acetone only, proving that acetaldehyde could not interfere with acetone detection. From the comparison with its counterpart oxide, tin disulfide showed a much higher resistivity, but a better selectivity with lower operating temperatures. They also tested the repeatability of the performances which suggested that the devices were stable over six weeks with satisfying results. The authors suggested possible applications to include plastic bottle industry and health-based applications with portable devices. Similarly, Gaiardo et al. [217] also developed conductometric gas sensors based on thick-films of SnS_2 which they tested in thermo-activation mode with several gases in dry. Tin disulfide proved its very interesting gas sensing properties, by deemonstrating very good selectivity to acetone and acetaldehyde, with best results at an operating temperature of 300 °C. The responses to the different gases analyzed were reproducible and stable over the time. Guidi et al. studied the chemical sensing properties of CdS and SnS_2 and compared their activities to their oxide counterparts. The

metal sulfides tested highlighted a very high selectivity and sensitivity to particular classes of molecules at a working temperature relatively lower than the classic metal oxide. In particular, CdS thick films allowed room temperature operation due to to its photo-chemical properties. The responses of the sensors were reproducible over time, showing a particular stability of the signal [218]. Fu et al. [219] synthetized this material with leaf-like morphology through hydrothermal method and studied its sensing properties exposed to four gases (isopropanol, methanol, acetone and ether) in thermo-activation mode. As part of this project, the electronic properties of indium monoselenide (InSe) nanostructures were investigated via fabrication of chemiresistive sensors. The sensors were used to test the presence of volatile organic compounds including methanol, formaldehyde, chloroform and acetone in the ambient. We demonstrated variation in conductivity experienced by the sensor in the presence of the volatile organic vapours (VOCs) and the sensitivity of the sensor was dependent on each vapour due to different mode of interaction with the sensing material. In addition, the morphology of the InSe nanostructure played a role on the overall analyte-InSe semiconductor interaction thus influencing the final sensitivity and selectivity of the sensor [220].

2.5.1 Mechanism and Principles of chemical sensors

2.5.1.1 Definition of chemical sensors

A chemical sensor is a device with the ability to determine the detectable presence, concentration and/or composition of a given analyte present in any desired medium by producing a measurable output signal. Primarily, it consists of a recognition element known as the receptor, that is sensitive to stimuli produced by various chemical compounds (analyte) and a transduction element (transducer part) that generates a signal whose magnitude is functionally related to the concentration of the analyte. During the sensing process, an

amplified electric signal is obtained as a result of the interaction of the analyte species and the receptor. The receptor in most cases is a semiconductor whose parameters such as resistivity and conductivity just to mention a few get altered upon interaction with the analyte. The changes are then transduced by the transducer into electrical output signal [189, 221, 222].

2.5.1.2 Types of chemical sensor

Classification of sensors is based on the following:

- The operating principles of the transducer as shown in Fig. 2-16.
- Method used in measuring the magnitude of the effect.
- Application to detect or determine a given analyte.

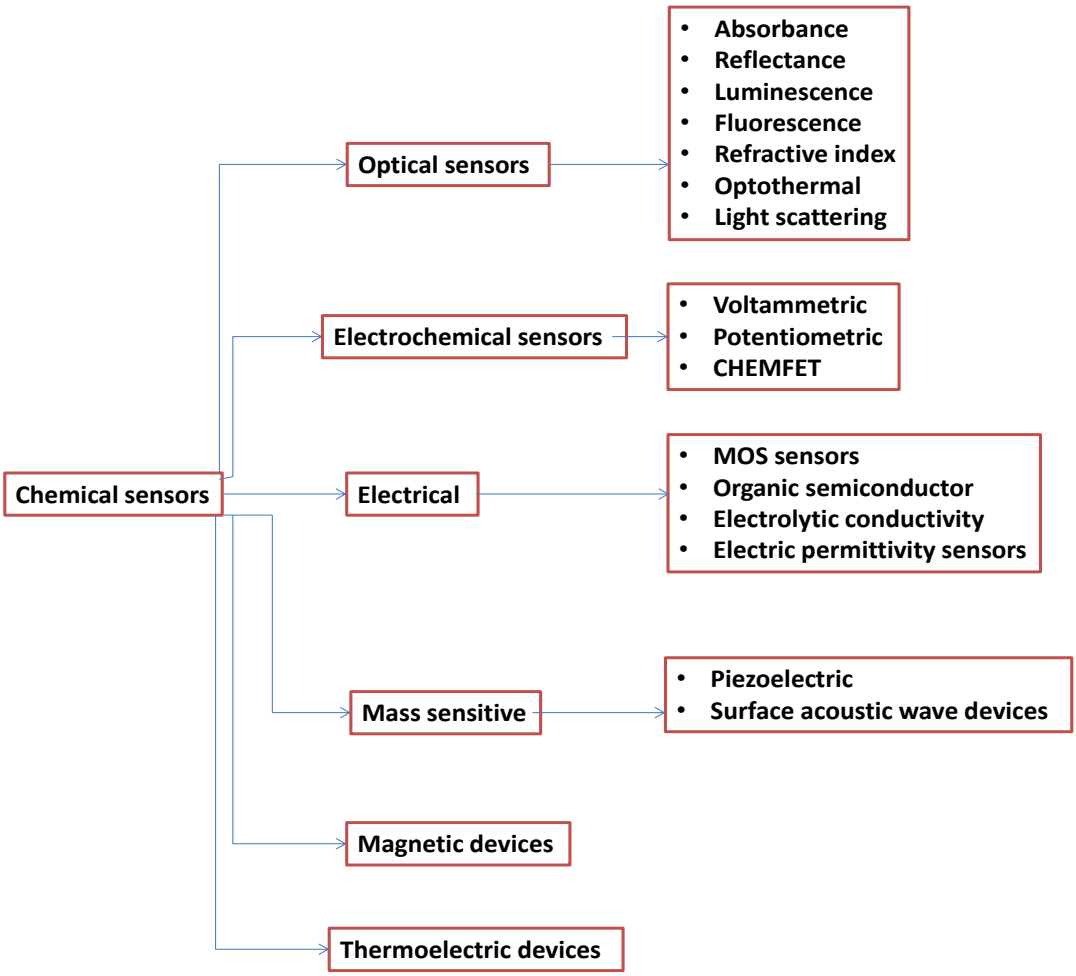

Figure 2-13: Schematic illustration of the classification of chemical sensors.

2.5.1.3 Semiconductor electronic structure for transduction mechanism in analyte detection

As discussed from the previous chapter, the electronic states of semiconductor surface atoms can be both spatially and energetically localized due to coordinative unsaturation of the surface atoms. As such, these surface states may have energies within the band gap, and thus have a great impact on the semiconductor electronic properties and adsorption processes with important consequences for analyte detection. Surface states that occur naturally within the semiconductor as a result of the solutions from the Schrodinger equation and the structural defects including atomic vacancies and local lattice mismatches are referred to as intrinsic

surface states. Also, new states (extrinsic surface states) may be introduced by an external adsorbate adsorbed on the surface of the semiconductor. They correspond to the dangling bonds of the adsorbate and may energetically lie within the band gap or overlap continuum states. The excited electron or hole can be trapped by these local energy minima and lead to non-radiative recombination during photoluminescence [210, 223, 224].

For the transduction processes in a general view, holes or electrons can become trapped at surface states to create a localized charge layer at the surface, resulting in an electrostatic field in the near-surface region within the semiconductor thus causing the band to bend as illustrated in Fig.2-17. The degree of band bending is quantified by surface potential, ϕ_s usually described by the surface Fermi level, E_{fs}. The surface Fermi level is commonly specified relative to the band edges. The width of this electric field region which is referred to as the depletion width plays a critical role in carrier dynamics. Modification of the energetic distribution and/or the surface density of states (SDOS) by adsorption can sometimes shift the energetic position of E_{fs} relative to the band edges, perturbing the electric field and giving rise to measurable changes in electrical and optical properties [210].

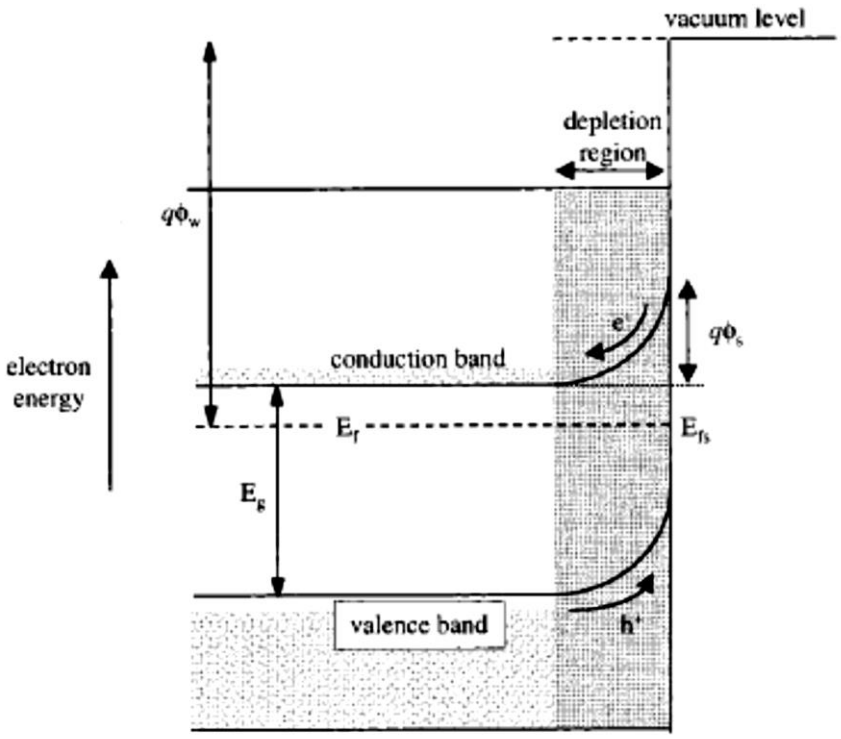

Figure 2-14: Diagram illustrating the electronic structure of a semiconductor for an n-type semiconductor with band gap, Eg, bulk Fermi level, E_f, surface Fermi level, E_{fs}, and surface potential, ϕs. The near-surface electric field, the depletion region, is shaded, and the filled electronic levels are speckled [210].

2.5.1.4 Sensing mechanisms

The semiconductor gas sensing devices are based on the conductivity change of the semiconductor material due to its interaction with gas. Below are some ways through which gases/vapours may interact with the semiconductor surface to bring about detection of the particular gas ambient;

2.5.1.4.1 Reduction/oxidation of the semiconductor

Conductivity in many compound semiconductors is attributed to the electrons and holes that arise as result of non-stoichiometry of the material. As such, the existence of an analyte gas on the surface of the semiconductor may tamper with this stoichiometry; hence a change in

conductance is experienced. For example, titanium oxide sometimes has excess titanium implying that electrons are present in the conduction of the material as a result of the excess metal. In the presence of other electroactive impurities, the material may approach stoichiometry thus increase in the resistance of the semiconductor may be experienced. On the contrary, cuprous oxide often has an excess of the oxygen ions and the corresponding cation vacancies trap electrons from the valence bonds in the crystals. These empty valence holes provide a high conductivity by moving freely through the crystal. Therefore an oxidation or reduction of these compounds by oxygen or reducing agents, the conductivity changes [225].

2.5.1.4.2 Adsorption

When gas molecules are adsorbed on the surface of a semiconductor, electron transfer occurs between the semiconductor and the adsorbates. If the adsorbate is a reducing agent, it will inject electrons into the semiconductor. In the opposite case, the semiconductor accepts electrons from the adsorbates. This electron transfer continues until the Fermi level of the gas-adsorbed semiconductor surface becomes equal to that of the bulk. As a result of this electron transfer, a depletion or accumulation of charges occurs near the semiconductor surface. Then the accompanying variation of surface potential barrier induces a change in the electrical conductivity or resistivity. In principle, to detect a reducing gas, it would be probable to use an n-type semiconductor with initially few electrons such that addition of either one or more electrons will increase the conductance. Similarly, for the detection of an oxidizing gas, a p-type with few holes would be preferred such that removal of electrons will offer the sensor sensitivity [225].

2.5.1.4.3 Surface states

From a general point of view, the influence of adsorbed gas arises by its interaction with the surface states, usually a surface state associated with pre-adsorbed oxygen. The whole adsorption process which can either be physisorption or chemisorption occurs after the diffusion of the analyte gas on the active area of the surface. It is worth noting that the diffusion process is dependent on the ambient temperature of the measured atmosphere generally assumed to be room temperature. Molecular oxygen adsorbs on the surface and dissociates to form O^- after which this O^- extracts an electron from the semiconductor. This electron extraction leads to the creation of a depletion region near the surface leading to an increase in (assuming *n*-type semiconductor) resistance of the gas sensor [225, 226]. Fig. 2-18 shows a three-dimensional view of the crystallite of gas-sensitive material after adsorption of oxygen. This whole process is according to a model originally put forward by Mark and Windischmann rationalizing the behavior of the sensor in the measured environment and is described by equation 2-16 and 2-17 where R (g) and RO (g) represent reducing gas and oxidized reducing gas, respectively [227].

$$\tfrac{1}{2}O_2 + e^- \rightarrow O^-_{ads} \quad \text{..... (2-16)}$$

$$R_{(g)} + O^-_{ads} \rightarrow RO_{(g)} + e^- \quad \text{..... (2-17)}$$

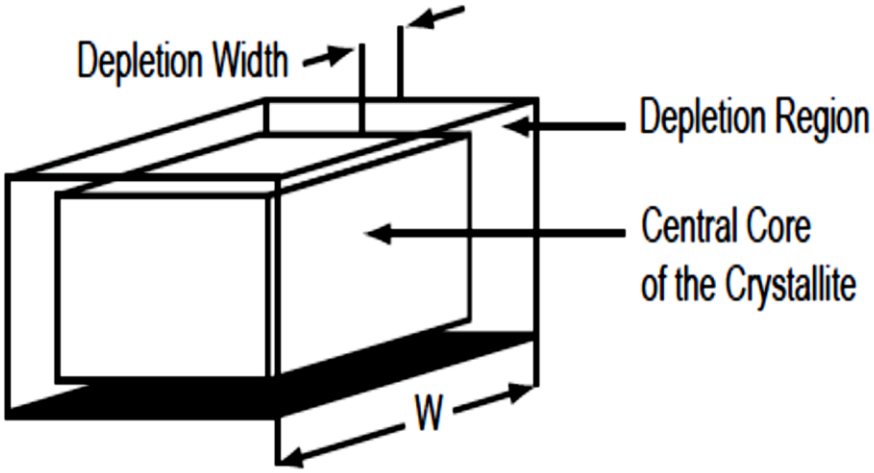

Figure 2-15: Shows a three-dimensional view of the crystallite of gas-sensitive material after adsorption of oxygen [227].

2.5.1.5 General response curve/characteristic curve

Figure 2-19 is the response curve describing the sensor response of a sensor to the primary species X. During sensing, apart from the analyte X, many other interfering species (i) also interact with and completely bind to the binding sites of the selective layer. Therefore equation 2-18 defines the three operating regions on the general response curve in consideration to the above argument where [24]:

$$a_0 = a_{ST}\frac{a_X + \sum_i K_i^{'} a_i}{a_X + \sum_i K_i^{'} a_i + 1/K_X} \quad \text{..... (2-18)}$$

a_0 represent the only occupied sites in or at the selective layer, a_{ST} is the total available binding sites, a_X is the activity of the occupied sites, a_i is the sites occupied by interferants, K_X and K_i are the binding constants of the single analyte and interferant respectively. $K_i^{'} = K_i/K_X$ is the selectivity coefficient. It applies to each interferant individually. The

smaller the value of $K_i^{'}$, the more selective the layer is to the analyte (X) than to the interferant species (i).

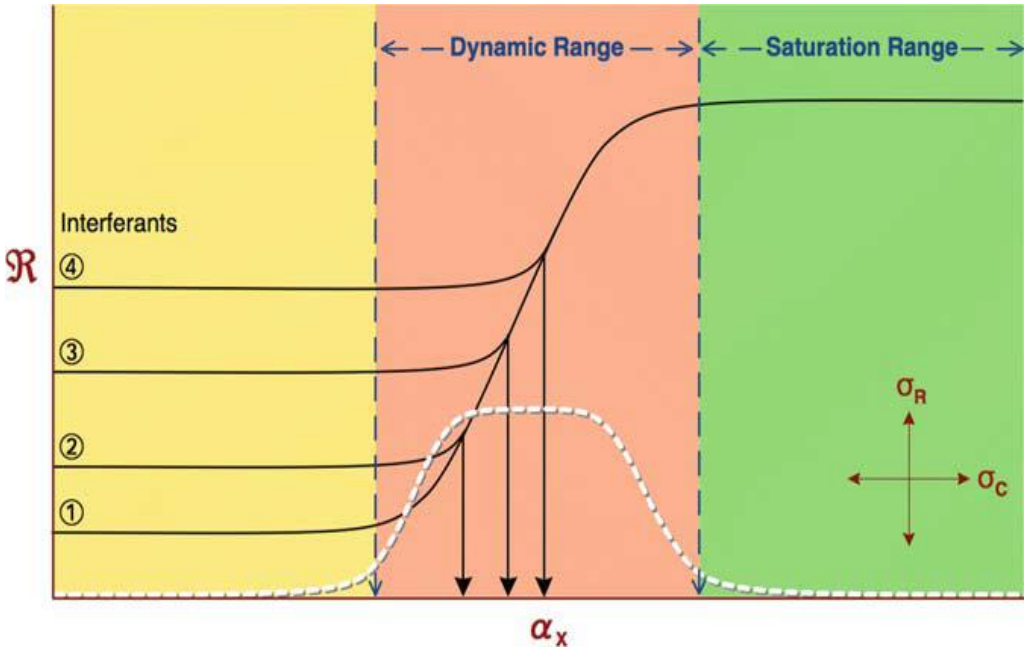

Figure 2-16: Defined regions of the general response curve [24].

2.5.1.5.1 Saturation limit of a sensor

At a higher activity of the analyte or higher level of the interferants such that $a_X \gg \sum_i K_i^{'} a_i + 1/K_X$ and/or $\sum_i K_i^{'} a_i \gg a_X + 1/K_X$, all of the available binding sites are occupied by one or the other species. Under these conditions the sensor does not respond to the analyte and is referred to as the saturation limit defined by equation 19:

$$a_0 = a_{ST} \quad \ldots\ldots\ldots\ldots\ldots\ldots\ldots\ldots\ldots\ldots\ldots\ldots \quad (2\text{-}19)$$

2.5.1.5.2 Dynamic range

This is the region that lies below the saturation region for which $\sum_i K_i' a_i \ll a_X \ll 1/K_X$. Here a fraction of the sites is occupied by X and their activities are linearly dependent on the activity of X in the sample and are represented as expressed in equation 2-20:

$$a_0 = a_{ST} K_X a_X \quad \text{..... (2-20)}$$

2.5.1.5.3 Interference region

In this region the activity of the analyte and/or its binding constant are low, that is, $a_X \ll (\sum_i K_i' a_i + 1/K_X)$, the binding sites are mostly by the interferants. In this region, the sensor again does not respond to the analyte and is represented by equation 2-21:

$$a_0 = a_{ST} \frac{\sum_i K_i' a_i}{\sum_i K_i' a_i + 1/K_X} \quad \text{..... (2-21)}$$

2.5.1.5.4 Detection limit

This is described by the intercept of the dynamic range and the interference region and can be expressed according to equation 2-22 where d.l is detection limit. Specifically it defines the minimum detectable response, usually above three times the standard deviation (i.e..,>3σ).

$$K_X (a_X)_{d.l} = \frac{\sum_i K_i' a_i}{\sum_i K_i a_i + 1/K_X} \quad \text{..... (2-22)}$$

2.5.1.6 Sensor parameters/Features of a sensor

The kinetics of the processes, which take place in the receptor part, determines the sensors parameters. The most common parameters are, sensitivity, selectivity, stability, response times, recovery time, reliability and working temperature. They are commonly given as three "S" factors and three "R" factors [189].

2.5.1.6.1 Sensitivity

Specifically, sensitivity of a sensor is the slope of the response curve in the dynamic range is defined by equation 2-23 in the case of resistive/conductiometric gas sensors. In other words sensitivity of a sensor refers to either the lowest level of chemical/analyte concentration or to the smallest increment of concentration that can be detected in the sensing environment. In a more general version, sensitivity of a sensor describes its ability to recognize a variation in physical and/or chemical properties of the sensing material under analyte.

$$\partial\left[\frac{\Delta G}{G_0}\right] \Big/ \partial[C] \quad \text{..... (2-23)}$$

G is the conductance of the sensor influenced by the vapors, and G_0 is the sensor conductance in the air and C is the concentration of the analyte [220, 226].

2.5.1.6.2 Selectivity

Selectivity though still a major challenge in most sensors is related to the discrimination capacity of a sensor device for a mixture of gases. In other words, selectivity refers to the ratio of the sensor's ability to detect what is of interest, over the sensor's ability to detect

what is not of interest. Unfortunately, the selectivity of the metal oxide gas sensor is broad, responding to all reducing gases that interact with oxygen on the surface of the sensor [226].

2.5.1.6.3 Robustness

Robustness at the sensor level refers to the ability of the sensor to perform its function over a range of ambient conditions with humidity, temperature, etc. and over a period of time in the presence of drift and stability variations. Unfortunately, the parameters of a chemical sensor technology adjusted to improve robustness are often the same parameters that result in a decrease in sensitivity and selectivity [228, 229]. For example, the most sensitive chemical sensor is often one whose reactions are totally irreversible. However, reversible reactions are desired. Design with the backing of the theory can result in a fine balance between robustness and sensitivity.

2.5.1.6.4 Speedy response and recovery

In gas detection, response time is usually defined as the time taken to achieve 90 percent of the final change in conductance, following the step-change in gas concentration at the sensor. However, sometimes 50 percent or 70 percent of the final change is also referred to as response time in literature. This is particularly the case in semiconductor metal oxide (SMO) gas sensors, because the sensors have a very fast initial response, followed by long drawn out tail before reaching the steady state values [230].

2.6 Application of semiconductor nanocrystals to dye sensitized solar cells

Dye-sensitized solar cells (DSSCs) are typical third-generation photovoltaic devices with mesoporous architecture which have achieved power conversion efficiency (PCE) up to 13 % [231, 232]. Just like photosynthesis in plants where chlorophyll absorbs photons but does not

participate in charge transfer, absorption of photons and charge transport are performed by separate components in the DSSCs. This is contrary to conventional PV cells where a semiconductor assumes both functions. The separation of functions eases the purity demand on the raw materials thereby making DSSCs a low cost alternative solar cell. In addition to the low cost of production, DSSCs have attracted a widespread interest owing to their environmental friendliness, easy processing and good performance (relatively high conversion efficiency) [57, 233-241]. Compared to the conventional silicon and the second generation photovoltaic cells, the power conversion efficiencies of DSSCs are still low [242]. However, there still is a high potential for improvement in their efficiency. With this regard, over the past two decades, intensive investigations to improve the DSSCs photovoltaic performance and further reduce the cost of production are underway [243-245].

2.6.1 Structure and operating principle of a dye sensitized solar cell

Typically, the basic structure of a DSSCs as illustrated in Fig. 2-21 mainly consist of three parts namely; the working electrode, the electrolyte and the couther electrode which is also known as the cathode.

2.6.1.1 Photoanode

The photoanode or photoelectrode also known as the working electrode is generally fabricated through deposition of a layer of mesoporous nanocrystalline semiconductor (e.g.,TiO_2 or ZnO) on a conductive substrate (e.g. FTO and ITO glass), after which a sensitizer such as dye or quantum dots is added onto the mesoporous semiconductor. The dye-sensitized nanocrystalline semiconductor photoanode plays an important role in converting photons into electrical energy. Light harvesting, electron injection and collection, and unwanted electron recombination are all connected within the photoanode. Therefore it is essential to optimize the morphology of the photoanode in order to develop DSSCs with high

conversion efficiencies. The ideal photoanode should have a nanostructured mesoscopic morphology, which can give a high specific surface area for dye adsorption. Secondly, the energy levels of the semiconductor oxide, sensitizer and the electrolyte should match each other so that the electron transfer is thermodynamically possible. Finally, other factors to be considered during optimization of the photoanode include, optical path length, porosity, and connectivity, should also be carefully considered to optimize the photoanode performance. These parameters ensure that electrons can efficiently inject into the conduction band of semiconductor oxide and, that the electron in the semiconductor has faster transfer speeds thereby reducing the electron recombination with electrolyte [246-248]. The most commonly used semiconductor electrode material is nanocrystalline TiO_2 due to its exemplary performance associated to its good photo stability, appropriate band gap and excellent photocatalytic activity. ZnO has a wide bandgap similar to TiO_2 thus can also a good choice as electrode materials [249, 250].

2.6.1.2 Electrolyte

In a DSSC, the electrolyte is considered one of the most crucial components as it is responsible not only for the charge carrier transport between the photoanode and the counter electrode but also for the regeneration of the dye and itself during the DSSC operation [240]. The power conversion efficiency and the long term stability of the device are dependent on the electrolyte. This is so because the three parameters namely, photocurrent density (Jsc), photovoltage (Voc) and fill factor (FF) that determine the efficiency of the device are greatly affected by (i) the electrolyte in DSSC and (ii) by the interaction of the electrolyte with the electrode interfaces. For instance, the transport redox couple components can influence the value of the Jsc while the redox potential of the electrolyte can affect the Voc. In addition, the diffusion of the charge carrier in the electrolyte and the charge transfer resistance on the electrolyte/electrode interface has impacts on the FF. In order to improve the performance of

the DSSCs, many scientists have been devoting their research to the electrolytes. Most highly efficient DSCs have been constructed with liquid electrolytes with the iodide/triiodide (I^-/I_3^-) redox couple and volatile organic solvents. This can be attributed to its favourable penetration into the mesoporous film, its fast dye regeneration combined and its extremely slow recombination. Some of the challenges experienced when using electrolyte include subsequent evaporation of toxic solvents, the leakage of liquid electrolytes as well as the sealing problem. This significantly hinders their practical applications. With this regard, other electrolytes such as (quasi) solid-state electrolytes, such as hole transport materials (HTMs), ionic liquids, or solid-state composite electrolytes are being considered [241, 248]; and they are illustrated in Fig. 2-20.

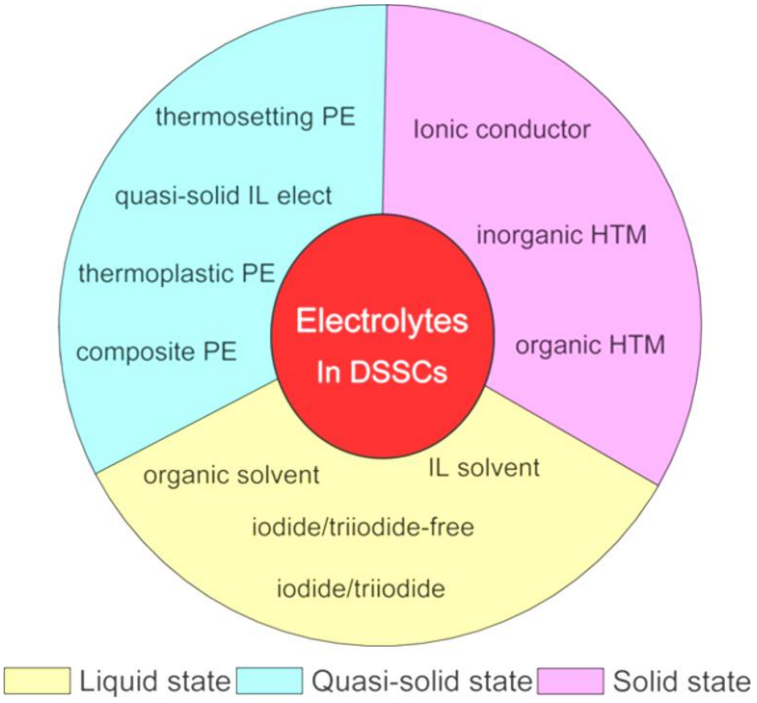

Figure 2-17: Classification of the electrolytes used in dye-sensitized solar cells. IL stands for ionic liquids, HTM for hole transport material and PE is polymer electrode [241].

2.6.1.3 Counter electrode (CE)

Another very essential component of the DSSC is the counter electrode (CE). One of the CE main functions is to collect electrons from the external circuit and transfer them, including electrons from the redox couple, to the electrolyte. Secondly, it acts as the catalyst during the reduction process of the redox species which are the mediators for the regeneration of the sensitizer (dye) after the electron injection. Therefore the nature of a catalyst is important in determining the photovoltaic performance of the DSSCs. As such, an effective CE should have good electrical conductivity, high/good catalytic activity for the reaction $I_3^- + 2e \rightarrow 3I^-$ which also minimizing the charge transfer over-potential, and chemical/electrochemical stability. Based on these standards, platinum (Pt) is the most commonly used catalytic material and it is usually deposited thermally on a conductive glass substrate such FTO. Despite the excellent performance and stability, Pt possess some challenges in the overall device fabrication cost as it is noble thus extremely expensive and its resources are limited. In addition, it can be corroded by iodine species in electrolyte solution. These factors consequently restrict the large-scale application of Pt-based CEs in DSSCs [57, 239, 248, 251]. Therefore, low cost, stable, and effective (maintaining the high performance) non-Pt catalysts should be exploited to fabricate novel CEs.

From the previous studies, a number of inexpensive materials including carbonaceous materials, conducting polymers and some inorganic compounds, such as oxides, nitrides, carbides, sulfides, phosphides, and tellurides have been developed for the fabrication of non-Pt CEs [252-276]. For instance, electrochemically deposited CoS and NiS have been reported as efficient CE materials with remarkable stability and conversion efficiency of about 6.5 % and 6.83 % respectively [277, 278], thereby demonstrating a new way to find novel catalytic materials. As emerging functional materials, transition-metal selenides (TMSs) have portrayed unique electrical properties, interesting chemical behaviour and good chemical

stability which are suitable features for electro/photocatalysis applications. Despite being used for the oxygen reduction reaction in fuel cells [59, 279-283], TMSs are also starting to receive attention as CEs in DSSCs and their conversion efficiencies are comparable with conventional Pt-CEs. For example, using hydrazine hydrate as the reductant in an in situ hydrothermal process, Gong et al. reported the synthesis of two selenides, $Co_{0.85}Se$ and $Ni_{0.85}Se$, for application as CEs in DSCs. Subsequently, high PCEs of 9.40% and 8.32% were obtained which established new records for DSCs with non-Pt CEs [59]. In 2013, Guo and the group prepared $NbSe_2$ nanosheets, nanorods and $NbSe_2$/carbon composite via a reductant-free solvothermal approach which they later used as CEs in DSSCs. They demonstrated that that the devices achieved comparable performance to Pt-CEs with efficiencies amounting 7.34 %, 6.8 %, 7.8 % for $NbSe_2$ nanosheets, $NbSe_2$ nanorods and the NbSe2/C composite respectively. These values were close to the one they obtained for the Pt-CE which was 7.9 %. They also demonstrated that different morphologies of $NbSe_2$ had different electrocatalytic behaviour towards the triiodide/iodide electrolyte [284]. Recently, Zhang et al synthesized NiSe-Ni_3Se_2 hollow hexagonal nanodisks on graphene via one step solvothermal technique using hydrazine hydrate as a reductant. These hollow hybrid nanostructures (NiSe-Ni_3Se_2/RGO) showed more remarkable electrocatalytic performance as CEs in DSSC resulting in about 7.83 % PCE compared to 7.28 % of Pt-CE [58]. Other transition metal selenide including CoSe, NiSe, $NiSe_2$, $MoSe_2$, WSe_2, and $TaSe_2$ have also been employed in DSSCs as CEs [57, 60, 285, 286]. Although TMSs are suitable for use as CE materials and can significantly replace Pt in DSCs, the origin of high electrocatalytic activity of TMSs remains unclear, thus still under a lot of scrutiny.

2.6.1.4 Working principle

The schematic diagram presented in Figure 2-21 illustrates the general operation principle of a DSSC. Upon illumination, the dye molecule (D) absorbs the photons which strike the transparent conducting oxide (FTO or ITO in most cases) film. The photons whose values match the HOMO-LUMO energy gap lead to the formation of electronically excited dye molecule/excited electron (D*) from the highest occupied molecular orbital (HOMO) in the ground state to the lowest unoccupied molecular orbital (LUMO) in the excited state (eqn 2-24). The excited dye molecule (D*) then undergoes oxidative quenching by injecting an electron into the conduction band (CB) of the mesoporous semiconducting film (TiO_2 mostly) to form oxidized dye (D^+) and the electrons transfer through TiO_2 film to the anode (eqn 2-25) where the electrons are collected. The charge transfer occurs via the dye–TiO_2 interfacial bond due a strong electronic coupling between the two. The main function of the electrolyte is the regeneration of the oxidized dye (D^+) by iodide (I^-), the electron donor in the electrolyte. In other words, the oxidized dye (D^+) receives electrons from the reduced component (RE = I^-) of the redox couple in electrolyte to regenerate the dye (D) and the reduced component (RE) is oxidized into the oxidized component (OX = I_3^-) of the redox couple (eqn 2-26). The oxidation of the iodide produces I_3^- ions which migrate to the cathode (CE) to compensate for its missing electrons from the cathode. The I^- is regenerated by the reduction of I_3^- catalysed by the CE and also by accepting electrons from the external circuit, and the circuit is completed by the immigration of an electron through the external load (eqn 2-27) [239, 241, 251, 287].

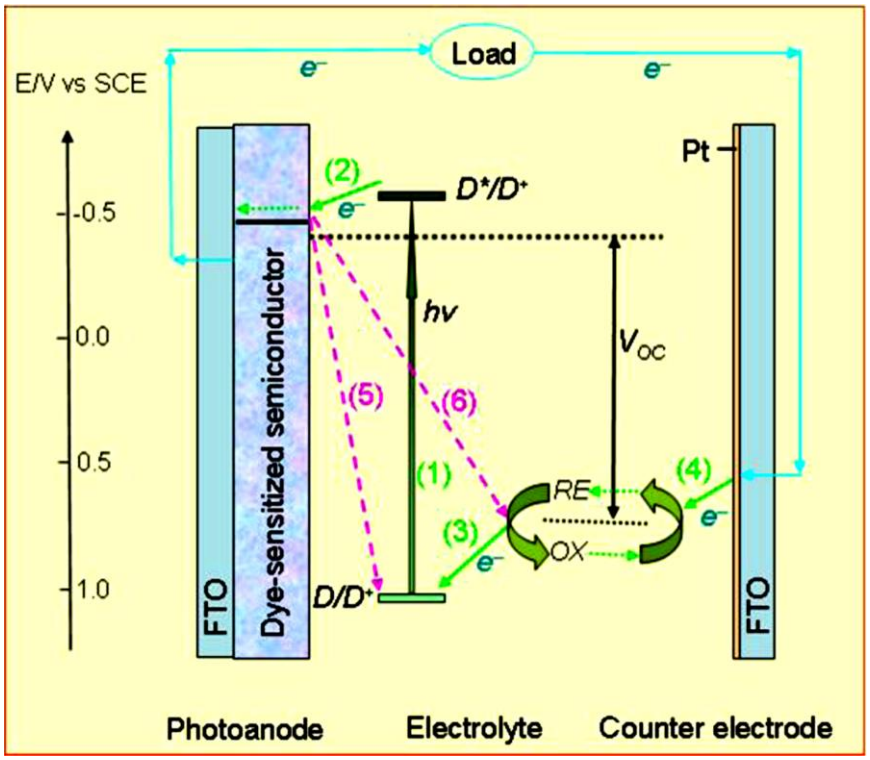

Figure 2-18: Operating principle of dye-sensitized solar cells [241].

Process 1: light-induced excitation of the dye to produce excitons (D*). Process 2: separation of the excitons at the dye/TiO_2 interface and injecting electrons into the conduction band of the TiO_2 semiconductor and leaving holes (D^+) in the dye. Process 3: dye regeneration via accepting electrons from the reduced state of the redox couple (RE) and producing the oxidized state of the redox couple (OX) in electrolyte. Process 4, involves the electrolyte regeneration via I_3^- accepting electrons from the counter electrode and producing I^-. Process 5: injected electrons recombination by donating electrons to D^+. Process 6; injected electrons recombination by donating electrons to I_3^-.

During the operation process of a DSSC, there exist two competitive reactions that may affect the efficiency of the device negatively. The photoelectrons may recombine back with the electrolyte or an oxidized dye molecule is the most probable recombination reaction. Mainly, two possible recombination routes are present in DSCs. One, is that the electrons in TiO_2 film

are captured by the oxidized dye (D^+), resulting in the recombination of electrons (eqn 2-28); the other is that the electrons in TiO_2 film are captured by I_3^- of the redox couple, also leading to the recombination of electrons (eqn 2-29). Both these recombination take place at the TiO_2/dye–electrolyte interface. It is noteworthy that the recombination processes do not play remarkable negative effect owing to their slower speed compared to the forward reactions (eqn 2-24 to 2-27). Also, the device generates electric power from light without suffering from any permanent chemical transformation [241, 251, 287].

Overall reaction in a DSSC

$$D/TiO_2 \xrightarrow[photoexcitation]{} D^*/TiO_2 \quad \text{..... (2-24)}$$

$$D^*/TiO_2 \xrightarrow[Electroninjection]{} D^+/TiO_2 + e^-/CB-TiO_2 \quad \text{..... (2-25)}$$

$$2D^+/TiO_2 + 3I^- \xrightarrow[dyeregeneration]{} 2D/TiO_2 + I_3^- \quad \text{..... (2-26)}$$

$$I_3^- + 2e^- \xrightarrow[electrolyteregeneration]{} 3I^- \quad \text{..... (2-27)}$$

$$e^-/TiO_2 + D^+/TiO_2 \xrightarrow[recombinationbyD^+]{} D/TiO_2 \quad \text{..... (2-28)}$$

$$e^-/TiO_2 + I_3^- \xrightarrow[recombinationbyI_3^-]{} 3I^- \quad \text{..... (2-29)}$$

2.6.2 Characterization of parameters

Peak power, P_{max}, short current density, J_{sc}, open circuit voltage, V_{oc} and fill factor, FF are the major parameters employed during the characterization a solar cell's performance. They can be obtained from the J-V characteristics of a cell under illumination or in the dark as depicted in Fig. 2-22.

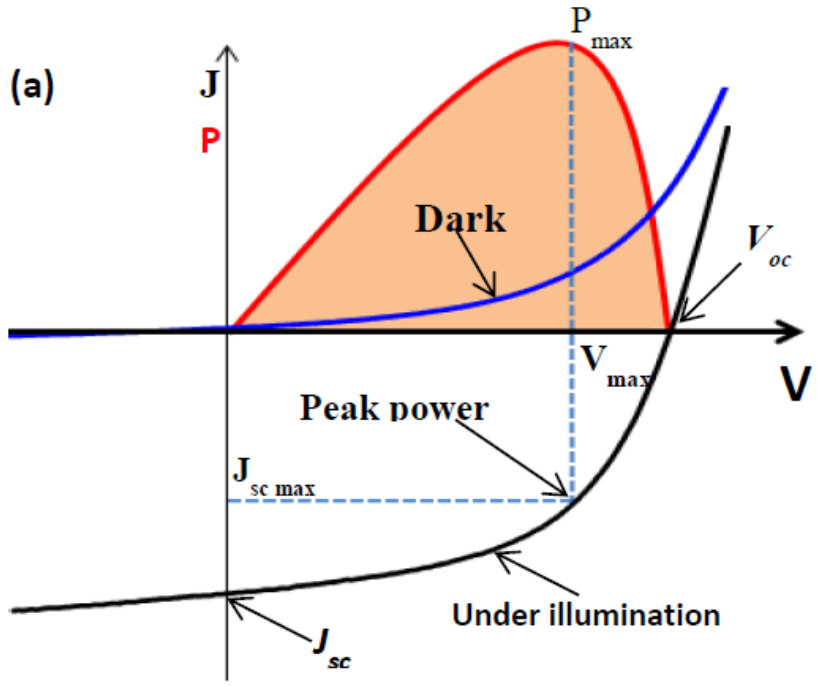

Figure 2-19: The J-V characteristics of solar cell in the dark and under illumination [289].

2.6.2.1 Short circuit current

This is the current flowing through the external circuit in the absence of a load (current when voltage equals zero). Short circuit current is determined by the photon flux density incident on the solar cell which depends on the spectrum of the incident light. For the standard solar cell measurements, the spectrum is standardized to the AM1.5 spectrum. The current density is roughly proportional to the area of the solar cell. The maximum current that can be delivered by the solar cell mainly depends on the optical properties of the cell which include absorption of the active layer and reflection from the back end electrodes. When a load is connected across the terminals of the cell, the current decreases as charges accumulate at the terminals. The resulting current is a superposition of short circuit current resulting from absorption of photons and the dark current. Dark current is caused by the potential across the load when the device is not illuminated and it flows in the opposite direction [288, 289].

2.6.2.2 Open circuit Voltage

This is the voltage between the terminals when no current is drawn (infinite load resistance). Voc corresponds to the forward bias voltage when the photocurrent is compensated by the dark current and it gives the maximum voltage that a solar cell can deliver. Open-circuit voltage depends on the energy difference between the highest occupied molecular orbital (HOMO) level of the donor and the lowest unoccupied molecular orbital (LUMO) level of the acceptor so long as there is a good electrical contact at the counter electrode-electrolyte interface. The HOMO level is approximated as the ionization potential of the donor whiles the LUMO as the electron affinity of the acceptor molecules. In general, for a DSSC, electrons flowing from the anode to the external load are collected at the counter electrode. The open-circuit voltage (V_{OC}) across the cell is thermodynamically determined by the difference between the quasi-Fermi level (QFL) of the semiconductor and the redox potential of the electrolyte [289].

2.6.2.3 Fill factor

The fill factor as portrayed by equation 30 is the ratio of maximum power generated to the product of *Voc* and *Jsc*. Fill factor is one parameter that may give the details about the quality of the cell. Therefore, it can be defined as a measure of the quantity of open circuit voltage and short circuit current utilized when maximum power is generated. From equation 30, factors affecting the nature of the Voc such as the level of the LUMO for both the acceptor and the donor also affect the value of the FF. The fill factor is also dependent on the series and resistance which are related to the slope of the tangent line to the current density (J)–voltage (V) curve at Voc. Therefore the resistances have a pronounced effect on the shape of *J–V* curve around Voc and Jsc respectively hence affecting the 'square' shape of the *J-V* curve [289].

$$FF = \frac{J_{max} V_{max}}{J_{sc} V_{oc}} \quad \text{..... (2-30)}$$

Charge extraction and recombination are always in constant competition since the all depend on the mobility of the carriers in the device. Optimization of the cell to obtain maximum FF is important as high mobility which is vital for the transport of the carriers may also result in charge recombination [290-292].

In a DSSC, the series resistance (Rs) is a combination of the Warburg impedance relative to the Nernst diffusion of the I_3^- species in the electrolyte (Zn), which is the impedance related to charge transfer and recombination at the TiO_2–dye–electrolyte interface (R_{AN}), resistance at the fluorine-doped tin oxide (FTO) glass (R_H), and the charge-transfer resistance at the CE and the electrolyte interface (R_{CT}). Fig. 2-23 shows the equivalent circuit used to represent interfaces in DSCs, where R_{CT} (solid) is the charge transfer resistance of the TiO_2–FTO or Pt–FTO interface, C(solid) is the capacitance of the TiO_2–FTO or Pt–FTO interface and W(sol) is the Warburg parameter describing the diffusion of the I_3^- electrolyte. Amongst all these resistances, a prominent role is handled by R_{CT} to determine Rs. A lower value of R_{CT} signifies tremendous electron transfer from the CE to the electrolyte for the reduction of the I_3^- ion to the I^- ion at the catalytic interfaces of the CE. A superficial electron transfer between the CE and electrolyte reduces the series resistance (Rs), thereby giving a higher FF, which results in a high conversion efficiency [251, 293-295].The catalytic activity of the CE can be explained in terms of the current density (J), which is calculated from the charge transfer resistance (RCT), given by the equation 31 where;

$$R_{CT} = \frac{RT}{nFJ} \quad \text{..... (2-31)}$$

R, T, n, and F are the gas constant, temperature, the number of electrons transferred in the elementary electrode reaction (n = 2) and Faradays constant respectively [296].

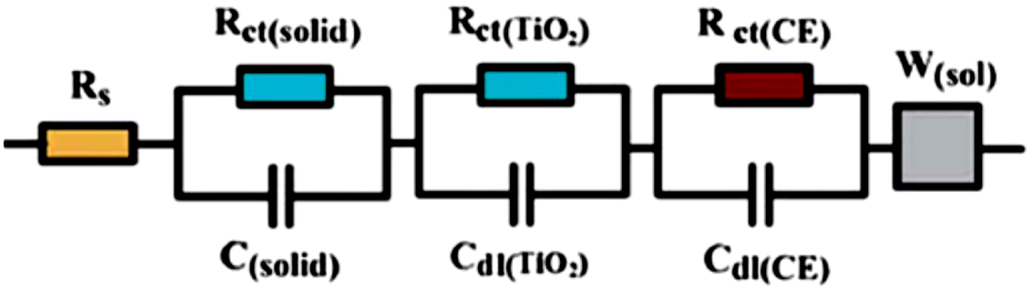

Figure 2-20: Equivalent circuit used to represent interfaces in solar cell [251, 297].

2.6.2.4 Efficiency parameters of a DSSC

The two most important parameters used to establish/ascertain the overall performance of the cell under monochromatic light include;

2.6.2.5. The incident photon-to-electrical (power) conversion efficiency (IPCE)

The incident photon-to-electric conversion efficiency represents the overall charge injection process measured using a single wavelength source and can be calculated using equation 2-32; where λ is the wavelength, I_{SC} is the short circuit current and φ is the incident radiative flux [251].

$$IPCE(\lambda) = 1240(I_{SC}/\lambda_{\varphi}) \quad \text{..... (2-32)}$$

2.6.2.6. Power conversion efficiency (PCE)

The power conversion efficiency is defined as the ratio of output power (maximum generated power) to incident power P_{in} expressed as a percentage. In other words, it is the overall sunlight-to-electric power conversion efficiency and is given by equation 2-33:

$$\eta = \frac{P_{\max}}{P_{in}} = \frac{J_{\max}V_{\max}}{J_{sc}V_{oc}} = \frac{J_{sc}V_{oc}FF}{P_{in}} \quad \text{..... (2-33)}$$

where P_{in} is the intensity of incident light [251, 289]. Similarly, in a DSSC, PCE can be expressed as the product of the three key terms as depicted in equation 2-34:

$$H = \eta_{abs}\eta_{inj}\eta_{coll} \quad \text{..... (2-34)}$$

where η_{abs} is the efficiency of light absorption by the dye, η_{inj} is the efficiency of the charge injection from the excited state of the dye and η_{coll} is the amount of charge collection in the mesoporous oxide layer [251, 298].

References

[1] A.L. Efros, D.J. Lockwood, L. Tsybeskov, Semiconductor Nanocrystals: From Basic Principles to Applications, Springer Science & Business Media, 2013.

[2] A. Srivastava, N. Tyagi, Semiconductor Nanocrystals, INTECH Open Access Publisher, 2012.

[3] N. Yaacobi-Gross, Colloidal Semiconductor Nanocrystals Based Solar Cells, Technion-Israel Institute of Technology, Faculty of Electrical Engineering, 2012.

[4] L. Brus, A simple model for the ionization potential, electron affinity, and aqueous redox potentials of small semiconductor crystallites, The Journal of Chemical Physics, 79 (1983) 5566-5571.

[5] J. Chang, E.R. Waclawik, Colloidal semiconductor nanocrystals: controlled synthesis and surface chemistry in organic media, RSC Advances, 4 (2014) 23505-23527.

[6] L.E. Brus, Electron–electron and electron-hole interactions in small semiconductor crystallites: The size dependence of the lowest excited electronic state, The Journal of Chemical Physics, 80 (1984) 4403-4409.

[7] L. Brus, Electronic wave functions in semiconductor clusters: experiment and theory, The Journal of Physical Chemistry, 90 (1986) 2555-2560.

[8] M.G. Bawendi, M.L. Steigerwald, L.E. Brus, The quantum mechanics of larger semiconductor clusters (" quantum dots"), Annual Review of Physical Chemistry, 41 (1990) 477-496.

[9] M.L. Steigerwald, L.E. Brus, Semiconductor crystallites: a class of large molecules, Accounts of Chemical Research, 23 (1990) 183-188.

[10] D. Norris, M. Bawendi, Measurement and assignment of the size-dependent optical spectrum in CdSe quantum dots, Physical Review B, 53 (1996) 16338.

[11] A.M. Smith, S. Nie, Semiconductor nanocrystals: structure, properties, and band gap engineering, Accounts of Chemical Research, 43 (2009) 190-200.

[12] A.P. Alivisatos, Perspectives on the physical chemistry of semiconductor nanocrystals, The Journal of Physical Chemistry, 100 (1996) 13226-13239.

[13] C. Yuan, The Study of II-VI Semiconductor Nanocrystals Sensitized Solar Cells, (2012).

[14] J. Luttinger, Quantum theory of cyclotron resonance in semiconductors: General theory, Physical Review, 102 (1956) 1030.

[15] W. Kohn, J. Luttinger, Theory of donor states in silicon, Physical Review, 98 (1955) 915.

[16] G.L. Bir, G.E. Pikus, P. Shelnitz, D. Louvish, Symmetry and strain-induced effects in semiconductors, Wiley New York, 1974.

[17] S.V. Gaponenko, Optical properties of semiconductor nanocrystals, Cambridge University Press, 1998.

[18] N. Moloto, Synthesis, properties and applications of Mn, Co, Ni and Cu chalogenide nanoparticles, in, 2011.

[19] A. Ekimov, A. Onushchenko, Quantum size effect in the optical-spectra of semiconductor micro-crystals, Soviet Physics Semiconductors-Ussr, 16 (1982) 775-778.

[20] J. Warnock, D. Awschalom, Quantum size effects in simple colored glass, Physical Review B, 32 (1985) 5529.

[21] N.F. Borrelli, D. Hall, H. Holland, D. Smith, Quantum confinement effects of semiconducting microcrystallites in glass, Journal of Applied Physics, 61 (1987) 5399-5409.

[22] D. Mocatta, G. Cohen, J. Schattner, O. Millo, E. Rabani, U. Banin, Heavily doped semiconductor nanocrystal quantum dots, Science, 332 (2011) 77-81.

[23] J. Wang, M.S. Gudiksen, X. Duan, Y. Cui, C.M. Lieber, Highly polarized photoluminescence and photodetection from single indium phosphide nanowires, Science, 293 (2001) 1455-1457.

[24] J. Hu, L.-s. Li, W. Yang, L. Manna, L.-w. Wang, A.P. Alivisatos, Linearly polarized emission from colloidal semiconductor quantum rods, Science, 292 (2001) 2060-2063.

[25] X. Peng, L. Manna, W. Yang, J. Wickham, E. Scher, A. Kadavanich, A.P. Alivisatos, Shape control of CdSe nanocrystals, Nature, 404 (2000) 59-61.

[26] V.F. Puntes, K.M. Krishnan, A.P. Alivisatos, Colloidal nanocrystal shape and size control: the case of cobalt, Science, 291 (2001) 2115-2117.

[27] T.S. Ahmadi, Z.L. Wang, T.C. Green, A. Henglein, M.A. El-Sayed, Shape-controlled synthesis of colloidal platinum nanoparticles, Science, 272 (1996) 1924.

[28] Z.A. Peng, X. Peng, Mechanisms of the shape evolution of CdSe nanocrystals, Journal of the American Chemical Society, 123 (2001) 1389-1395.

[29] Z.A. Peng, X. Peng, Nearly monodisperse and shape-controlled CdSe nanocrystals via alternative routes: nucleation and growth, Journal of the American Chemical Society, 124 (2002) 3343-3353.

[30] C. Pu, J. Zhou, R. Lai, Y. Niu, W. Nan, X. Peng, Highly reactive, flexible yet green Se precursor for metal selenide nanocrystals: Se-octadecene suspension (Se-SUS), Nano Research, 6 (2013) 652-670.

[31] Y. Yin, A.P. Alivisatos, Colloidal nanocrystal synthesis and the organic–inorganic interface, Nature, 437 (2005) 664-670.

[32] H. Weller, Synthesis and self–assembly of colloidal nanoparticles, Philosophical Transactions of the Royal Society of London A: Mathematical, Physical and Engineering Sciences, 361 (2003) 229-240.

[33] O. Chen, X. Chen, Y. Yang, J. Lynch, H. Wu, J. Zhuang, Y.C. Cao, Synthesis of metal–selenide nanocrystals using selenium dioxide as the selenium precursor, Angewandte Chemie International Edition, 47 (2008) 8638-8641.

[34] L.C. Roof, J.W. Kolis, New developments in the coordination chemistry of inorganic selenide and telluride ligands, Chemical Reviews, 93 (1993) 1037-1080.

[35] M. Han, X. Gao, J.Z. Su, S. Nie, Quantum-dot-tagged microbeads for multiplexed optical coding of biomolecules, Nature Biotechnology, 19 (2001) 631-635.

[36] I.L. Medintz, H.T. Uyeda, E.R. Goldman, H. Mattoussi, Quantum dot bioconjugates for imaging, labelling and sensing, Nature Materials, 4 (2005) 435-446.

[37] D.V. Talapin, C.B. Murray, PbSe nanocrystal solids for n-and p-channel thin film field-effect transistors, Science, 310 (2005) 86-89.

[38] L. Zhu, M.-Q. Zhu, J.K. Hurst, A.D. Li, Light-controlled molecular switches modulate nanocrystal fluorescence, Journal of the American Chemical Society, 127 (2005) 8968-8970.

[39] M. Kazes, D.Y. Lewis, Y. Ebenstein, T. Mokari, U. Banin, Lasing from semiconductor quantum rods in a cylindrical microcavity, Advanced Materials, 14 (2002) 317-321.

[40] S. Coe, W.-K. Woo, M. Bawendi, V. Bulović, Electroluminescence from single monolayers of nanocrystals in molecular organic devices, Nature, 420 (2002) 800-803.

[41] I. Gur, N.A. Fromer, M.L. Geier, A.P. Alivisatos, Air-stable all-inorganic nanocrystal solar cells processed from solution, Science, 310 (2005) 462-465.

[42] C. Murray, D.J. Norris, M.G. Bawendi, Synthesis and characterization of nearly monodisperse CdE (E= sulfur, selenium, tellurium) semiconductor nanocrystallites, Journal of the American Chemical Society, 115 (1993) 8706-8715.

[43] Z. Peng, X. Peng, Synthesis of high quality Cadmium chalcogenides semiconductor nanocrystals using CdO as precursor, J. Am. Chem. Soc, 123 (2001) 183.

[44] M.A. Hines, P. Guyot-Sionnest, Synthesis and characterization of strongly luminescing ZnS-capped CdSe nanocrystals, The Journal of Physical Chemistry, 100 (1996) 468-471.

[45] X. Peng, M.C. Schlamp, A.V. Kadavanich, A.P. Alivisatos, Epitaxial growth of highly luminescent CdSe/CdS core/shell nanocrystals with photostability and electronic accessibility, Journal of the American Chemical Society, 119 (1997) 7019-7029.

[46] D.J. Norris, A.L. Efros, S.C. Erwin, Doped nanocrystals, Science, 319 (2008) 1776-1779.

[47] N. Pradhan, D. Goorskey, J. Thessing, X. Peng, An alternative of CdSe nanocrystal emitters: pure and tunable impurity emissions in ZnSe nanocrystals, Journal of the American Chemical Society, 127 (2005) 17586-17587.

[48] P. Reiss, ZnSe based colloidal nanocrystals: synthesis, shape control, core/shell, alloy and doped systems, New Journal of Chemistry, 31 (2007) 1843-1852.

[49] N.S. Norberg, G.L. Parks, G.M. Salley, D.R. Gamelin, Giant excitonic Zeeman splittings in colloidal Co^{2+}-doped ZnSe quantum dots, Journal of the American Chemical Society, 128 (2006) 13195-13203.

[50] D.A. Bussian, S.A. Crooker, M. Yin, M. Brynda, A.L. Efros, V.I. Klimov, Tunable magnetic exchange interactions in manganese-doped inverted core–shell ZnSe–CdSe nanocrystals, Nature Materials, 8 (2009) 35-40.

[51] M. Ibáñez, R. Zamani, A. LaLonde, D. Cadavid, W. Li, A. Shavel, J. Arbiol, J.R. Morante, S. Gorsse, G.J. Snyder, $Cu_2ZnGeSe_4$ nanocrystals: synthesis and thermoelectric properties, Journal of the American Chemical Society, 134 (2012) 4060-4063.

[52] C. Xiao, J. Xu, K. Li, J. Feng, J. Yang, Y. Xie, Superionic phase transition in silver chalcogenide nanocrystals realizing optimized thermoelectric performance, Journal of the American Chemical Society, 134 (2012) 4287-4293.

[53] F.J. Fan, Y.X. Wang, X.J. Liu, L. Wu, S.H. Yu, Large-Scale Colloidal Synthesis of Non-Stoichiometric $Cu_2ZnSnSe_4$ Nanocrystals for Thermoelectric Applications, Advanced Materials, 24 (2012) 6158-6163.

[54] K.S. Leschkies, T.J. Beatty, M.S. Kang, D.J. Norris, E.S. Aydil, Solar cells based on junctions between colloidal PbSe nanocrystals and thin ZnO films, ACS nano, 3 (2009) 3638-3648.

[55] Q. Guo, S.J. Kim, M. Kar, W.N. Shafarman, R.W. Birkmire, E.A. Stach, R. Agrawal, H.W. Hillhouse, Development of $CuInSe_2$ nanocrystal and nanoring inks for low-cost solar cells, Nano Letters, 8 (2008) 2982-2987.

[56] J.M. Luther, M. Law, Q. Song, C.L. Perkins, M.C. Beard, A.J. Nozik, Structural, optical, and electrical properties of self-assembled films of PbSe nanocrystals treated with 1, 2-ethanedithiol, ACS Nano, 2 (2008) 271-280.

[57] J. Guo, S. Liang, Y. Shi, C. Hao, X. Wang, T. Ma, Transition metal selenides as efficient counter-electrode materials for dye-sensitized solar cells, Physical Chemistry Chemical Physics, 17 (2015) 28985-28992.

[58] X. Zhang, M. Zhen, J. Bai, S. Jin, L. Liu, Efficient NiSe-Ni_3Se_2/Graphene Electrocatalyst in Dye-Sensitized Solar Cells: The Role of Hollow Hybrid Nanostructure, ACS Applied Materials & Interfaces, 8 (2016) 17187-17193.

[59] F. Gong, H. Wang, X. Xu, G. Zhou, Z.-S. Wang, In situ growth of $Co_{0.85}Se$ and $Ni_{0.85}Se$ on conductive substrates as high-performance counter electrodes for dye-sensitized solar cells, Journal of the American Chemical Society, 134 (2012) 10953-10958.

[60] F. Gong, X. Xu, Z. Li, G. Zhou, Z.-S. Wang, $NiSe_2$ as an efficient electrocatalyst for a Pt-free counter electrode of dye-sensitized solar cells, Chemical Communications, 49 (2013) 1437-1439.

[61] A.I. Ekimov, A.L. Efros, A.A. Onushchenko, Quantum size effect in semiconductor microcrystals, Solid State Communications, 56 (1985) 921-924.

[62] M. Chamarro, C. Gourdon, P. Lavallard, A.I. Ekimov, Enhancement of exciton exchange interaction by quantum confinement in CdSe nanocrystals, Japanese Journal of Applied Physics, 34 (1995) 12.

[63] D. Norris, M. Bawendi, Structure in the lowest absorption feature of CdSe quantum dots, The Journal of Chemical Physics, 103 (1995) 5260-5268.

[64] P. Rodrigues, G. Tamulaitis, Y.Y. Peter, S.H. Risbud, Size selective photoluminescence excitation spectroscopy in CdSe nanocrystals, Solid State Communications, 94 (1995) 583-587.

[65] D.J. Norris, Electronic structure in semiconductor nanocrystals, Marcel Dekker: New York, 2004.

[66] C. De Oliveira, A. De Paula, F. Plentz Filho, J.M. Neto, L. Barbosa, O. Alves, E. Menezes, J. Rios, H. Fragnito, C.B. Cruz, Probing of the quantum dot size distribution in CdTe-doped glasses by photoluminescence excitation spectroscopy, Applied Physics Letters, 66 (1995) 439-441.

[67] W. Hoheisel, V. Colvin, C. Johnson, A. Alivisatos, Threshold for quasicontinuum absorption and reduced luminescence efficiency in CdSe nanocrystals, The Journal of Chemical Physics, 101 (1994) 8455-8460.

[68] M. Nirmal, C. Murray, M. Bawendi, Fluorescence-line narrowing in CdSe quantum dots: Surface localization of the photogenerated exciton, Physical Review B, 50 (1994) 2293.

[69] D. Norris, M. Nirmal, C. Murray, A. Sacra, M. Bawendi, Size dependent optical spectroscopy of II–VI semiconductor nanocrystallites (quantum dots), Zeitschrift für Physik D Atoms, Molecules and Clusters, 26 (1993) 355-357.

[70] D. Norris, A. Sacra, C. Murray, M. Bawendi, Measurement of the size dependent hole spectrum in CdSe quantum dots, Physical Review Letters, 72 (1994) 2612.

[71] V. Esch, B. Fluegel, G. Khitrova, H. Gibbs, X. Jiajin, K. Kang, S.W. Koch, L. Liu, S. Risbud, N. Peyghambarian, State filling, Coulomb, and trapping effects in the optical nonlinearity of CdTe quantum dots in glass, Physical Review B, 42 (1990) 7450.

[72] A.O. Nejo, Synthesis of organically capped and water soluble metal sulfide semiconductor nanoparticles, in, University of Zululand, 2013.

[73] A.L. Efros, A.L. Efros, Interband absorption of light in a semiconductor sphere, Soviet Physics Semiconductors-Ussr, 16 (1982) 772-775.

[74] A.L. Efros, M. Rosen, The Electronic structure of semiconductor nanocrystals 1, Annual Review of Materials Science, 30 (2000) 475-521.

[75] A. Ekimov, A. Onushchenko, A. Plyukhin, A.L. Efros, Size quantization of excitons and determination of the parameters of their energy spectrum in CuCl, Sov. Phys. JETP, 61 (1985) 891-897.

[76] A.I. Ekimov, A.A. Onushchenko, Quantum size effect in three-dimensional microscopic semiconductor crystals, ZhETF Pisma Redaktsiiu, 34 (1981) 363.

[77] T. Itoh, Y. Iwabuchi, T. Kirihara, Size-Quantized Excitons in Microcrystals of Cuprous Halides Embedded in Alkali-Halide Matrices, Physica Status Solidi (b), 146 (1988) 531-543.

[78] A. Ekimov, A. Onushchenko, A.L. Éfros, Quantization of the energy spectrum of holes in the adiabatic potential of the electron, ZhETF Pisma Redaktsiiu, 43 (1986) 292.

[79] A. Ekimov, A.L. Efros, M. Ivanov, A. Onushchenko, S. Shumilov, Donor-like exciton in zero-dimension semiconductor structures, Solid State Communications, 69 (1989) 565-568.

[80] G. Mshvelidse, O. Gogolin, E. Tsitsishvili, C. Märkle, J. Chadha, A. Hepting, F. Gindele, W. Petri, W. Send, D. Gerthsen, Optical properties of AgI quantum dots embedded in a glass matrix, Physica Status Solidi B Basic Research, 207 (1998) 369-376.

[81] M. Nirmal, L. Brus, Luminescence photophysics in semiconductor nanocrystals, Accounts of Chemical Research, 32 (1999) 407-414.

[82] E. Groeneveld, Synthesis and optical spectroscopy of (hetero)-nanocrystals: An exciting interplay between Chemistry and Physics, (2012).

[83] R. Koole, E. Groeneveld, D. Vanmaekelbergh, A. Meijerink, C. de Mello Donegá, Size Effects on Semiconductor Nanoparticles, in: Nanoparticles, Springer, 2014, pp. 13-51.

[84] C. de Mello Donegá, Synthesis and properties of colloidal heteronanocrystals, Chemical Society Reviews, 40 (2011) 1512-1546.

[85] V.I. Klimov, Spectral and dynamical properties of multiexcitons in semiconductor nanocrystals, Annu. Rev. Phys. Chem., 58 (2007) 635-673.

[86] A.I. Ekimov, I. Kudryavtsev, A.L. Efros, T. Yazeva, F. Hache, M. Schanne-Klein, A.V. Rodina, D. Ricard, C. Flytzanis, Absorption and intensity-dependent photoluminescence measurements on CdSe quantum dots: assignment of the first electronic transitions, JOSA B, 10 (1993) 100-107.

[87] P. Kambhampati, Hot exciton relaxation dynamics in semiconductor quantum dots: radiationless transitions on the nanoscale, The Journal of Physical Chemistry C, 115 (2011) 22089-22109.

[88] A. Euteneuer, R. Hellmann, E. Göbel, S. Shevel, V. Vozny, M. Vytrykhivsky, W. Petrie, C. Klingshirn, The effect of disorder on the exciton dynamics in cation-substituted $Zn_x Cd_{1-x}$ S mixed crystals, Journal of Crystal Growth, 184 (1998) 1081-1084.

[89] K. Shimakawa, A. Kolobov, S. Elliott, Photoinduced effects and metastability in amorphous semiconductors and insulators, Advances in Physics, 44 (1995) 475-588.

[90] K.D. Kepler, G.C. Lisensky, M. Patel, L.A. Sigworth, A.B. Ellis, Surface-bound carbonyl compounds as lewis acids. Photoluminescence as a probe for the binding of ketones and aldehydes to cadmium sulfide and cadmium selenide surfaces, The Journal of Physical Chemistry, 99 (1995) 16011-16017.

[91] C. de Mello Donega, S.G. Hickey, S.F. Wuister, D. Vanmaekelbergh, A. Meijerink, Single-step synthesis to control the photoluminescence quantum yield and size dispersion of CdSe nanocrystals, The Journal of Physical Chemistry B, 107 (2003) 489-496.

[92] K. Novoselov, A.K. Geim, S. Morozov, D. Jiang, M. Katsnelson, I. Grigorieva, S. Dubonos, A. Firsov, Two-dimensional gas of massless Dirac fermions in graphene, Nature, 438 (2005) 197-200.

[93] Y. Zhang, Y.-W. Tan, H.L. Stormer, P. Kim, Experimental observation of the quantum Hall effect and Berry's phase in graphene, Nature, 438 (2005) 201-204.

[94] A. Splendiani, L. Sun, Y. Zhang, T. Li, J. Kim, C.-Y. Chim, G. Galli, F. Wang, Emerging photoluminescence in monolayer MoS_2, Nano Letters, 10 (2010) 1271-1275.

[95] T. Cao, G. Wang, W. Han, H. Ye, C. Zhu, J. Shi, Q. Niu, P. Tan, E. Wang, B. Liu, Valley-selective circular dichroism of monolayer molybdenum disulphide, Nature Communications, 3 (2012) 887.

[96] K.F. Mak, K. He, J. Shan, T.F. Heinz, Control of valley polarization in monolayer MoS_2 by optical helicity, Nature Nanotechnology, 7 (2012) 494-498.

[97] H. Zeng, J. Dai, W. Yao, D. Xiao, X. Cui, Valley polarization in MoS2 monolayers by optical pumping, Nature Nanotechnology, 7 (2012) 490-493.

[98] Y. Zhang, T. Oka, R. Suzuki, J. Ye, Y. Iwasa, Electrically switchable chiral light-emitting transistor, Science, 344 (2014) 725-728.

[99] A.M. Jones, H. Yu, N.J. Ghimire, S. Wu, G. Aivazian, J.S. Ross, B. Zhao, J. Yan, D.G. Mandrus, D. Xiao, Optical generation of excitonic valley coherence in monolayer WSe_2, Nature Nanotechnology, 8 (2013) 634-638.

[100] K.F. Mak, K.L. McGill, J. Park, P.L. McEuen, The valley Hall effect in MoS_2 transistors, Science, 344 (2014) 1489-1492.

[101] D. Xiao, G.-B. Liu, W. Feng, X. Xu, W. Yao, Coupled spin and valley physics in monolayers of MoS_2 and other group-VI dichalcogenides, Physical Review Letters, 108 (2012) 196802.

[102] K.F. Mak, C. Lee, J. Hone, J. Shan, T.F. Heinz, Atomically thin MoS_2: a new direct-gap semiconductor, Physical Review Letters, 105 (2010) 136805.

[103] S. Tongay, J. Zhou, C. Ataca, K. Lo, T.S. Matthews, J. Li, J.C. Grossman, J. Wu, Thermally driven crossover from indirect toward direct bandgap in 2D semiconductors: $MoSe_2$ versus MoS_2, Nano Letters, 12 (2012) 5576-5580.

[104] W. Zhao, Z. Ghorannevis, L. Chu, M. Toh, C. Kloc, P.-H. Tan, G. Eda, Evolution of electronic structure in atomically thin sheets of WS_2 and WSe_2, ACS Nano, 7 (2012) 791-797.

[105] I.G. Lezama, A. Arora, A. Ubaldini, C. Barreteau, E. Giannini, M. Potemski, A.F. Morpurgo, Indirect-to-direct band gap crossover in few-layer $MoTe_2$, Nano Letters, 15 (2015) 2336-2342.

[106] Y. Zhang, T.-R. Chang, B. Zhou, Y.-T. Cui, H. Yan, Z. Liu, F. Schmitt, J. Lee, R. Moore, Y. Chen, Direct observation of the transition from indirect to direct bandgap in atomically thin epitaxial $MoSe_2$, Nature Nanotechnology, 9 (2014) 111-115.

[107] G.W. Mudd, S.A. Svatek, T. Ren, A. Patanè, O. Makarovsky, L. Eaves, P.H. Beton, Z.D. Kovalyuk, G.V. Lashkarev, Z.R. Kudrynskyi, Tuning the bandgap of exfoliated InSe nanosheets by quantum confinement, Advanced Materials, 25 (2013) 5714-5718.

[108] P. Hu, Z. Wen, L. Wang, P. Tan, K. Xiao, Synthesis of few-layer GaSe nanosheets for high performance photodetectors, ACS Nano, 6 (2012) 5988-5994.

[109] M.A. Airo, S. Gqoba, F. Otieno, M.J. Moloto, N. Moloto, Structural modification and band-gap crossover in indium selenide nanosheets, RSC Advances, 6 (2016) 40777-40784.

[110] E. Matijevic, Production of monodispersed colloidal particles, Annual Review of Materials Science, 15 (1985) 483-516.

[111] T. Sugimoto, Preparation of monodispersed colloidal particles, Advances in Colloid and Interface Science, 28 (1987) 65-108.

[112] T. Sugimoto, The theory of the nucleation of monodisperse particles in open systems and its application to AgBr systems, Journal of Colloid and Interface Science, 150 (1992) 208-225.

[113] E. Matijevic, Preparation and properties of uniform size colloids, Chemistry of Materials, 5 (1993) 412-426.

[114] E. Matijevic, Uniform inorganic colloid dispersions. Achievements and challenges, langmuir, 10 (1994) 8-16.

[115] V. Privman, D.V. Goia, J. Park, E. Matijević, Mechanism of formation of monodispersed colloids by aggregation of nanosize precursors, Journal of Colloid and Interface Science, 213 (1999) 36-45.

[116] Y. Jiang, Forced hydrolysis and chemical co-precipitation, Handbook of Nanophase and Nanostructured Materials, 59 (2003).

[117] B.R. Pamplin, Crystal Growth: International Series on the Science of the Solid State, Elsevier, 2013.

[118] E. Matijevic, Monodispersed metal (hydrous) oxides-A fascinating field of colloid science, Accounts of Chemical Research, 14 (1981) 22-29.

[119] P. Cozzoli, Advanced Wet-Chemical Synthetic Approaches to Inorganic Nanostructures, Transworld Research Network, Kerala, India, (2008).

[120] M. Casavola, R. Buonsanti, G. Caputo, P.D. Cozzoli, Colloidal Strategies for Preparing Oxide-Based Hybrid Nanocrystals, European Journal of Inorganic Chemistry, 2008 (2008) 837-854.

[121] S. Kumar, T. Nann, Shape control of II–VI semiconductor nanomaterials, Small, 2 (2006) 316-329.

[122] C. de Mello Donegá, P. Liljeroth, D. Vanmaekelbergh, Physicochemical Evaluation of the Hot-Injection Method, a Synthesis Route for Monodisperse Nanocrystals, Small, 1 (2005) 1152-1162.

[123] H. Yükselici, P. Persans, T. Hayes, Optical studies of the growth of $Cd_{1-x}Zn_xS$ nanocrystals in borosilicate glass, Physical Review B, 52 (1995) 11763.

[124] D.W. Oxtoby, Nucleation of first-order phase transitions, Accounts of Chemical Research, 31 (1998) 91-97.

[125] R.L. Penn, G. Oskam, T.J. Strathmann, P.C. Searson, A.T. Stone, D.R. Veblen, Epitaxial assembly in aged colloids, The Journal of Physical Chemistry B, 105 (2001) 2177-2182.

[126] C.J. Dalmaschio, C. Ribeiro, E.R. Leite, Impact of the colloidal state on the oriented attachment growth mechanism, Nanoscale, 2 (2010) 2336-2345.

[127] R.L. Penn, J.F. Banfield, Morphology development and crystal growth in nanocrystalline aggregates under hydrothermal conditions: insights from titania, Geochimica et Cosmochimica Acta, 63 (1999) 1549-1557.

[128] M. Ocana, M.P. Morales, C.J. Serna, The growth mechanism of α-Fe 2 O 3 ellipsoidal particles in solution, Journal of Colloid and Interface Science, 171 (1995) 85-91.

[129] R.L. Penn, J.F. Banfield, Imperfect oriented attachment: dislocation generation in defect-free nanocrystals, Science, 281 (1998) 969-971.

[130] R.L. Penn, J.F. Banfield, Oriented attachment and growth, twinning, polytypism, and formation of metastable phases: Insights from nanocrystalline TiO2, American Mineralogist, 83 (1998) 1077-1082.

[131] H. Cölfen, M. Antonietti, Mesocrystals: inorganic superstructures made by highly parallel crystallization and controlled alignment, Angewandte Chemie International Edition, 44 (2005) 5576-5591.

[132] M. Niederberger, H. Cölfen, Oriented attachment and mesocrystals: non-classical crystallization mechanisms based on nanoparticle assembly, Physical Chemistry Chemical Physics, 8 (2006) 3271-3287.

[133] J.F. Banfield, S.A. Welch, H. Zhang, T.T. Ebert, R.L. Penn, Aggregation-based crystal growth and microstructure development in natural iron oxyhydroxide biomineralization products, Science, 289 (2000) 751-754.

[134] A. Alivisatos, Naturally aligned nanocrystals, Science, 289 (2000) 736-737.

[135] Y. Wang, J. He, C. Liu, W.H. Chong, H. Chen, Thermodynamics versus kinetics in nanosynthesis, Angewandte Chemie International Edition, 54 (2015) 2022-2051.

[136] Y. Xia, Y. Xiong, B. Lim, S.E. Skrabalak, Shape-Controlled Synthesis of Metal Nanocrystals: Simple Chemistry Meets Complex Physics?, Angewandte Chemie International Edition, 48 (2009) 60-103.

[137] A.R. Tao, S. Habas, P. Yang, Shape control of colloidal metal nanocrystals, small, 4 (2008) 310-325.

[138] J.W. Mullin, Crystallization, Butterworth-Heinemann, 2001.

[139] S. Polarz, Shape matters: anisotropy of the morphology of inorganic colloidal particles–synthesis and function, Advanced Functional Materials, 21 (2011) 3214-3230.

[140] C. Herring, Some theorems on the free energies of crystal surfaces, Physical Review, 82 (1951) 87.

[141] J.C. Love, L.A. Estroff, J.K. Kriebel, R.G. Nuzzo, G.M. Whitesides, Self-assembled monolayers of thiolates on metals as a form of nanotechnology, Chemical reviews, 105 (2005) 1103-1170.

[142] N. Pradhan, D. Reifsnyder, R. Xie, J. Aldana, X. Peng, Surface ligand dynamics in growth of nanocrystals, Journal of the American Chemical Society, 129 (2007) 9500-9509.

[143] J.B. Schlenoff, M. Li, H. Ly, Stability and self-exchange in alkanethiol monolayers, Journal of the American Chemical Society, 117 (1995) 12528-12536.

[144] X. Peng, Mechanisms for the Shape-Control and Shape-Evolution of Colloidal Semiconductor Nanocrystals, Advanced Materials, 15 (2003) 459-463.

[145] V. Germain, J. Li, D. Ingert, Z. Wang, M. Pileni, Stacking faults in formation of silver nanodisks, The Journal of Physical Chemistry B, 107 (2003) 8717-8720.

[146] Y. Sun, B. Mayers, T. Herricks, Y. Xia, Polyol synthesis of uniform silver nanowires: a plausible growth mechanism and the supporting evidence, Nano Letters, 3 (2003) 955-960.

[147] M.J. Bierman, Y.A. Lau, A.V. Kvit, A.L. Schmitt, S. Jin, Dislocation-driven nanowire growth and Eshelby twist, Science, 320 (2008) 1060-1063.

[148] L. Spanhel, M. Haase, H. Weller, A. Henglein, Photochemistry of colloidal semiconductors. 20. Surface modification and stability of strong luminescing CdS particles, Journal of the American Chemical Society, 109 (1987) 5649-5655.

[149] M.-M. Titirici, M. Antonietti, A. Thomas, A generalized synthesis of metal oxide hollow spheres using a hydrothermal approach, Chemistry of Materials, 18 (2006) 3808-3812.

[150] D.L. Morgan, H.-Y. Zhu, R.L. Frost, E.R. Waclawik, Determination of a morphological phase diagram of titania/titanate nanostructures from alkaline hydrothermal treatment of Degussa P25, Chemistry of Materials, 20 (2008) 3800-3802.

[151] A. Mamakhel, C. Tyrsted, E.D. Bøjesen, P. Hald, B.B. Iversen, Direct formation of crystalline phase pure rutile TiO2 nanostructures by a facile hydrothermal method, Crystal Growth & Design, 13 (2013) 4730-4734.

[152] Y. Li, H. Liao, Y. Ding, Y. Fan, Y. Zhang, Y. Qian, Solvothermal elemental direct reaction to CdE (E= S, Se, Te) semiconductor nanorod, Inorganic Chemistry, 38 (1999) 1382-1387.

[153] J. Xu, J.-P. Ge, Y.-D. Li, Solvothermal synthesis of monodisperse PbSe nanocrystals, The Journal of Physical Chemistry B, 110 (2006) 2497-2501.

[154] H.G. Yang, G. Liu, S.Z. Qiao, C.H. Sun, Y.G. Jin, S.C. Smith, J. Zou, H.M. Cheng, G.Q. Lu, Solvothermal synthesis and photoreactivity of anatase TiO2 nanosheets with dominant {001} facets, Journal of the American Chemical Society, 131 (2009) 4078-4083.

[155] X. Wang, J. Zhuang, Q. Peng, Y. Li, A general strategy for nanocrystal synthesis, Nature, 437 (2005) 121-124.

[156] X. Wang, Q. Peng, Y. Li, Interface-mediated growth of monodispersed nanostructures, Accounts of Chemical Research, 40 (2007) 635-643.

[157] D. Pan, Q. Wang, L. An, Controlled synthesis of monodisperse nanocrystals by a two-phase approach without the separation of nucleation and growth processes, Journal of Materials Chemistry, 19 (2009) 1063-1073.

[158] A. Rabenau, The role of hydrothermal synthesis in preparative chemistry, Angewandte Chemie International Edition in English, 24 (1985) 1026-1040.

[159] R.I. Walton, Subcritical solvothermal synthesis of condensed inorganic materials, Chemical Society Reviews, 31 (2002) 230-238.

[160] G. Demazeau, Solvothermal processes: a route to the stabilization of new materials, Journal of Materials Chemistry, 9 (1999) 15-18.

[161] G. Demazeau, Solvothermal and hydrothermal processes: the main physico-chemical factors involved and new trends, Research on Chemical Intermediates, 37 (2011) 107-123.

[162] B. Gersten, Solvothermal synthesis of nanoparticles, Chemfiles, 5 (2005) 11-12.

[163] X. Tan, J. Zhou, Q. Yang, Ascorbic acid-assisted solvothermal growth of γ-In 2 Se 3 hierarchical flowerlike architectures, CrystEngComm, 13 (2011) 2792-2798.

[164] B. Yuan, W. Luan, S.-t. Tu, One-step solvothermal synthesis of nickel selenide series: Composition and morphology control, CrystEngComm, 14 (2012) 2145-2151.

[165] A. Sobhani, F. Davar, M. Salavati-Niasari, Synthesis and characterization of hexagonal nano-sized nickel selenide by simple hydrothermal method assisted by CTAB, Applied Surface Science, 257 (2011) 7982-7987.

[166] A. Sobhani, M. Salavati-Niasari, Synthesis and characterization of a nickel selenide series via a hydrothermal process, Superlattices and Microstructures, 65 (2014) 79-90.

[167] X. Peng, J. Wickham, A. Alivisatos, Kinetics of II-VI and III-V colloidal semiconductor nanocrystal growth:'Focusing'of size distributions, Journal of the American Chemical Society, 120 (1998).

[168] Y. Cao, U. Banin, Growth and properties of semiconductor core/shell nanocrystals with InAs cores, Journal of the American Chemical Society, 122 (2000) 9692-9702.

[169] D. Battaglia, X. Peng, Formation of high quality InP and InAs nanocrystals in a noncoordinating solvent, Nano Letters, 2 (2002) 1027-1030.

[170] W.W. Yu, X. Peng, Formation of high-quality CdS and other II–VI semiconductor nanocrystals in noncoordinating solvents: tunable reactivity of monomers, Angewandte Chemie International Edition, 41 (2002) 2368-2371.

[171] J.S. Steckel, J.P. Zimmer, S. Coe-Sullivan, N.E. Stott, V. Bulović, M.G. Bawendi, Blue luminescence from (CdS) ZnS core–shell nanocrystals, Angewandte Chemie International Edition, 43 (2004) 2154-2158.

[172] Y.-w. Jun, S.-M. Lee, N.-J. Kang, J. Cheon, Controlled synthesis of multi-armed CdS nanorod architectures using monosurfactant system, Journal of the American Chemical Society, 123 (2001) 5150-5151.

[173] J. Joo, H.B. Na, T. Yu, J.H. Yu, Y.W. Kim, F. Wu, J.Z. Zhang, T. Hyeon, Generalized and facile synthesis of semiconducting metal sulfide nanocrystals, Journal of the American Chemical Society, 125 (2003) 11100-11105.

[174] S.-M. Lee, Y.-w. Jun, S.-N. Cho, J. Cheon, Single-crystalline star-shaped nanocrystals and their evolution: programming the geometry of nano-building blocks, Journal of the American Chemical Society, 124 (2002) 11244-11245.

[175] M.A. Hines, G.D. Scholes, Colloidal PbS nanocrystals with size-tunable near-infrared emission: observation of post-synthesis self-narrowing of the particle size distribution, Advanced Materials, 15 (2003) 1844-1849.

[176] Y.A. Yang, H. Wu, K.R. Williams, Y.C. Cao, Synthesis of CdSe and CdTe nanocrystals without precursor injection, Angewandte Chemie, 117 (2005) 6870-6873.

[177] Y.C. Cao, J. Wang, One-pot synthesis of high-quality zinc-blende CdS nanocrystals, Journal of the American Chemical Society, 126 (2004) 14336-14337.

[178] H. Zhong, S.S. Lo, T. Mirkovic, Y. Li, Y. Ding, Y. Li, G.D. Scholes, Noninjection gram-scale synthesis of monodisperse pyramidal CuInS2 nanocrystals and their size-dependent properties, ACS Nano, 4 (2010) 5253-5262.

[179] M.D. Regulacio, C. Ye, S.H. Lim, M. Bosman, E. Ye, S. Chen, Q.H. Xu, M.Y. Han, Colloidal nanocrystals of Wurtzite-type Cu2ZnSnS4: facile noninjection synthesis and formation mechanism, Chemistry–A European Journal, 18 (2012) 3127-3131.

[180] M.A. Airo, S. Gqoba, M.P. Kalenga, S. Govindraju, M.J. Moloto, N. Moloto, Synthesis and characterization of indium monoselenide nanosheets: a proposed pseudo top-down mechanism, Journal of Crystal Growth, 406 (2014) 1-7.

[181] A.K. Geim, Graphene: status and prospects, Science, 324 (2009) 1530-1534.

[182] K. Novoselov, D. Jiang, F. Schedin, T. Booth, V. Khotkevich, S. Morozov, A. Geim, Two-dimensional atomic crystals, Proceedings of the National Academy of Sciences of the United States of America, 102 (2005) 10451-10453.

[183] A. Ayari, E. Cobas, O. Ogundadegbe, M.S. Fuhrer, Realization and electrical characterization of ultrathin crystals of layered transition-metal dichalcogenides, Journal of Applied Physics, 101 (2007) 14507-14507.

[184] M.N. Tahir, J.K. Sahoo, F. Hoshyargar, W. Tremel, Growth mechanism and surface functionalization of metal chalcogenides nanostructures, Metal Chalcogenide Nanostructures for Renewable Energy Applications, (2014) 83-121.

[185] J.N. Coleman, M. Lotya, A. O'Neill, S.D. Bergin, P.J. King, U. Khan, K. Young, A. Gaucher, S. De, R.J. Smith, Two-dimensional nanosheets produced by liquid exfoliation of layered materials, Science, 331 (2011) 568-571.

[186] P.K. Sekhar, E.L. Brosha, R. Mukundan, F.H. Garzon, Chemical sensors for environmental monitoring and homeland security, The Electrochemical Society Interface, 19 (2010) 35.

[187] V. Vaishnav, S. Patel, J. Panchal, Development of indium tin oxide thin film toluene sensor, Sensors and Actuators B: Chemical, 210 (2015) 165-172.

[188] G. Korotcenkov, Chemical Sensors: Comprehensive Sensor Technologies Volume 6: Chemical Sensors Applications, Momentum Press, 2011.

[189] J.N. Panchal, Ph.D thesis, in: Electronics, 2014.

[190] M. Cristina, A. Giberti, V. Guidi, C. Malagù, B. Vendemiati, G. Martinelli, Gas sensors based on semiconductor oxides: basic aspects onto materials and working principles, in: MRS Proceedings, Cambridge Univ Press, 2004, pp. A4. 6.

[191] B. Adhikari, S. Majumdar, Polymers in sensor applications, Progress in polymer science, 29 (2004) 699-766.

[192] S. Wang, Y. Kang, L. Wang, H. Zhang, Y. Wang, Y. Wang, Organic/inorganic hybrid sensors: A review, Sensors and Actuators B: Chemical, 182 (2013) 467-481.

[193] J. Stephens, A. Batra, J.R. Currie, Characteristics of Nanoparticles-Based Chemical Sensors, (2012).

[194] H.R. Kim, A. Haensch, I.D. Kim, N. Barsan, U. Weimar, J.H. Lee, The Role of NiO Doping in Reducing the Impact of Humidity on the Performance of SnO2-Based Gas Sensors: Synthesis Strategies, and Phenomenological and Spectroscopic Studies, Advanced Functional Materials, 21 (2011) 4456-4463.

[195] N. Yamazoe, Toward innovations of gas sensor technology, Sensors and Actuators B: Chemical, 108 (2005) 2-14.

[196] S.W. Lee, P.P. Tsai, H. Chen, Comparison study of SnO 2 thin-and thick-film gas sensors, Sensors and Actuators B: Chemical, 67 (2000) 122-127.

[197] T. Becker, S. Ahlers, C.B.-v. Braunmühl, G. Müller, O. Kiesewetter, Gas sensing properties of thin-and thick-film tin-oxide materials, Sensors and Actuators B: Chemical, 77 (2001) 55-61.

[198] W.J.W. HANAPI, ROOM TEMPERATURE OF LIQUIFIED PETROLEUM GAS (LPG) SENSOR, in, Universiti Malaysia Pahang, 2008.

[199] R. Leghrib, R. Pavelko, A. Felten, A. Vasiliev, C. Cané, I. Gràcia, J.-J. Pireaux, E. Llobet, Gas sensors based on multiwall carbon nanotubes decorated with tin oxide nanoclusters, Sensors and Actuators B: Chemical, 145 (2010) 411-416.

[200] J. Gong, J. Sun, Q. Chen, Micromachined sol–gel carbon nanotube/SnO 2 nanocomposite hydrogen sensor, Sensors and Actuators B: Chemical, 130 (2008) 829-835.

[201] U. Resch-Genger, M. Grabolle, S. Cavaliere-Jaricot, R. Nitschke, T. Nann, Quantum dots versus organic dyes as fluorescent labels, Nature methods, 5 (2008) 763-775.

[202] A.Y. Nazzal, L. Qu, X. Peng, M. Xiao, Photoactivated CdSe nanocrystals as nanosensors for gases, Nano letters, 3 (2003) 819-822.

[203] A.Y. Nazzal, X. Wang, L. Qu, W. Yu, Y. Wang, X. Peng, M. Xiao, Environmental effects on photoluminescence of highly luminescent CdSe and CdSe/ZnS core/shell nanocrystals in polymer thin films, The Journal of Physical Chemistry B, 108 (2004) 5507-5515.

[204] R.A. Potyrailo, A.M. Leach, Selective gas nanosensors with multisize CdSe nanocrystal/polymer composite films and dynamic pattern recognition, Applied physics letters, 88 (2006) 4110.

[205] O.V. Vassiltsova, Z. Zhao, M.A. Petrukhina, M.A. Carpenter, Surface-functionalized CdSe quantum dots for the detection of hydrocarbons, Sensors and Actuators B: Chemical, 123 (2007) 522-529.

[206] Z. Zhao, M. Arrandale, O.V. Vassiltsova, M.A. Petrukhina, M.A. Carpenter, Sensing mechanism investigation on semiconductor quantum dot/polymer thin film based hydrocarbon sensor, Sensors and Actuators B: Chemical, 141 (2009) 26-33.

[207] M. Hasani, A.M.C. García, J.M. Costa-Fernández, A. Sanz-Medel, Sol–gels doped with polymer-coated ZnS/CdSe quantum dots for the detection of organic vapors, Sensors and Actuators B: Chemical, 144 (2010) 198-202.

[208] T. Li, Y. Zhou, J. Sun, K. Wu, Ultrasensitive detection of glyphosate using CdTe quantum dots in sol-gel-derived silica spheres coated with calix [6] arene as fluorescent probes, American Journal of Analytical Chemistry, 3 (2012) 12.

[209] Z. Zhao, T.M. Dansereau, M.A. Petrukhina, M.A. Carpenter, Nanopore-array-dispersed semiconductor quantum dots as nanosensors for gas detection, Applied Physics Letters, 97 (2010) 113105.

[210] F. Seker, K. Meeker, T.F. Kuech, A.B. Ellis, Surface chemistry of prototypical bulk II-VI and III-V semiconductors and implications for chemical sensing, Chemical Reviews, 100 (2000) 2505-2536.

[211] R. De Angelis, M. Casalboni, F. Hatami, A. Ugur, W. Masselink, P. Prosposito, Vapour sensing properties of InP quantum dot luminescence, Sensors and Actuators B: Chemical, 162 (2012) 149-152.

[212] R. De Angelis, L. D'Amico, M. Casalboni, F. Hatami, W. Masselink, P. Prosposito, Surface InP Quantum Dots: Effect of Morphology on the Photoluminescence Sensitivity, Procedia Engineering, 47 (2012) 1251-1254.

[213] K. Hestroffer, R. Braun, A. Ugur, J.W. Tomm, S. Hackbarth, B. Röder, F. Hatami, Surface InP/In0. 48Ga0. 52P quantum dots: Carrier recombination dynamics and their interaction with fluorescent dyes, Journal of Applied Physics, 114 (2013) 163510.

[214] A. Gaiardo, B. Fabbri, V. Guidi, P. Bellutti, A. Giberti, S. Gherardi, L. Vanzetti, C. Malagù, G. Zonta, Metal Sulfides as Sensing Materials for Chemoresistive Gas Sensors, Sensors, 16 (2016) 296.

[215] A. Giberti, D. Casotti, G. Cruciani, B. Fabbri, A. Gaiardo, V. Guidi, C. Malagù, G. Zonta, S. Gherardi, Electrical conductivity of CdS films for gas sensing: Selectivity properties to alcoholic chains, Sensors and Actuators B: Chemical, 207 (2015) 504-510.

[216] A. Giberti, A. Gaiardo, B. Fabbri, S. Gherardi, V. Guidi, C. Malagù, P. Bellutti, G. Zonta, D. Casotti, G. Cruciani, Tin (IV) sulfide nanorods as a new gas sensing material, Sensors and Actuators B: Chemical, 223 (2016) 827-833.

[217] A. Gaiardo, P. Bellutti, S. Gherardi, G. Zonta, B. Fabbri, A. Giberti, V. Guidi, C. Malagù, Tin (IV) Sulfide chemoresistivity: A possible new gas sensing material, in: AISEM Annual Conference, 2015 XVIII, IEEE, 2015, pp. 1-4.

[218] V. Guidi, B. Fabbri, A. Gaiardo, S. Gherardi, A. Giberti, C. Malagù, G. Zonta, P. Bellutti, Metal Sulfides as a New Class of Sensing Materials, Procedia Engineering, 120 (2015) 138-141.

[219] X. Fu, J. Liu, Y. Wan, X. Zhang, F. Meng, J. Liu, Preparation of a leaf-like CdS micro-/nanostructure and its enhanced gas-sensing properties for detecting volatile organic compounds, Journal of Materials Chemistry, 22 (2012) 17782-17791.

[220] M.A. Airo, R. Rodrigues, S. Gqoba, N. Ntholeng, F. Otieno, M.J. Moloto, M.W. Greenshields, I.A. Hümmelgen, N. Moloto, Colloidal InSe Nanostructures: Effect of Morphology on their Chemical Sensitivity to Methanol and Formaldehyde Fumes, Sensors and Actuators B: Chemical, (2016).

[221] N. Yamazoe, N. Miura, New approaches in the design of gas sensors, in: Gas sensors, Springer, 1992, pp. 1-42.

[222] I. Simon, N. Bârsan, M. Bauer, U. Weimar, Micromachined metal oxide gas sensors: opportunities to improve sensor performance, Sensors and Actuators B: Chemical, 73 (2001) 1-26.

[223] M.F. Frasco, N. Chaniotakis, Semiconductor quantum dots in chemical sensors and biosensors, Sensors, 9 (2009) 7266-7286.

[224] C.J. Murphy, Peer reviewed: optical sensing with quantum dots, Analytical Chemistry, 74 (2002) 520 A-526 A.

[225] S.R. Morrison, Semiconductor gas sensors, Sensors and Actuators, 2 (1982) 329-341.

[226] M. Alim, B. Penn, J. Currie Jr, A. Batra, M. Aggarwal, Micro-and Nanostructured Metal Oxide Chemical Sensors for Volatile Organic Compounds, (2008).

[227] H. Windischmann, P. Mark, A Model for the Operation of a Thin-Film SnO_x Conductance-Modulation Carbon Monoxide Sensor, Journal of the electrochemical society, 126 (1979) 627-633.

[228] C. Xu, J. Tamaki, N. Miura, N. Yamazoe, Grain size effects on gas sensitivity of porous SnO_2-based elements, Sensors and Actuators B: Chemical, 3 (1991) 147-155.

[229] S. Nicoletti, L. Dori, F. Corticelli, M. Leoni, P. Scardi, Tin Oxide Thin-Film Sensors for Aromatic Hydrocarbons Detection: Effect of Aging Time on Film Microstructure, Journal of the American Ceramic Society, 82 (1999) 1201-1206.

[230] D.E. Williams, P.T. Moseley, Dopant effects on the response of gas-sensitive resistors utilising semiconducting oxides, Journal of Materials Chemistry, 1 (1991) 809-814.

[231] A. Yella, H. Lee, H. Tsao, C. Yi, A. Chandiran, Porphyrin-sensitized solar cells with cobalt (II/III)-based redox electrolyte exceed 12 percent efficiency (vol 334, pg 629, 2011), Science, 334 (2011) 1203-1203.

[232] S. Mathew, A. Yella, P. Gao, R. Humphry-Baker, B.F. Curchod, N. Ashari-Astani, I. Tavernelli, U. Rothlisberger, M.K. Nazeeruddin, M. Grätzel, Dye-sensitized solar cells with 13% efficiency achieved through the molecular engineering of porphyrin sensitizers, Nature Chemistry, 6 (2014) 242-247.

[233] B. O'regan, M. Grfitzeli, A low-cost, high-efficiency solar cell based on dye-sensitized, Nature, 353 (1991) 737-740.

[234] M. Grätzel, Photoelectrochemical cells, Nature, 414 (2001) 338-344.

[235] A. Hagfeldt, M. Graetzel, Light-induced redox reactions in nanocrystalline systems, Chemical Reviews, 95 (1995) 49-68.

[236] A. Hagfeldt, M. Grätzel, Molecular photovoltaics, Accounts of Chemical Research, 33 (2000) 269-277.

[237] M. Grätzel, Solar energy conversion by dye-sensitized photovoltaic cells, Inorganic Chemistry, 44 (2005) 6841-6851.

[238] M. Grätzel, Recent advances in sensitized mesoscopic solar cells, Accounts of Chemical Research, 42 (2009) 1788-1798.

[239] A. Hagfeldt, G. Boschloo, L. Sun, L. Kloo, H. Pettersson, Dye-sensitized solar cells, Chemical Reviews, 110 (2010) 6595-6663.

[240] L.M. Gonçalves, V. de Zea Bermudez, H.A. Ribeiro, A.M. Mendes, Dye-sensitized solar cells: A safe bet for the future, Energy & Environmental Science, 1 (2008) 655-667.

[241] J. Wu, Z. Lan, J. Lin, M. Huang, Y. Huang, L. Fan, G. Luo, Electrolytes in dye-sensitized solar cells, Chemical Reviews, 115 (2015) 2136-2173.

[242] M.A. Green, K. Emery, Y. Hishikawa, W. Warta, E.D. Dunlop, Solar cell efficiency tables (Version 45), Progress in photovoltaics: Research and Applications, 23 (2015) 1-9.

[243] A. Kay, M. Grätzel, Low cost photovoltaic modules based on dye sensitized nanocrystalline titanium dioxide and carbon powder, Solar Energy Materials and Solar Cells, 44 (1996) 99-117.

[244] F. Gao, Y. Wang, D. Shi, J. Zhang, M. Wang, X. Jing, R. Humphry-Baker, P. Wang, S.M. Zakeeruddin, M. Grätzel, Enhance the optical absorptivity of nanocrystalline TiO2 film with high molar extinction coefficient ruthenium sensitizers for high performance dye-sensitized solar cells, Journal of the American Chemical Society, 130 (2008) 10720-10728.

[245] A. Yella, C.L. Mai, S.M. Zakeeruddin, S.N. Chang, C.H. Hsieh, C.Y. Yeh, M. Grätzel, Molecular engineering of push–pull porphyrin dyes for highly efficient dye-sensitized solar cells: The role of benzene spacers, Angewandte Chemie, 126 (2014) 3017-3021.

[246] A. Shah, P. Torres, R. Tscharner, N. Wyrsch, H. Keppner, Photovoltaic technology: the case for thin-film solar cells, Science, 285 (1999) 692-698.

[247] P.V. Kamat, K. Tvrdy, D.R. Baker, J.G. Radich, Beyond photovoltaics: semiconductor nanoarchitectures for liquid-junction solar cells, Chemical Reviews, 110 (2010) 6664-6688.

[248] Y. Luo, D. Li, Q. Meng, Towards Optimization of Materials for Dye-Sensitized Solar Cells, Advanced Materials, 21 (2009) 4647-4651.

[249] K.-T. Kuo, D.-M. Liu, S.-Y. Chen, C.-C. Lin, Core-shell CuInS 2/ZnS quantum dots assembled on short ZnO nanowires with enhanced photo-conversion efficiency, Journal of Materials Chemistry, 19 (2009) 6780-6788.

[250] L.E. Greene, M. Law, D.H. Tan, M. Montano, J. Goldberger, G. Somorjai, P. Yang, General route to vertical ZnO nanowire arrays using textured ZnO seeds, Nano Letters, 5 (2005) 1231-1236.

[251] S. Thomas, T. Deepak, G. Anjusree, T. Arun, S.V. Nair, A.S. Nair, A review on counter electrode materials in dye-sensitized solar cells, Journal of Materials Chemistry A, 2 (2014) 4474-4490.

[252] T.N. Murakami, S. Ito, Q. Wang, M.K. Nazeeruddin, T. Bessho, I. Cesar, P. Liska, R. Humphry-Baker, P. Comte, P. Péchy, Highly efficient dye-sensitized solar cells based on carbon black counter electrodes, Journal of the Electrochemical Society, 153 (2006) A2255-A2261.

[253] M. Wu, X. Lin, T. Wang, J. Qiu, T. Ma, Low-cost dye-sensitized solar cell based on nine kinds of carbon counter electrodes, Energy & Environmental Science, 4 (2011) 2308-2315.

[254] Z. Huang, X. Liu, K. Li, D. Li, Y. Luo, H. Li, W. Song, L. Chen, Q. Meng, Application of carbon materials as counter electrodes of dye-sensitized solar cells, Electrochemistry Communications, 9 (2007) 596-598.

[255] K. Li, Y. Luo, Z. Yu, M. Deng, D. Li, Q. Meng, Low temperature fabrication of efficient porous carbon counter electrode for dye-sensitized solar cells, Electrochemistry Communications, 11 (2009) 1346-1349.

[256] J. Chen, K. Li, Y. Luo, X. Guo, D. Li, M. Deng, S. Huang, Q. Meng, A flexible carbon counter electrode for dye-sensitized solar cells, Carbon, 47 (2009) 2704-2708.

[257] W.J. Lee, E. Ramasamy, D.Y. Lee, J.S. Song, Efficient dye-sensitized solar cells with catalytic multiwall carbon nanotube counter electrodes, ACS Applied Materials & Interfaces, 1 (2009) 1145-1149.

[258] Y. Saito, W. Kubo, T. Kitamura, Y. Wada, S. Yanagida, I−/I 3− redox reaction behavior on poly (3, 4-ethylenedioxythiophene) counter electrode in dye-sensitized solar cells, Journal of Photochemistry and Photobiology A: Chemistry, 164 (2004) 153-157.

[259] J. Xia, N. Masaki, K. Jiang, S. Yanagida, The influence of doping ions on poly (3, 4-ethylenedioxythiophene) as a counter electrode of a dye-sensitized solar cell, Journal of Materials Chemistry, 17 (2007) 2845-2850.

[260] Q. Li, J. Wu, Q. Tang, Z. Lan, P. Li, J. Lin, L. Fan, Application of microporous polyaniline counter electrode for dye-sensitized solar cells, Electrochemistry Communications, 10 (2008) 1299-1302.

[261] H. Sun, Y. Luo, Y. Zhang, D. Li, Z. Yu, K. Li, Q. Meng, In situ preparation of a flexible polyaniline/carbon composite counter electrode and its application in dye-sensitized solar cells, The Journal of Physical Chemistry C, 114 (2010) 11673-11679.

[262] W. Zhou, D. Hou, Y. Sang, S. Yao, J. Zhou, G. Li, L. Li, H. Liuc, S. Chen, Materials Chemistry A, (2014).

[263] S. Yun, H. Zhou, L. Wang, H. Zhang, T. Ma, Economical hafnium oxygen nitride binary/ternary nanocomposite counter electrode catalysts for high-efficiency dye-sensitized solar cells, Journal of Materials Chemistry A, 1 (2013) 1341-1348.

[264] S. Yun, L. Wang, W. Guo, T. Ma, Non-Pt counter electrode catalysts using tantalum oxide for low-cost dye-sensitized solar cells, Electrochemistry Communications, 24 (2012) 69-73.

[265] X. Lin, M. Wu, Y. Wang, A. Hagfeldt, T. Ma, Novel counter electrode catalysts of niobium oxides supersede Pt for dye-sensitized solar cells, Chemical Communications, 47 (2011) 11489-11491.

[266] M. Wu, X. Lin, L. Wang, W. Guo, Y. Wang, J. Xiao, A. Hagfeldt, T. Ma, In situ synthesized economical tungsten dioxide imbedded in mesoporous carbon for dye-sensitized solar cells as counter electrode catalyst, The Journal of Physical Chemistry C, 115 (2011) 22598-22602.

[267] M. Wu, Q. Zhang, J. Xiao, C. Ma, X. Lin, C. Miao, Y. He, Y. Gao, A. Hagfeldt, T. Ma, Two flexible counter electrodes based on molybdenum and tungsten nitrides for dye-sensitized solar cells, Journal of Materials Chemistry, 21 (2011) 10761-10766.

[268] Y. Wang, M. Wu, X. Lin, Z. Shi, A. Hagfeldt, T. Ma, Several highly efficient catalysts for Pt-free and FTO-free counter electrodes of dye-sensitized solar cells, Journal of Materials Chemistry, 22 (2012) 4009-4014.

[269] S. Yun, M. Wu, Y. Wang, J. Shi, X. Lin, A. Hagfeldt, T. Ma, Pt-like Behavior of High-Performance Counter Electrodes Prepared from Binary Tantalum Compounds Showing High Electrocatalytic Activity for Dye-Sensitized Solar Cells, ChemSusChem, 6 (2013) 411-416.

[270] M. Wu, T. Ma, Platinum-Free Catalysts as Counter Electrodes in Dye-Sensitized Solar Cells, ChemSusChem, 5 (2012) 1343-1357.

[271] M. Wu, X. Lin, A. Hagfeldt, T. Ma, Low-Cost Molybdenum Carbide and Tungsten Carbide Counter Electrodes for Dye-Sensitized Solar Cells, Angewandte Chemie International Edition, 50 (2011) 3520-3524.

[272] M. Wu, X. Lin, Y. Wang, L. Wang, W. Guo, D. Qi, X. Peng, A. Hagfeldt, M. Grätzel, T. Ma, Economical Pt-free catalysts for counter electrodes of dye-sensitized solar cells, Journal of the American Chemical Society, 134 (2012) 3419-3428.

[273] S. Yun, L. Wang, C. Zhao, Y. Wang, T. Ma, A new type of low-cost counter electrode catalyst based on platinum nanoparticles loaded onto silicon carbide (Pt/SiC) for dye-sensitized solar cells, Physical Chemistry Chemical Physics, 15 (2013) 4286-4290.

[274] M. Wu, Y. Wang, X. Lin, N. Yu, L. Wang, L. Wang, A. Hagfeldt, T. Ma, Economical and effective sulfide catalysts for dye-sensitized solar cells as counter electrodes, Physical Chemistry Chemical Physics, 13 (2011) 19298-19301.

[275] M. Wu, J. Bai, Y. Wang, A. Wang, X. Lin, L. Wang, Y. Shen, Z. Wang, A. Hagfeldt, T. Ma, High-performance phosphide/carbon counter electrode for both iodide and organic redox couples in dye-sensitized solar cells, Journal of Materials Chemistry, 22 (2012) 11121-11127.

[276] J. Guo, Y. Shi, Y. Chu, T. Ma, Highly efficient telluride electrocatalysts for use as Pt-free counter electrodes in dye-sensitized solar cells, Chemical Communications, 49 (2013) 10157-10159.

[277] M. Wang, A.M. Anghel, B.t. Marsan, N.-L. Cevey Ha, N. Pootrakulchote, S.M. Zakeeruddin, M. Grätzel, CoS supersedes Pt as efficient electrocatalyst for triiodide reduction in dye-sensitized solar cells, Journal of the American Chemical Society, 131 (2009) 15976-15977.

[278] H. Sun, D. Qin, S. Huang, X. Guo, D. Li, Y. Luo, Q. Meng, Dye-sensitized solar cells with NiS counter electrodes electrodeposited by a potential reversal technique, Energy & Environmental Science, 4 (2011) 2630-2637.

[279] L.-f. Zhang, C.-y. Zhang, Multifunctional Co 0.85 Se/graphene hybrid nanosheets: controlled synthesis and enhanced performances for the oxygen reduction reaction and decomposition of hydrazine hydrate, Nanoscale, 6 (2014) 1782-1789.

[280] M.R. Gao, Q. Gao, J. Jiang, C.H. Cui, W.T. Yao, S.H. Yu, A Methanol-Tolerant Pt/CoSe2 Nanobelt Cathode Catalyst for Direct Methanol Fuel Cells, Angewandte Chemie, 123 (2011) 5007-5010.

[281] Y. Feng, T. He, N. Alonso-Vante, Carbon-Supported CoSe2 Nanoparticles for Oxygen Reduction Reaction in Acid Medium, Fuel Cells, 10 (2010) 77-83.

[282] M.-R. Gao, S. Liu, J. Jiang, C.-H. Cui, W.-T. Yao, S.-H. Yu, In situ controllable synthesis of magnetite nanocrystals/CoSe2 hybrid nanobelts and their enhanced catalytic performance, Journal of Materials Chemistry, 20 (2010) 9355-9361.

[283] Y. Feng, N. Alonso-Vante, Carbon-supported cubic CoSe 2 catalysts for oxygen reduction reaction in alkaline medium, Electrochimica Acta, 72 (2012) 129-133.

[284] J. Guo, Y. Shi, C. Zhu, L. Wang, N. Wang, T. Ma, Cost-effective and morphology-controllable niobium diselenides for highly efficient counter electrodes of dye-sensitized solar cells, Journal of Materials Chemistry A, 1 (2013) 11874-11879.

[285] Z. Zhang, S. Pang, H. Xu, Z. Yang, X. Zhang, Z. Liu, X. Wang, X. Zhou, S. Dong, X. Chen, Electrodeposition of nanostructured cobalt selenide films towards high performance counter electrodes in dye-sensitized solar cells, RSC Advances, 3 (2013) 16528-16533.

[286] Y. Duan, Q. Tang, B. He, R. Li, L. Yu, Transparent nickel selenide alloy counter electrodes for bifacial dye-sensitized solar cells exceeding 10% efficiency, Nanoscale, 6 (2014) 12601-12608.

[287] J. Wu, Z. Lan, S. Hao, P. Li, J. Lin, M. Huang, L. Fang, Y. Huang, Progress on the electrolytes for dye-sensitized solar cells, Pure and Applied Chemistry, 80 (2008) 2241-2258.

[288] Y.-N. Huang, Semi-transparent ZnO: Al/Cu2O Thin-film Heterojunction Fabricated At Low Temperature: Effect Of An Intrinsic ZnO Buffer Layer At The Junction, (2012).

[289] F.O. Otieno, Enhancement of photo-conversion efficiency of organic solar cells by plasmon resonance effect, in, 2016.

[290] R. Mauer, I.A. Howard, F. Laquai, Effect of nongeminate recombination on fill factor in polythiophene/methanofullerene organic solar cells, The Journal of Physical Chemistry Letters, 1 (2010) 3500-3505.

[291] W. Tress, A. Petrich, M. Hummert, M. Hein, K. Leo, M. Riede, Imbalanced mobilities causing S-shaped IV curves in planar heterojunction organic solar cells, Applied Physics Letters, 98 (2011) 063301.

[292] B. Qi, J. Wang, Fill factor in organic solar cells, Physical Chemistry Chemical Physics, 15 (2013) 8972-8982.

[293] X. Yin, Z. Xue, B. Liu, Electrophoretic deposition of Pt nanoparticles on plastic substrates as counter electrode for flexible dye-sensitized solar cells, Journal of Power Sources, 196 (2011) 2422-2426.

[294] C.-M. Chen, C.-H. Chen, T.-C. Wei, Chemical deposition of platinum on metallic sheets as counterelectrodes for dye-sensitized solar cells, Electrochimica Acta, 55 (2010) 1687-1695.

[295] S. Park, H. Boo, T.D. Chung, Electrochemical non-enzymatic glucose sensors, Analytica Chimica Acta, 556 (2006) 46-57.

[296] T.N. Murakami, M. Grätzel, Counter electrodes for DSC: application of functional materials as catalysts, Inorganica Chimica Acta, 361 (2008) 572-580.

[297] B. Zhang, D. Wang, Y. Hou, S. Yang, X.H. Yang, J.H. Zhong, J. Liu, H.F. Wang, P. Hu, H.J. Zhao, Facet-dependent catalytic activity of platinum nanocrystals for triiodide reduction in dye-sensitized solar cells, Scientific reports, 3 (2013) 1836.

[298] K. Kalyanasundaram, Dye-sensitized solar cells, EPFL press, 2010.

Chapter 3 : Synthesis and characterization of indium selenide nanocrystals

3.1 Background

Among the non-transition metal chalcogenides, indium selenide is a group III-VI compound semiconductor which has triggered attention in research due to its potential applications in a number of fields such as photovoltaics [1-4], electro and photo-memory devices [5], as a precursor in the synthesis of CuInSe/S [6] and photodetectors [7] and thermoelectric materials [8, 9]. These applications are dependent on the physical, optical and electrical properties of indium selenides and are mainly determined by their intrinsic structural characteristics such as their compositions, phases, crystal structures, and structural imperfections [8]. The binary phase diagram [8] of indium selenide is shown in Fig. 3-1 and like many group III-VI compounds, it is complicated. Structurally, it illustrates that indium selenide exist in a complex regime with stoichiometric phases including In_4Se_3, In_2Se_3, InSe, and In_6Se_7. The arrangements of cation vacancies differ in each stoichiometry thus bringing about the difference in the phases and somewhat the difference in properties. As a result the complexity of the In_xSe_y species coins from the many energetically similar ways that trivalent and divalent atoms can combine to satisfy their bonding requirements [10]. For example, in layered In_2Se_3 and InSe, the cation vacancies form a plane resulting in a weak Se–Se bonding [11] with atomic layers consisting of Se–In–Se–In–Se [12] and Se–In–In–Se [13] respectively thus resulting in electronic properties that are anisotropic with high resistivity. In addition, several crystalline allotrope phases and crystal structures may coexist in the same stoichiometric ratio such that In_2Se_3 forms rhombohedral/hexagonal α/β phases and hexagonal γ and δ phases while and InSe may exist as hexagonal β–InSe and rhombohedral γ–InSe). In_4Se_3 on the other hand is a highly conducting smaller-bandgap orthorhombic

semiconductor [14]. The higher conductivity of In_4Se_3 is attributed to the presence of In–In bonds, while in the other In–Se compounds indium bonds only to selenium [15].

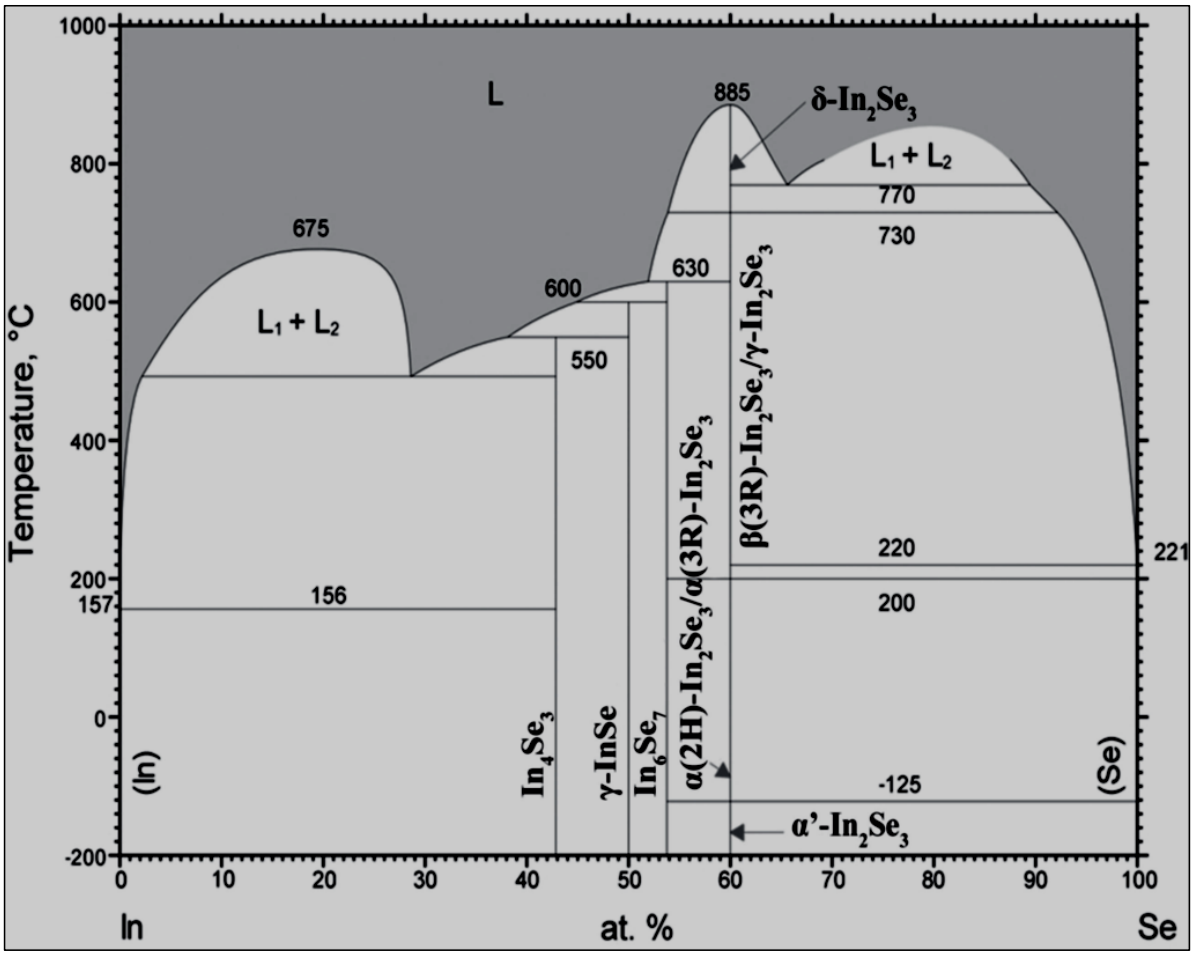

Figure 3-1: Binary phase diagram of indium selenide as adopted from Han et al. [8].

3.2 Properties of different polymorphs of indium selenide

The valence electron mismatch in the indium selenide system generally complicates its synthesis and leads to the formation of different phases and crystal structures, as well as numerous stoichiometries of the material as discussed below.

3.2.1 Indium (III) selenide, In_2Se_3

This is the most complex stoichiometry of the indium selenide series yet the most studied due to it multiple phases and excellent optical properties. In_2Se_3 has a tetrahedral bonding structure and is a direct band gap semiconductor material [16]. It exhibits five known crystalline forms denoted as α, β, γ, δ and κ existing at different temperatures [17-19]. The transition temperature occur at that 200 °C and 650 °C, respectively, for α–β and β–γ phase transitions [20]. The two common forms in nature of In_2Se_3 are α–phase and β–phase which share a layered crystallographic structure differing in lattice parameters and properties of materials. Another stable crystal structure known to exist is a defect wurtzite structure (γ–phase) that is vacancy ordered in screw form (VOSF) [21]. The layered structure is considered to be a spontaneous superlattice along the *c*-axis (perpendicular to the layers) consisting of rather loose stacks of covalently bonded layers, including five atomic layers of Se–In–Se–In–Se [12, 22] as shown in Fig. 3-2. In contrast, the structure of γ–In_2Se_3 is basically a wurtzite structure, but vacancies assume a screw arrangement in the [001] direction; therefore, this structure shows large optical rotatory power [23, 24]. In spite of the intrinsic chemical complexity, In_2Se_3 has attracted substantial attention due to its polymorphism and related metal ion defects thus posing the potential application in photovoltaics [12, 13, 25, 26], solid state batteries [27], phase change memories [28-30] and in the manufacture of detectors of ionizing radiation [31].

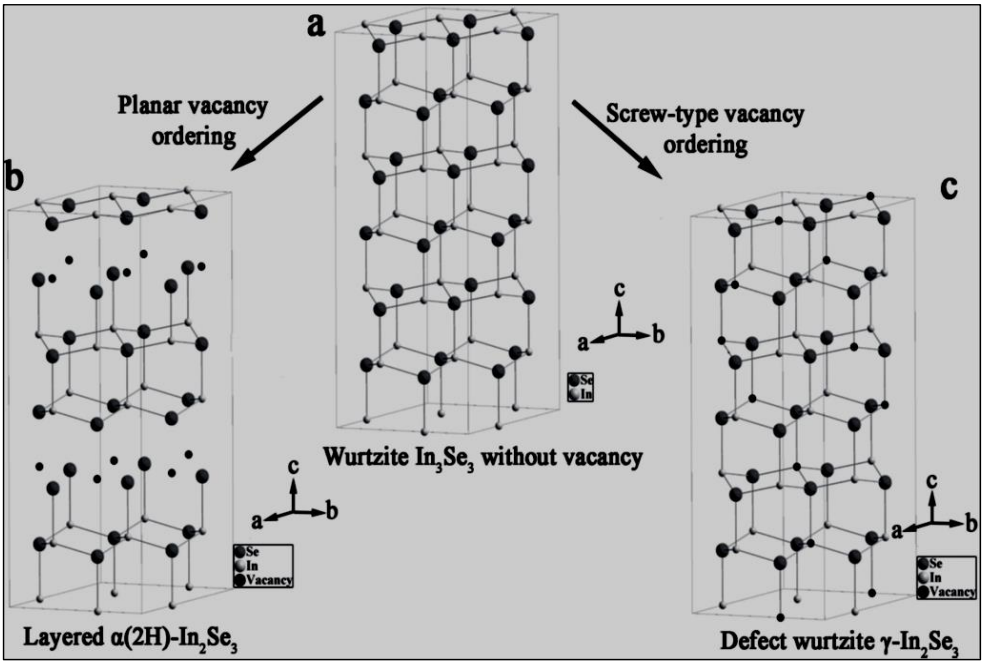

Figure 3-2: Crystal structures of In_2Se_3 stochiometry as adopted from ref [8].

3.2.2 Tetraindium triselenide, In_4Se_3

Tetraindium triselenide forms a layered n-type semiconductor with a bandgap that ranges between 0.5 – 1.0 eV [32]. It is known to crystallize in the orthorhombic structure, space group Pnnm, with unit-cell dimensions a = 15.297 Å, b = 12.308 Å and c = 4.081 Å [33]. The layered structure comprises of a five membered ring consisting of $(In_3)^{+5}$ clusters covalently bonded to Se ions in the b - c planes while the layers are held together by van der Waals interactions along the a axis as shown in Fig. 3-3. In_4Se_3 is highly conductive compared to the other members of the $A_{III}B_{VI}$ family due to strong In-In units cross linked in the structure during the formation of a continuous sheet [14, 34]. Therefore, it has exhibited potential application in thermoelectric materials [9].

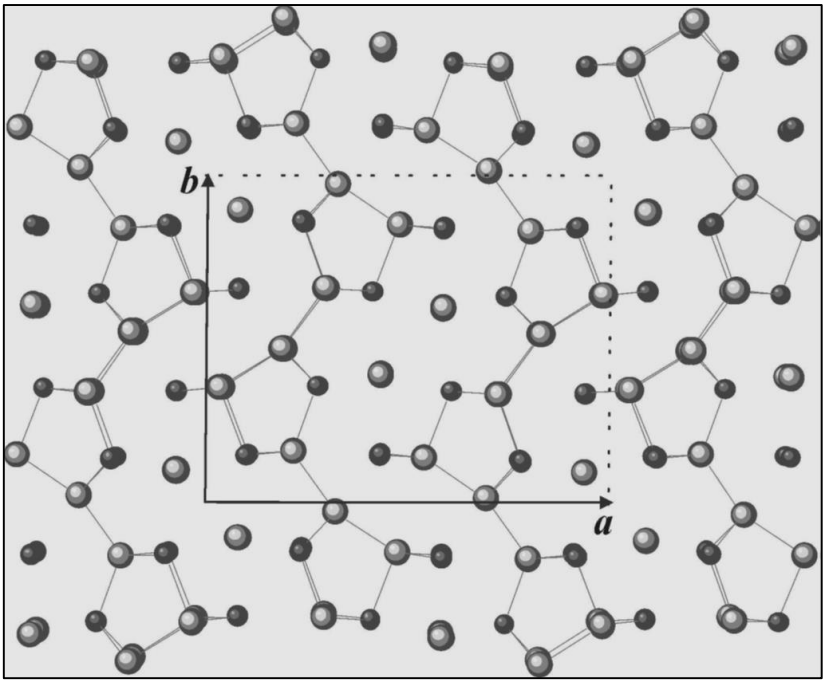

Figure 3-3: Crystal structure model of In_4Se_3 [8].

3.2.3 Indium monoselenide, InSe

InSe crystallizes in either hexagonal (β–InSe) or rhombohedral (γ–InSe) layered crystal structures [35, 36]. The basic unit consist of a diatomic cation $[In_2]^{4+}$ sandwiched between two planes of two Se^{2-} anions. The atoms are bound by a mixture of covalent and ionic bonds within a layer leading to a 4 atomic Se–In–In–Se; while the interlayer bonding is due to the weak van der Waal forces [37, 38] as presented by the crystal structure in Fig. 3-4. Many researchers have focussed on InSe studies since it has a direct band gap in bulk and its electronic properties are excellent and anisotropic. Compared to In_2Se_3, it exhibits only a few crystalline phases thus a possibility of getting a single phase. Its exfoliated layers have shown potential applications in photovoltaics [1] and photodetectors [7, 39].

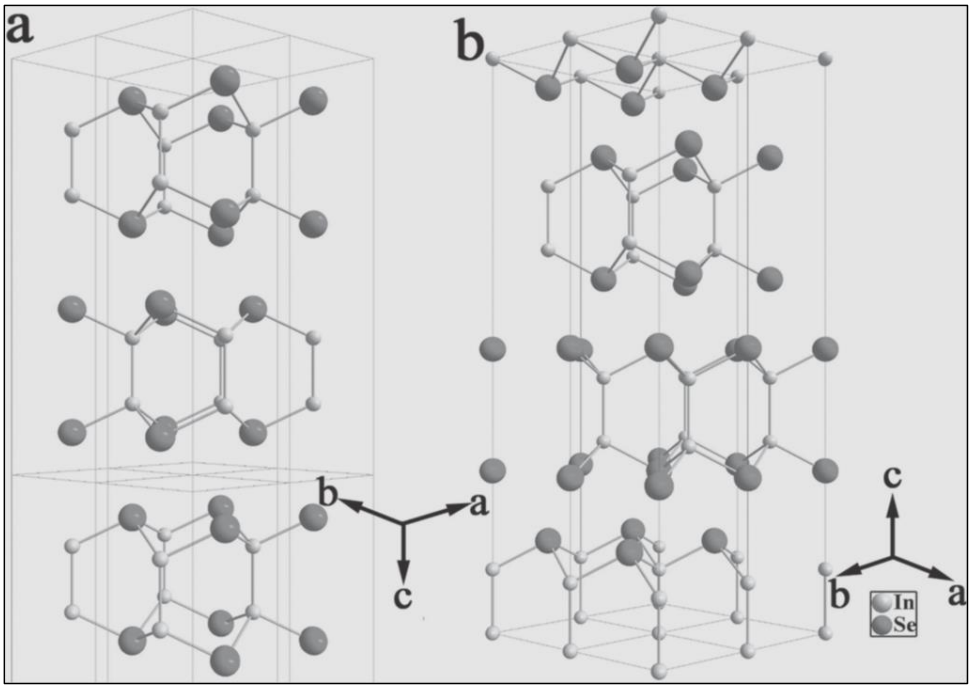

Figure 3-4: Crystal structure models of (a) β-InSe and (b) γ-InSe [8].

3.2.4 In_6Se_7

It is also one of the stable phases of the In-Se system though it has not received much attention. In_6Se_7 has been established to crystallize in a monoclinic crystal structure with a space group of P21 [8, 40]. The unit cell, which contains two formula units, is monoclinic with a = 9.430 Å, b = 4.063 Å , c = 18.378 Å. Basically the structure consists of two separate sections of almost cubic close-packed arrays of Se atoms with In atoms in octahedral coordination, the two sections having equivalent directions at 61 ° to each other.

3.3 Synthetic methods to make of indium selenide

On the basis of the binary In–Se system, the route and/or the technique employed for the fabrication, the starting material and the parameters used during synthesis have been

established to have a strong influence on the stoichiometries and particularly the polytypes obtained; thus presenting several structural characteristics of indium selenides [15, 41]. Several methods including solid state reaction, melting and annealing which employ In and Se elemental powders as raw materials have been used to obtain the bulk form [8]. For the thin film, techniques that include thermal evaporation, flash evaporation, molecular beam epitaxy (MBE), metal-organic chemical vapour deposition (MOCVD), [8, 42-44] chemical vapour transport [45], and electrostatic spray pyrolysis deposition [46] have been used. Briefly, thin films are formed by evaporating elemental (In and Se) or compound (e.g. In_2Se_3) sources onto a specific substrate which is then further annealed to improve crystallinity [8]. In thin films a variety of different In-Se phases may be formed depending on the deposition method and parameters. However one of the main problems concerning indium selenide is the existence of multi-phases in a single film [10].

Nanostructuring of materials is known to improve the quality of semiconductors and introduce unique and novel properties of the material that are completely different from their bulk. As a result researchers have embarked on producing indium selenide nanostructures to improve their optical, electrical and structural properties to enhance their use in different devices. Vapour based methods [44] are the most commonly used techniques to fabricate indium selenide nanostructures with relatively few reporting on the controllable synthesis of indium selenide nanostructures [8]. For example, via Au–catalysed vapour liquid solid mechanism, α–In_2Se_3 and β–In_2Se_3 nanowires have been obtained at 700 °C while MOCVD made it possible to fabricate γ–In_2Se_3 [20, 47]. Also the vapour transport method has generated κ–In_2Se_3 nanowires [48].

In addition to the vapour–based solid reaction techniques, solution-based methods are essential for the fabrication of inorganic solid state materials. As far as indium selenide is

concerned, very little work has been done on the solution phase synthesis compared to other metal chalcogenides. The challenges experienced when this route of synthesis is applied originate from the complexity of the indium selenide stoichiometries including the formation of InSe, In_2Se_3, In_4Se_3, and In_6Se_7 [49] which have the ability to thermodynamically coexist in a large range of temperatures and often emerge in similar reaction system. Another possible hurdle experienced during solution synthesis arises from the fact that the hydrolyzation of In(III) cations is very common in aqueous solution due to their deficient electron properties, which probably enhances the formation of indium selenides in aqueous solution [50]. Despite these, investigations have reported on the fabrication of the nanostructures via solution methods. Xiaoyan et al. [50] synthesized pure γ-In_2Se_3 with hierarchical flowerlike microspheres solvothermally for the first time through the reaction of indium chloride and selenium powders in the presence of ascorbic acid at 220 °C for 20 h in ethanol. Tabernor et al. [51] successfully used the thermal decomposition of indium and selenium dodamicylamine complexes via the heating-up process to prepare In_2Se_3 nanocrystallites. Revaprasadu et al. [52] reported the preparation of InSe nanoparticles capped with tri-n-octylphosphine oxide (TOPO) by a single-source route. Yang and Kelly [53] have synthesized several different sizes of InSe nanoparticles from organometallic precursors. Dimitrijevic et al. [54] prepared colloids of In_2Se_3 stabilized with poly (vinyl alcohol) or sodium metaphosphate in aqueous medium. Currently, attention is focussed on fabrication of atomically thin flakes of indium selenide nanoplates/nanosheets via exfoliation method. Exfoliation is known to produce atomically thin flakes of considerable lateral dimension; however, control over the dimensions is still a challenge.

As it has been established, the properties of the indium selenides strongly depend on the methods used to grow the materials, more work is therefore needed to try and strike a balance in the synthetic procedures that will result in desirable properties. Herein we report on the

colloidal synthesis of indium selenide nanocrystals via pyrolysis of the metal precursors in a coordinating solvent. Herein we report on an attempt to better control the nanoparticles size distribution, the resulting morphology and isolation of one particular In-Se phase per given conditions of synthesis. Different growth conditions such as reaction time, concentration of the starting materials (metal precursors), and coordinating and/or reducing solvent were varied in the course of the reaction and their effect on the nanocrystals' properties such as the crystalline structure, morphology and the electro-optical properties were investigated.

3.4 Experimental

3.4.1 Chemicals and materials

Indium (III) chloride, 99 % selenium powder, 70 % oleylamine (OLA), chloroform and 96 % ethanol were obtained from Sigma Aldrich.

3.4.2 Synthesis of indium monoselenide nanocrystals using the non-hot injection method

InSe nanoparticles were synthesized by a simple one pot method. About 0.3948 g (5 mmol) of indium chloride and 1.1059 g (5 mmol) of selenium powder for mole ratio 1:1, were placed into a three neck flask with a capacity of 50 mL, and 10 mL of OLA was added in as a solvent, surfactant and a reductant to reduce selenium. The mixture was then heated rapidly to 200 ºC under nitrogen gas with strong magnetic stirring. During the heating process, the mixture, which appeared to be homogenous, changed the colour from black to yellow and then to dark brown when the temperature of 200 ºC was attained. At this temperature, aliquots were obtained at different time intervals and then allowed to cool to 80 ºC naturally. The samples were washed with ethanol to flocculate the particles. The particles were then collected by centrifugation for 10 min at 3000 rpm. The washing was done several times in order to remove lingering impurities and the products were left to dry at room temperature for

12 h to obtain dark brown powders. The time intervals used were 10 min, 30 min and 60 min respectively. We then considered three other different mole ratios of $InCl_3$:Se following the same procedure. For 1:1, 2:1 and 3:1, the concentration of the In–precursor was varied and that of selenium was kept constant while vice versa was used in the case of the mole ratio 1:2.

3.4.3. Synthesis of In_2Se_3 nanocrystals using a non – hot injection method

A mixture of 5 mL of 1-dodecanthiol and 5 mL of oleylamine were put in a 3 neck round bottom flask, then 5 mmol of $InCl_3$ and 5 mmol of Se were added. The mixture was then heated quickly to 200 °C after which the temperature was maintained throughout the reaction. Aliquots were obtained at different times then washed several times with ethanol to remove the unreacted starting materials and the excess ligands. The clean products were then left to dry overnight. For the synthesis of the In_2Se_3 nanowires, 2 mL of 1-dodecanthiol and 8 ml of oleylamine were used maintaining the other parameters unchanged.

3.5 Characterization techniques

3.5.1 Optical characterization

A Varian Cary Eclipse (Cary 50) UV-vis spectrophotometer was used to carry out the absorption measurements. A Varian Cary Eclipse EL04103870 fluorescence spectrophotometer with a medium PMT voltage at an excitation wavelength of 250 nm was used to measure the photoluminescence of the particles. For both spectral analysis, the powders were dissolved in chloroform and placed in quartz cuvettes (1cm path length).

3.5.2 Structural characterization

The phase purity, crystallinity and preferred crystal orientation of the products were examined by using XRD on a Bruker MeasSrv (D2-205530)/D2-205530 diffractometer using secondary graphite monochromated CoKα radiation (λ 1.78897 Å) at 30 kV/30 mA. Measurements were taken using a glancing angle of incidence detector at an angle of 2°, for 2θ values over 10 - 90° in steps of 0.026° with a step time of 37 s and at a temperature of 25 °C.

The sample sizes and morphologies were determined by the transmission electron microscopy (TEM) carried out on a FEI Technai T12 TEM microscopy operated at an acceleration voltage of 200 kV with a beam spot size of 20 - 100 nm in TEM mode. The HRTEM images were obtained from a JEOL JEM-2100 microscopy with a LAB6 filament and an EDS detector, operated at 200 kV. The samples were prepared by placing a drop of the suspended nanoparticles in chloroform, on a carbon-copper grid. The grid with the sample was then allowed to dry at room temperature.

3.6 Results and discussions

3.6.1 Interdependency of time and precursor concentration: their effect on the properties of the nanocrystals

3.6.1.1 Indium:selenium, 1:1 mole ratio

Equivalent amounts of the metal precursors were used. 10 mL of OLA was used as both the solvent and the reducing agent. During the course of the reaction, which was programmed to be 60 min, aliquots were drawn from the reaction mixture at 8 min, 10 min, 30 min and 60 min after the reaction temperature of 200 °C was attained. The effects of time on the structural and optical properties of the nanocrystals obtained were investigated via TEM, HRTEM, XRD, UV-vis and PL.

To elucidate the phase structure and crystallinity of nanocrystals obtained, XRD analysis was carried out and the results are presented in Fig. 3-5. The four samples exhibited similar patterns that were indexed to rhombohedral InSe phase (JCPDS card 00-042-0919) with lattice parameters $a = 4$ Å and $c = 24.32$ Å; which are characteristic of rhombohedral InSe from previous reports [38]. The shoulder peak for the 10 min particles was indexed to the (101) plane of rhombohedral InSe using a different card number (JCPDS card 03-065-3660). The existence of the two card numbers within the same sample has been cited in literature as one of the challenges experienced during the fabrication of indium selenide; it is the possibility of co-existence of different allotropes in a sample [55]. The diffraction peak intensity was also seen to decrease with the increasing time of synthesis. Pattern (a) obtained sharper peaks compared to (b) and (c). This was indicative of the formation of more larger and crystalline particles for the 10 min synthesis. As the time of the synthesis was prolonged, the peaks slightly broadened an indication of decrease in particle sizes.

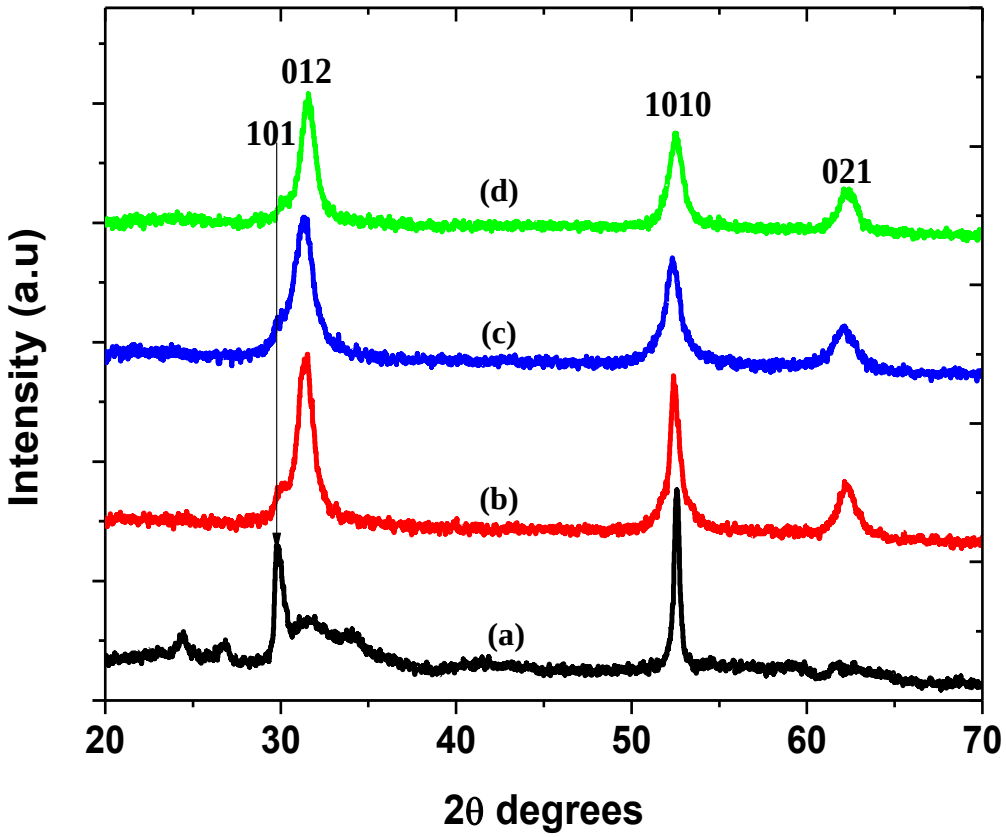

Figure 3-5: XRD patterns of InSe nanoparticles synthesized at temperature of 200 ºC with a mole ratio of 1:1 ($InCl_3$:Se) after: (a) 8 min which gave the InSe layers, (b) 10 min, (c) 30 min and (d) 60 min.

It is known that rhombohedral InSe has a layered crystal structure that extends over in three layers; however the order of formation of the nanoparticles/nanosheets (nanostructures) is not known, especially in wet chemical synthesis. As such, TEM analysis (illustrated in Fig. 3-6) of the products obtained at 8 min, 10 min, 30 min and 60 min were not only used to provide morphological insight about the InSe nanocrystals but also the formation pathway of the InSe nanoparticles. The 8 min sample was used as a control to investigate the effect of a lower reaction time on the resulting nanostructures. It is northworthy to mention that a further reduction in the reaction time (lower than 8 min) did not result in any nanostructures;

however, the TEM images portrayed a coalescence of the nuclei into 2D – like nanostructures as shown in the appendix A1.

Contrary to the previous reports on colloidal growth indicating that the shorter the reaction time the smaller the size/diameter of the nanocrystals obtained [56-59], Fig. 3-6(a-c) which are images of aliquots obtained after 8 min into the synthesis, clearly indicated that this sample comprised of nanosheets (bigger nanoparticles). Similarly, the micrographs suggested that individual layers of InSe were formed at lower reaction time. A slight increase in the reaction time to 10 min resulted in the disintegration of the nanosheets as illustrated by Fig. 3-6(d–f). Fig. 3-6 (d) and (e) portrayed broken nanosheets (bigger) and smaller nanoparticles whilst Fig. 3-6f showed nanosheets with cracked surfaces. The cracked surface allowed us to conclude that the nanosheets were in the process of disintegration after a certain maximum lateral dimension was attained. Generally, these images portrayed that during the shortest time in the reaction pathway, the bigger nanocrystals (the nanosheets) were formed first which then broke down as the reaction progressed.

As the reaction time was prolonged to 30 min, the sheets were seen to disintegrate further into finer nanoparticles as shown in Fig. 3-6 (g – i), in fact; Fig. 3-6g shows large pieces of broken down sheets. However, the nanosheets were observed to break down non- uniformly and the shapes of the nanoparticles are irregular. It should be noted that the disintegration occurred at random as shown in Fig. 3-6g thus the final smaller particles are not expected to have a definite shape. Fig. 3-6 (j) and (k) portrays the images of the aliquots obtained after 60 min. They revealed that the nanosheets were completely broken down and transformed to smaller nanoparticles. The particle size of these nanoparticles ranged between 7 and 8nm as shown by the histogram for the particle size distribution (Fig. 3-6i). The nanoparticles were seen to be nearly monodispersed.

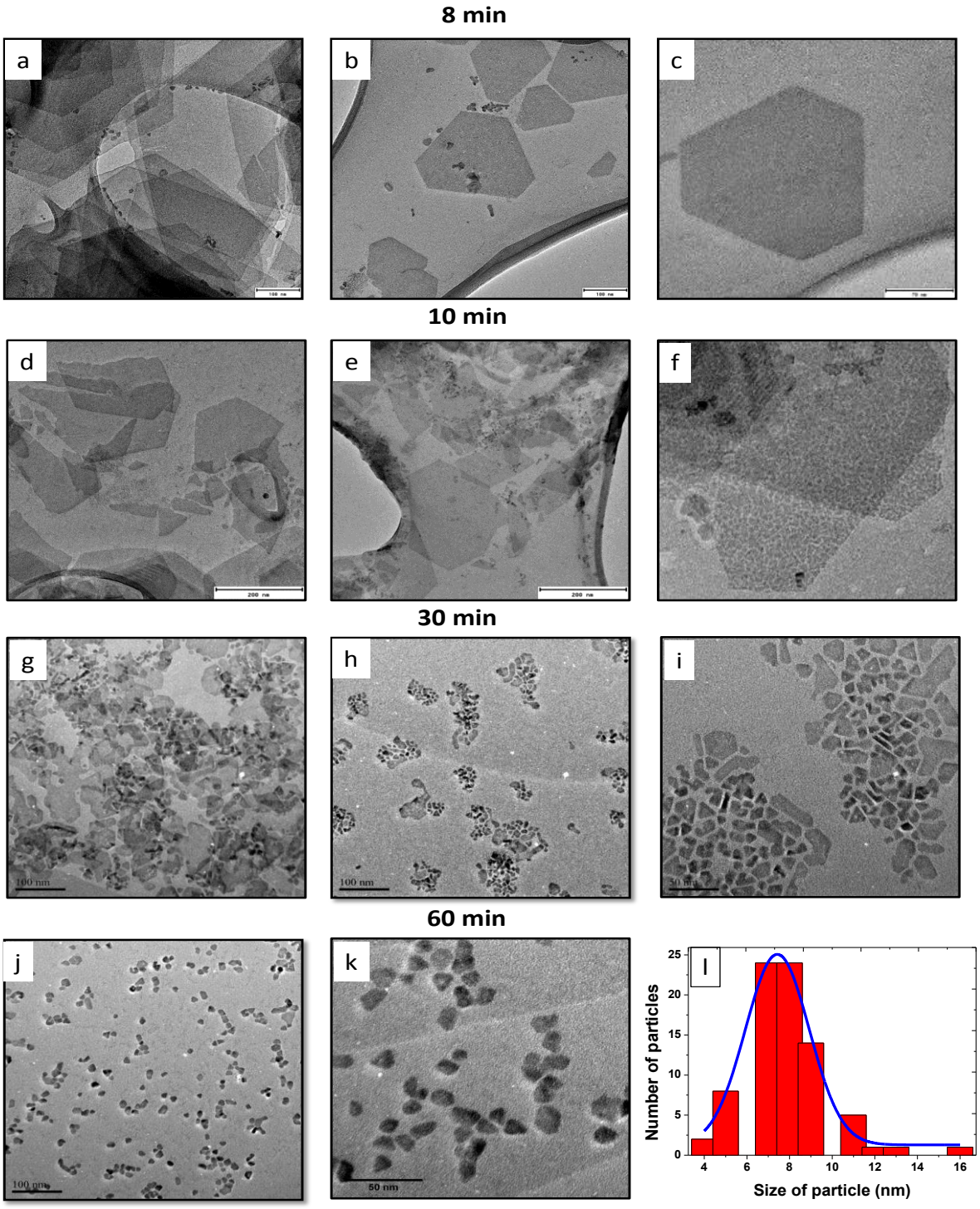

Figure 3-6 Multiple TEM images of InSe samples synthesized at temperature of 200 ºC with a mole ratio of 1:1 ($InCl_3$:Se) after (a-c) 8 min, (d-f) 10 min (g-i) 30 min and (j-k) 60 min. (l) show the particle size distribution of the nanoparticles.

HRTEM was also used to analyse the 10 min sample and the 60 min sample and their results are presented in Fig. 3-7. The lattice fringes observed in the HRTEM images have a d-spacing (0.33 nm) similar to the (012) lattice plane of rhombohedral InSe for both the 10 min nanosheets and the 60 min nanoparticles. The crystallinity of the nanosheets and the nanoparticles were revealed by the FFT images included as insets. The nanosheets synthesized in 10 min and the nanoparticles synthesized in 60 min showed similar crystal orientation as shown by the d-spacing of the lattice fringes. This therefore substantiates our conclusion that the nanosheets fragment with time to form smaller nanoparticles. The fragmentation is due to strain. Strain is due to imperfections in bonding which is indicated by the formation of kinks and zigzag in the bonds. This can be observed in the HRTEM image in Fig. 3-7 (circled). An increase in strain will eventually cause the breakage of the sheet. This has been observed in other 2D nanosheets such as that of XS_2 form and graphene [60-62].

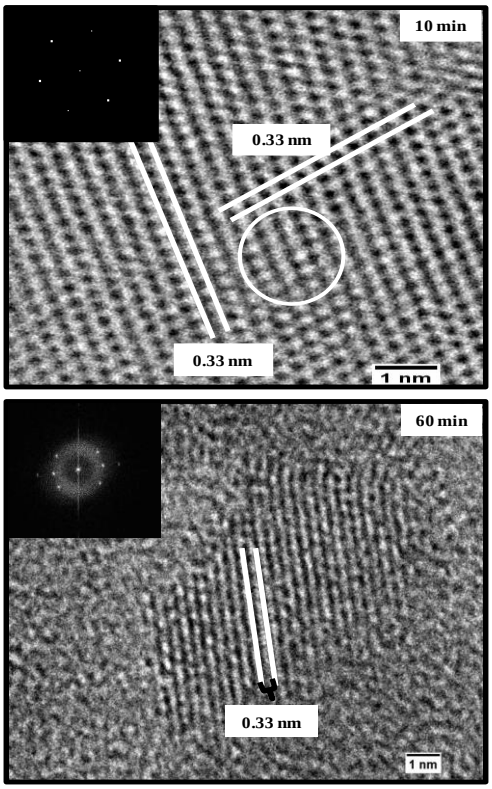

Figure 3-7: HRTEM images of the nanosheets synthesized in 10 min and the nanoparticles synthesized in 60 min (insets are the FFT images of the corresponding HRTEM images).

Fig.3-8 shows the energy dispersive spectroscopy data that was used to determine the elemental composition of the nanosheets and the nanoparticles. It confirmed that both the nanosheets and the nanoparticles contained indium and selenium. However impurities such as chlorine which was part of the In source and oxygen were also detected. These impurities were more prominent in the 10 min sample due to the short reaction time compared to the 60 min sample.

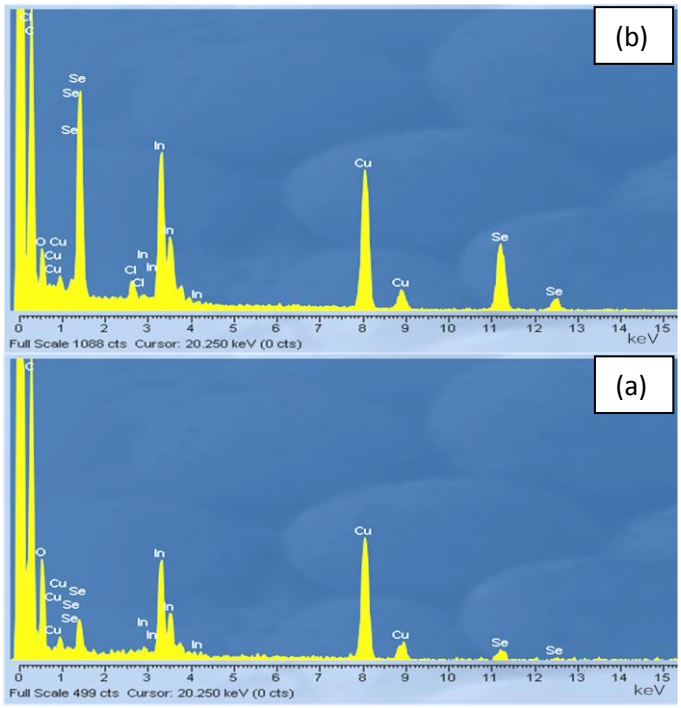

Figure 3-8: EDS spectra of the nanosheets synthesized in (a) 10 min and the nanoparticles synthesized in (b) 60 min.

Absorption and emission (PL) spectroscopy were employed to investigate the optical properties of the obtained InSe nanoparticles. The UV-vis spectra of the 8 min, 10 min, 30 min and 60 min samples are presented in Fig. 3-9 (a), (b), (c) and (d) respectively. The nanosheets produced after 8 min were of different sizes and shapes as observed TEM. This reflected on their absorption as they gave a tailing spectrum. A slight bend was however seen at about 725 nm for the 8 min sample indicating their onset of absorption. Similarly the 10 min sample had band edge at 725 nm (Fig. 3-9b), the 30 min's band edge was at 517 nm (Fig. 3-9c) while that of 60 min was at 495 nm (Fig. 3-9d). The samples exhibited considerable quantum confinement effect as their band edges were blue shifted compared to the bulk band gap of 1.24 eV (1000 nm). It was also evident that the value of the band edge increased with increasing time of synthesis suggesting that the 60 min sample had smaller nanoparticles than the ones produced after 30 min and 10 min.

Fig. 3-10 represents the emission spectra of the samples obtained at mole ratio 1:1. The 8 min sample exhibited two emission peaks centred at about 515 nm due to the band gap transition and 650 nm due to the P_x-P_y transitions (position (I) and (II) respectively). This observation was in accordance with the corresponding band scheme of bulk InSe virtually identical to the one represented in Fig. 3-11 [63, 64]. The electronic transition from $p_{x,y}$ like orbitals to the bottom of the conduction band are the E' transition (2.4 eV) while the p_z like orbitals to the bottom of the conduction band is the band gap (1.27 eV). Our measurements were performed at an excitation wavelength of 240 nm to provide energy greater than the band gap of InSe. This has been reported to allow the occurrence of the transition between $p_{x,y}$ and the bottom of the conduction [64]. In addition, the peak positions were blue shifted compared to their onset of absorption which was seen at about 725 nm; a phenomena reported in the previous studies on InSe and GaSe nanosheets [63, 65] and other nanosheets obtained from transition metals dichalcogenides as band gap crossover due to the modification of the band structure experienced when the material moves from a three layered crystal structure to a monolayer system [66]. The 10 min, 30 min and the 60 min had their emission maxima centred at 712 nm, 512 nm and 433 nm and are presented by spectrum (b), (c) and (d) respectively. These are shifted compared to their band edges. The results generated from UV – vis and the emission profiles are tabulated in Table 1.

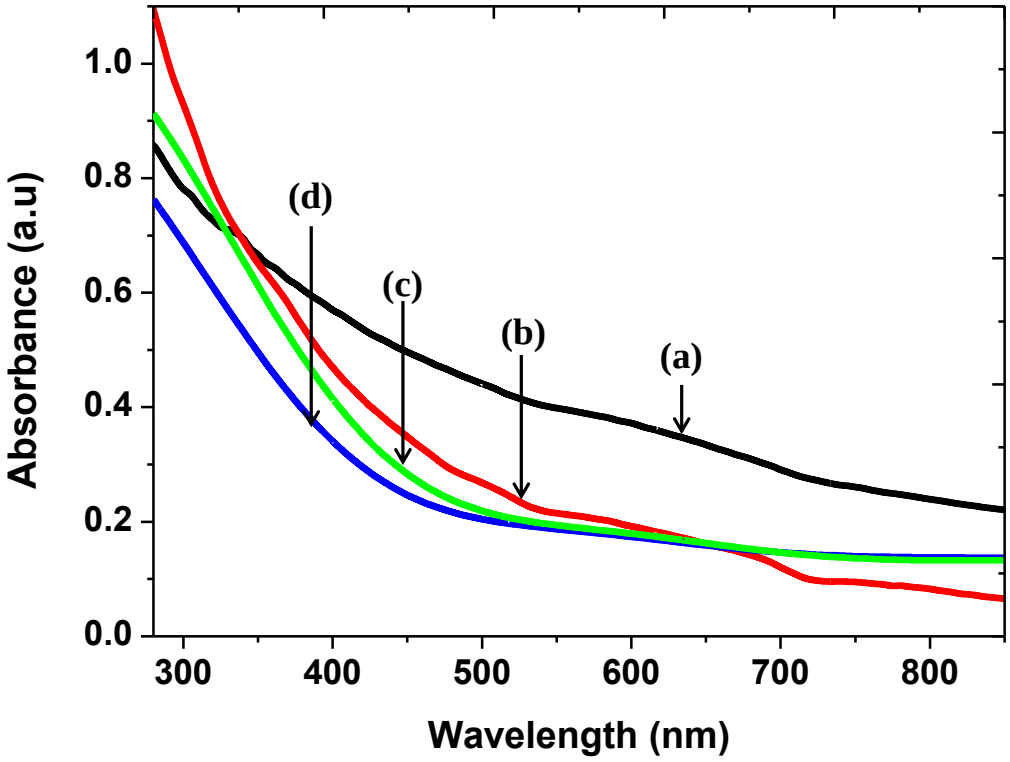

Figure 3-9: Absorption spectra for InSe nanoparticles synthesized at 200 ºC with a mole ratio of 1:1 after (a) 8 min, (b) 10 min, (c) 30 min and 60 min.

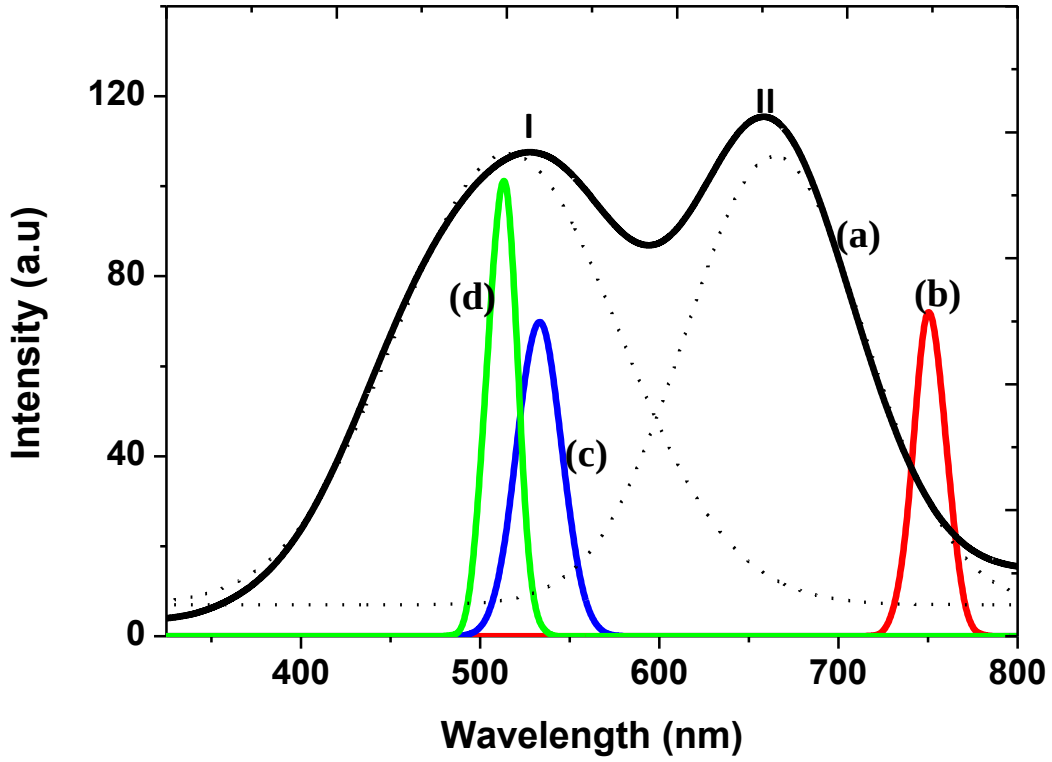

Figure 3-10: Photoluminescence spectra of InSe synthesized at a temperature of 200 ºC and a mole ratio of 1:1 after (a) 10 min (b) 30 min and (c) 60 min.

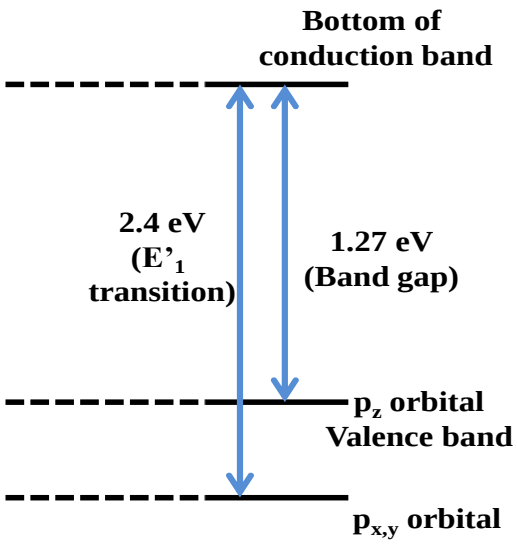

Figure 3-11: The band structure of InSe with the bulk band gap and electronic transitions.

Table 3-1: A summary of the results generated from UV – vis and the emission profiles.

Spectrum	Time (min)	Band edge (nm)	Emission peak (nm)
A	8	725	515 (pos. I) 650 (pos. II)
B	10	725	712
C	30	517	512
d	60	495	433

3.6.1.2 Indium: selenium, 1:2 mole ratio

Excess chalcogenide in a setup is known to produce better morphology in colloidal synthesis. Therefore in the first part of this investigation, an indium deficient situation was used. About 2.5 mmol of $InCl_3$ and 5 mmol of selenium powder were used in 10 mL of OLA at a temperature of 200 °C. Aliquots were obtained after 10 min, 30 min and 60 min to study the effect of time on the properties of the products was done via UV-Vis, PL, XRD and TEM.

The XRD results in Fig. 3-12 showed that the samples contained a mixed phase of rhombohedral InSe as indexed from the card JCPDS card 00-042-0919 with lattice parameters $a = 4$ Å and $c = 24.32$ Å and In_2Se_3 (showed by the *). Spectrum (a) and (b) are the patterns for the 10 min and the 60 min samples respectively. Spectrum (a) portrayed broader peaks whilst spectrum (b) resulted in sharper peaks; an indication that the 10 min sample comprised of smaller sized nanoparticle compared to the 60 min sample. This was so because an increase in the reaction time resulted into the addition of more material into the existing nuclei thus creating bigger nanoparticles.

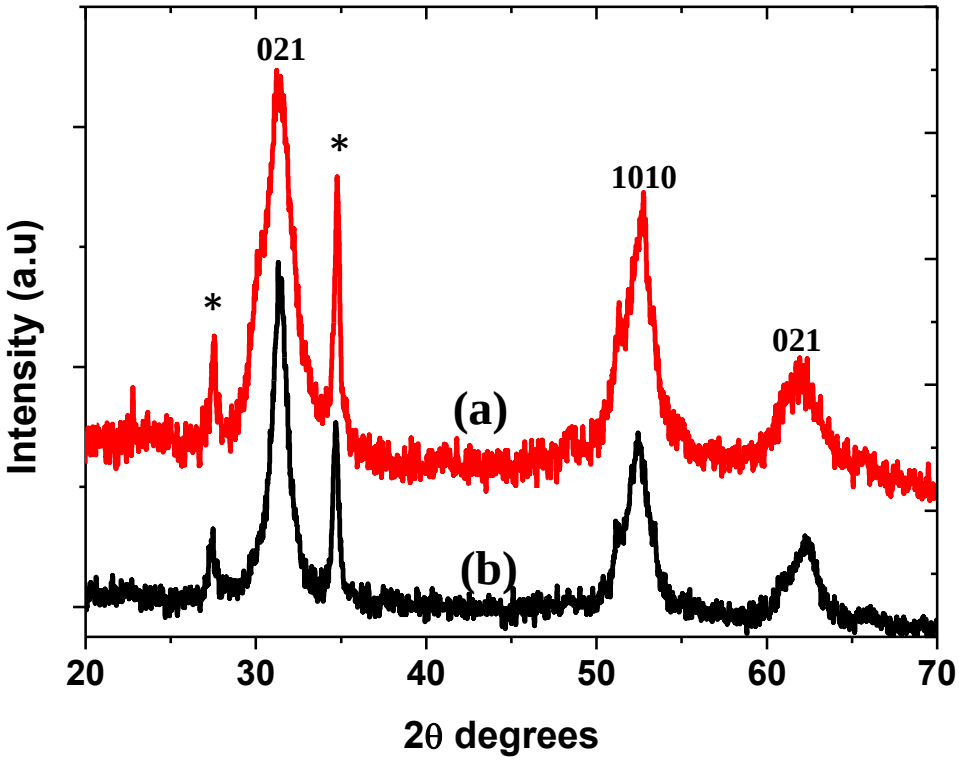

Figure 3-12: XRD spectra of InSe nanocrystals from 1:2 mole ratio ($InCl_3$:Se) a) 10 min and b) 60 min. The peaks marked with (*) are indexed to In_2Se_3

Fig. 3-13 shows the TEM images of the as-synthesized nanocrystals. For all the three samples obtained at different durations, no defined morphology was obtained however agglomeration of the nanocrystals increased with increasing growth time as shown in Fig. 3-13 (a) and (c) respectively.

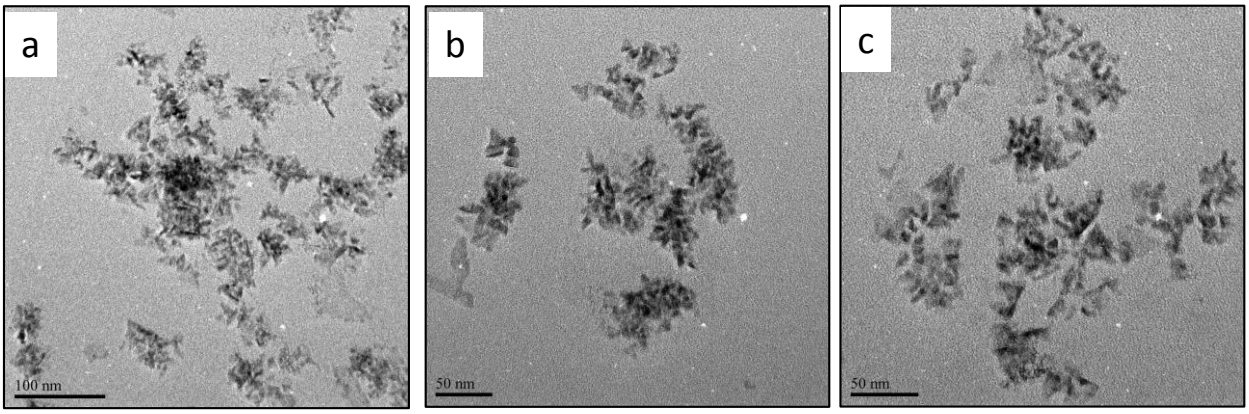

Figure 3-13: TEM images of InSe nanocrystals from 1:2 mole ratio ($inCl_3$:Se) a) 10 min, b) 30 min and c) 60 min.

The agglomeration of the nanoparticles was further confirmed by the UV-Vis results. The spectra presented in Fig. 3-14 illustrated a tailing behaviour with the 60 min sample (Fig. 3-14a) tailing more than the 10 min sample (Fig. 3-14b). The absorption band edge of the nanocrystals which was about 700 nm was blue shifted compared to the bulk one which is about 1000 nm despite the indefinite morphology.

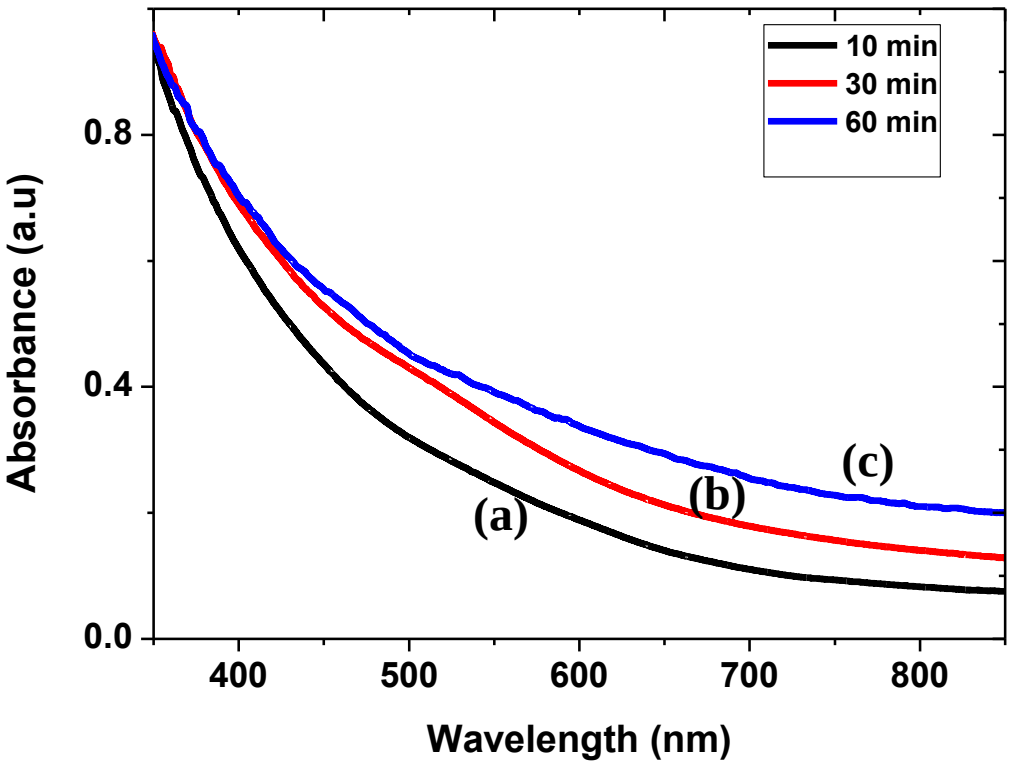

Figure 3-14: UV-vis spectra of InSe nanocrystals from 1:2 mole ratio ($InCl_3$:Se) (a) 10 min, (b) 30 min and (c) 60 min.

3.6.1.3 Indium: selenium, 2:1 mole ratio

Here, the amount of In precursor ($InCl_3$) was maintained at 5 mM while that of selenium was reduced to 2.5 mM in order to achieve a mole ratio of 2:1. 10 mL of oleylamine was used as both surfactant and reductant. The effect of using less selenium on the nanocrystals properties during the course of the synthesis was then studied with emphasis on the 8 min sample (because this is what gave the complete 2D nanocrystals when mole ratio 1:1 was used), 30 min and 60 min.

To determine the structural information of the InSe nanocrystals synthesized at 2:1 mole ratio, XRD and TEM techniques were applied. XRD spectra presented in Fig. 3-15 showed that all the three samples had similar crystal structures predominantly indexed to rhombohedral InSe phase (JCPDS card 03-065-3660). The lattice parameters were also determined as a = 4 Å and c = 24.32 Å with a d-spacing of 3.33Å along 101 planes; these parameters are comparable to those obtained for InSe flakes by Mudd et al. [38] and Rigoult et al. [67]. The intensity of the diffraction peaks were seen to increase with increasing time, that is from 8 min (Fig. 3-15a) to 30 min (Fig. 3-15b) to 60 min (Fig. 3-15c), an indication that they became more crystalline with time.

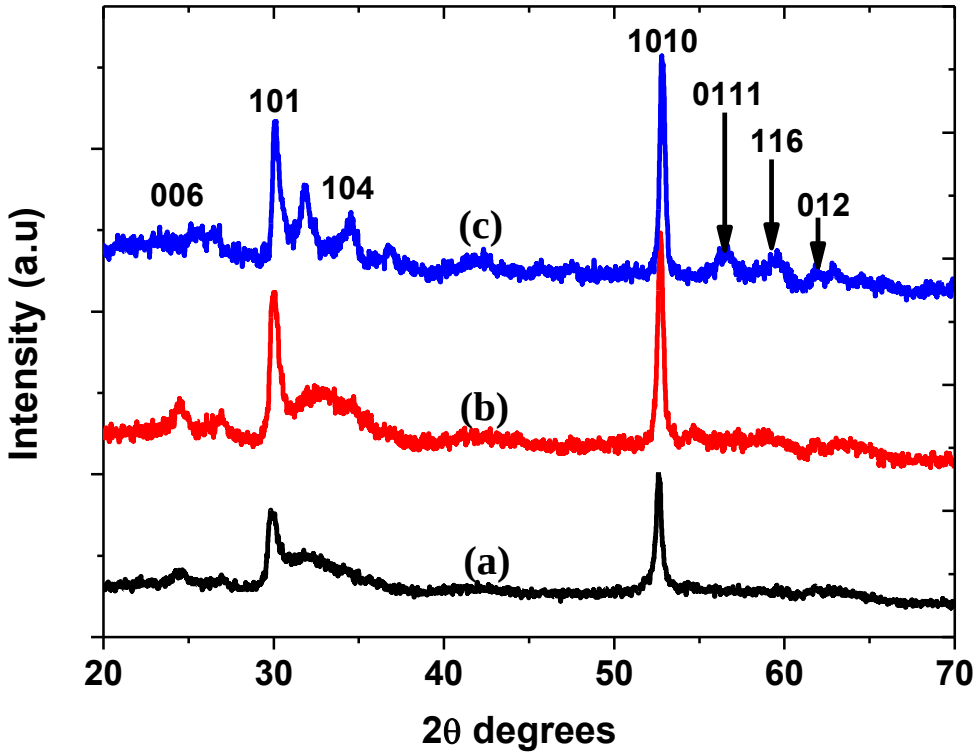

Figure 3-15: XRD patterns of InSe nanosheets synthesized at temperature of 200 ºC with a mole ratio of 2:1 ($InCl_3$:Se) after: (a) 8 min, (b) 30 min and (c) 60 min.

TEM analysis illustrated in Fig. 3-16 clearly revealed that InSe nanosheets were formed; however regular faceted edges nanosheets were obtained after 60 min. At 8 min,

agglomerated nanocrystals coalesce then extend in 2D like nanostructures as depicted in Fig. 3-16a. As the synthetic time progressed, individual nanosheets begun to form and were more disperse. At this stage, as presented in Fig. 3-16b, the nanosheets portrayed irregular facets with undefined shapes. Complete and perfect nanosheets with regular faceted edges of six sides almost hexagonal, though the sides were determined to differ by a few nanometres, were obtained at 60 min. The 60 min sampled contained nanosheets of different shapes as shown in Fig. 3-16c though the lateral dimension was approximated as 130 nm. The thickness of the individual nanosheet was also determined via TEM micrograph technique and was found to be about 60 nm according to the procedure described in the appendix. Aliquots obtained at 90 min showed broken/damaged nanosheets implying that after the nanosheets obtained a maximum lateral dimension, they then experienced the same phenomenon described in the mole ratio 1:1 where the nanosheets broke to form smaller nanoparticles.

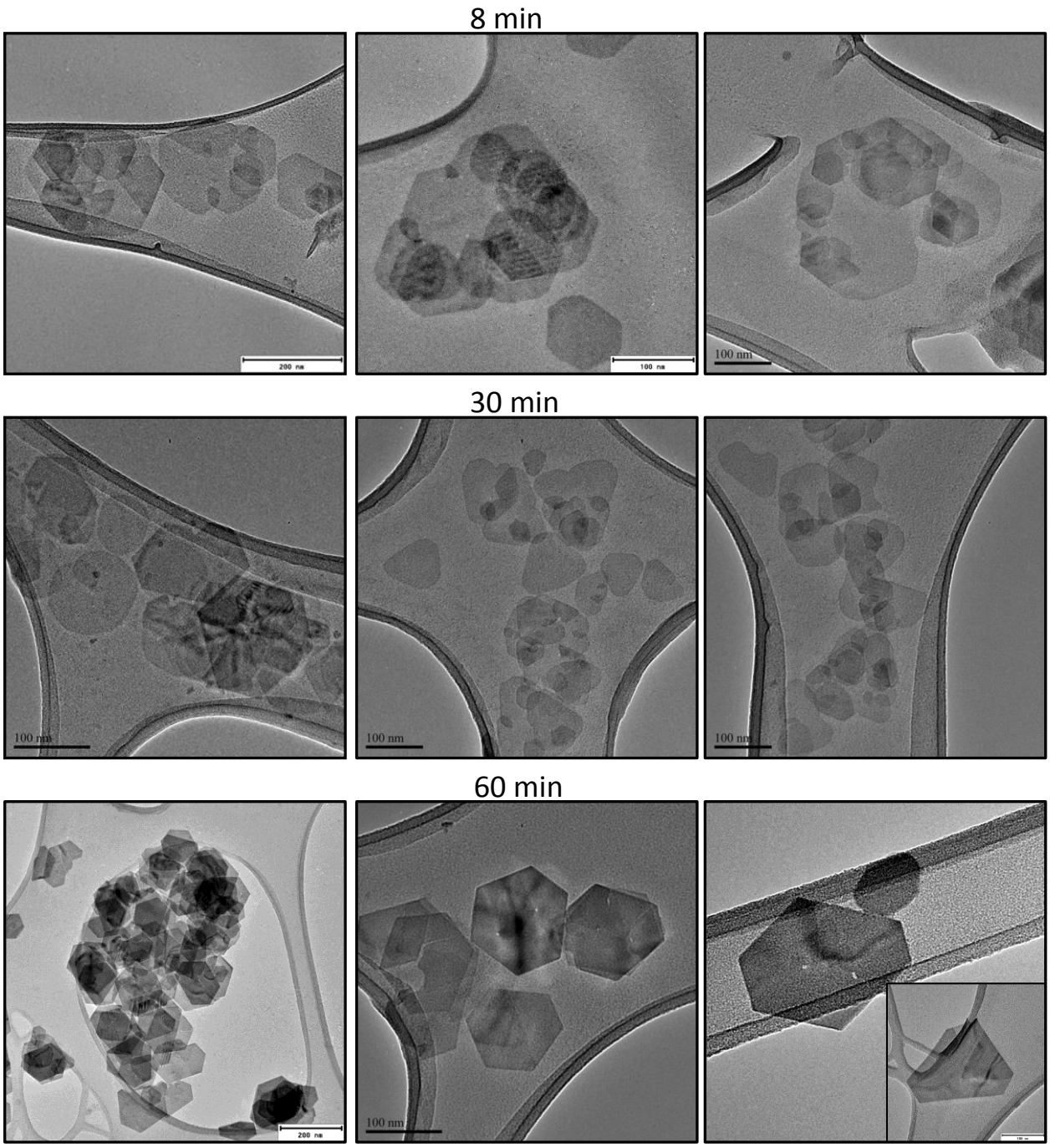

Figure 3-16: Multiple TEM images of InSe samples synthesized at temperature of 200 ºC with a mole ratio of 2:1 ($InCl_3$:Se) after (a) 8 min, (b) 30 min and (c) 60 min.

Optical studies were done by analysing the absorption and emission spectra of the nanosheets. Examination of the absorption spectra displayed in Fig. 3-17 revealed that the 8 min (Fig. 3-17a) and the 30 min (Fig. 3-17b) sample presented tailing spectra as a result of the agglomeration in the 8 min sample and the different sizes and irregular shapes in the 30 min sample as confirmed by the TEM images, therefore it was challenging to extract the band edges. For the 60 min sample with the perfect nanosheets, the band edge was extracted at about 725 nm, though the spectrum was slightly tailing. The slight tailing was attributed to the different shapes of the nanosheets observed in TEM micrographs. The nanosheets exhibited quantum confinement effects, that is, their absorption band edges were blue shifted compared to that of bulk InSe which is about 1000 nm.

The emission spectra shown in Fig. 3-18 exhibited two peaks that were centred at position (I) due to the E' transition and (II) as a result of the band gap transition and the extracted values are summarized in Table 2. In addition, the peak positions were blue shifted compared to their absorption band edges. The dotted spectra are the Gaussian fitted peaks from where the centres of the emission peaks were extracted.

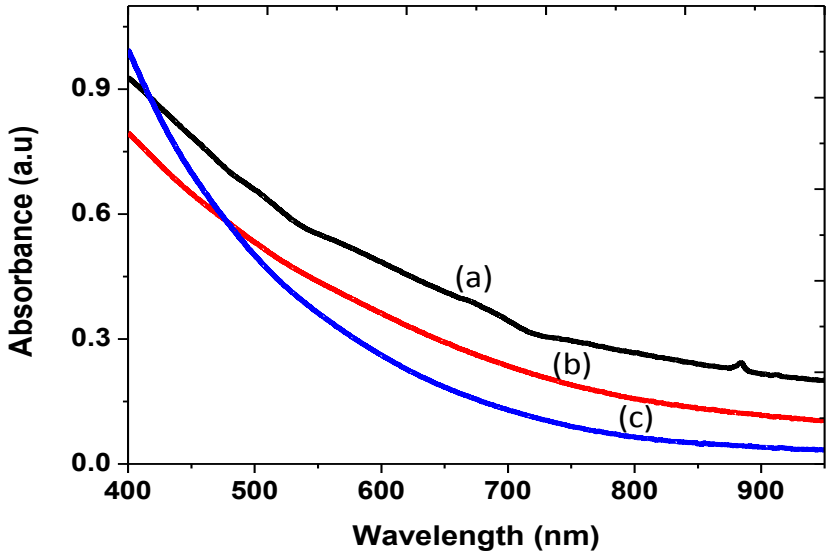

Figure 3-17: Absorption spectra for InSe nanosheets synthesized at 200 ºC with a mole ratio of 2:1 after (a) 8 min (b) 30 min and (c) 60 min.

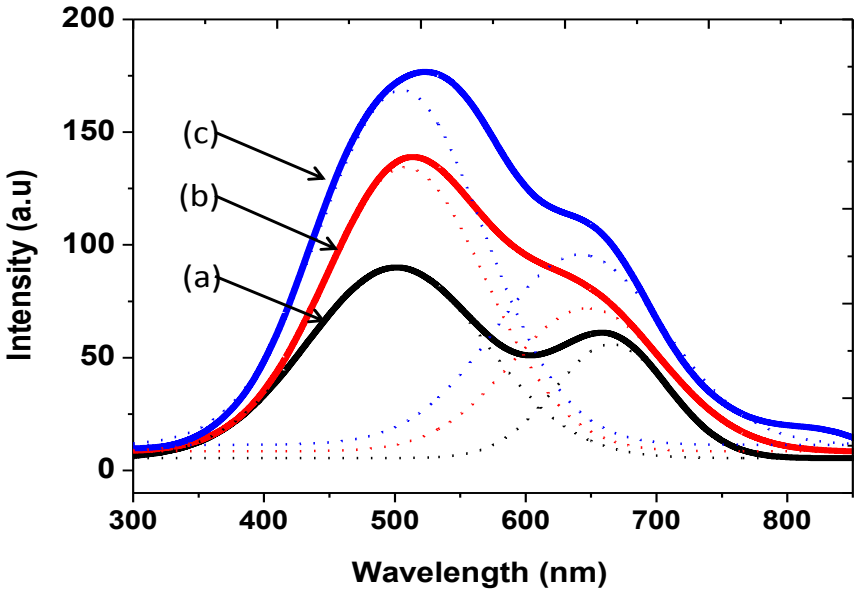

Figure 3-18: Photoluminescence spectra of InSe synthesized at a temperature of 200 ºC and a mole ratio of 2:1 after (a) 8 min (b) 30 min and (c) 60 min.

Table 3-2: A summary of the UV-vis and the emission profile results

Spectrum	Time (min)	Band edge (nm)	Emission peak (nm)	Emission peak (nm)
A	8	Tailing	501	665
B	30	Tailing	508	647
C	60	725	515	641

3.6.1.4 Indium: selenium, 3:1 mole ratio

A further increase in the indium precursor source was herein and the effect on the nanocrystals studied via TEM and XRD for structural studies and UV – vis and PL for the optical studies.

The XRD was used to confirm the crystal structure and composition of the nanocrystal. From the XRD pattern in Fig. 3-19, it was evident from the spectra that InSe were produced and they matched the rhombohedral crystal structure. The peaks were more diffracted in the 30 min (Fig. 3-19b) and they were more intense than in the 8 min sample (Fig. 3-19a); thus deducing an improvement in the crystallinity of the nanosheets with increasing reaction time.

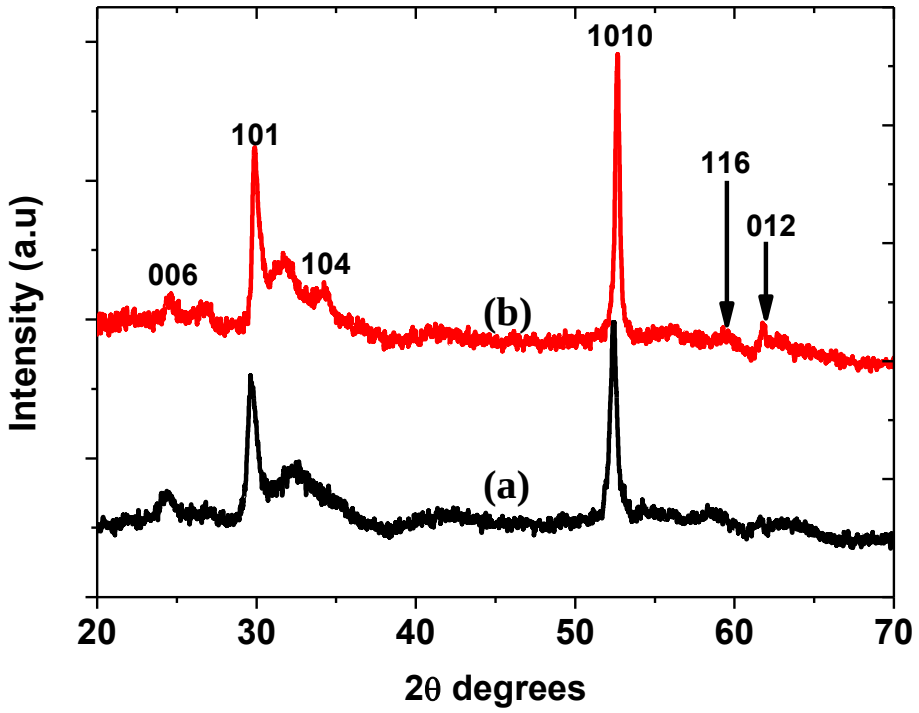

Figure 3-19: XRD patterns of InSe nanosheets synthesized at temperature of 200 ºC with a mole ratio of 3:1 ($InCl_3$:Se) after: (a) 8 min and (b) 30 min.

TEM images illustrated in Fig. 3-20 suggested that at this mole ratio, the perfect and complete nanosheets were formed after 30 min of the reaction. The 8 min sample presented in Fig. 3-20 (a-c) contained nanosheets of different shapes and non-uniform dimensions and they were not completely developed. Aliquot obtained at 30 min (Fig. 3-20 (d-f)) gave transparent individual nanosheets with defined regular faceted edges. The nanosheets were six sided though not hexagonal because the sides were slightly different and had a lateral dimension of 130 nm. Increasing the time to 60 min resulted in the breaking down of the nanosheets into smaller particles (Fig. 3-20 (g-h)) thus repeating the same scenario discussed on section of mole ratio 1:1 30 min and the 60 min samples and the formation pathway of InSe nanoparticles. This observation indicated that after the maximum lateral dimension of

130 nm has been reached, the nanosheets then experienced strain or stress that caused defects in their structures thus resulting in the disintegration of the nanosheets.

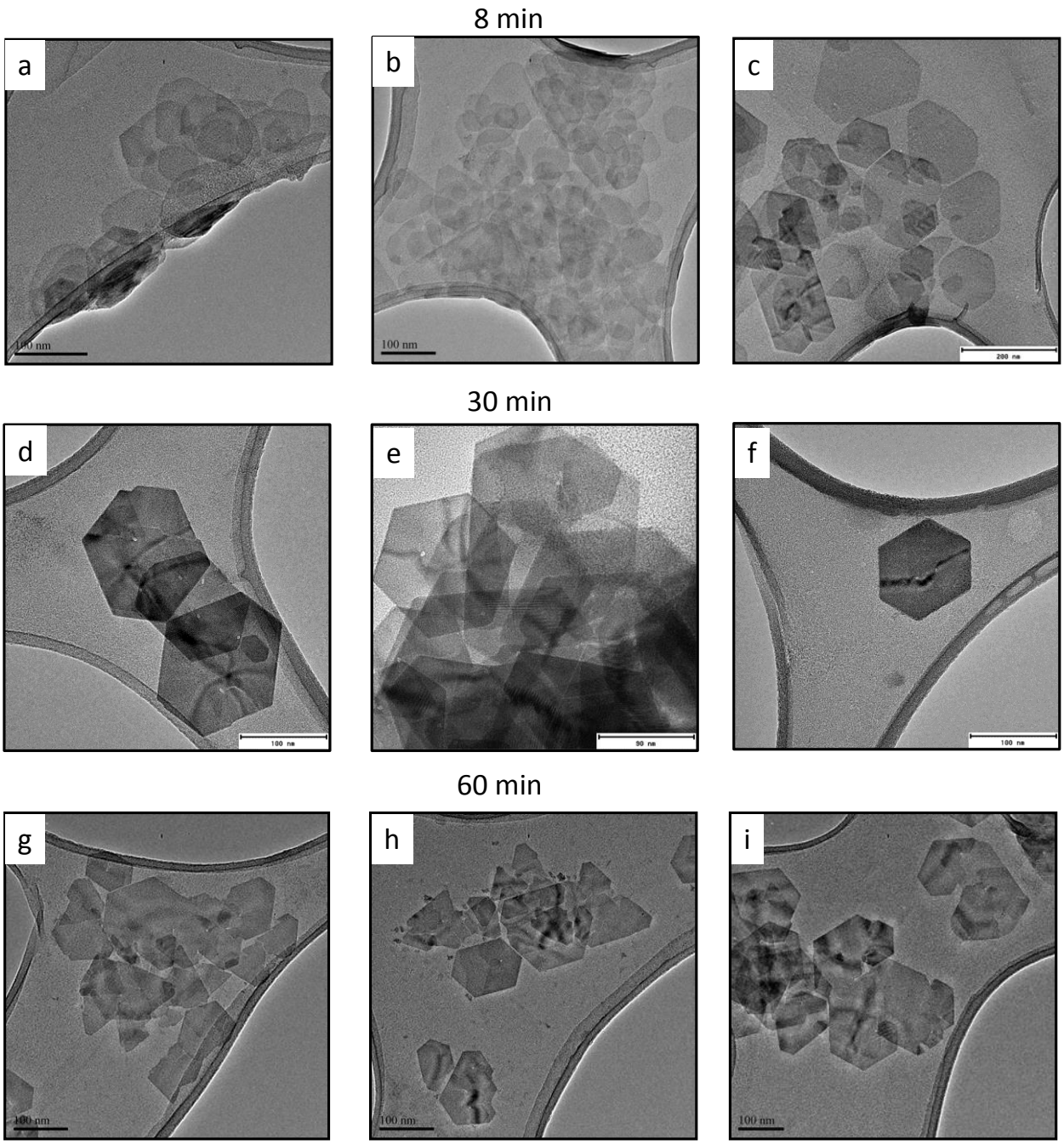

Figure 3-20: Multiple TEM images of InSe samples synthesized at temperature of 200 ºC with a mole ratio of 3:1 ($InCl_3$:Se) after (a-c) 8 min, (d-f) 30 min and (g-i) 60 min.

The optical studies were undertaken for the 8 min sample and the 30 min sample. The spectrum for the 8 min sample represented by Fig. 3-21a showed a tailing behaviour which was due to the different sizes and shapes seen in TEM. The nanosheets obtained after 30 min

experienced absorption onset at about 725 nm (Fig. 3-21b), though the spectrum had a slight tailing as a result of the different shapes. The PL spectra (Fig. 3-22) exhibited two emission peaks centred at (I) and (II) which are characteristic of the InSe E' transition and band gap transition respectively. The values extracted from UV and the PL are summarized in Table 3. In addition, the peak positions were blue shifted compared to their absorption band edges.

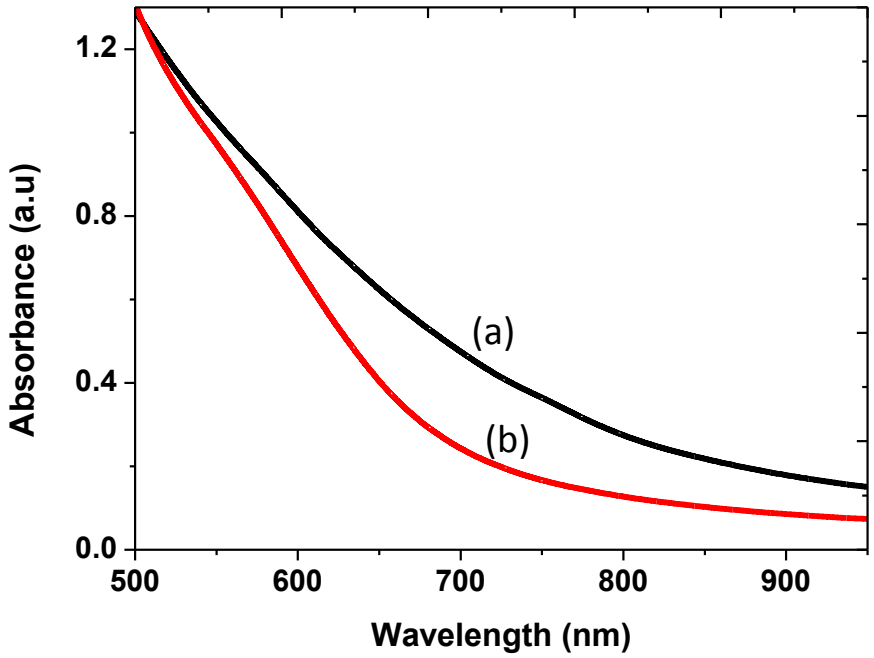

Figure 3-21: Absorption spectra for InSe nanosheets synthesized at 200 ºC with a mole ratio of 3:1 after (a) 8 min (b) 30 min.

.

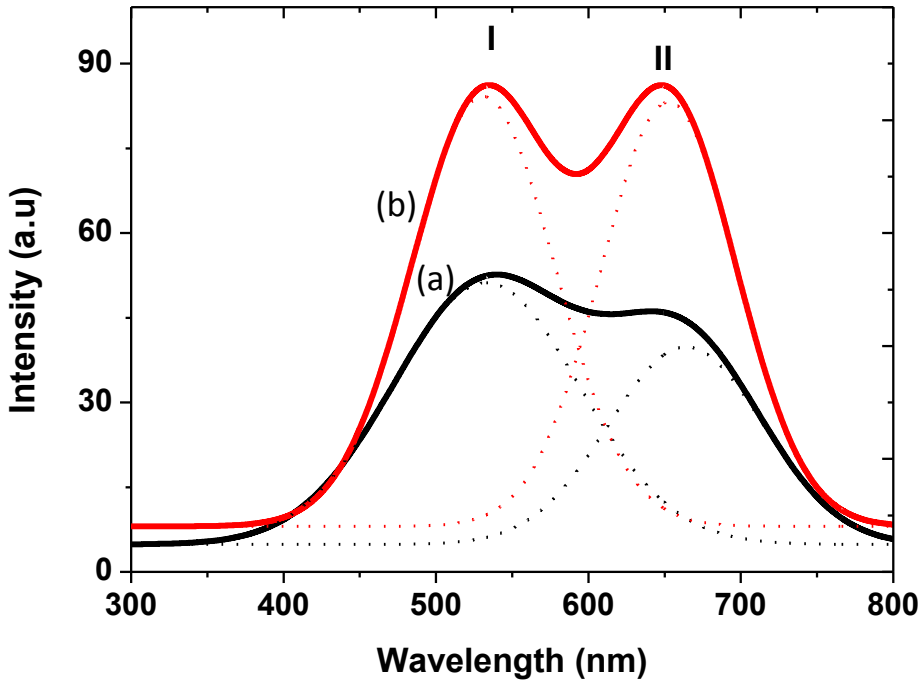

Figure 3-22: Photoluminescence spectra of InSe synthesized at a temperature of 200 ºC and a mole ratio of 3:1 after (a) 8 min and (b) 30 min.

Table 3-3: A summary of the UV-vis and the emission profiles

Spectrum	Time (min)	Band edge (nm)	Emission peak (nm)	Emission peak (nm)
a	8	Tailing	518	650
b	30	725	520	651

3.6.2 Formation mechanism of InSe nanosheets

There are competing arguments in literature as to how the nanosheets form however evident from all the studies including ours is that it is difficult to pin point the exact mechanism of

formation of the nanosheets [68-72]. Nevertheless, the formation of two dimensional InSe nanosheets may be explained by the mechanism reported by Lu et al. [71]. The mechanism suggests that nanosheet formation can be elucidated by the anisotropic nature of the crystal structure of the layered materials coupled with the type of coordinating solvent used during synthesis. Thus as shown in Scheme 1a, the γ–InSe polytype crystalline structure of InSe contains layers of covalently bonded In–Se and In–In bonds. The orientation of the atoms in each layer is such that the orbitals of the valence electrons involved in bond formation are located inside the layer. Therefore there is no chance of an overlap with orbitals of the valence electrons from the neighbouring layer [73]. As a result, these layers are held together through van der Waals bonds and stack vertically along the c-axis of the crystal structure. This then allows for intercalation of the layered crystal by foreign atoms or molecules as shown in Scheme 1b. When InSe begins to form in solution, the coordinating solvent (in this case OLA) infiltrates into the van der Waal space as it tries to bind to the nanocrystal, thereby preventing growth along the c– axis and supporting growth within the a–b plane to form two-dimensional nanosheets.

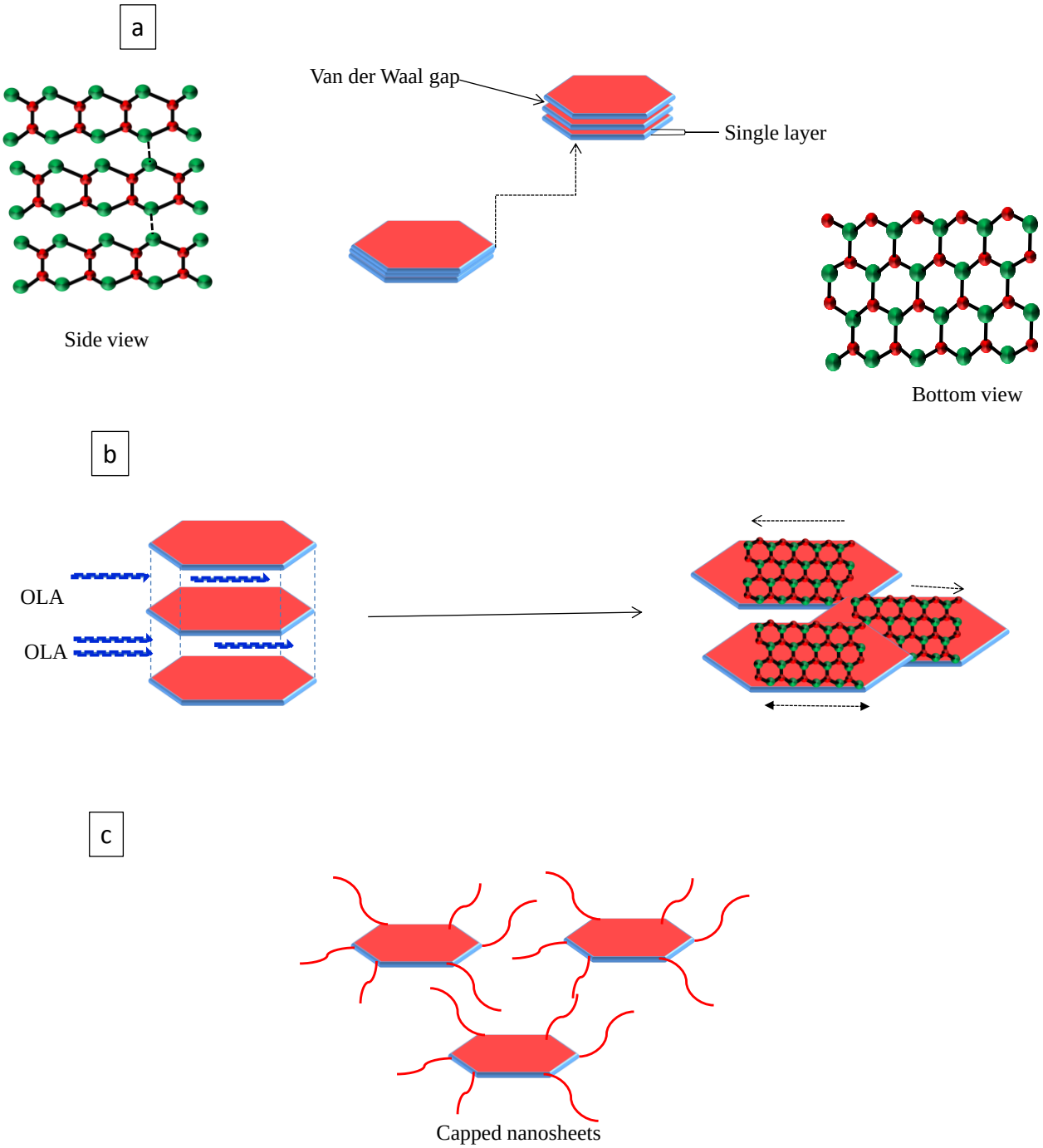

Scheme 3-1: Formation pathway of InSe nanosheets

3.6.3 Formation pathway of InSe nanoparticles

The findings on the structural and optical properties of InSe indicate that the nanosheet's lateral growth continue with time. After attaining a certain maximum lateral dimension of

about 130 nm, they experience strain or stress then they begin to break/disintegrate until smaller nanoparticles are attained. This is contrary to the most quoted growth mechanism by Lamer and Dinegars involving nuclei formation from precursor, followed by the growth of the nuclei via Ostwald ripening process and the termination of growth when the precursor is depleted is the most quoted growth mechanism in colloidal synthesis [74]. After 10 min of synthesis in mole ratio 1:1, 60 min in mole ratio 2:1 and 30 min in mole ratio 3:1, it is assumed that the nanosheets attain maximum lateral dimension after which they start to experience some kind of strain until they start to crack or break. As we have mentioned earlier, nanosheets are seen to disintegrate further as the reaction time is prolonged to 30 min for mole ratio 1:1 (Fig. 3-6 (g-i) , and after one hour, finer nanocrystals are obtained, that is, the longer reaction time gives smaller particles and vice-versa. Similarly, the band edge of nanoparticles produced after 60 min (longer time) is blue shifted compared to the ones produced after 10 min (shorter time) indicating that the longer reaction time gives smaller nanoparticles. These findings on the structural and optical properties of InSe were contrary to those expected from the classical semiconductor nanoparticles synthesized via colloidal synthesis. Colloidal synthesis used herein for the fabrication of InSe nanoparticles is an example of a bottom up approach, where the particles are expected to undergo two important processes, the nucleation stage and the growth process. Usually with this approach, the nanoparticles seek to be smaller at the beginning of the synthesis then later grow to bigger ones through the Ostwald ripening process as the time of synthesis progresses, when all other parameters are held constant [56-59]. With the results discussed above, scheme 3-1 represents a preliminary proposal of the growth mechanism for the formation of InSe nanoparticles. This mechanism mimics the top down approach because it begins by the formation of a big layer (sheet) which then disintegrates into smaller nanoparticles. However, the layers break down chemically in a coordinating solvent without any physical means and the beginning

precursors are $InCl_3$ and Se which react to give the InSe nanoparticles. For this reason, we suggest to name the proposed mechanism as a pseudo top-down approach.

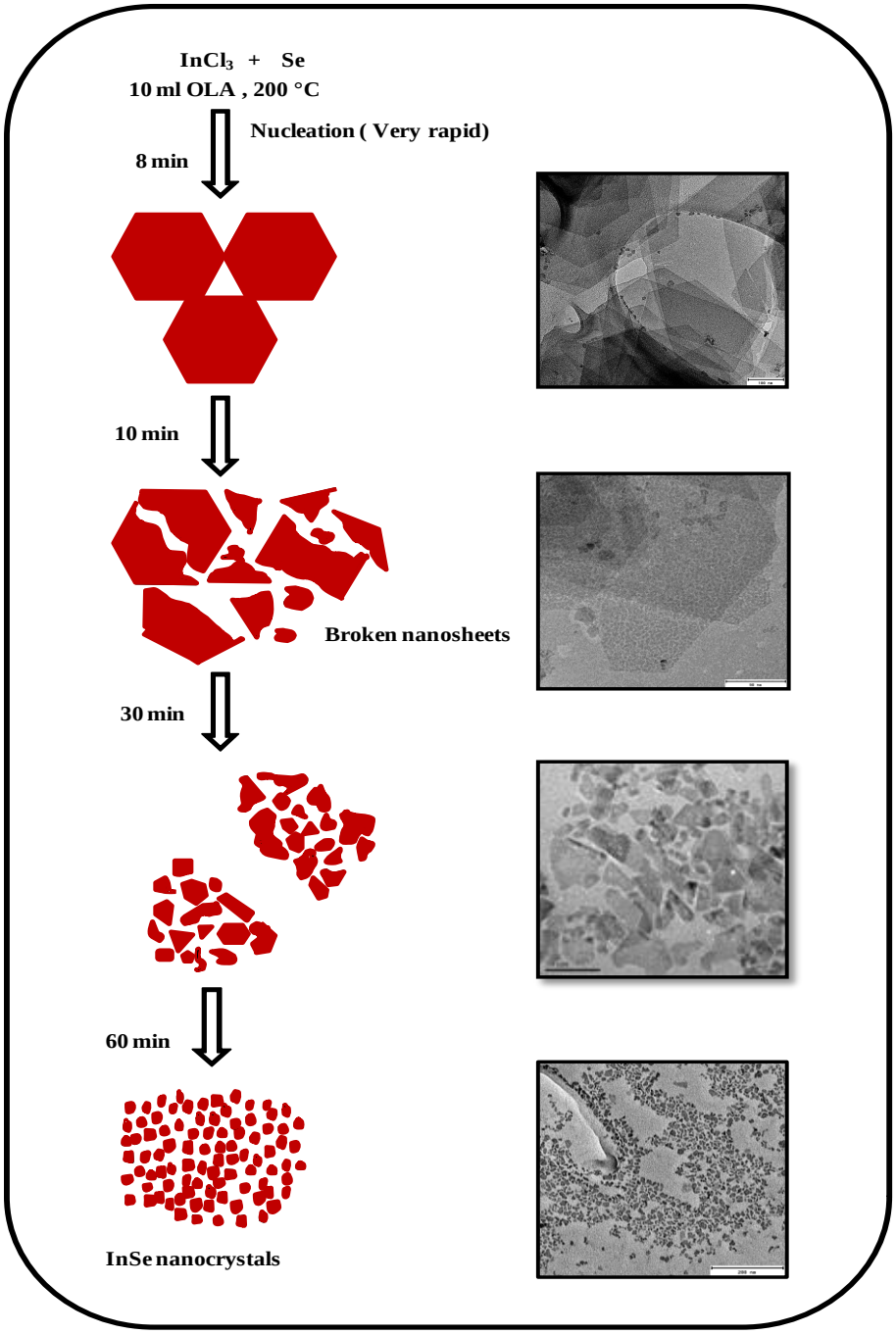

Scheme 3-2: Schematic illustration of the proposed growth mechanism for the InSe nanoparticles with the images based on TEM images obtained in the course of the 60 min synthesis.

3.7 Effect of ligand variation and time on the properties on In_xSe_y (incomplete)

Using oleylamine as both the coordinating solvent and a reducing agent in the above studies, it was evident that InSe nanosheets were formed in all the three mole ratios, 1:1, 2:1 and 3:1; though at different reaction times. Therefore in order to understand the role of oleylamine in the reaction mixture, a second ligand was introduced into the system. This experiment was also conducted in attempt to change the phase of the resulting nanostructures. Typically, 1-DDT of different volumes was used as a co-ligand together with oleylamine in the synthesis of the In_xSe_y nanocrystals and a mole ratio of 1:1 of the metal precursors (5 mM of $InCl_3$ and Se) was selected. This method was adapted from Ramasamy et al. [33]. Oleylamine alone in the reaction setup acts as both ligand and a mild reducing agent according to scheme 1 where it reduces In^{3+} to In^{2+} and selenium to Se^{2-}. Presence of 1-DDT in the reaction mixture results in the stabilization of In^{3+} ions through the formation of an In-DDT complex while the selenium was reduced by the oleylamine to Se^{2-} as depicted in scheme 3. Scheme 3 (b) elaborates the interaction of In^{3+} and Se^{2-} ions to form In_2Se_3 nanostructures.

3.7.1 50 % OLA and 50 % 1-DDT

About 5 mL of OLA and 5 mL of 1-DDT were used. For preliminary purposes, the duration of synthesis was programmed to 30 min after which the aliquots were obtained for analysis by TEM and XRD.

Fig. 3-23 presents the resulting XRD pattern and peaks were indexed to hexagonal β-In_2Se_3 according to the standard on card number JCPDS card 00-023-0294 with lattice parameters a = 7.11 Å, b = 7.11 Å and c = 19.25 Å. The peaks were well diffracted and were sharp and intense indicating that the structures had good crystallinity and slightly big sizes.

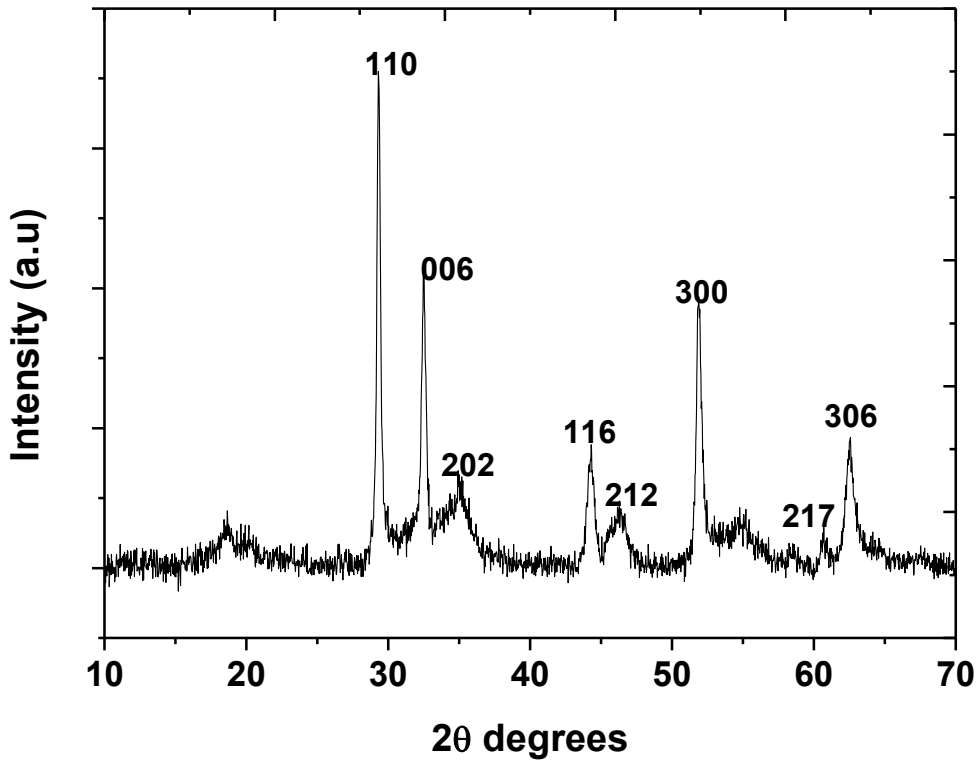

Figure 3-23: XRD pattern of In_2Se_3 nanosheets synthesized at temperature of 200 ºC with a mole ratio of 1:1 ($InCl_3$:Se) after 30 min 50 % OLA and 1-DDT.

The TEM analysis showed that this solvent ratio gave agglomerated and conically stacked rods of different sizes with traces of nanosheets as portrayed in Fig. 3-24. The agglomeration of products in this environment containing 1-DDT with 50 % oleylamine (5 ml OLA + 5 ml 1-DDT) was attributed to insufficient reducing agent to reduce the elemental selenium thus introducing impurities during the reaction hence the poor morphology.

30 min

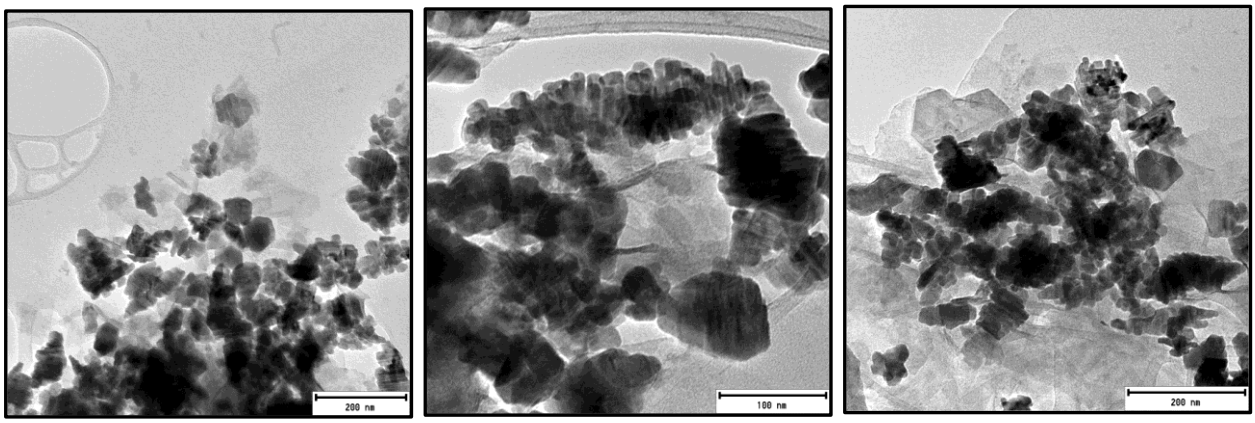

Figure 3-24: TEM images of In_2Se_3 samples synthesized at temperature of 200 ºC with a mole ratio of 1:1 ($InCl_3$:Se) for 30 min.

3.7.2 80 % OLA and 20 % 1-DDT

About 8 mL of OLA and 2 mL of 1-DDT were used for the synthesis. And aliquots were obtained after 15 min, 30 min and 60 min. This was done with the aim of improving the morphology of the nanostructures obtained in an OLA/1-DDT environment. The structural and the optical properties of the resulting products were then studied to establish the correlation with time.

The XRD pattern (Fig. 3-25) matched hexagonal In_2Se_3 (JCPDS card 00-012-0117) with lattice parameters, a = 7.11 Å, b = 7.11 Å and c = 19.3 Å. There was one peak marked with * that matched one of the peaks of In_3Se_4 phase. The observed peaks were broad and this could be indicative of the poor crystallinity or small sizes of the particles.

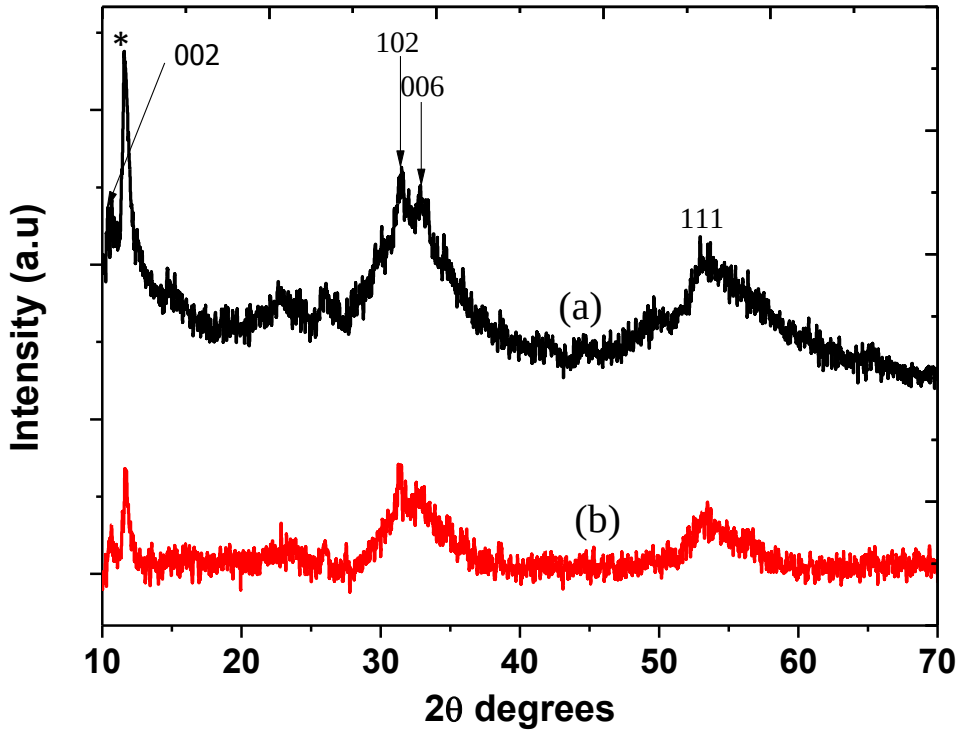

Figure 3-25: XRD patterns of InSe nanoparticles synthesized at temperature of 200 ºC with a mole ratio of 1:1 (InCl3:Se) after: (a) 10 min which gave the InSe layers, (b) 30 min and (c) 60 min.

TEM micrographs of the 15 min sample illustrated in Fig. 3-26(a – c) showed that the products were In_2Se_3 nanocables comprising of several nanowires stacked compactly together. Also evident from this sample was the possibility of orientation attachment (Fig. 3-26a) at the tips of the In_2Se_3 nanocables (possibly the reactive sites). As the time of synthesis progressed to 30 min, the nanocables begun to unwind (Fig. 3-26(d – f) resulting in very long nanowires, therefore the samples had a combination of the nanocables plus the nanowires. 60 min sample composed only the nanowires as depicted in Fig. 3-26(g–i). The nanowires are seen to be very long to the extent of folding to find space with an approximate

diameter of 5 nm. The lengthiness of the nanowires was attributed to orientation attachment of the individual nanowires at the tips.

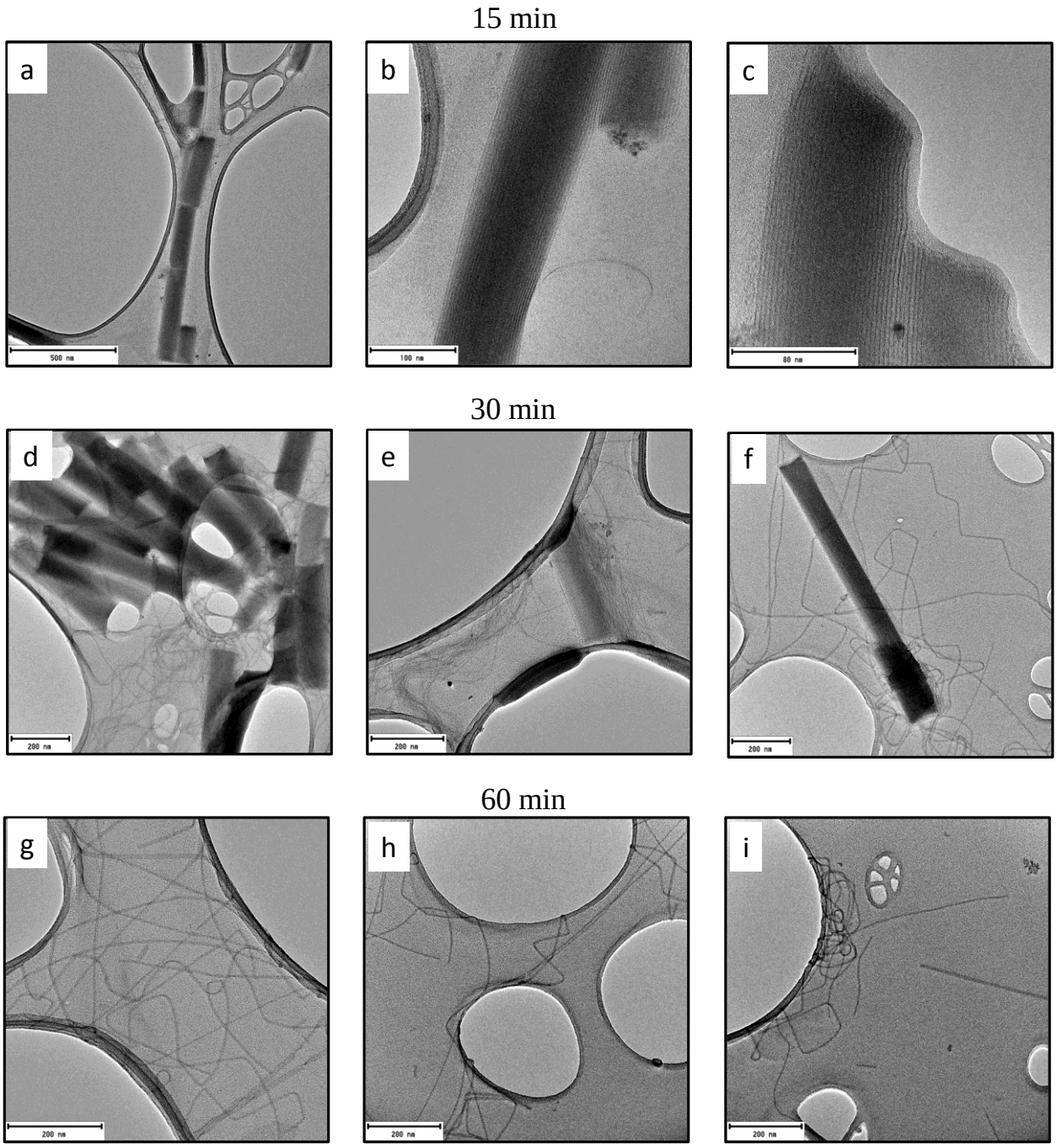

Figure 3-26: Multiple TEM images of In_2Se_3 samples synthesized at temperature of 200 ºC with a mole ratio of 1:1 ($InCl_3$:Se) after (a) 15 min, (b) 30 min and (c) 60 min 50 % OLA/1-DDT.

To further confirm the elemental composition of the nanocables and the nanowires, EDS analysis was employed. The EDS of the 15 min sample (Fig. 3-27a) and the 60 min sample (Fig. 3-27b) confirmed the elemental composition of the nanocables and nanowires to have indium and selenium. An oxygen impurity peak also appeared in both the samples.

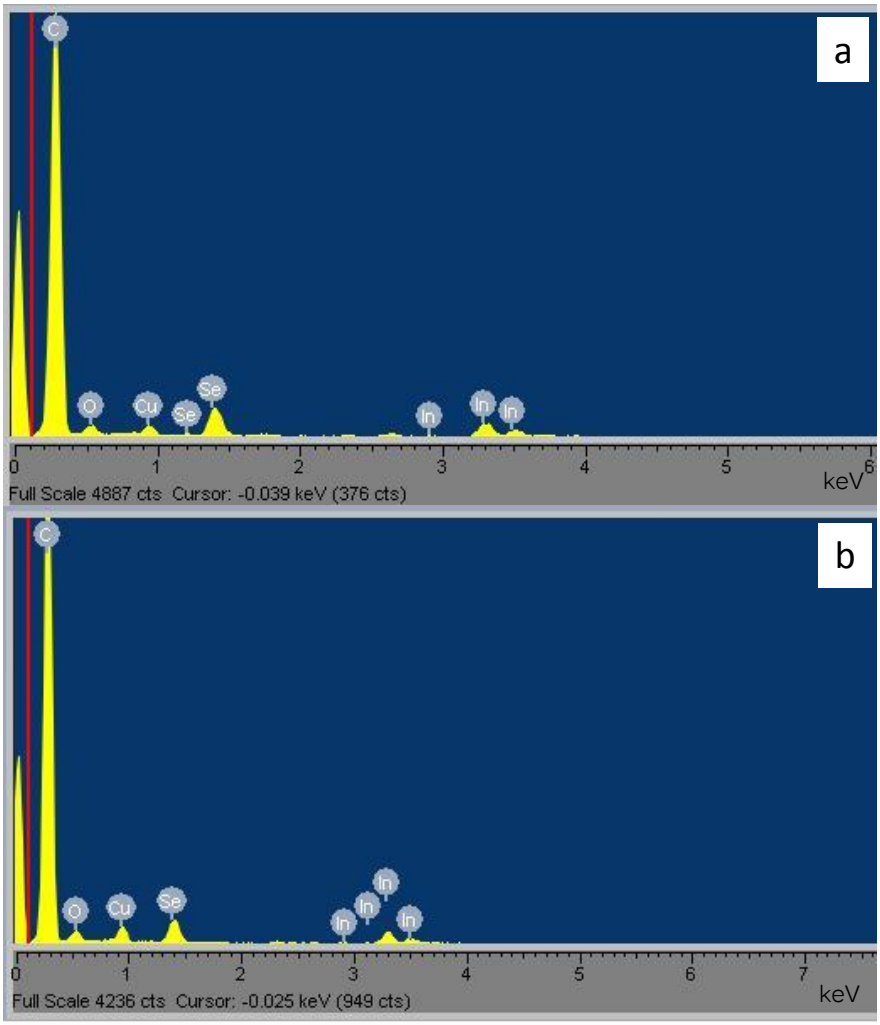

Figure 3-27: EDS spectra of the nanocables and nanowires synthesized in 80 % OLA+ 20 % 1-DDT at 200° C for (a) 15 min and (b) 30 min respectively.

The optical properties of as-prepared In_2Se_3 nanocrystals were analysed using absorption and emission spectroscopy. Fig. 3-28 portrays the absorption profile of the nanocables and the nanowires. The 15 min and the 30 min samples exhibited excitonic peaks at about 401 nm

(spectrum a) and 395 nm (spectrum b) respectively with evidence of tailing. The tailing was associated with the different morphologies that existed within the same sample as was seen from their TEM images. The 60 min sample portrayed a spectrum with a excitonic peak at about 425 nm. The nanowires had very narrow diameter however some of them were very long compared to the others; as a result their absorption spectrum exhibited the first bend for the slightly shorter nanowires while the very long ones started absorbing at about 600 nm. The emission studies of the nanocrystals were also conducted and the results are presented in Fig. 3-29. The 15 min and the 30 min samples portrayed two emission peaks centred at 492 nm and 727 nm for the 15 min sample and 477 nm and 725 nm for the 60 min sample. The stronger emission bands at 492 nm and 477 nm were associated to near band edge emission resulting from electron-hole combination while the weaker emission bands at 725 nm and 727 nm were assumed to be surface state emissions caused by defects [75] .The FWHM of these peaks are 123 nm and 121 nm respectively for the 15 min sample and 146 nm and 104 nm for the 30 min sample. This large FWHM is an indication of poly-dispersity. The 60 min sample exhibited three emission peaks at about 473 nm, 540 nm and 701 nm with FWHM of 49 nm, 65 nm and 145 nm respectively.

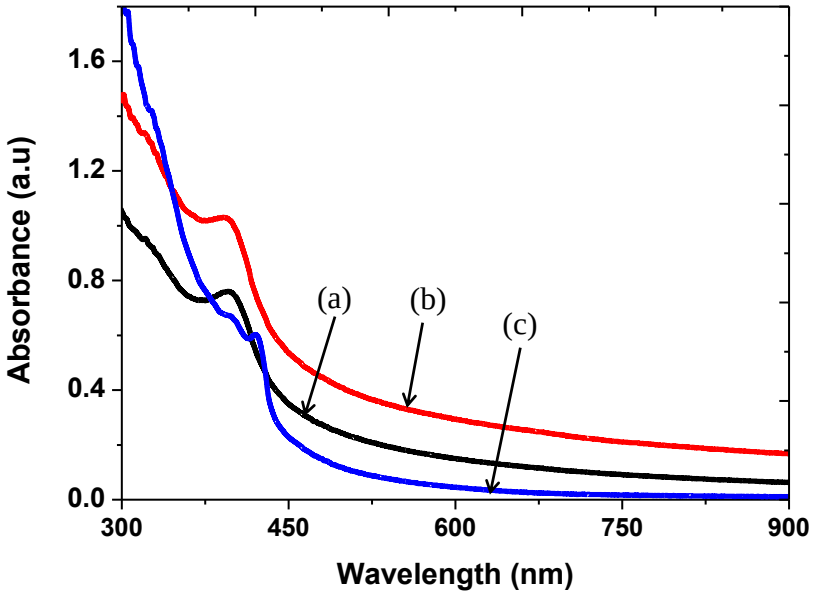

Figure 3-28: Absorption spectra of the samples obtained at (a) 15 min, (b) 30 min and (c) 60 min.

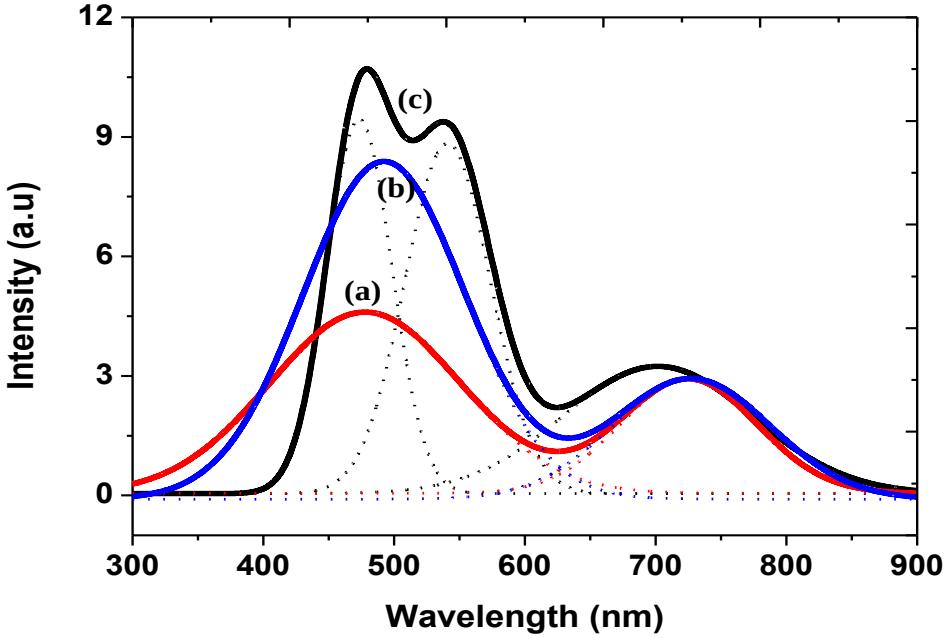

Figure 3-29: PL spectra of the In_2Se_3 nanocrystals produced in 80 % OLA + 20 % 1-DDT at 200 C for (a) 15 min, (b) 30 min and (c) 60 min.

3.8 Mechanism of formation of InSe phase and In_2Se_3 phase

Based on the above results a possible mechanism explaining the function of OLA in the formation of In_xSe_y nanocrystals is proposed. OLA has been reported to not only act as a solvent in many organic and inorganic syntheses, but also it can be a surfactant and even a mild reducing agent, depending on the reaction conditions and the nature of the target nanocrystals [76]. For example, Park et al. [77] and Chen et al. [78] used OLA as a stabilizer and a solvent during their synthesis of β-In_2S_3 at 215 °C. In other studies, the concentration of OLA as a co-ligand affected the composition and the size of the nanocrystals obtained [77]. In addition, in the presence of a stronger reducing agent, the role of OLA is limited to act as a surfactant and/or solvent [79]. In our case, when OLA is used as the sole coordinating solvent and a mild reducing agent, In^{3+} ions are reduced to In^{2+} ions and the elemental selenium reduced to Se^{2-} ions thus resulting in the formation of InSe. This is illustrated in scheme 3 and it was experienced in all the three concentration used in the formation of InSe nanosheets regardless of the amount of the In-precursor added, thus explaining the existence of one particular morphology of the obtained nanocrystals with comparable characteristics. On the other hand, the presence of 1-DDT in the reaction mixture resulted in the stabilization of the In^{3+} ions through the formation of an In–DDT complex while the selenium was reduced by the OLA to Se^{2-}. Scheme 3b elaborates the interaction of In^{3+} and Se^{2-} ions to form In_2Se_3 nanostructures. Another suggestion from the reaction environment containing 1-DDT was that 50% OLA (5 ml OLA + 5 ml 1-DDT) produced agglomerated products. This was due to the insufficient reducing agent to reduce the elemental selenium thus introducing impurities during the reaction hence the poor morphology unlike when 80% of oleylamine was used which resulted in the nanowires.

100% of Oleylamine (OLA)

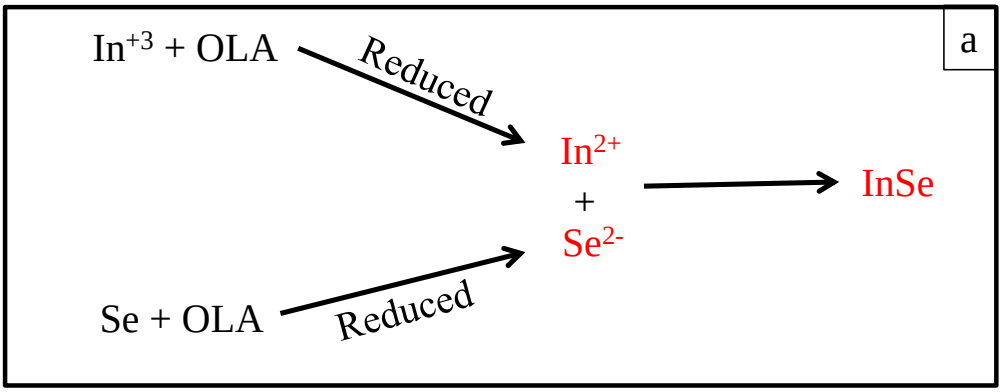

80 % OLA + 20 % 1-DDT and 50 % OLA +50 % 1-DDT

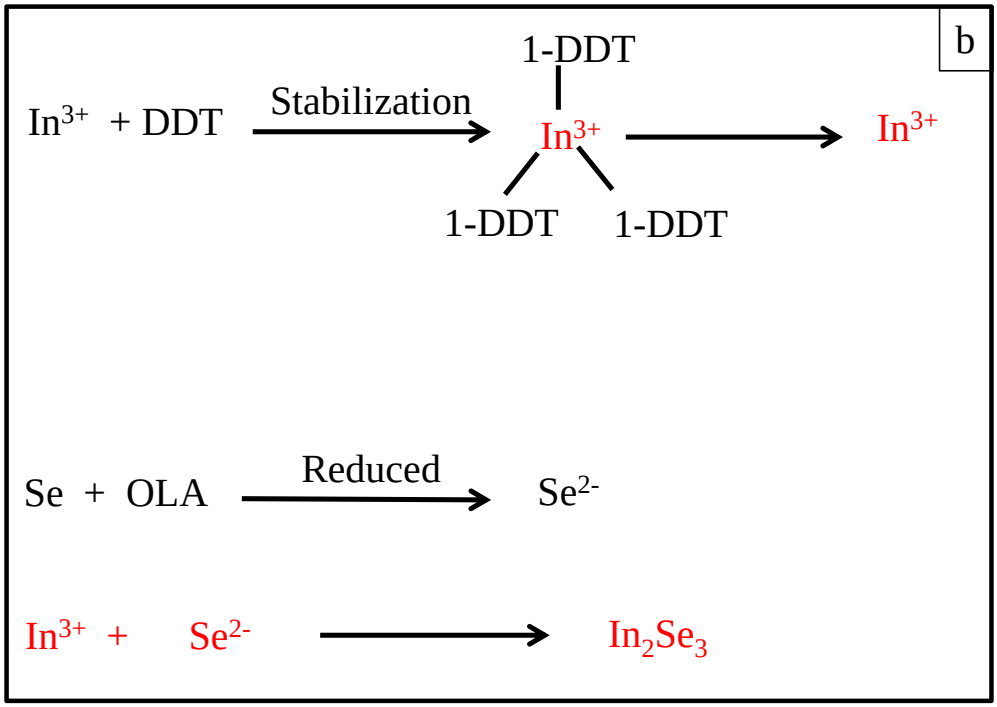

Figure 3-30: Schematic representation of (a) reduction process In^{+3} to In^{+2} and Se to Se^{-2} when 100 % oleylamine was used and (b) the stabilization process of In^{+3} ions by both 2 ml and 5 ml of 1-DDT introduced in the reaction mixture.

3.9 Conclusions

In summary, rhombohedral InSe nanocrystals were synthesized using a simple route with reaction conditions that are easy to maintain. The size of the InSe nanoparticles became smaller with the increment in the reaction time and the particles obtained were monodispersed. The growth mechanism suggested a pseudo top-down mechanism. This type of growth can allow one to choose 2D structures or 0D structures depending on the application.

Our investigations also confirmed that the formation of In_xSe_y nanocrystals is conceivable *via* a direct colloidal route. Hexagonal like InSe nanosheets were synthesized at different optimum times depending on the amount of the indium precursor. Also evident was the fact that regardless of the amount of the indium precursor used, the product remained unchanged *i.e.* InSe. This was attributed to the nature of the oleylamine capping agent. Oleylamine is known to be a reducing agent and in this case resulted in the reduction of In^{3+} to In^{2+} and elemental selenium to Se^{2-} thus always resulting in the formation of rhombohedral InSe 2D nanosheets. To consolidate this observation, a non-reducing 1-dodecanthiol co-surfactant was used. DDT which is a much softer and polarized ligand than OLA was thought to stabilize the In^{3+} ion by coordinating and forming a complex thus preserving the +3 oxidation state of indium hence resulting in the formation of the final product of In_2Se_3nanocrystals. The morphology of In_2Se_3 changed depending on the amount of OLA used. The optical properties of InSe were further evidence that 2D nanosheets had been synthesized due to the band gap crossover readily observed in 2D nanosheets.

References

[1] J. Martínez-Pastor, A. Segura, J. Valdes, A. Chevy, Electrical and photovoltaic properties of indium-tin-oxide/p-InSe/Au solar cells, Journal of applied physics, 62 (1987) 1477-1483.

[2] A. Segura, J. Guesdon, J. Besson, A. Chevy, Photoconductivity and photovoltaic effect in indium selenide, Journal of applied physics, 54 (1983) 876-888.

[3] J. Guesdon, B. Kobbi, C. Julien, M. Balkanski, Electrical and photovoltaic properties of InxSe1− x thin films, physica status solidi (a), 102 (1987) 327-335.

[4] J. Sanchez-Royo, A. Segura, O. Lang, C. Pettenkofer, W. Jaegermann, A. Chevy, L. Roa, Photovoltaic properties of indium selenide thin films prepared by van der Waals epitaxy, Thin Solid Films, 307 (1997) 283-287.

[5] A. Abdinov, A. Kyazym-Zade, Photomemory and Electromemory Phenomena in High-Resistivity n-Type InSe Single Crystals, Soviet Physics-Semiconductors, 9 (1975) 1113-1115.

[6] M.A. Contreras, A.M. Gabor, A.L. Tennant, S. Asher, J. Tuttle, R. Noufi, Accelerated publication 16.4% total-area conversion efficiency thin-film polycrystalline MgF2/ZnO/CdS/Cu (In, Ga) Se_2/Mo solar cell, Progress in Photovoltaics: Research and Applications, 2 (1994) 287-292.

[7] S. Lei, L. Ge, S. Najmaei, A. George, R. Kappera, J. Lou, M. Chhowalla, H. Yamaguchi, G. Gupta, R. Vajtai, Evolution of the electronic band structure and efficient photo-detection in atomic layers of InSe, ACS nano, 8 (2014) 1263-1272.

[8] G. Han, Z.G. Chen, J. Drennan, J. Zou, Indium selenides: structural characteristics, synthesis and their thermoelectric performances, Small, 10 (2014) 2747-2765.

[9] J.-S. Rhyee, K.H. Lee, S.M. Lee, E. Cho, S.I. Kim, E. Lee, Y.S. Kwon, J.H. Shim, G. Kotliar, Peierls distortion as a route to high thermoelectric performance in In_4Se_3-&dgr; crystals, Nature, 459 (2009) 965-968.

[10] A. Chaiken, G. Gibson, H. Lee, C. Yang, J. Wu, J. Ager, K. Yu, W. Walukiewicz, Structural and electronic properties of amorphous and polycrystalline In_2Se_3 films, Journal of Applied Physics, 94 (2003) 2390-2397.

[11] W. Jaegermann, A. Klein, C. Pettenkofer, Electronic properties of van der Waals-epitaxy films and interfaces, in: Electron Spectroscopies Applied to Low-Dimensional Materials, Springer, 2002, pp. 317-402.

[12] T. Zhai, X. Fang, M. Liao, X. Xu, L. Li, B. Liu, Y. Koide, Y. Ma, J. Yao, Y. Bando, Fabrication of high-quality In_2Se_3 nanowire arrays toward high-performance visible-light photodetectors, ACS Nano, 4 (2010) 1596-1602.

[13] C. Julien, E. Hatzikraniotis, A. Chevy, K. Kambas, Electrical behavior of Lithium intercalated layered In-Se compounds, Materials Research Bulletin, 20 (1985) 287-292.

[14] C. Julien, A. Khelfa, N. Benramdane, J. Guesdon, Preparation and characterization of In_4Se_3 films, Materials Science and Engineering: B, 27 (1994) 53-60.

[15] S. Marsillac, J. Bernede, A. Conan, Change in the type of majority carriers in disordered ln_xSe_{100-x} thin-film alloys, Journal of Materials Science, 31 (1996) 581-587.

[16] X. Yu, T. Hou, X. Sun, Y. Li, Atomistic structures and phase transition of In_2Se_3 nanowires studied by DFT calculations and synchrotron radiation X-ray diffraction, Solid State Communications, 162 (2013) 28-33.

[17] T. Ohtsuka, K. Nakanishi, T. Okamoto, A. Yamada, M. Konagai, U. Jahn, Epitaxial growth of γ-In_2Se_3 films by molecular beam epitaxy, Japanese Journal of Applied Physics, 40 (2001) 509.

[18] M. Eddrief, C. Julien, M. Balkanski, K. Kambas, Optimization of growth conditions for In_2Se_3 films, Materials Letters, 2 (1984) 432-436.

[19] C. Amory, J. Bernede, S. Marsillac, Study of a Growth Instability of γ-In_2Se_3, Journal of Applied Physics, 94 (2003) 6945-6948.

[20] X. Sun, B. Yu, G. Ng, T.D. Nguyen, M. Meyyappan, III-VI compound semiconductor indium selenide (In2Se3) nanowires: Synthesis and characterization, Applied Physics Letters, 89 (2006) 233121.

[21] T. Ohtsuka, T. Okamoto, A. Yamada, M. Konagai, Molecular Beam Epitaxy and Characterization of Layered In2Se3 Films Grown on Slightly Misoriented (001) GaAs Substrates, Japanese Journal of Applied Physics, 38 (1999) 668.

[22] T. Okamoto, A. Yamada, M. Konagai, Growth and characterization of In_2Se_3 epitaxial films by molecular beam epitaxy, Journal of crystal growth, 175 (1997) 1045-1050.

[23] J. Ye, S. Soeda, Y. Nakamura, O. Nittono, Crystal structures and phase transformation in In2Se3 compound semiconductor, Japanese Journal of Applied Physics, 37 (1998) 4264.

[24] J. Ye, T. Yoshida, Y. Nakamura, O. Nittono, Optical activity in the vacancy ordered III2VI3 compound semiconductor (Ga0. 3In0. 7) 2Se3, Applied Physics Letters, 67 (1995) 3066-3068.

[25] S. Lakshmikumar, A. Rastogi, Selenization of Cu and In thin films for the preparation of selenide photo-absorber layers in solar cells using Se vapour source, Solar Energy Materials and Solar Cells, 32 (1994) 7-19.

[26] M. Kenawy, H. Zayed, A.A. El-Soud, Ac photoconductivity and optical properties of bulk polycrystalline and amorphous In_xSe_{1-x} thin films, Journal of Materials Science: Materials in Electronics, 1 (1990) 115-117.

[27] P.G. da Costa, M. Balkanski, R. Wallis, Effect of intercalated lithium on the electronic band structure of indium selenide, Physical Review B, 43 (1991) 7066.

[28] B. Yu, S. Ju, X. Sun, G. Ng, T.D. Nguyen, M. Meyyappan, D.B. Janes, Indium selenide nanowire phase-change memory, Applied Physics Letters, 91 (2007) 133119.

[29] S. Xuhui, Y. Bin, G. Ng, M. Meyyappan, J. Sanghyun, D. Janes, Electron Devices, IEEE Transactions on, 55 (2008) 3131-3135.

[30] S. Meister, H. Peng, K. McIlwrath, K. Jarausch, X.F. Zhang, Y. Cui, Synthesis and characterization of phase-change nanowires, Nano Letters, 6 (2006) 1514-1517.

[31] V. Koshkin, L. Gal'chinetskii, V. Kulik, B. Minkov, U. Ulmanis, Unstable equilibrium and radiation defects in solids, Solid State Communications, 13 (1973) 1-4.

[32] Y.B. Losovyj, L. Makinistian, E. Albanesi, A. Petukhov, J. Liu, P. Galiy, O. Dveriy, P. Dowben, The anisotropic band structure of layered In_4Se_3 (001), Journal of applied physics, 104 (2008) 083713.

[33] O. Balitskii, V. Savchyn, B. Jaeckel, W. Jaegermann, Surface characterization of In_4Se_3 single crystals, Physica E: Low-dimensional Systems and Nanostructures, 22 (2004) 921-923.

[34] J. Hogg, H. Sutherland, D. Williams, The crystal structure of tetraindium triselenide, Acta Crystallographica Section B: Structural Crystallography and Crystal Chemistry, 29 (1973) 1590-1593.

[35] S. Popović, A. Tonejc, B. Gržeta-Plenković, B. Čelustka, R. Trojko, Revised and new crystal data for indium selenides, Journal of Applied Crystallography, 12 (1979) 416-420.

[36] B. Celustka, S. Popovic, Synthesis of In_5Se_6 and In_2Se From InSe by Zone-Melting Process, J. Physics Chem. Solids, 35 (1974) 287-289.

[37] C. Levy-Clement, J. Rioux, J. Dahn, W. McKinnon, In-situ X-ray characterisation of the reaction of lithium with InSe, Materials Research Bulletin, 19 (1984) 1629-1634.

[38] G.W. Mudd, S.A. Svatek, T. Ren, A. Patanè, O. Makarovsky, L. Eaves, P.H. Beton, Z.D. Kovalyuk, G.V. Lashkarev, Z.R. Kudrynskyi, Tuning the bandgap of exfoliated InSe nanosheets by quantum confinement, Advanced Materials, 25 (2013) 5714-5718.

[39] S.R. Tamalampudi, Y.-Y. Lu, R. Kumar U, R. Sankar, C.-D. Liao, K. Moorthy B, C.-H. Cheng, F.C. Chou, Y.-T. Chen, High performance and bendable few-layered InSe photodetectors with broad spectral response, Nano Letters, 14 (2014) 2800-2806.

[40] J. Hogg, The crystal structure of In6Se7, Acta Crystallographica Section B: Structural Crystallography and Crystal Chemistry, 27 (1971) 1630-1634.

[41] A. Onys'kiv, Y.M. Orishchin, V. Savchin, Electronic properties of indium monoselenide and subselenide films, Soviet Physics--Semiconductors(English Translation), 24 (1990) 264-266.

[42] D. Lyu, T. Lin, J. Lin, S. Tseng, J. Hwang, H. Chiang, C. Chiang, S. Lan, Growth and properties of single-phase γ-In 2 Se 3 thin films on (111) Si substrate by AP-MOCVD using H 2 Se precursor, Solar Energy Materials and Solar cells, 91 (2007) 888-891.

[43] K. Chang, S. Lahn, J. Chang, Growth of single-phase In2Se3 by using metal organic chemical vapor deposition with dual-source precursors, Applied Physics Letters, 89 (2006) 2118.

[44] Y.-C. Huang, Z.-Y. Li, W.-Y. Uen, S.-M. Lan, K. Chang, Z.-J. Xie, J. Chang, S.-C. Wang, J.-L. Shen, Growth of γ-In 2 Se 3 films on Si substrates by metal-organic chemical

vapor deposition with different temperatures, Journal of Crystal Growth, 310 (2008) 1679-1685.

[45] C.-H. Ho, Y.-C. Chen, Thickness-tunable band gap modulation in γ-In_2Se_3, RSC Advances, 3 (2013) 24896-24899.

[46] T. Kato, T. Hiramatsu, N. Onojima, Growth of γ-In2Se3 Thin Films by Electrostatic Spray Pyrolysis Deposition, Japanese Journal of Applied Physics, 50 (2011) 05FB11.

[47] H. Peng, D.T. Schoen, S. Meister, X.F. Zhang, Y. Cui, Synthesis and phase transformation of In_2Se_3 and $CuInSe_2$ nanowires, Journal of the American Chemical Society, 129 (2007) 34-35.

[48] Y. Li, J. Gao, Q. Li, M. Peng, X. Sun, Y. Li, G. Yuan, W. Wen, M. Meyyappan, Thermal phase transformation of In_2Se_3 nanowires studied by in situ synchrotron radiation X-ray diffraction, Journal of Materials Chemistry, 21 (2011) 6944-6947.

[49] G.P. Vassilev, B. Daouchi, M.-C. Record, J.-C. Tedenac, Thermodynamic studies of the In–Se system, Journal of Alloys and Compounds, 269 (1998) 107-115.

[50] X. Tan, J. Zhou, Q. Yang, Ascorbic acid-assisted solvothermal growth of γ-In 2 Se 3 hierarchical flowerlike architectures, CrystEngComm, 13 (2011) 2792-2798.

[51] J. Tabernor, P. Christian, P. O'Brien, A general route to nanodimensional powders of indium chalcogenides, Journal of Materials Chemistry, 16 (2006) 2082-2087.

[52] M. áAzad Malik, P. áO'Brien, Novel single-molecule precursor routes for the direct synthesis of InS and InSe quantum dots, Journal of Materials Chemistry, 9 (1999) 2885-2888.

[53] S. Yang, D.F. Kelley, The spectroscopy of InSe nanoparticles, The Journal of Physical Chemistry B, 109 (2005) 12701-12709.

[54] N.M. Dimitrijevic, P.V. Kamat, Formation and corrosion processes of colloidal indium sesquiselenide, Langmuir, 3 (1987) 1004-1009.

[55] R. Sreekumar, R. Jayakrishnan, C.S. Kartha, K. Vijayakumar, S. Khan, D. Avasthi, Enhancement of band gap and photoconductivity in gamma indium selenide due to swift heavy ion irradiation, Journal of Applied Physics, 103 (2008) 023709.

[56] N. Moloto, M.J. Moloto, N.J. Coville, S.S. Ray, Synthesis and characterization of nickel selenide nanoparticles: size and shape determining parameters, Journal of Crystal Growth, 324 (2011) 41-52.

[57] Y. Mastai, R. Polsky, Y. Koltypin, A. Gedanken, G. Hodes, Pulsed sonoelectrochemical synthesis of cadmium selenide nanoparticles, Journal of the American Chemical Society, 121 (1999) 10047-10052.

[58] N.L. Pickett, P. O'Brien, Syntheses of semiconductor nanoparticles using single-molecular precursors, The Chemical Record, 1 (2001) 467-479.

[59] X. Peng, L. Manna, W. Yang, J. Wickham, E. Scher, A. Kadavanich, A.P. Alivisatos, Shape control of CdSe nanocrystals, Nature, 404 (2000) 59-61.

[60] Y. Lin, J.W. Connell, Advances in 2D boron nitride nanostructures: nanosheets, nanoribbons, nanomeshes, and hybrids with graphene, Nanoscale, 4 (2012) 6908-6939.

[61] X. Huang, Z. Zeng, H. Zhang, Metal dichalcogenide nanosheets: preparation, properties and applications, Chemical Society Reviews, 42 (2013) 1934-1946.

[62] A. Zandiatashbar, G.-H. Lee, S.J. An, S. Lee, N. Mathew, M. Terrones, T. Hayashi, C.R. Picu, J. Hone, N. Koratkar, Effect of defects on the intrinsic strength and stiffness of graphene, Nature Communications, 5 (2014).

[63] M. Osada, T. Sasaki, Chemical nanomanipulation of two-dimensional nanosheets and its applications, INTECH Open Access Publisher, 2011.

[64] A. Segura, J. Bouvier, M. Andrés, F. Manjón, V. Munoz, Strong optical nonlinearities in gallium and indium selenides related to inter-valence-band transitions induced by light pulses, Physical Review B, 56 (1997) 4075.

[65] P. Hu, Z. Wen, L. Wang, P. Tan, K. Xiao, Synthesis of few-layer GaSe nanosheets for high performance photodetectors, ACS Nano, 6 (2012) 5988-5994.

[66] S. Tongay, J. Zhou, C. Ataca, K. Lo, T.S. Matthews, J. Li, J.C. Grossman, J. Wu, Thermally driven crossover from indirect toward direct bandgap in 2D semiconductors: $MoSe_2$ versus MoS_2, Nano Letters, 12 (2012) 5576-5580.

[67] J. Rigoult, A. Rimsky, A. Kuhn, Refinement of the 3R γ-indium monoselenide structure type, Acta Crystallographica Section B: Structural Crystallography and Crystal Chemistry, 36 (1980) 916-918.

[68] Z. Li, X. Peng, Size/shape-controlled synthesis of colloidal CdSe quantum disks: ligand and temperature effects, Journal of the American Chemical Society, 133 (2011) 6578-6586.

[69] J.S. Son, J.H. Yu, S.G. Kwon, J. Lee, J. Joo, T. Hyeon, Colloidal Synthesis of Ultrathin Two-Dimensional Semiconductor Nanocrystals, Advanced Materials, 23 (2011) 3214-3219.

[70] K.D. Oyler, X. Ke, I.T. Sines, P. Schiffer, R.E. Schaak, Chemical Synthesis of Two-Dimensional Iron Chalcogenide Nanosheets: FeSe, FeTe, Fe (Se, Te), and $FeTe_2$, Chemistry of Materials, 21 (2009) 3655-3661.

[71] W. Lu, Y. Ding, Y. Chen, Z.L. Wang, J. Fang, Bismuth telluride hexagonal nanoplatelets and their two-step epitaxial growth, Journal of the American Chemical Society, 127 (2005) 10112-10116.

[72] G. Zhang, W. Wang, X. Lu, X. Li, Solvothermal Synthesis of V− VI Binary and Ternary Hexagonal Platelets: The Oriented Attachment Mechanism, Crystal Growth and Design, 9 (2008) 145-150.

[73] Y. Zhirko, V. Trachevsky, Z. Kovalyuk, On the Possibility of Layered Crystals Application for Solid State Hydrogen Storages-InSe and GaSe Crystals, INTECH Open Access Publisher, 2012.

[74] V.K. LaMer, R.H. Dinegar, Theory, production and mechanism of formation of monodispersed hydrosols, Journal of the American Chemical Society, 72 (1950) 4847-4854.

[75] W.J. Mir, A. Swarnkar, R. Sharma, A. Katti, K. Adarsh, A. Nag, Origin of Unusual Excitonic Absorption and Emission from Colloidal Ag2S Nanocrystals: Ultrafast Photophysics and Solar Cell, The Journal of Physical Chemistry Letters, 6 (2015) 3915-3922.

[76] S. Mourdikoudis, L.M. Liz-Marzán, Oleylamine in nanoparticle synthesis, Chemistry of Materials, 25 (2013) 1465-1476.

[77] K.H. Park, K. Jang, S.U. Son, Synthesis, Optical Properties, and Self-Assembly of Ultrathin Hexagonal In2S3 Nanoplates, Angewandte Chemie International Edition, 45 (2006) 4608-4612.

[78] B. Chen, S. Chang, D. Li, L. Chen, Y. Wang, T. Chen, B. Zou, H. Zhong, A.L. Rogach, Template Synthesis of $CuInS_2$ Nanocrystals from In_2S_3 Nanoplates and Their Application as Counter Electrodes in Dye-Sensitized Solar Cells, Chemistry of Materials, 27 (2015) 5949-5956.

[79] J. Joo, H.B. Na, T. Yu, J.H. Yu, Y.W. Kim, F. Wu, J.Z. Zhang, T. Hyeon, Generalized and facile synthesis of semiconducting metal sulfide nanocrystals, Journal of the American Chemical Society, 125 (2003) 11100-11105.

Chapter 4 : Applications of indium selenide nanocrystal in chemical sensors for detection of volatile organic compounds.

4.1 Background

4.1.1 Definition and sources of VOCs

Volatile organic compounds (VOCs) are a large group of carbon based chemicals that easily evaporate at room temperature [1]. The chemicals produced by these VOCs may have short and long term adverse health effects. Most exposure to these VOCs occurs indoors as a result of numerous indoor emission sources, poor ventilation and the time spent in a particular building [2]. Examples of household products (which in turn become sources of VOCs) that contain organic chemicals as ingredients include paints, varnishes, wax, and many cleaning agents, disinfectants, cosmetics and degreasing products. Furniture, floor and wall coverings among other building products also outgas VOCs. In addition, Africa as a whole depends on fuel to drive most of their industrial and domestic process and these fuels are made up of organic chemicals. All these products can release organic compounds while in use them and to some degree, when they are stored. Therefore the concentrations of the VOCs are consistently higher (up to ten times higher) indoors than outdoors [3] as a result a sensor that would facilitate in detecting and controlling the indoor and outdoor pollutants is of essence.

4.1.2 Importance of formaldehyde detection

Formaldehyde, is one of the examples of VOCs that has been reported to have harmful effects [4]. It is widely used in It is used in the production of fertilizer, paper, plywood, and urea-formaldehyde resins. It is present in the air in iron foundries. It is also used in the production of cosmetics like nail polish and sugar, in well-drilling fluids, in agriculture as a preservative for grains and seed dressings, in the rubber industry in the production of latex, in leather tanning, in wood preservation, and in photographic film production. Formaldehyde is

combined with methanol and buffers to make embalming fluid. Formaldehyde is also used in many hospitals and laboratories to preserve tissue specimens. Therefore, human beings as such interact with it in most occasions [5]. Formaldehyde has been established as a probable human carcinogen and allergenic. It is also known to cause the sick building syndrome and an intense irritant of the eyes and mucous membranes. Therefore HCHO is highly problematic as an indoor pollutant. Consequently, the World Health Organization (WHO) has set a standard for 30 min exposure limit of 0.08 ppm (*Air Quality Guidelines*, 2nd ed.; WHO Regional Office for Europe: Copenhagen, Denmark, 2001), OSHA has set the permissible exposure level (PEL) to 0.75 ppm and the immediately dangerous to life or health (IDLH) level at 20 ppm, and the US National Institute for Occupational Safety and Health (NIOSH) has established a maximum long-term exposure limit of 0.016 ppm (TWA) [6]. Therefore the demand for continuous and real time monitoring of formaldehyde at very low concentration is critical and increasing in both living environment and industries. At present, numerous methods for detecting and measuring gaseous formaldehyde exist. Detection using semiconductor metal oxide as their detection portion has considerable impact to date owing to their advantages of their robust nature, their weak sensitivity to moisture and temperature influence, simple electronic interface, quick response and recovery time [7]. However, these type of sensors need to operate at higher temperatures ranging between 150 °C - 350 °C, thus often limiting their detection capability. In addition the available gas sensors in the market are quite expensive and have reduced sensitivity with respect to low concentration, selectivity, reversibility in specified temperature conditions and long term stability. As a result, there remains a need to improve the response, selectivity, stability and the working temperature of the sensors.

4.1.3 Use of nanostructures to improve the performance of chemical sensors

The improvement in the performance of a sensor is in particular dependent on the properties of the sensing materials [8]. Semiconductor nanostructures compared to their bulk counterpart have been reported to possess unique and novel characteristics and offer large surface area to volume ratios which is advantageous to electron transport and gas diffusion, thus leading to enhanced sensing performance. Nanostructured materials including semiconductor nanocrystals used as sensor building materials offer novel and advanced properties as a result of their finite size effect and the enhanced density of structural imperfections [9]; thus providing a promising route of improving the device performance as they would dramatically change the operating characteristics of chemical sensors. Several nanometric materials have attracted attention in the sensing field. Among them, several sensors based on thin films of organic polymers, metal oxide nanoparticles and most recently carbon nanotubes and related composites have been explored [10]. In addition high quality colloidal semiconducting nanocrystals (metal sulphides and selenides) are also gaining mileage in this area. A considerable amount of work has been done on the application of colloidal nanocrystals in optical sensors, though not as much work as their counterparts produced via gas phase techniques [11]. This is because high-quality colloidal semiconductor nanocrystals (NCs) are generally coated by a dense monolayer of organic ligands whose sole purpose is to reduce agglomeration of the nanocrystals that is bound to happen as a result of increased van der Waal attraction due to reduction in dimensionality of the nanocrystals. The monolayer of organic ligand covering the nanocrystal act as a substantial barrier for the diffusion of gas molecules between the environment and the surface of the NCs, thus compromising the sensing ability of these nanocrystals. Despite this major drawback, colloidal nanostructures have presented enormous potential for investigation in sensing technologies due to their various types of structures and tunable electro-optical properties and

their ability to be sensitive to their surrounding environment. A slight change in the ambient may result in a change in their electro-optical properties, a characteristic which can be exploited for the development of sensing technologies [12-14].

Herein we focus on indium monoselenide obtained via colloidal synthesis. InSe has attracted substantial attention as a semiconductor material. It has shown potential in many applications such as optoelectronic devices [15], solar energy conversion [16] and Li ion batteries [17] due to its appealing optical properties, tunable electronic properties under different conditions [18, 19] and good transport properties [20, 21]. Nanostructuring has been reported to transform the above bulk properties of InSe to completely new physical phenomena without changing the chemical composition thus expanding its applicability in device architecture [22]. Lei et al. studied the effect of reducing the number of layers on the optical properties of InSe. They deduced that a few layered material gave a good photo-response in their photodetectors producing a photo-responsivity of 34.7 mA/W and fast response time of 488 μs [15]. Sánchez-Royo et al. also managed to tune the dimensionality of the lattice dynamics and electronic properties of atomically thin InSe flakes via gradual enhancement of quantum size confinement [23]. For our studies, we synthesized InSe nanostructures via the colloidal route to enable us to have control on the morphology and reduction in dimensionality. The studies on the properties of the InSe nanosheets and nanoparticles obtained indicated a difference in the optical properties. This suggested that the distribution of the density of state was dependent on the shape and size of the InSe nanostructure. To provide an intuition on their electronic properties, investigation on their chemical sensing ability was done. Sensors based on the nanostructures were exposed to methanol and formaldehyde fumes and variation on the conductance and capacitance were studied.

4.1 Experimental procedures

4.1.1 Chemicals and materials

Indium (III) chloride, 99 % selenium powder, 70 % oleylamine (OLA), chloroform and 96 % ethanol, 99.9 % methanol (MeOH), 37 % formaldehyde (HCHO) solution, 99.9 % acetone, 98 % isopropyl alcohol and distilled water were used as purchased from Sigma Aldrich. Interdigitated electrodes of ENIG (Electroless Nickel Immersion Gold) with a gap of 0.1 mm between electrode strips and a FR4 epoxy resin/fiber glass board were supplied by Micropress SA.

4.2.2 Device fabrication and characterization

About 5 mg of indium selenide nanopowders synthesized and characterized in chapter 3 were dispersed in 2 mL of chloroform by ultra-sonication for 20 min at room temperature. The substrates were cleaned sequentially in acetone, deionized water and isopropyl alcohol using sonication for 20 min each step. The substrates were then allowed to dry by air blowing. The sensors devices were prepared by dropping 20 µL on the active area of the interdigitated electrodes and then the device was allowed to dry overnight in vacuum at 120 °C. The surfaces of the formed thin films were characterized by SEM analysis using an FEI Nova Nanolab 600 FIB/SEM instrument operating at 30 kV. Thereafter the sensors were exposed to different concentrations of the analyte vapours of methanol and formaldehyde using the procedure described by Greenshields et al. [24]. For the record, the HCHO used herein contained 10 % MeOH for its stabilization. Therefore, MeOH studies were also done to confirm that it did not have much impact on the HCHO detection. Typically, the measurements of conductance and capacitance were done in the dark using an Agilent 4284A LCR meter at an AC input signal with amplitude of 0.5 V and a frequency of 5 kHz. The analytes were dropped at varied volumes using a micropipette into a sealed glass chamber

with a volume of 2.4 L (sketch shown in Scheme. 4-1) changing the vapour concentration inside the chamber. For complete evaporation of the analytes into vapours, the measurements were started 5 min after dropping the analyte into the chamber. The sensor exposure was switched between ambient air (outside the chamber) and analyte gas environment (inside the chamber) for 300 s and the change in the device conductance was monitored at room temperature. In the course of the measurements, the sensor was initially exposed to the ambient for 60 s to obtain a baseline, then placed inside the glass chamber with the analyte vapour for 140 s and finally taken back to the ambient for the last 100 s to allow sensor recovery.

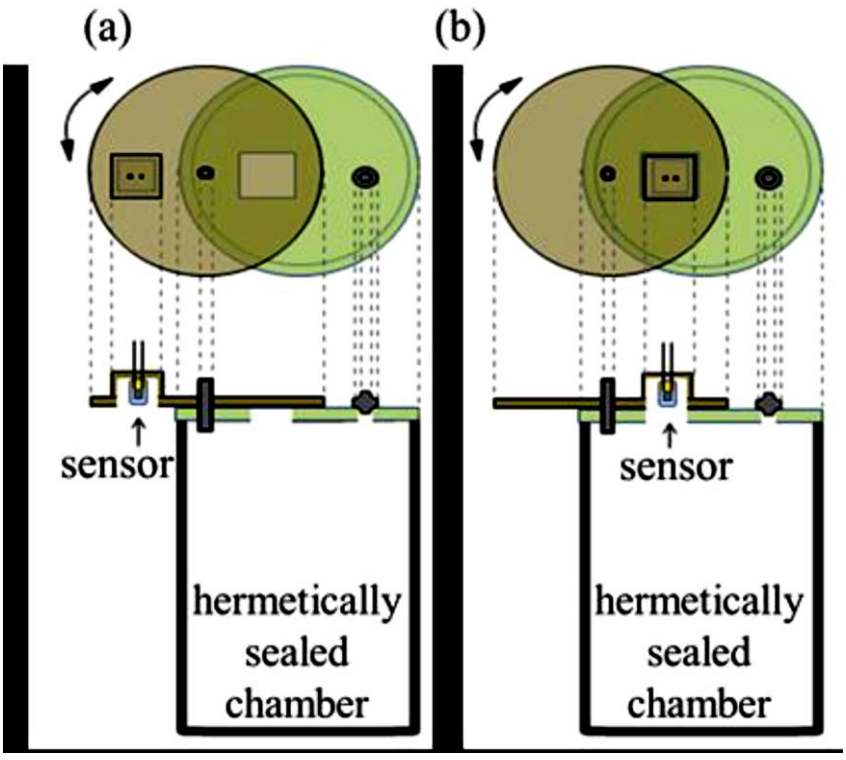

Scheme 4-1: Sealable chamber for dynamic measurements rotating the cap 180° to expose the sensor from (a) ambient air to (b) the environment containing the VOC.

4.3 Results and Discussions

Two morphologies of the InSe nanocrystals were used in the device fabrication. Fig. 4-1 (a) and (b) are TEM images of the InSe while (c) and (d) are the SEM micrographs of the InSe nanoparticles and nanosheets films respectively.

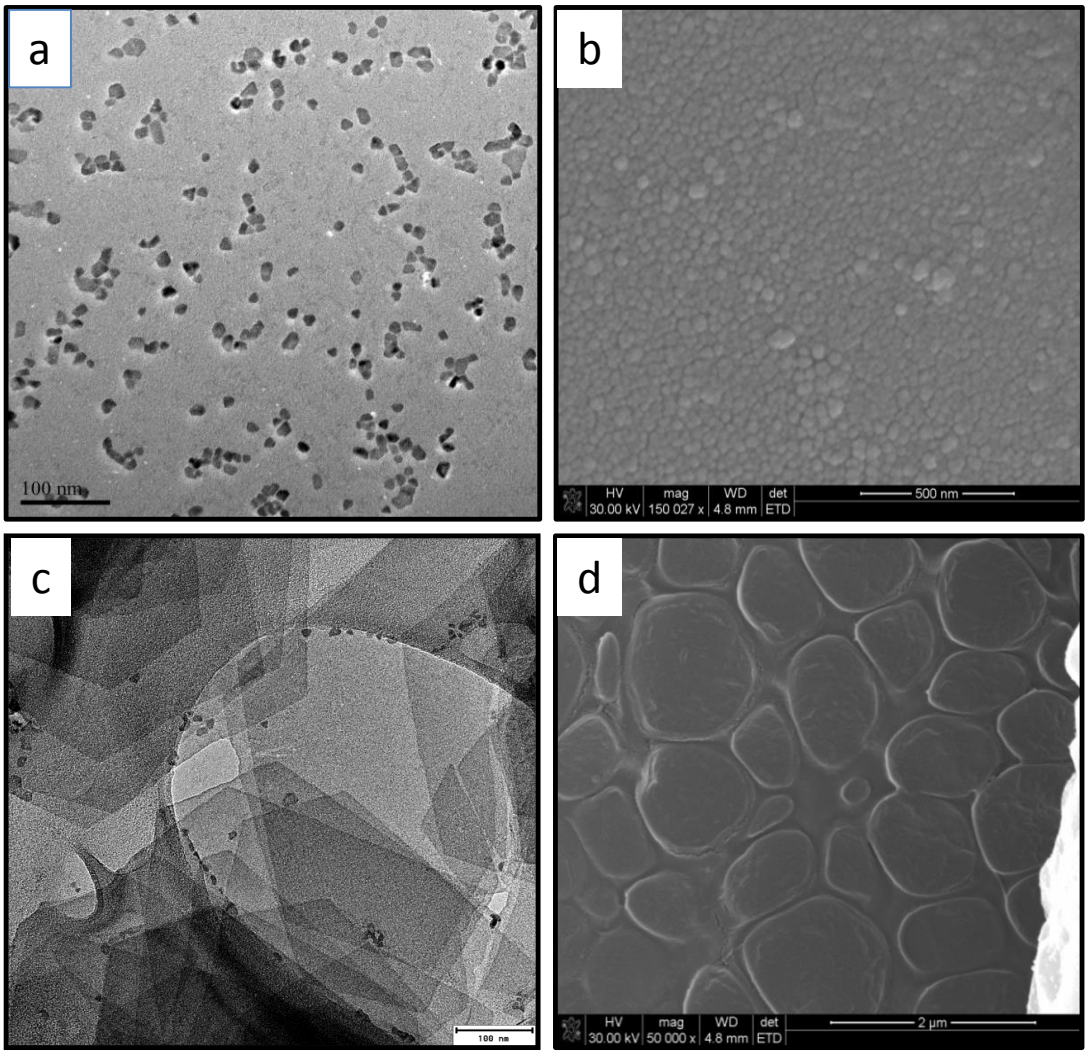

Figure 4-1: TEM images of InSe (a) nanoparticle and (b) nanosheets used in the device fabrication while (c) is the film of the nanoparticles and (d) is the film of the nanosheets based sensors.

Among the basic electrochemical parameters that can yield sensory information is the conductance of the electrochemical cell. Conductance is the reciprocal of resistance [25]. It is related to current and potential through the generalized form of Ohm's law. If the measurement is done with AC signal, conductance (G) becomes frequency-dependent $G(\omega)$ and the resistance R becomes impedance $Z(\omega)$ [25].

$$G(\omega) = I(\omega)/E(\omega) \quad \ldots\ldots\ldots\ldots\ldots\ldots\ldots\ldots\ldots\ldots\ldots\ldots\ldots\ldots \quad (4\text{-}1)$$

Therefore, a study to determine the working frequency range was conducted for both sensors fabricated using InSe nanoparticles and the nanosheets. During this study, the sensors response in air, in the presence of HCOH fumes and MeOH fumes were compared and the results are presented in Fig. 4-2. The nanoparticle based sensor gave an insight that the sensor could work best at high frequency ranges as shown in Fig. 4-2a. This is because there was a distinct difference between the three ambient at high frequencies. In addition Fig. 4-2b shows capacitance versus frequency plot of the devices. It was seen that the capacitance initially fell sharply as the frequency increased and then saturated to some value as the frequency approached 5 kHz. When the same study was done on the nanosheet based sensors, there was an indication that the device was sensing (Fig. 4-2c), however the noise to signal ratio was as high as shown in Fig. 4-2d. As a result, the device with the nanoparticles was used to determine the operation frequencies. A few experiments at high frequencies (above 5 kHz) gave a very high to noise ratio. Therefore a frequency of 5 kHz was decided upon for all the measurements done herein.

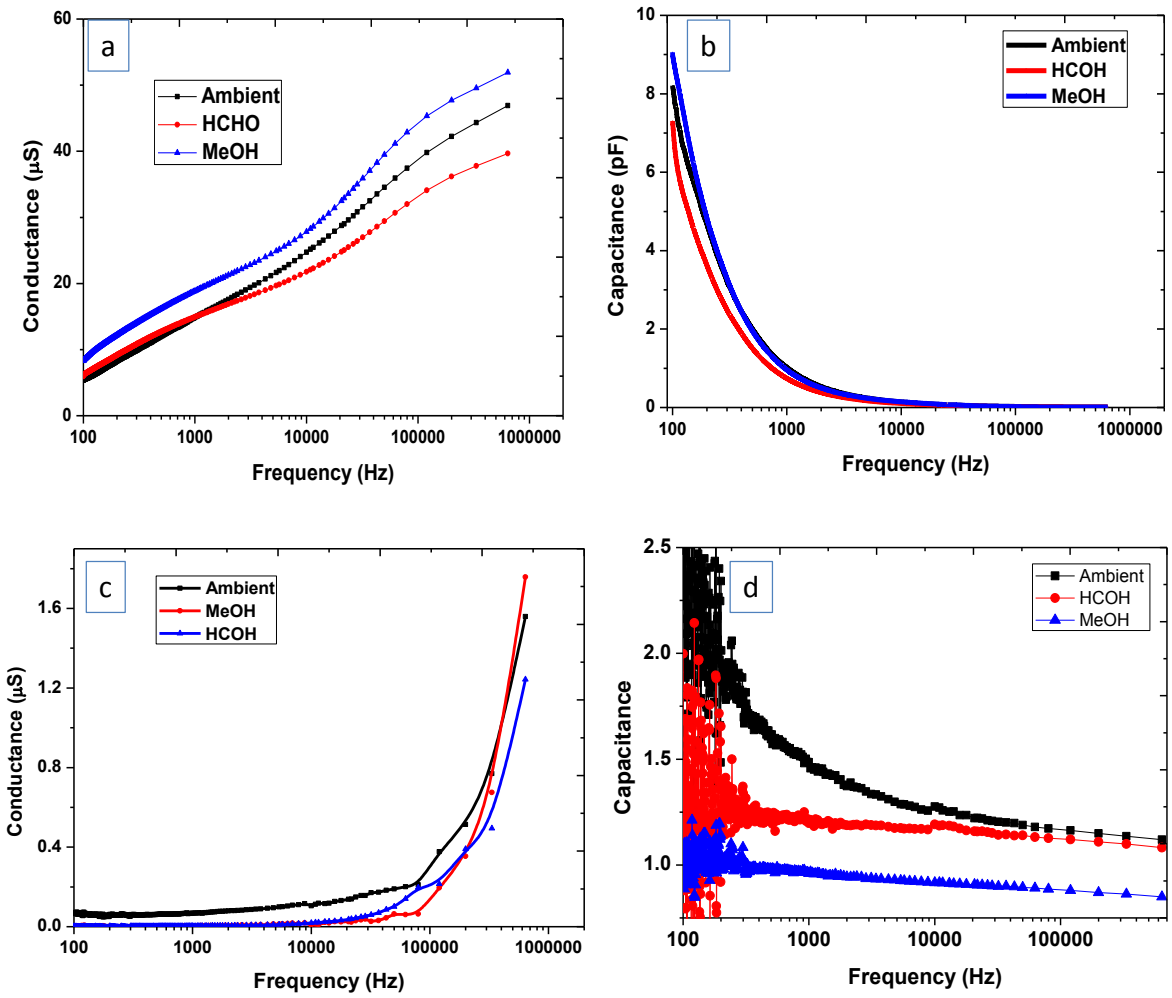

Figure 4-2: Graphs of (a) conductance and (b) capacitance verses frequency for the nanoparticles based sensors while c) is the conductance and d) the capacitance verses frequency for the nanosheets based sensors used to determine the working frequency.

4.3.1 Formaldehyde and methanol sensing properties of InSe nanostructures

The above variation in conductance with increasing frequency when the devices were exposed to the three environments showed the sensing ability of InSe as a semiconductor. As such, further studies were done to ascertain the potential use of colloidal InSe nanostructures for HCHO detection. For the record, the HCHO used herein contained 10 % MeOH for its

stabilization. Therefore MeOH studies were also done to confirm that it did not have much impact on the HCHO detection.

4.3.2 InSe nanoparticle based sensors

Response and recovery time are important factors for gas/vapour sensors. A short detection time is usually associated with a fast response and recovery of the sensor. Fig. 4-3 presents the dynamic response recovery curves of InSe nanoparticle based sensors when exposed to 15 mL of MeOH and HCHO at room temperature. The sensors showed clean response to methanol fumes (Fig. 4-3 spectrum x) and were able to reach saturation as confirmed by the repeatability curve in Fig. 4-4a. In addition, the time required to achieve 90 % of the saturation signal value (response time) was established to be 117 s and a time necessary to achieve 90 % of the signal recovery (recovery time) was found to be 92 s. Comparing the response behaviour of the device in MeOH and HCHO ambient, there is a distinct difference in the sinus of the curves as shown in Fig. 4-3 spectrum y; an indication that the two fumes interact with the surface of the InSe nanoparticles differently. Firstly, the curve for the response to HCHO is much bigger when compared to that of MeOH. Thus it can be concluded that the percentage of MeOH used for stabilizing HCHO in this study has negligible effect and does not comprise the detection of HCHO. The ability of the sensor to reach saturation in the detection of MeOH within the exposure is contrary to when there is HCHO. One interesting feature though that is not attained when the nanosheets are used is that the nanoparticle devices recover completely after detection in both fumes. In Fig. 4-4b, the HCHO sensor showed an increased response when the repeatability test was done recovering fully within 96 s to the baseline. This suggested that HCHO may have taken a longer time than the 5 min to vaporize thus more analyte vapours were being formed while the measurements were in progress hence the continuous sharp increase in the sensitivity of

HCHO detection. An increased response was also observed with increased HCHO concentration and the responsivity curve is presented in Fig. 4-5a. Jason et al. explained this phenomenon as due to a lower concentration of the analyte being associated with a lower coverage of the analyte molecules on the surface when the surface area is fixed while an increase in vapour concentration raises the surface coverage and thus an increase in sensitivity is observed. The sensitivity of the sensor defined as

$$\partial\left[\frac{\Delta G}{G_0}\right] \Big/ \partial[C] \quad \text{..... (4-2)}$$

the slope of the nearly linearly responsivity curve in Fig. 4-6b and it was found to be 0.09861 μL^{-1}, which is approximately 9 %. This relatively low sensitivity was attributed to the fact that the nanoparticles were encapsulated with the long chain oleylamine ligand that was used during their synthesis, thus interfering with the nanoparticles' electrical properties.

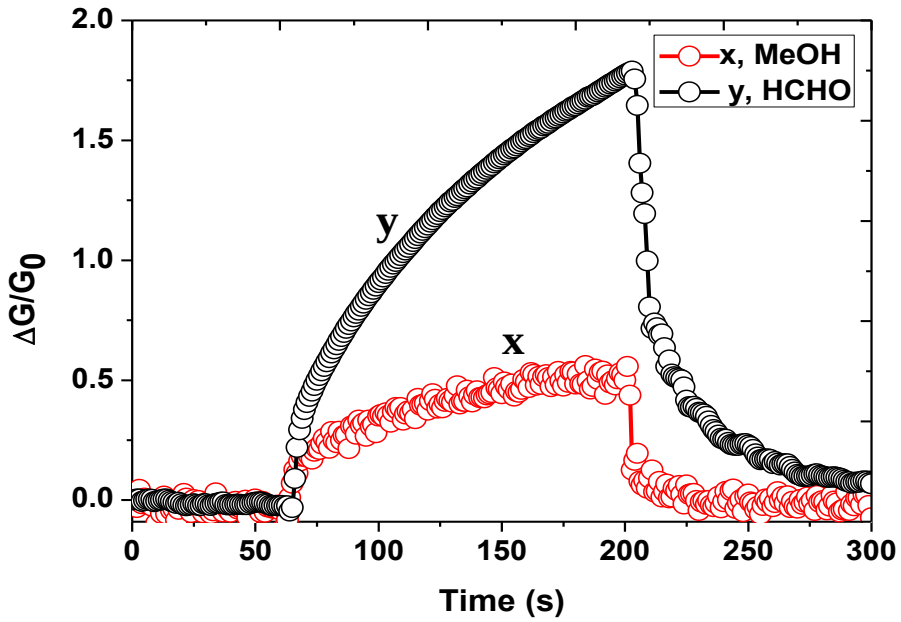

Figure 4-3: The dynamic response recovery curves of InSe nanoparticle based sensors when exposed to 15 ml of (x) methanol and y) formaldehyde at room temperature.

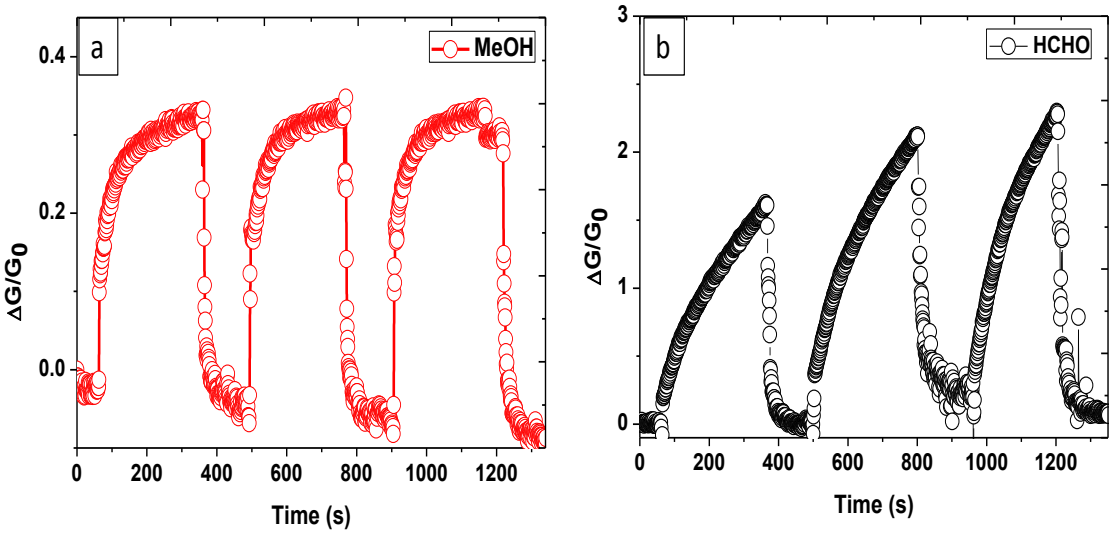

Figure 4-4: Repeatability curves for the nanoparticle based sensors when exposed to (a) methanol and b) formaldehyde fumes.

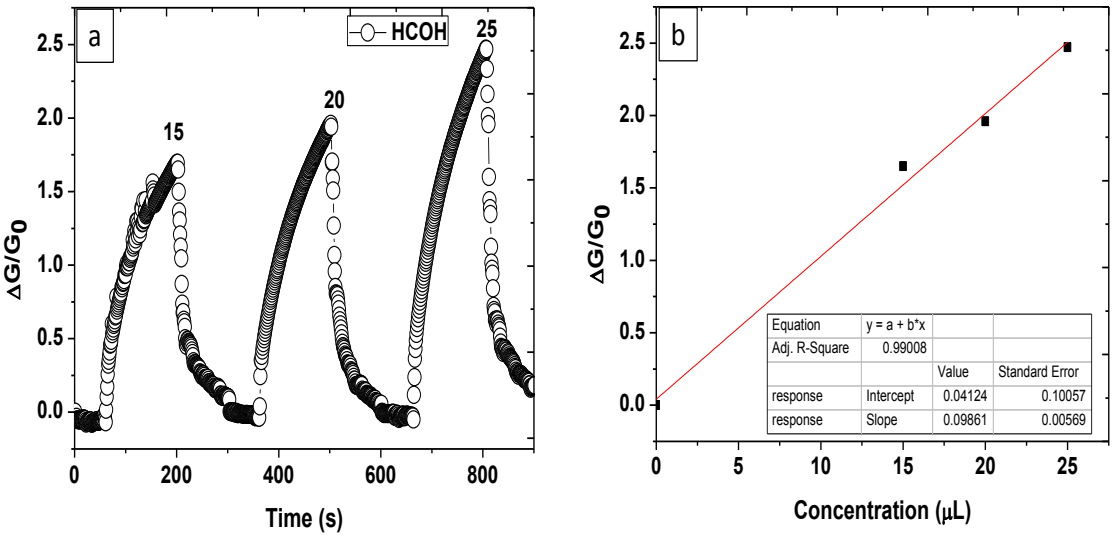

Figure 4-5: a) is the nanoparticle sensor response to different concentration of formaldehyde fumes and b) is the sensitivity curve of the same sensor.

In an attempt to attain saturation, the sensor was exposed to the HCHO fumes for longer duration. Fig. 4-6 shows that after 800 s the sensor reached saturation though it had an extended dynamic range. The extension of the dynamic range according to literature [26] is

attributed to the availability of different binding sites with multiple binding constant for analyte species as a result of a number of lattice defects and a high level of doping impurities; thus each site experiences an individual dynamic range which then overlaps with the next one, resulting to a much greater range compared to what would be obtained for any single type of binding site with only one equilibrium constant. According to J. Janata [25], the interaction of the adsorbate (chemical species *X*) with the sensor (*S*) is described by equilibrium:

$$X + S \underset{K_r}{\longleftrightarrow} SX \quad \ldots\ldots\ldots\ldots\ldots\ldots\ldots\ldots\ldots\ldots\ldots\ldots \text{(4-3)}$$

where K_f and K_r are the rates of forward and reverse reactions. The equilibrium constant is expressed in terms of the activities (*a*):

$$a = fC \quad \ldots\ldots\ldots\ldots\ldots\ldots\ldots\ldots\ldots\ldots\ldots\ldots\ldots\ldots \text{(4-4)}$$

Where f is the activity coefficient and *C* is the concentration of the analyte. Therefore the equilibrium constant is:

$$K_X = \frac{a_{SX}}{a_S a_X} = \frac{k_f}{k_r} \quad \ldots\ldots\ldots\ldots\ldots\ldots\ldots\ldots\ldots\ldots\ldots\ldots \text{(4-5)}$$

where a_{SX} a_X and a_S are, respectively, the activities of the bound species, species in the sample and of the binding site in the sensor.

$$a_{SX} = a_X K_X a_S \quad \ldots\ldots\ldots\ldots\ldots\ldots\ldots\ldots\ldots\ldots\ldots\ldots\ldots\ldots \text{(4-6)}$$

In the case of multiple activities, the activity of the bound species can be described as:

$$a_{SX} = a_X \left[K_1 a_{T_1} + K_2 a_{T_2} \ldots\ldots\ldots\ldots\ldots\ldots\ldots\ldots\ldots\ldots K_n a_{T_n} \right] \quad \ldots\ldots \text{(4-7)}$$

Where a_T are the total activities of individual binding sites.

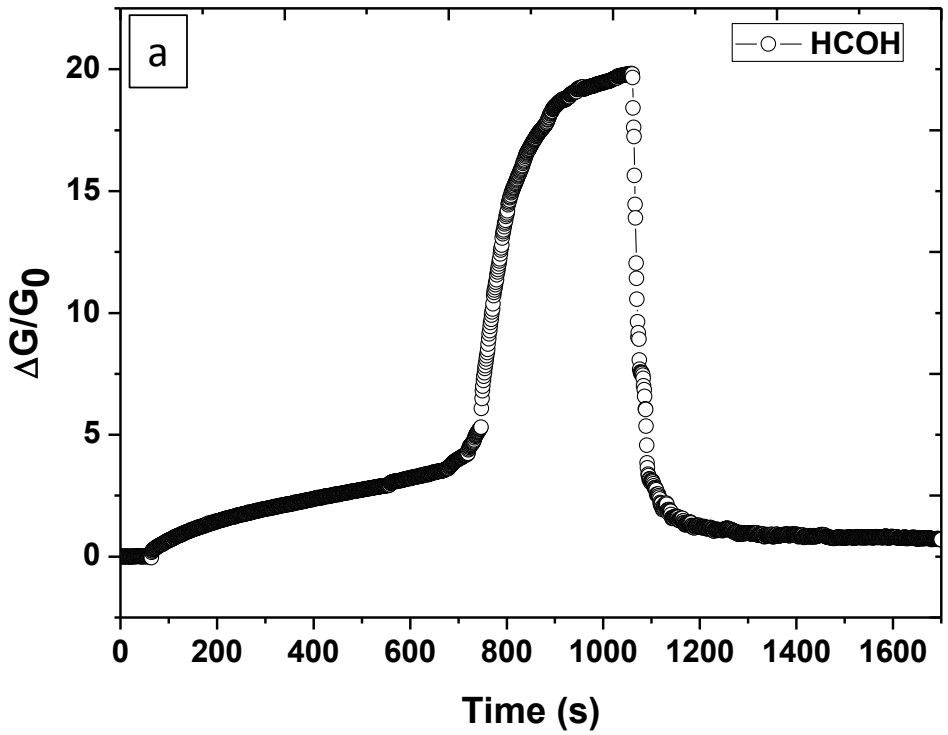

Figure 4-6: Response curve for nanoparticle based sensor when exposed to formaldehyde fumes for longer duration to ascertain the possibility of the sensor reaching saturation point.

4.3.3 Temperature studies for nanoparticles based sensors during the detection of formaldehyde and methanol

The working temperature of semiconductor gas sensors is one of the very vital functional parameters with many studies reported on this [1]. The operating temperature of the sensor is an important issue as it influences the physical properties of the semiconductor materials as well as the diffusion of reactants to the active region, which is dependent on the ambient temperature of the measured atmosphere [27-29]. To study the effect of temperature on the sensor response, the whole chamber was placed in a bath filled with glycerin. Glycerin was used in the bath instead of water in order to reduce humidity in the sensing environment. Initial conductance was measured for 120 s after which the different concentration of analyte

(HCHO and MeOH fumes with boiling points of 93 ± 3 °C and 62 °C respectively) was introduced in the chamber at varied temperature ranging from 30 ± 1 °C – 90 ± 1 °C. At each temperature and concentration, the sensor was exposed to the analyte for 10 min after which the final conductance was obtained. The results of this study are shown in Fig. 4-7 where the sensor response was found to decrease with the increasing temperature for the InSe nanoparticles. This portrayed that the sensors' operating temperature for detection of MeOH and HCHO vapors lie within the near room temperature range. It was also evident that for the case of HCOH (Fig. 4-7a) the higher concentration gave higher response though it was nonlinear when compared to its behavior at near room temperature. Also the response was seen to increase after 75 ± 1 °C for concentrations 20 µL and 25 µL. The methanol response at varied temperatures (Fig. 4-7b) is not linear and a decrease was observed which later increase at 60 ± °C, then dropped for all the three concentration. The fluctuation continues for 20 ± 1 °C and 25 ± 1 °C as the response is seen to rise again at 90 ± 1 °C.

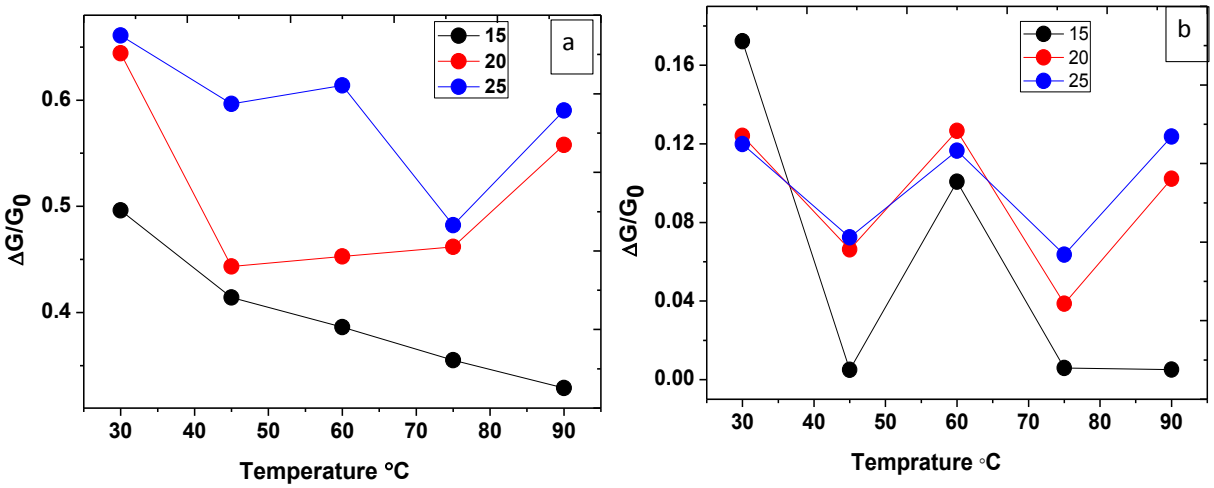

Figure 4-7: Response verses temperature curves when the nanoparticle based sensor was exposed to different concentration of (a) formaldehyde and b) methanol fumes.

4.3.4 Response of nanoparticles based sensor to other VOCs for selectivity study

Among the kinetic processes that affect the performance of the sensor is its ability to be selective towards other analytes [27, 30]. To provide an insight on the selectivity of InSe devices, a set of the sensors were exposed to fumes of acetone and chloroform following a similar procedure used for MeOH and HCHO detection described above. The value of the slopes of the response curves in Fig. 4-8 were lower than that obtained from the HCHO response curve, an indication that the devices were more sensitive to HCOH fumes compared to chloroform and acetone. Table 4-1 summarizes the sensitivity of the devices towards the different VOCs.

Table 4-1: Shows the sensitivity of the InSe nanostructured devices to the presence of different volatile organic compounds.

Analyte	Nanoparticle based Sensor (μL^{-1})	Nanosheet based Sensor (μL^{-1})
Formaldehyde	0.0986	0.00426
Chloroform	0.0017	0.00584
Acetone	0.0045	0.0079

The response is controlled by reaction kinetics, mass transport and the geometric topography of the nanostructures. Thus to be able to understand the mechanism governing such electrochemical process for the purpose of improving the performance of nanostructure ba sed electrode, it is necessary to investigate the role of the reaction kinetics and mass transport in biosensing when nanostructured electrode are used.

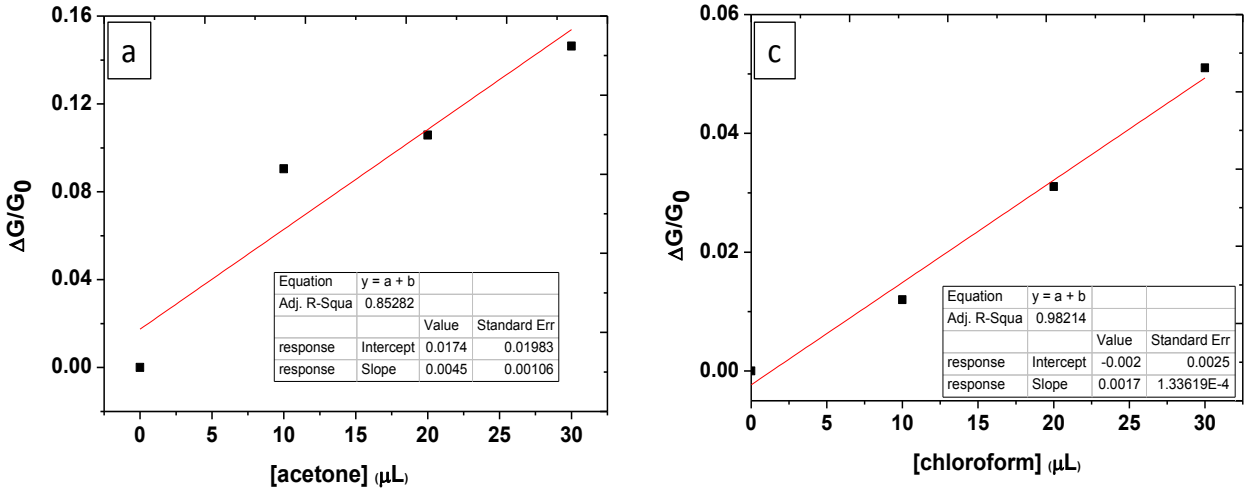

Figure 4-8: Sensitivity curves of the nanoparticle based sensors when exposed to different concentration.

4.3.5 Formaldehyde and methanol sensing properties of InSe nanosheets

For comparison purposes, another set of experiments were conducted using InSe nanosheet sensors to detect MeOH and HCHO fumes following the procedures described above. Fig. 4-9a shows the response obtained for MeOH which portrayed a high noise to signal ratio as well as a very minimal variation in conductance. This therefore confirmed that the MeOH in the formaldehyde had negligible effect on the sensing of HCHO using the InSe nanostructures. Also it was deduced that the nanosheets formed relatively poor sensors for MeOH detection. However in a HCHO environment, the sensor saturated rapidly thus a steady state was achieved as shown in Fig. 4-9b; though with a poor baseline. Also as seen in Fig. 4-9b, the sensor did not recover completely probably due to strong bound states formed when the analyte fumes interacted with the active layer, InSe nanosheets. This becomes a hiccup for sensor fabrication using the nanosheets as the active material. From the literature [31], it has been established that an increase in chemical sensor sensitivity for analyte detection is normally due to enhanced charge transfer between the adsorbate and the semiconductor, implying stronger and more irreversible analyte binding. This is a possible

explanation for the failure of the nanosheets based device to recover completely when it was taken back to the ambient after a very quick steady state achievement in HCHO environment. The response amplitude of the nanosheet based sensors slightly increased with the increasing HCOH concentration with a negligible increase between the 15 µL and 20 µL concentration and an increase at 25 µL as shown in Fig. 4-10a. From the sensitivity curve, the nanosheets based sensor exhibited a sensitivity 0.00426 μL^{-1} to the HCHO fumes.

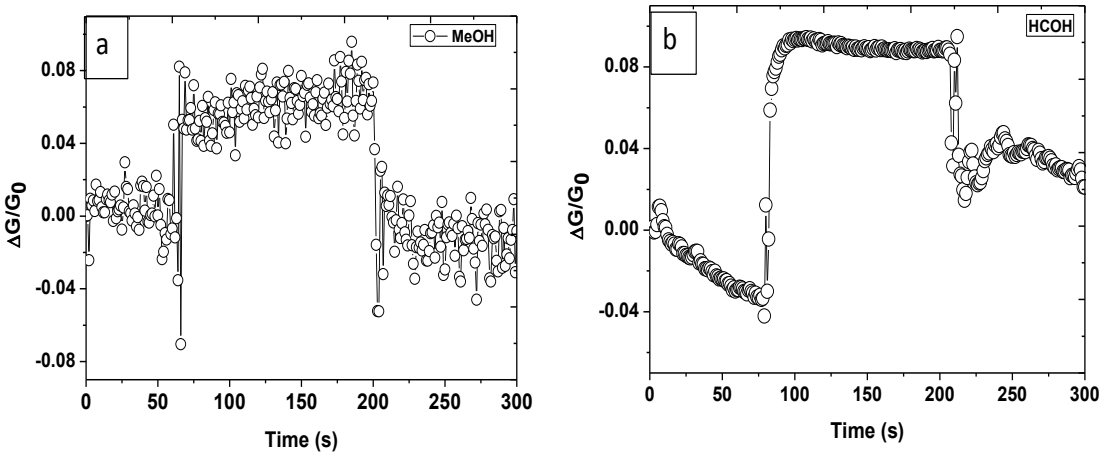

Figure 4-9: Dynamic response curves for nanosheets based sensors when exposed to a) methanol and b) formaldehyde fumes.

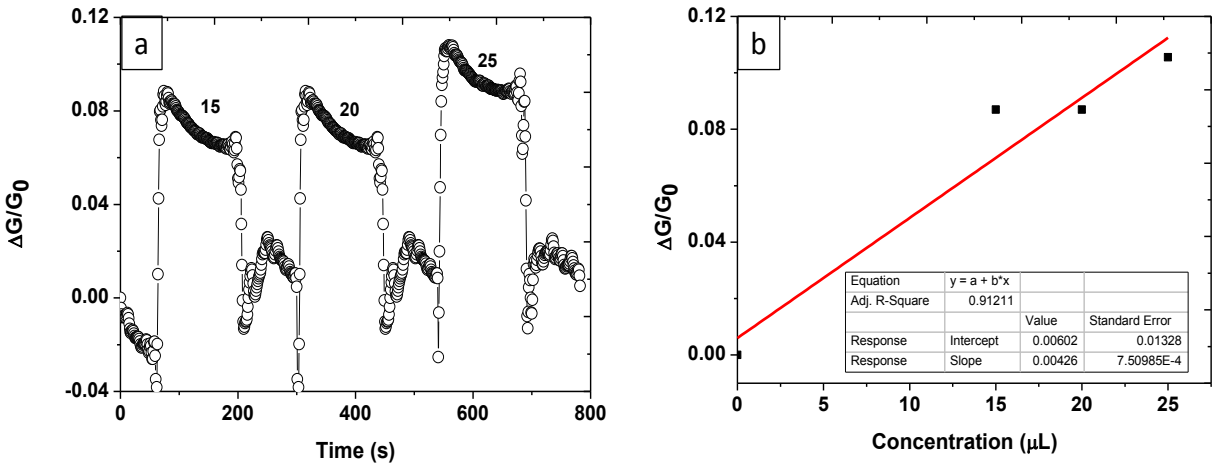

Figure 4-10: a) Response curve for nanosheet based sensors when exposed in different concentration of formaldehyde and b) is the sensor's sensitivity profile.

4.3.6 Temperature studies for nanosheets based sensors during the detection of formaldehyde and methanol

The temperatures ran during this study ranged from 30 °C – 90 °C for the different concentration of HCHO, that is, 15 µL, 20 µL and 25 µL. For all the three concentrations, a decrease in the response of the device to formaldehyde fumes declined with increasing temperature to 75 °C (Fig. 4-11a), after which the response started going up again. Since a glycerine bath was used to provide a variation in the temperature, no studies were made for temperatures greater than 90 °C. The sensors still performed better at temperatures near the room temperature. However, the sensor showed potential of increased response at temperatures above 75 °C. A similar trend was observed when the sensors were exposed at varied temperatures to different concentrations of methanol as depicted in Fig. 4-11b.

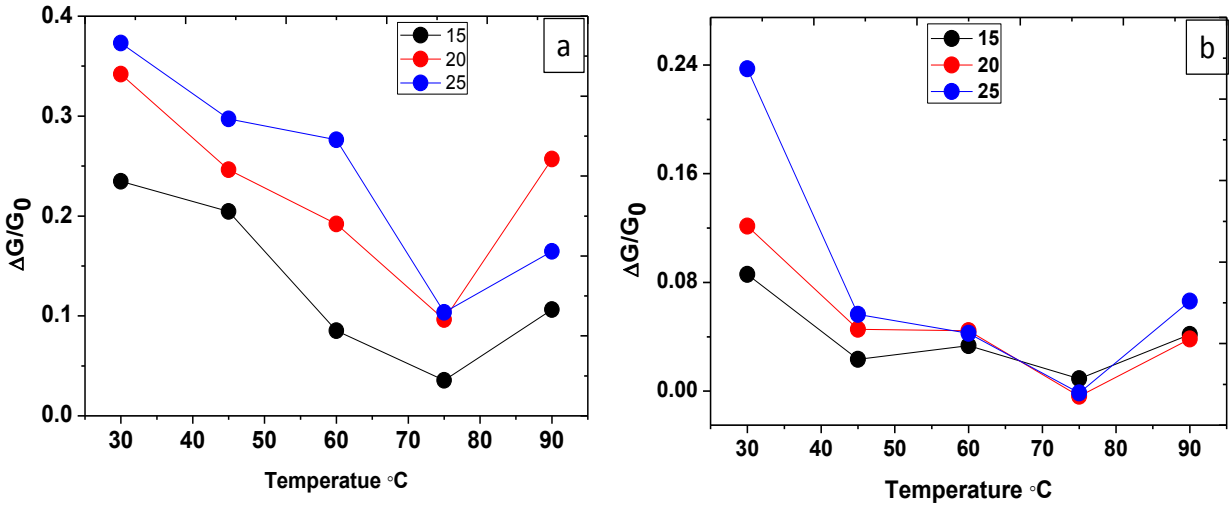

Figure 4-11: Response verses temperature curves when the nanosheets based sensor was exposed to different concentration of (a) formaldehyde and b) methanol fumes.

4.3.7 Response of nanosheets based sensor to other VOCs for selectivity study

The sensor responded better to acetone with a sensitivity of 0.00584 μL^{-1} compared to HCHO which was 0.00426 μL^{-1} and the acetone sensitivity profile is presented in Fig. 4-12a. Therefore, more work on acetone sensing using InSe nanostructures is appropriate. However, the sensor performed dismally when it was exposed to chloroform (Fig. 4-12b). The sensitivity of the device to acetone, chloroform and formaldehyde are presented in Table 4-1 for comparison purposes.

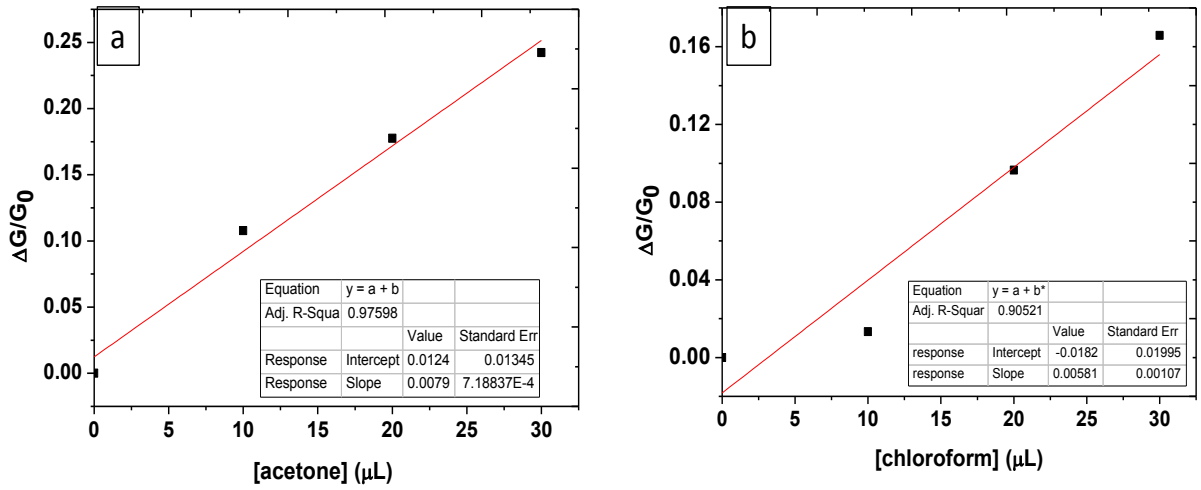

Figure 4-12: Sensitivity profiles of the nanosheets based sensors when exposed to a) acetone and b) chloroform fumes.

4.3.8 Comparison of the activity of nanoparticles and nanosheets devices on detection of formaldehyde; difference in the shape of the curves.

For comparison purposes, the gas response curve of the nanoparticles based sensor and nanosheets based sensor to HCHO were plotted as shown in Fig. 4-13. The sinus for the nanoparticles based sensor (Fig. 4-13a) was bigger than that for the nanosheets (Fig. 4-13b). This was attributed to the fact that the nanoparticles are smaller in size (their sizes range between 4 nm – 14 nm) compared to the nanosheet thickness which ranges from 18 nm – 62 nm as obtained in our previous studies [32, 33] thus increased surface area. Similarly, from the SEM micrographs of the sensing films, it was observed that quite a numbers of uniformly distributed nanoparticles were deposited on the substrate. As a result, a lot of material was exposed for sensing such that, filling all the sensing sites not only took longer thereby taking time to saturate, but also resulted in a bigger response. This was contrary to the nanosheets film as the nanosheets appeared stuck on each other thus exposing just few sites for sensing, thus the quick saturation and the smaller response. In addition, BET studies on the two

nanostructures also confirmed the dependence of the surface area to the particle size giving values of 18.9 m^2/g and 8.1 m^2/g for the nanoparticles and the nanosheets respectively. Therefore there was increased adsorption of the analyte on the surface of the nanoparticles sensor. This is in agreement with the findings in Fig. 4-14 which evidently showed that the nanoparticles based sensor responded better at frequencies about 5 kHz (Fig. 4-14a) than the nanosheets (Fig. 4-14b) when they were both exposed to the analyte ambient. In addition, the sensitivity values of the two sensors which were obtained from the slopes of the nearly linear response curves were $0.09861\mu L^{-1}$ and $0.00426\ \mu L^{-1}$ for nanoparticles-based and nanosheets-based sensors respectively. Fig. 4-13 also portrays a difference in the shape of the sensing curves for the two devices, a phenomenon that is explained by the availability of the surface atoms on each structure to interact with the analyte. It has been established that as the crystals become smaller, the number of atoms on the surface increases thus leaving more dangling orbitals on each atom pointed outward of the crystals as they are incompletely bonded within the crystal lattice [34-36]. Therefore, hypothetically, considering the thickness of nanosheets and the size of the nanoparticles, the nanosheets have few surface atoms thus they easily get filled by the analyte thereby attaining saturation rapidly unlike nanoparticles which take time to reach saturation. During the colloidal synthesis of InSe nanocrystals, surface coordinating ligands were used to passivate their surfaces thus modifying them. This modification may have introduced defects on the nanocrystal surface. In addition, oleylamine used as the ligand in the synthesis is a basic ligand, thus it tends to bind poorly on the Se^{-2} rich facets thereby making these surfaces prone to surface trapping. Also, the indium atom in the structure of InSe is less electronegative compared to the selenium atom enabling it to accept electron from an electron donating molecule. As a result, there are three possible ways an analyte can interact with the surface of the InSe nanocrystals. For an electron donating analyte like formaldehyde and methanol whose oxygen atoms has two lone pairs of electron, the analyte

may get trapped on the defects or bond weakly to the indium atom. This interaction will then affect the conductivity of the nanocrystals. However the sensing mechanism is not yet well understood and is still under investigation.

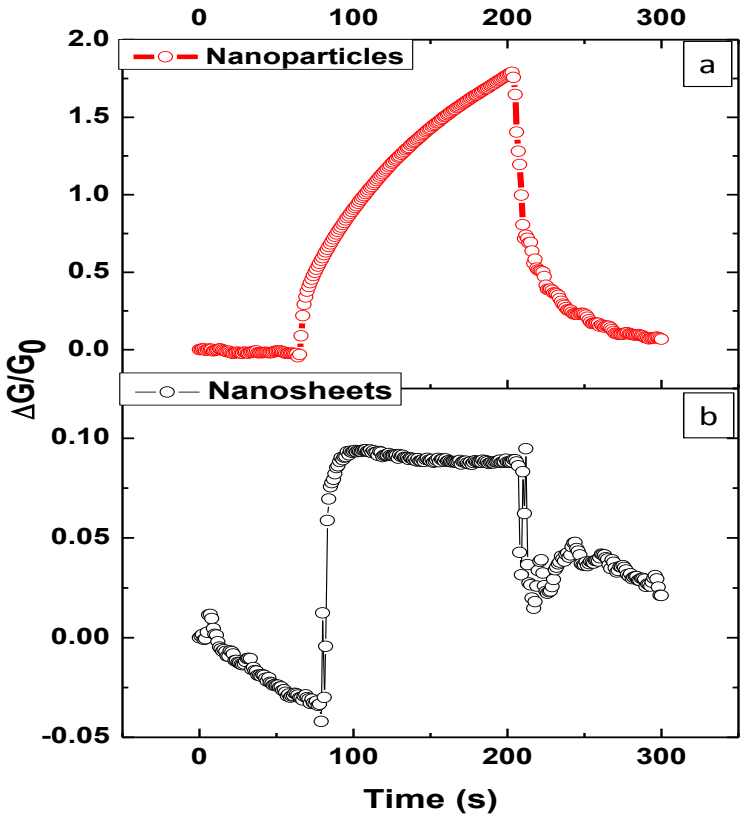

Figure 4-13: Gas response curves of a) nanoparticle b) nanosheet based sensors when exposed to 15 µL formaldehyde gas.

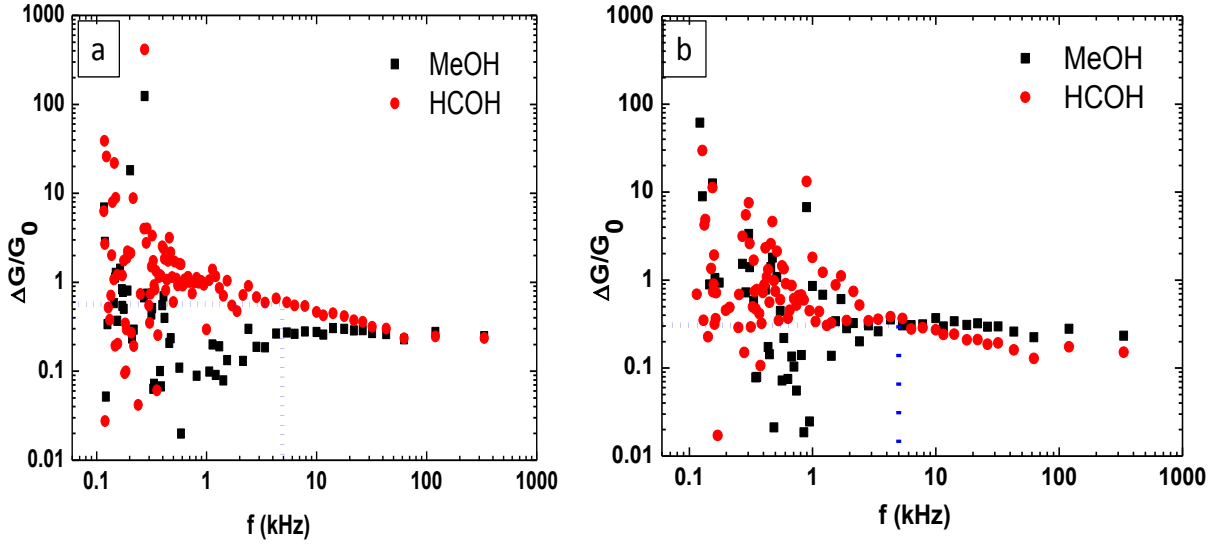

Figure 4-14: Gas response verses frequency curves of a) nanoparticles and b) nanosheets based sensors when exposed to methanol and formaldehyde.

4.4 Conclusions

In conclusion, we have demonstrated that sensors fabricated using InSe nanocrystals response to methanol and formaldehyde fumes. The sensors fabricated using the InSe nanoparticles gave relatively good sensitivity towards HCHO and selectivity to HCHO over acetone and chloroform. The nanosheet based sensors also detected the presence of the HCOH, however the sensor recovered half way, indicating a strong interaction between analyte and binding site. In addition, it was not selective to formaldehyde fumes. Based on the above results, the nanoparticle based sensors are more selective and sensitive to the presence of HCHO. Evident from the results, the surface capping molecule (oleylamine) employed to stabilize the nanostructures during synthesis as well as render them soluble in various solvents may be responsible for the poor sensing abilities of the nanostructures. Nevertheless, a number of studies in other applications have shown that the surface capping molecules can be easily removed as they form dative bonds with the surface of the semiconductor [37, 38]. However this may result in increased surface defects which may hinder the recovery of the sensor

hence a comprehensive study is necessary. Incorporating the nanostructures in conductive polymers can also be explored as the conductivity of the polymers may increase and this may eliminate some of the problems associated with nanostructures [39].

References

[1] J.N. Panchal, Ph.D thesis, in: Electronics, 2014.

[2] L. Sparks, Z. Guo, J. Chang, B. Tichenor, Volatile organic compound emissions from latex paint–part 2. Test house studies and indoor air quality (iaq) modeling, Indoor Air, 9 (1999) 18-25.

[3] E.H.I.A.Q.I. », Volatile Organic Compounds' Impact on Indoor Air Quality, (2016).

[4] P.-R. Chung, C.-T. Tzeng, M.-T. Ke, C.-Y. Lee, Formaldehyde gas sensors: A Review, Sensors, 13 (2013) 4468-4484.

[5] U.S. Department of Health Services, Toxicological Profile for Formaldehyde, Atlanta: Agency for Toxic Substances and Disease Registry, (1999).

[6] U.S. Department of Health and Human Services: Washington, USA, Occupational Safety and Health Guideline for Formaldehyde Potential Human Carcinogen, (1988).

[7] J. Stephens, A. Batra, J.R. Currie, Characteristics of Nanoparticles-Based Chemical Sensors, (2012).

[8] L. Feng, C.J. Musto, K.S. Suslick, A simple and highly sensitive colorimetric detection method for gaseous formaldehyde, Journal of the American Chemical Society, 132 (2010) 4046-4047.

[9] G. Korotcenkov, Chemical Sensors: Comprehensive Sensor Technologies Volume 6: Chemical Sensors Applications, Momentum Press, 2011.

[10] G. Jiménez-Cadena, J. Riu, F.X. Rius, Gas sensors based on nanostructured materials, Analyst, 132 (2007) 1083-1099.

[11] A.Y. Nazzal, L. Qu, X. Peng, M. Xiao, Photoactivated CdSe nanocrystals as nanosensors for gases, Nano Letters, 3 (2003) 819-822.

[12] L. Qu, X. Peng, Control of photoluminescence properties of CdSe nanocrystals in growth, Journal of the American Chemical Society, 124 (2002) 2049-2055.

[13] M. Kuno, J.-K. Lee, B.O. Dabbousi, F.V. Mikulec, M.G. Bawendi, The band edge luminescence of surface modified CdSe nanocrystallites: Probing the luminescing state, The Journal of Chemical Physics, 106 (1997) 9869-9882.
[14] J.M. Costa-Fernández, R. Pereiro, A. Sanz-Medel, The use of luminescent quantum dots for optical sensing, TrAC Trends in Analytical Chemistry, 25 (2006) 207-218.
[15] S. Lei, L. Ge, S. Najmaei, A. George, R. Kappera, J. Lou, M. Chhowalla, H. Yamaguchi, G. Gupta, R. Vajtai, Evolution of the electronic band structure and efficient photo-detection in atomic layers of InSe, ACS Nano, 8 (2014) 1263-1272.
[16] J. Martínez-Pastor, A. Segura, J. Valdes, A. Chevy, Electrical and photovoltaic properties of indium-tin-oxide/p-InSe/Au solar cells, Journal of Applied Physics, 62 (1987) 1477-1483.
[17] C. Julien, M. Balkanski, Thin-film growth and structure for solid-state batteries, Applied Surface Science, 48 (1991) 1-11.
[18] F. Manjón, D. Errandonea, A. Segura, V. Muñoz, G. Tobías, P. Ordejón, E. Canadell, Experimental and theoretical study of band structure of InSe and In 1− x Ga x Se (x< 0.2) under high pressure: Direct to indirect crossovers, Physical Review B, 63 (2001) 125330.
[19] D. Errandonea, A. Segura, F. Manjón, A. Chevy, E. Machado, G. Tobias, P. Ordejón, E. Canadell, Crystal symmetry and pressure effects on the valence band structure of γ-InSe and ε-GaSe: Transport measurements and electronic structure calculations, Physical Review B, 71 (2005) 125206.
[20] A. Segura, J. Guesdon, J. Besson, A. Chevy, Photoconductivity and photovoltaic effect in indium selenide, Journal of Applied Physics, 54 (1983) 876-888.
[21] J. Guesdon, B. Kobbi, C. Julien, M. Balkanski, Electrical and photovoltaic properties of InxSe1− x thin films, Physica Status Solidi (a), 102 (1987) 327-335.
[22] G.W. Mudd, S.A. Svatek, T. Ren, A. Patanè, O. Makarovsky, L. Eaves, P.H. Beton, Z.D. Kovalyuk, G.V. Lashkarev, Z.R. Kudrynskyi, Tuning the bandgap of exfoliated InSe nanosheets by quantum confinement, Advanced Materials, 25 (2013) 5714-5718.
[23] J.F. Sánchez-Royo, G. Muñoz-Matutano, M. Brotons-Gisbert, J.P. Martínez-Pastor, A. Segura, A. Cantarero, R. Mata, J. Canet-Ferrer, G. Tobias, E. Canadell, Electronic structure, optical properties, and lattice dynamics in atomically thin indium selenide flakes, Nano Research, 7 (2014) 1556-1568.
[24] M.W. Greenshields, I.A. Hümmelgen, M.A. Mamo, A. Shaikjee, S.D. Mhlanga, W.A. Van Otterlo, N.J. Coville, Composites of polyvinyl alcohol and carbon (coils, undoped and

nitrogen doped multiwalled carbon nanotubes) as ethanol, methanol and toluene vapor sensors, Journal of Nanoscience and Nanotechnology, 11 (2011) 10211-10218.
[25] J. Janata, Principles of chemical sensors, Springer Science & Business Media, 2010.
[26] E.M. Moreno, Kinetics of charge carriers in Si/SiNx heterojunctions, in, Freie Universität Berlin, Germany, 2009.
[27] M. Alim, B. Penn, J. Currie Jr, A. Batra, M. Aggarwal, Micro-and Nanostructured Metal Oxide Chemical Sensors for Volatile Organic Compounds, (2008).
[28] W. Moritz, V. Fillipov, A. Vasiliev, G. Cherkashinin, J. Szeponik, A field effect based hydrogen sensor for low and high concentrations, ECS Transactions, 3 (2006) 223-230.
[29] R. De Angelis, M. Casalboni, I. Colantoni, L. D'Amico, F. De Matteis, F. Hatami, W.T. Masselink, P. Prosposito, Chemical Sensitivity of Luminescent Epitaxial Surface InP Quantum Dots, (2013).
[30] V. Vaishnav, S. Patel, J. Panchal, Development of indium tin oxide thin film toluene sensor, Sensors and Actuators B: Chemical, 210 (2015) 165-172.
[31] F. Seker, K. Meeker, T.F. Kuech, A.B. Ellis, Surface chemistry of prototypical bulk II-VI and III-V semiconductors and implications for chemical sensing, Chemical Reviews, 100 (2000) 2505-2536.
[32] M.A. Airo, S. Gqoba, M.P. Kalenga, S. Govindraju, M.J. Moloto, N. Moloto, Synthesis and characterization of indium monoselenide nanosheets: A proposed pseudo top-down mechanism, Journal of Crystal Growth, 406 (2014) 1-7.
[33] M. Airo, S. Gqoba, F. Otieno, M.J. Moloto, N. Moloto, Structural modification and band-gap crossover in indium selenide nanosheets, RSC Advances, (2016).
[34] S. Pokrant, K. Whaley, Tight-binding studies of surface effects on electronic structure of CdSe nanocrystals: the role of organic ligands, surface reconstruction, and inorganic capping shells, The European Physical Journal D-Atomic, Molecular, Optical and Plasma Physics, 6 (1999) 255-267.
[35] D.F. Underwood, T. Kippeny, S.J. Rosenthal, Ultrafast carrier dynamics in CdSe nanocrystals determined by femtosecond fluorescence upconversion spectroscopy, The Journal of Physical Chemistry B, 105 (2001) 436-443.
[36] A.M. Smith, S. Nie, Semiconductor nanocrystals: structure, properties, and band gap engineering, Accounts of Chemical Research, 43 (2009) 190-200.

[37] K.S. Leschkies, R. Divakar, J. Basu, E. Enache-Pommer, J.E. Boercker, C.B. Carter, U.R. Kortshagen, D.J. Norris, E.S. Aydil, Photosensitization of ZnO nanowires with CdSe quantum dots for photovoltaic devices, Nano Letters, 7 (2007) 1793-1798.
[38] G. Zhang, S. Finefrock, D. Liang, G.G. Yadav, H. Yang, H. Fang, Y. Wu, Semiconductor nanostructure-based photovoltaic solar cells, Nanoscale, 3 (2011) 2430-2443.
[39] N. Moloto, N.J. Coville, S.S. Ray, M.J. Moloto, Morphological and optical properties of MnS/polyvinylcarbazole hybrid composites, Physica B: Condensed Matter, 404 (2009) 4461-4465.

Chapter 5 : Synthesis and characterization of nickel selenide nanocrystals

5.1 Background

Nickel selenides are p-type semiconductors which have attracted the attention of researchers due to their interesting electrical, catalytic and magnetic properties; characteristics desirable for many applications [1-3]. The valence electronic configuration of nickel is $3d^8 4s^2$ and the difference in the electronegativity between nickel and selenium is small; these two when coupled enable nickel and selenium to form complexes with a number of stoichiometries [1, 4-6] . According to the Ni – Se binary phase diagram, there exist three stable phases namely; $NiSe_2$ which can exist in either cubic and orthorhombic phases, $Ni_{1-x}Se$ whose nickel content can vary from 1.00 to 0.85 relative to 1 Se (x=0-0.15), and Ni_3Se_2 which can also exist either as rhombohedral or hexagonal phases [7]. In addition, other phases such as Ni_2Se_3, Ni_2Se, Ni_3Se_4, Ni_7Se_5 and Ni_6Se_5 are known to exist [4]. The commonly observed crystal structures for the three stable phases at room temperature are represents Fig. 5-1. [7]. Like many other semiconducting materials, the properties and applications of nickel selenides are dependent on their composition and morphologies [8-16]. Different polymorphs of nickel selenides have exhibited potential use in energy research such as catalysis, electrochemistry and energy storage [8, 9, 17, 18]. Specifically, $NiSe_2$ are examples of Pauli paramagnets with metallic conductivity and they have been regarded as model materials for studies of physical characteristics resulting from narrow band gap systems [19]. Thermodynamically stable cubic $NiSe_2$ particles have been found as a suitable energy storage material [17, 18] and as counter electrode in DSSCs due to its unique electrochemistry properties. In addition, Ni_3Se_4 have been reported to have potential use in DSSCs [20]. Also NiSe has a band gap of 2.0 eV, which can be utilized in photovoltaic technologies [17].

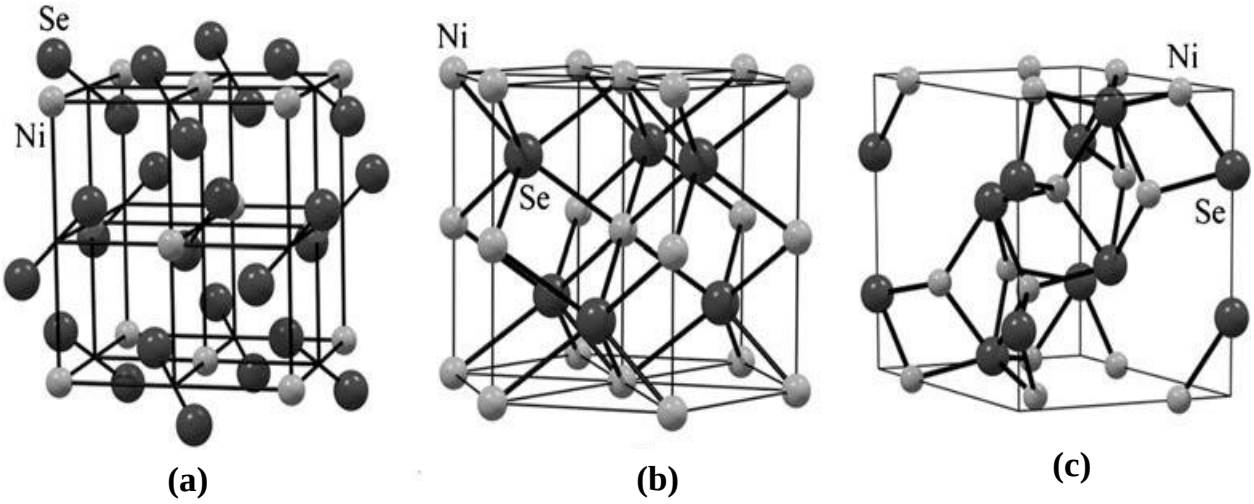

Figure 5-1: Schematic illustrations of the commonly observed crystal structures of a) $NiSe_2$, b) $Ni_{1-x}Se$ and c) Ni_3Se_2.

The numerous and promising potential applications of Ni – Se series are a strong drive for more studies on the nanoparticles of this systems. Therefore, one of the main concerns is to develop the best possible methods of fabrication and the conditions associated with them that will not only result in Ni-Se nanostructures with high purity , but also with desired properties for a particular application. Several methods have been employed for the synthesis of nickel selenides. In particular, $NiSe_2$, $Ni_{0.85}Se$ and Ni_3Se_2 have been prepared by solvothermal process [21, 22], hydrothermal synthesis [7, 23], and mechanical alloying [5, 19] $NiSe_2$, $Ni_{1-x}Se$ and Ni_3Se_2 materials have been produced using mechanical alloying [5]. These methods have resulted in various morphologies of nickel selenide series including nanowires, nanocables, hollow sub-microspheres, and microspheres among. Using the above methods, control of morphologies and sizes of Ni-Se systems has been and still is a great challenge. Consequently for organic solution phase syntheses, steps including varying the reaction conditions such reaction temperature, reaction time, molar ratios of the reactants (Ni/Se), the capping agent and even the method of synthesis are manipulated during fabrication with the aim of solving the challenge. These parameters have been reported to play important roles in

the formation of the nickel selenide series. In this chapter, we report on the synthesis of nickel selenides via the colloidal route. We have investigated the effect of several parameters such as reaction temperature, time, precursor concentration and the coordinating solvent on the properties of produced Ni-Se nanoparticles.

5.2 Experimental

5.2.1 Chemicals and materials

Nickel (II) chloride, selenium powder, hexadecylamine (HDA), trioctylphosphine (TOP), oleic acid (OA), octadecylamine (ODA), oleylamine (OLA), methanol, ethanol, chloroform, toluene and hexane were purchased from Sigma Aldrich.

5.2.2 Synthesis of nickel selenide nanostructures

5.2.2.1 Hot injection with TOP

About 0.3948 g of Se powder and 0.648 g of $NiCl_2$ were each dissolved in 5 mL of TOP in separate vials under ultrasonication until a colourless solution of TOP-Se and a red solution of TOP-$NiCl_2$ were obtained. 10 mL of oleylamine was placed in a three neck flask Nitrogen gas was bubbled through to provide an inert atmosphere. This was then heated to 200 °C. 2 mL of TOP-Se and 2 mL of TOP-$NiCl_2$ were then injected in the flask at the same time at 200 °C. The temperature dropped to 180 °C due to the addition of the cold precursors injected. The temperature was allowed to stabilize to 200 °C and thereafter aliquots were obtained at different times. The aliquots were then allowed to cool to 80 °C after which the methanol/ ethanol was added to flocculate the nanoparticles. The nanoparticles were collected via centrifugation at 4000 rpm for 15 min. The products were washed several times with methanol/ethanol/hexane/toluene after which they were left to dry at room temperature overnight. A yield of about 1 g was obtained. The effects of concentration, temperature (180

°C and 220 °C) and ligand (6 g of HDA and 6 g of ODA) on the properties of the nanostructures were studied. Scheme 5-1 shows a representation of the reaction procedure followed for the hot injection method.

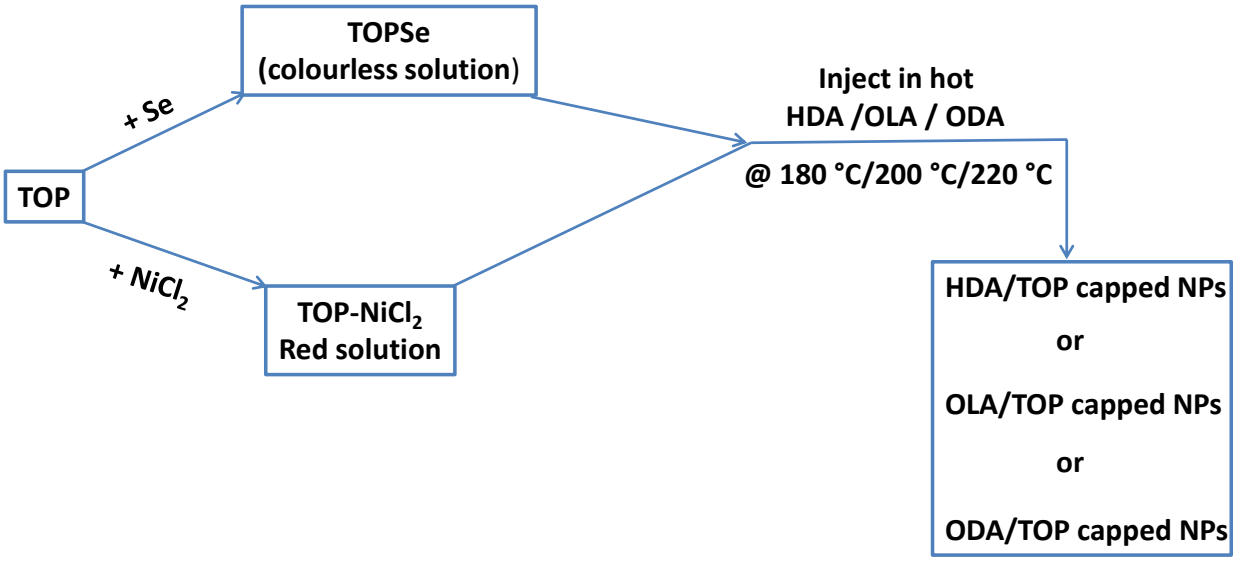

Scheme 5-1: Schematic representation of the reaction procedure followed for the hot injection method.

5.2.2.2 Without TOP/Non hot injection/Direct heating

About 0.3948 g of Se powder and 0.648 g of $NiCl_2$ (mole ratio 1:1) were placed in a 50 mL three neck round bottom flask. 10 mL of OLA was added to the flask to act as the solvent, a reducing agent and a capping agent. The mixture was degassed for 20 min then heated quickly to the working temperature under nitrogen and strong magnetic stirring. The reaction was then maintained to the working temperature and aliquots were obtained at particular durations. The dark solution formed was cooled to approximately 80 °C. After cooling the reaction mixture, an excess of hot methanol was added and the solid isolated by

centrifugation. The solid was washed several times with a mixture of ethanol/hexane/toluene in the mole ratio 1:1:1 and left to dry at room temperature. Other materials were also prepared by similar procedures. All experiments were carried out at 180 °C, 200 °C and 220 °C, the mole ratios (varied from 1:1 and 1:2) and the time of synthesis ranged between 10 min to 60 min. The same procedure was repeated however the solvent contained 5 mL of OLA and 5 mL of oleic acid for mole ratio 1:1. Scheme 5-2 shows a representation of the reaction procedure followed for the direct heating method.

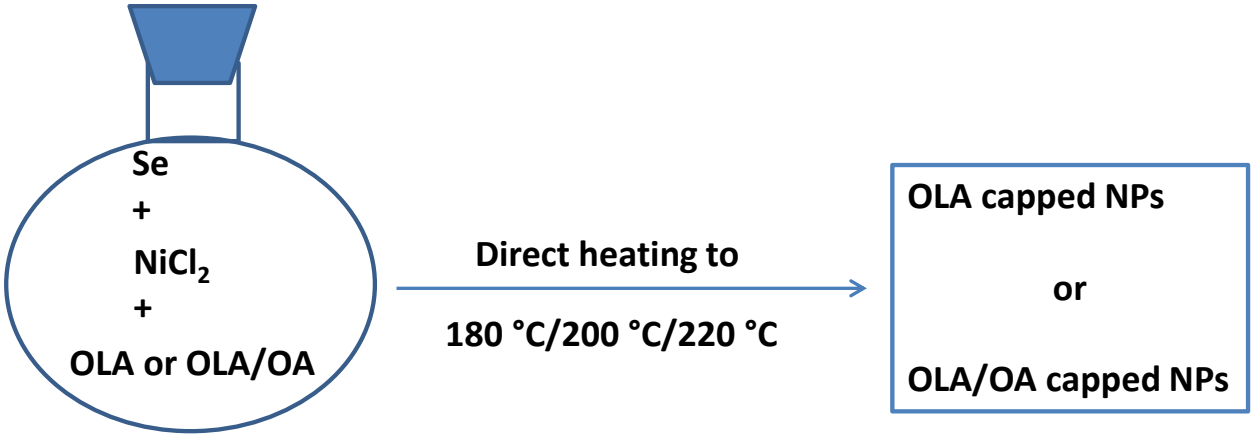

Scheme 5-2: Illustration of the synthetic procedure followed in the direct heating/non-hot injection method.

5.2.3 Characterization techniques

5.2.3.1 Optical characterization

A Varian Cary Eclipse (Cary 50) UV-vis spectrophotometer was used to carry out the absorption measurements. A Varian Cary Eclipse EL04103870 fluorescence spectrophotometer with a medium PMT voltage at an excitation wavelength of 250 nm was used to measure the photoluminescence of the particles. For both spectral analyses, the powders were dissolved in chloroform and placed in quartz cuvettes (1cm path length).

5.2.3.2 Structural characterization

The phase purity, crystallinity and preferred crystal orientation of the products were examined by using XRD on a Bruker MeasSrv (D2-205530)/D2-205530 diffractometer using secondary graphite monochromated CoKα radiation (λ 1.78897 Å) at 30 kV/30 mA. Measurements were taken using a glancing angle of incidence detector at an angle of 2°, for 2θ values between 10 - 90° in steps of 0.026° with a step time of 37 s and at a temperature of 25 °C.

The sample sizes and morphologies were determined by transmission electron microscopy (TEM) carried out on a FEI Technai T12 TEM microscope operated at an acceleration voltage of 200 kV with a beam spot size of 20 - 100 nm in TEM mode. The HRTEM images were obtained from a JEOL JEM-2100 microscope with a LAB6 filament and an EDS detector, operated at 200 kV. The samples were prepared by placing a drop of the suspended nanoparticles in chloroform, on a carbon-copper grid. The grid with the sample was then allowed to dry at room temperature. The morphology of the formed nanocrystals were also characterized by SEM analysis using an FEI Nova Nanolab 600 FIB/SEM instrument operating at 30 kV.

5.3 Results and Discussion

The size and shape control of nanocrystals, (which later determine the overall properties of NCs) is highly correlated to the kinetics of nucleaction and growth processes. As discussed in chapter 2 section 2.3.2.3, it is clear that the concentration of the existing monomer in the reaction solution plays a key role in shape determination and shape evolution. Just to mention, by increasing the reaction temperature, the concentration of the monomer is increased. This in turn increases the monomer diffusion rate which subsequently elevates the monomer flux. A high monomer flux is known to favour kinetic controlled and anisotropic

growth (1D) while low fluxes favours thermodynamic control and leads to isotropic growth (3D). The coordinating ligand also plays a critical role during the growth of the nanocrystal and size distribution. By choice of a facet specific ligand/surfactant can result in variation in the relative growth rates of different facets thus leading to the formation of anisotropic shapes by promoting inequivalent growth. Similarly, interacting both with the solvent and with the crystal surface, the ligand layer also modulates the thermodynamic stability of the facets, thereby influencing the end states of the nanocrystal growth. In general, the following reaction parameters are of important concern during the synthesis of nanocrystals: (i) the reaction temperature and time, (ii) the reactivity and the concentration of precursors, (iii) the effect of solvent, surfactant, and the synthetic method. This section therefore demonstrates the effect of the above mentioned parameters on nickel selenide nanostructures.

5.3.1 Synthesis of Ni_3Se_2 nanostructures via hot injection in HDA (with TOP)

In this section, Ni_3Se_2 nanostructures were prepared via the decomposition of the metal precursors in hot HDA at 180°C and 200°C. The effect of the temperature and time of synthesis on the nanoparticles properties were examined via TEM, XRD, UV-vis and PL.

5.3.1.1 Properties of Ni_3Se_2 quantum dots synthesized at 180 °C

The effects of the reaction parameters on the structural properties of the nanoparticles were determined using TEM and XRD and used to verify the crystal phase and crystallinity of the final nanoparticles. The results are presented in Fig. 5-2. Apart from the intense peaks at the lower angles (between 20° and 30°) which were associated with the capping agent, most of the other peaks could be indexed to rhombohedral Ni_3Se_2. The values were consistent with the value given in the standard card JCP2.2CA:00-085-0754 and the lattice parameters were a = 6.03382 and c = 7.25102 and a space group of R32 (155). The patterns become more

intense with increasing reaction time, spectrum (c) has more intense peaks compared to (b) and (a), an indication that crystallinity improved with time. The size of the nanocrystals in the 10 min sample were smaller compared to the 30 min and 60 min samples and thus resulting in broader. This is consistent with Ostwald ripening that is also time driven. However a few peaks marked with the * associated to rhombohedral NiSe of PDF number JCP2.2CA:00-018-0887 were also observed. The NiSe peaks appeared to decrease thus implying that longer reaction led to the dissolving (transformation) of the NiSe phase thereby resulting into a more pure phase of Ni_3Se_2.

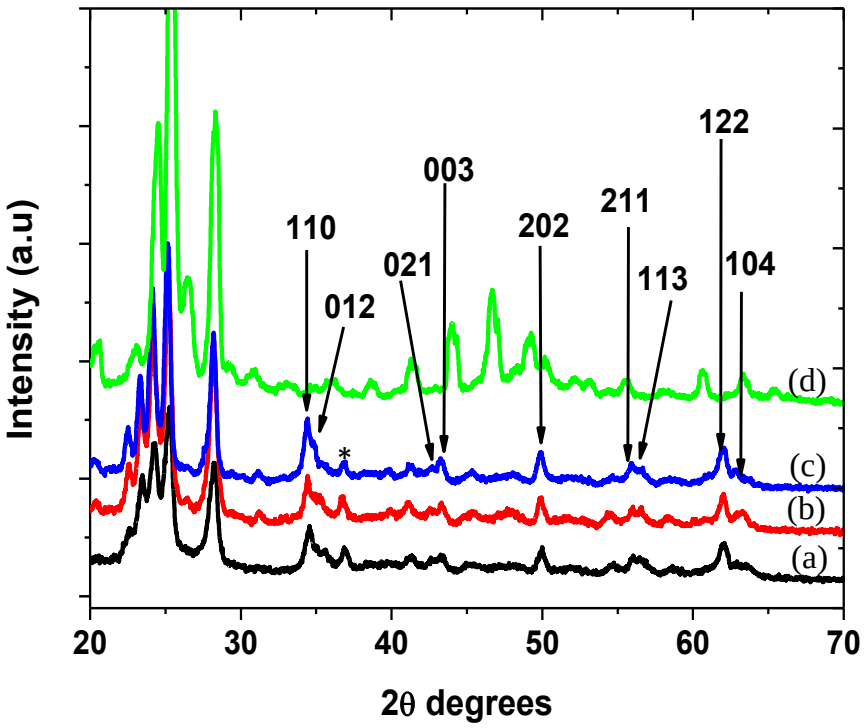

Figure 5-2: XRD pattern of Ni_3Se_2 synthesized in HDA at 180 °C after (a) 10 min, (b) 30 min (c) 60 min and (d) is the XRD pattern for pure HDA.

The morphologies and sizes of the as-obtained Ni_3Se_2 nanocrystals were characterized using TEM. Fig. 5-3 shows the TEM images of Ni_3Se_2 nanocrystals obtained at 180 °C in HDA at

different durations. It demonstrates that the particles consisted of nearly spherical nanocrystals whose diameters increased with reaction time due to Ostwald ripening. 10 min after nucleation, the seeds grew into nearly monodispersed nanocrystals as shown in Fig. 5-3a with an average particle size of 3 nm. On increasing the time to 30 min (Fig. 5-3b), the particle sizes increased to approximately 7 nm as a result of ripening process without compromising the uniformity in the sizes and shapes of the nanocrystals. However, a further increase in time resulted in particles that appeared agglomerated with a slight increase in size to 12 nm. The nanocrystals were also seen to arrange themselves in a thread-like pattern; an indication of probable orientated attachment of the particles at this duration of synthesis as depicted in Fig. 5-3c. The nanoparticles sizes increased with the increasing reaction time from an average of 3 nm to 7 nm and finally to 12 nm according to histograms (b), (d) and (f) showing the size distribution at 10 min, 30 min and 60 min respectively.

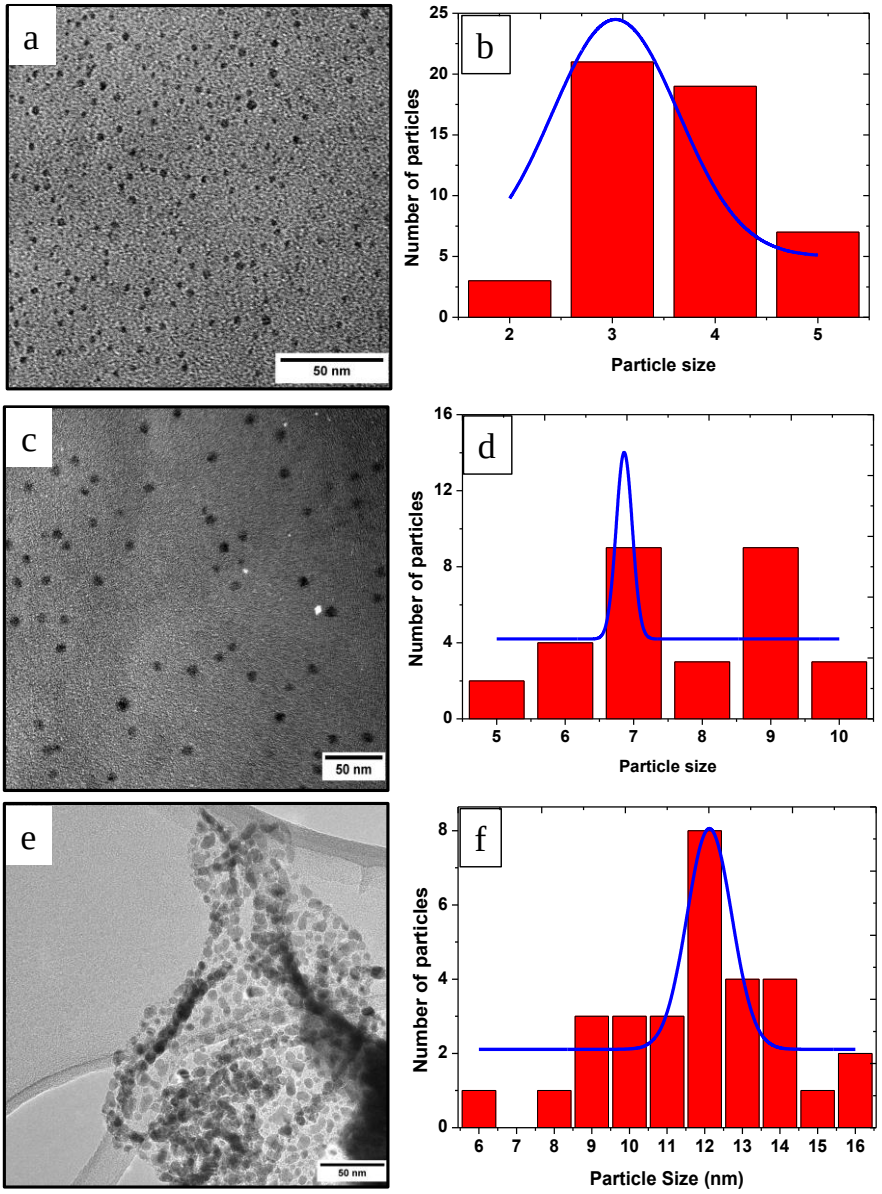

Figure 5-3: TEM images of Ni_3Se_2 synthesized in HDA at 180 °C after (a) 10 min, (c) 30 min and (e) 60 min. The particles sizes demonstrated Ostwald ripening process.

The results of the optical properties of nickel selenide nanoparticles synthesized at 180 °C in HDA are shown in Fig. 5-4 and Fig. 5-5. The absorption spectra as evident in Fig. 5-4 appeared as a series of overlapping peaks with the 10 min and the 30 min sample exhibiting three excitonic peaks. The first, second and third excitonic peaks for the 10 min sample are positioned at 355 nm, 374 nm and 394 nm (Fig. 5-4a) whilst those of the 30 min sample are

positioned at 357 nm, 377 nm and 398 nm (Fig. 5-4b) respectively. The wavelength of each excitonic peak may be associated to either different transitions within the semiconductor nanoparticles or different nanoparticle sizes within the sample. In this case, based on the histograms from TEM images in Fig. 5-3 which indicated polydispersity within each sample, the multiple excitonic peaks were associated to the different nanoparticle sizes. The first excitonic peaks in the short wavelength region were as a result of photon absorption by the smaller nanoparticles. Though the difference between the position of the first excitonic peaks and subsequently the second and third for the 10 min and the 30 min samples were relatively small, these nanoparticles exhibited Ostwald ripening process. The results indicated that the nanoparticle sizes increased with increasing reaction time, thus the slight red shift in the wavelength of the 30 min samples compared to the 10 min sample. The 60 min sample had the nanoparticles coming together as a result of orientation attachment thus forming clusters. This resulted into a tailing absorption spectrum as portrayed in Fig. 5-4c with excitonic peaks at 350 nm and 400 nm. There was also a disappearance of one of the excitonic peaks in the 60 min sample associated with the fact that most nanoparticles sizes were about 12 nm. The wavelengths of excitonic peaks of the three samples were blue shifted compared to the band gap which is 620 nm thus demonstrating quantum size effect experienced within the nanoparticles.

The overlapping natures of the absorption spectra were further confirmed by the emission spectra depicted in Fig. 5-5. The 10 min samples had three emission spectra centred at 348 nm, 401 nm and 469 nm respectively while the 30 min samples had emission peaks centred at 349 nm, 406 nm and 474 nm respectively. The wavelengths of these maximum emissions are red shifted from the absorption peaks. The 60 min sample experiences near band edge emission such that the emission peaks are centred at 350 nm and 400 nm respectively, wavelengths equal to the absorption wavelengths.

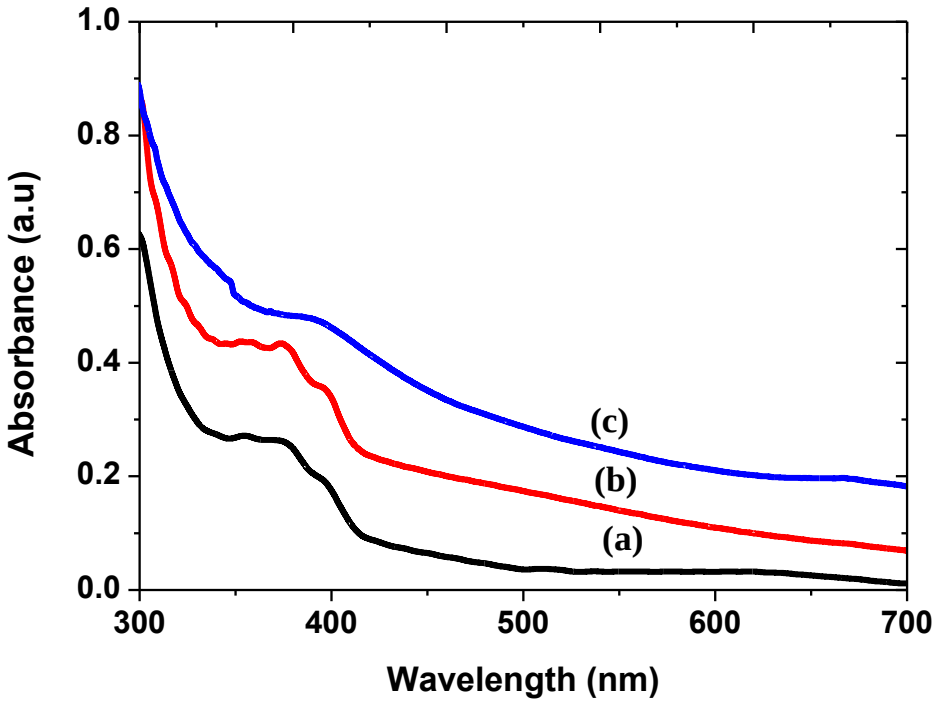

Figure 5-4: Absorption spectra of quantum dots synthesized at 180 °C in HDA for (a) 10 min, (b) 30 min and c) 60 min.

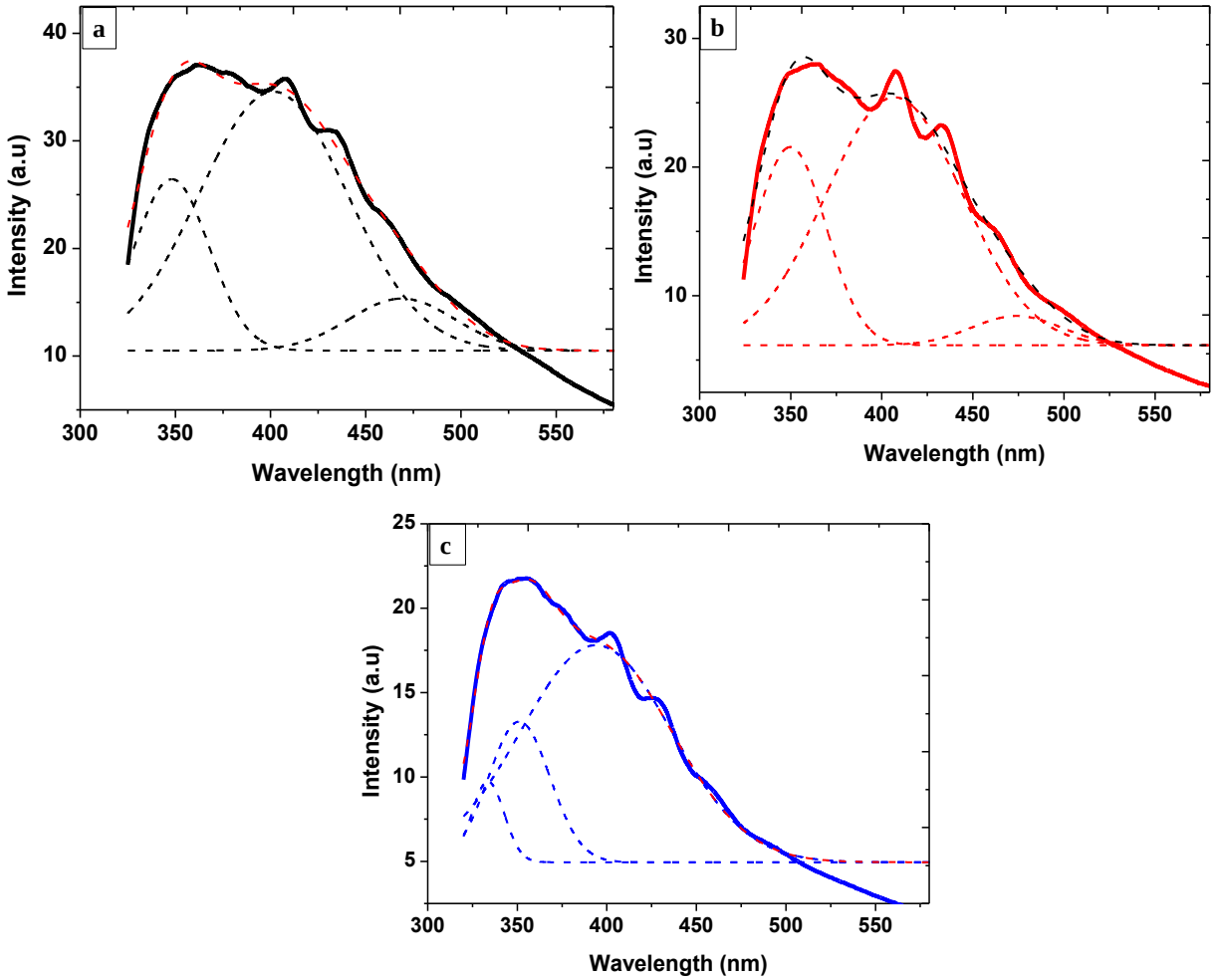

Figure 5-5: The emission spectra of quantum dots synthesized in HDA at 180 °C at (a) 10 min, (b) 30 min and (c) 60 min.

5.3.1.2 Properties of Ni_3Se_2 nanowires synthesized at 200 °C

XRD studies presented in Fig. 5-6 revealed that the nanowires had a rhombohedral Ni_3Se_2 crystal phase that belonged to a space group R32 (155) with cell parameters a = 6.03382 and c = 7.25102. Almost all the peaks in the pattern corresponded to that given in the card JCP2.2CA:00-085-0754. The peaks of the sample obtained at 60 min (Fig. 5-6c) had more intense and better diffracted peaks compared to those from the 30 min (Fig. 5-6b) and the 10 min (Fig. 5-6a) samples. This implied that the crystallinity of the nanowires improved with an increase in time of synthesis. The peaks marked with (*) were associated with rhombohedral

NiSe of card JCP2.2CA:00-018-0887. The NiSe peaks disappeared at longer synthesis time thus implying that longer reaction led to the dissolving of the NiSe phase thereby resulting into a more pure phase of Ni_3Se_2.

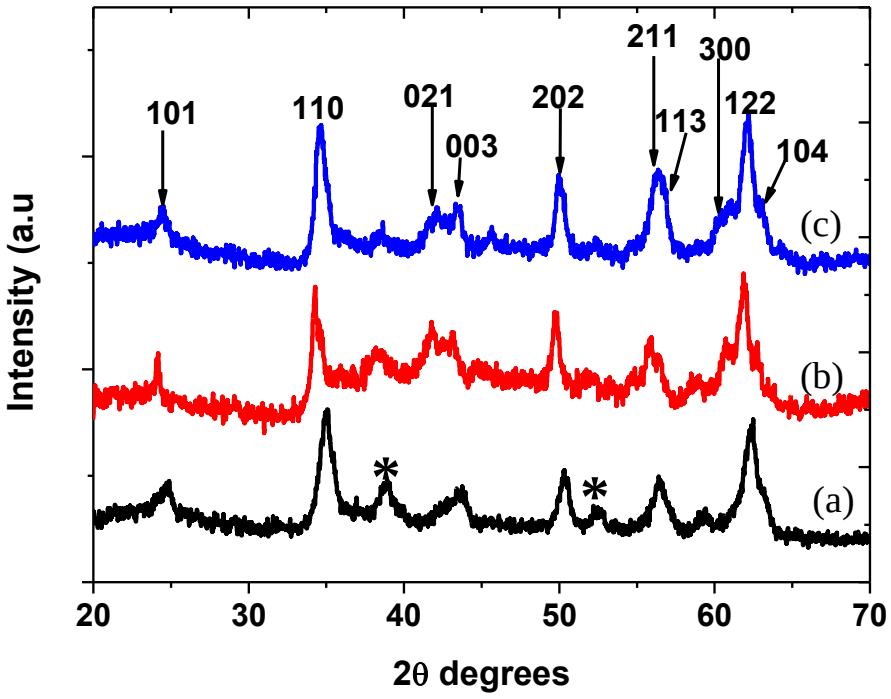

Figure 5-6: XRD pattern of Ni_3Se_2 synthesized in HDA at 200 °C after (a) 10 min, b) 30 min and c) 60 min.

Fig. 5-7 shows the TEM images of the products when the reaction is carried out at 200 °C with HDA as the capping agent. It clearly reveals that after nucleation, the seeds grew towards each other and a secondary growth was experienced in a one dimension pattern/cluster as illustrated in the 10 min sample (Fig. 5-7a and 5-7b). Also evident within the sample are the non-uniform structure suspected to be NiSe nanostructures. In the 30 min sample (Fig. 5-7c and 5-7d), the clusters developed into nanowires with average length of 400 nm and diameter of 4 nm. As time was prolonged to 60 min, the nanowire agglomerated.

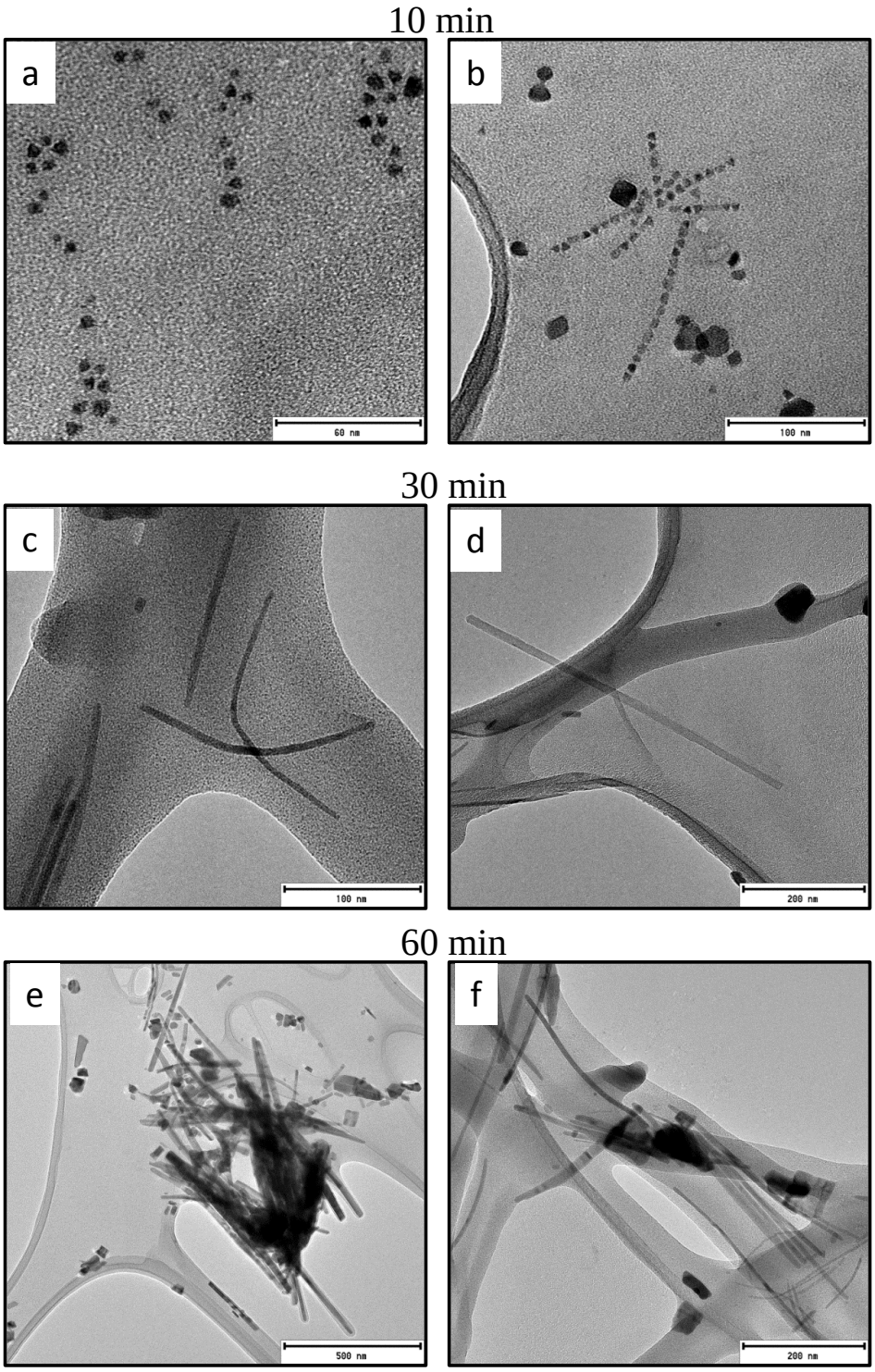

Figure 5-7: TEM micrographs of Ni_3Se_2 nanocrystals obtained at (a) and (b) 10 min, (c) and (d) 30 min, (e) and (f) 60 min in HDA at 200 °C.

Details of the optical properties of Ni_3Se_2 nanoparticles synthesized at 200 °C are presented in the absorption and emission spectra. The absorption profile displayed in Fig. 5-8 revealed that the 10 min sample exhibited an excitonic peak at 366 nm. This was contrary to the 30 min and the 60 min samples which portrayed two excitonic peaks. The first and the second excitonic peaks of the 30 min samples were positioned at 313 nm and 367 nm while the 60 min ones were positioned at 317 nm and 372 nm respectively. From the TEM images in Fig.5-7a, the nanocrystals appeared to have the same relative sizes thus the existence of just one excitonic peak in the 10 min sample. However the spectrum portrayed a tailing behaviour which was associated to the presence of other shapes as seen in Fig. 5-7b. The existence of the two excitonic peaks in the 30 min and the 60 min samples were attributed to the possibility of polydispersity. The first excitonic peak was as a result of the absorption by the shorter nanowires and the longer ones contributed to the second excitonic peak. The presence of other shapes, which according to XRD were associated to NiSe, and agglomeration of the nanowires as depicted in Fig. 5-7e contributed to the tailing behaviour of the spectra.

The emission spectrum displayed in Fig. 5-9 illustrated that the nanostructures emitted at slightly longer wavelengths compared to their excitonic peak positions in the absorption spectrum. The emission maximum for the 10 min sample was centres at 466 nm (Fig. 5-9a), thus exhibiting a stoke shift of 100 nm from the absorption spectrum. The emission curve deviated from the Gaussian distribution curve thereby resulting in a broad curve. This confirmed uneven distribution of nanoparticles and the effect of other shapes. The 30 min and the 60 min samples displayed two emission peaks associated with the two excitonic peaks as displayed in Fig. 5-9 (b) and (c) respectively. For the 30 min, the peaks were centred at 393 nm and 477 nm resulting in a stoke shift of 80 and 110. The 60 min sample had its peaks centred at 397 nm and 482 nm resulting in a stoke shift of 80 and 110 nm. The values of the Stokes shifts for all the nanoparticles suggested good passivation. The fitted emission spectra

for the second excitonic peak also deviated from the Gaussian distribution curve implying a non-uniform distribution. However all the nanoparticles synthesized at 200 °C in HDA showed high level of quantization from the bulk which has a band gap of 620 nm.

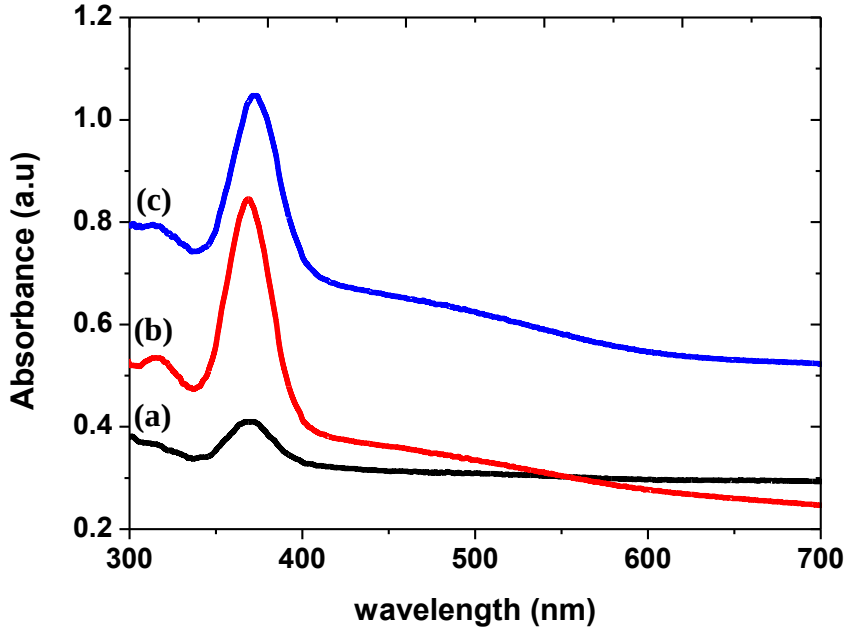

Figure 5-8: Absorption spectra of the Ni_3Se_2 synthesized at 200° C at (a) 10 min, (b) 30 min and (c) 60 min in HDA.

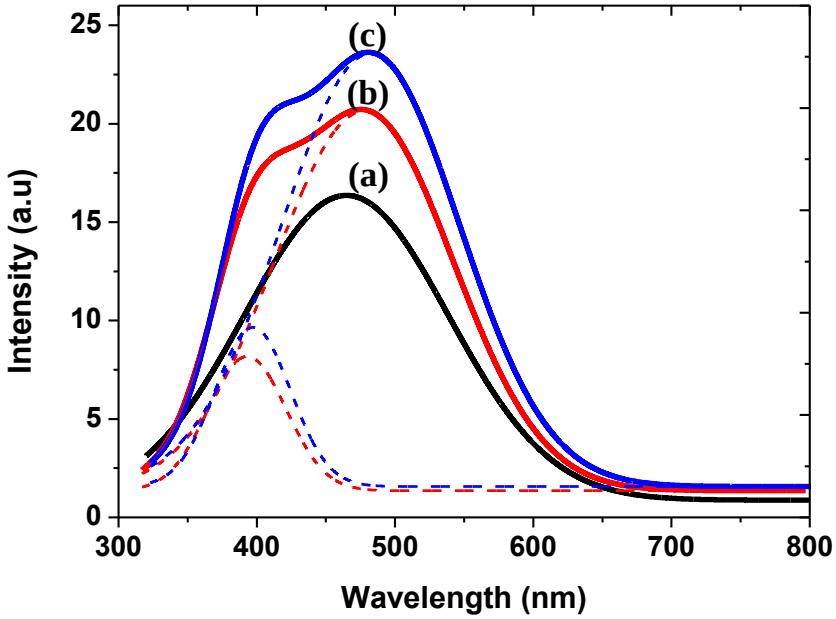

Figure 5-9: Emission spectra of the Ni_3Se_2 synthesized at 200° C at (a) 10 min, (b) 30 min and (c) 60 min in HDA.

The findings above were consistent with the monomer-concentration-dependent growth model where a low monomer concentration yields spherical particles while higher monomer concentrations may yield anisotropic nanostructures. To achieve higher monomer concentrations, a fast decomposition rate of the metal precursor was required, which was necessitated by the use of high reaction temperatures, in this case 200 °C. Thus, the spherical Ni_3Se_2 dots obtained upon the injection of metal precursors at 180 °C may be due to low monomer concentration at that temperature while nanowires were obtained upon injection of the metal precursors at 200 °C, which provided a higher monomer influx.

5.3.2 Synthesis of Ni_3Se_2 nanostructures in OLA

In this subsection, two sets of experiments were conducted; one where the metal precursors were dispersed in TOP then injected into the hot solvent (hot injection method) and the other via a non-hot injection where the metal precursors were added to OLA directly then heated

quickly to the working temperature. The effect of the injection temperature and the duration of synthesis on the properties of the obtained nanoparticles were studied via TEM, XRD, UV-vis and PL. From the observations from the previous studies discussed above, 60 min resulted to agglomerated nanoparticles. Therefore, herein, 10 min and 30 min were the only investigated reaction times.

5.3.2.1 Synthesis of nickel selenide nanostructures via hot injection in OLA (with TOP)

5.3.2.1.1 Properties of nanostructures obtained at 200 °C

Rhombohedral Ni_3Se_2 nanostructures were obtained in the 10 min and 30 min samples as depicted in Fig. 5-10 (a) and (b) respectively. The peaks were indexed according to the card number JCP2.2CA:00-085-0754 and the lattice parameters were a = 6.03382 and c = 7.25102 with a space group of R32 (155). The 30 min sample had more intense diffraction peaks compared to the 10 min sample. This suggested that the crystallinity of the nanoparticles improved with prolonged time of synthesis.

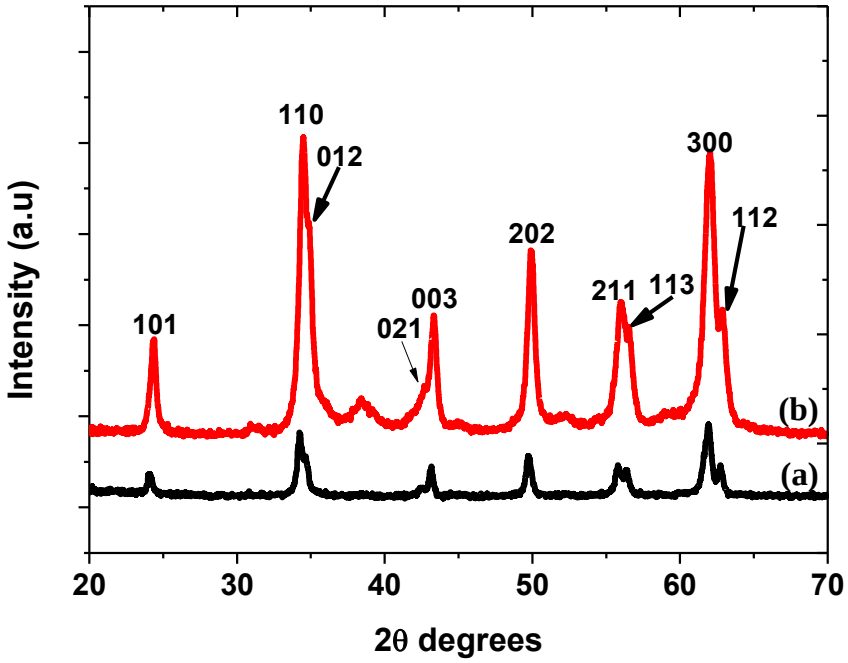

Figure 5-10: XRD patterns for Ni_3Se_2 fabricated in OLA at 200 °C for (a) 10 min and (b) 30 min.

TEM micrographs of the products obtained in the presence of OLA at different reaction times are shown in Fig. 5-11. The particles synthesized in 10 min shown in Fig. 5-11a depicted particles with triangular and diamond like morphologies. As the time was prolonged to 30 min, particles with rectangular-like shapes and cubes were observed as shown in Fig. 5-11b. The particle sizes also increased as a result of Ostwald ripening.

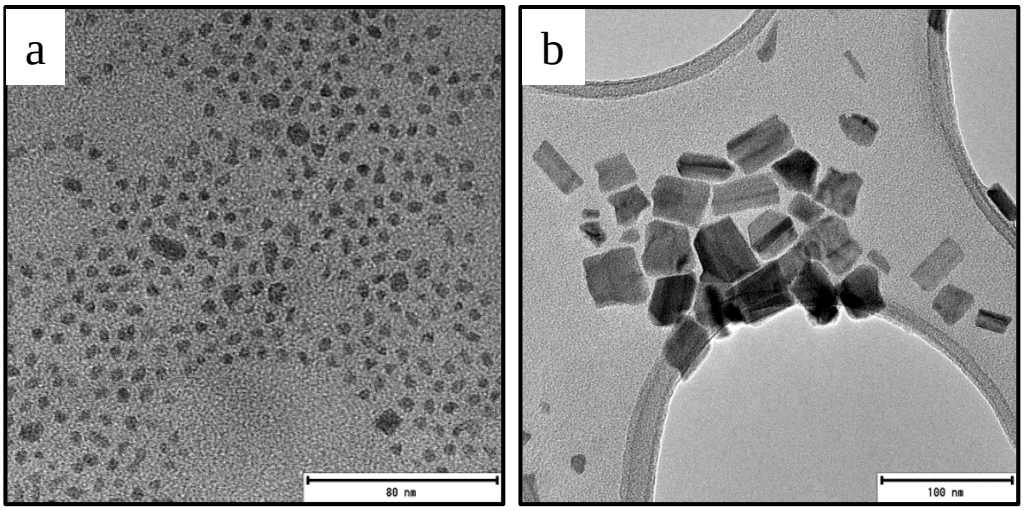

Figure 5-11: TEM images of Ni_3Se_2 synthesized in OLA at 200 °C after (a) 10 min and (b) 30 min.

To determine the optical properties of the Ni_3Se_2 nanoparticles, absorption spectra of the nanoparticles were obtained and the results are presented in Fig. 5-12. The nanoparticles synthesized at 10 min exhibited an excitonic peak centred at 387 nm as shown in Fig. 5-12a. The 30 min had its excitonic peak slightly red shifted because of their bigger sizes at 396 nm as depicted in Fig. 5-12b. The peak also became more distinct with increasing particle size. The emission spectra displayed in Fig. 5-13 showed that the 10 min sample represented by spectrum (a) had a narrow Gaussian distribution curve signifying a nearly monodispersed particle distribution. However 30 min resulted in non-uniform distribution and polydispersed nanoparticles confirmed by the broad emission spectrum (b). Emission maxima for both the 10 min and 30 min sample were centred at 486 nm. Despite the broad curve, all the wavelength positions of both the spectra were blue shifted compared to bulk which occurs at 620 nm thereby exhibiting quantum size effects.

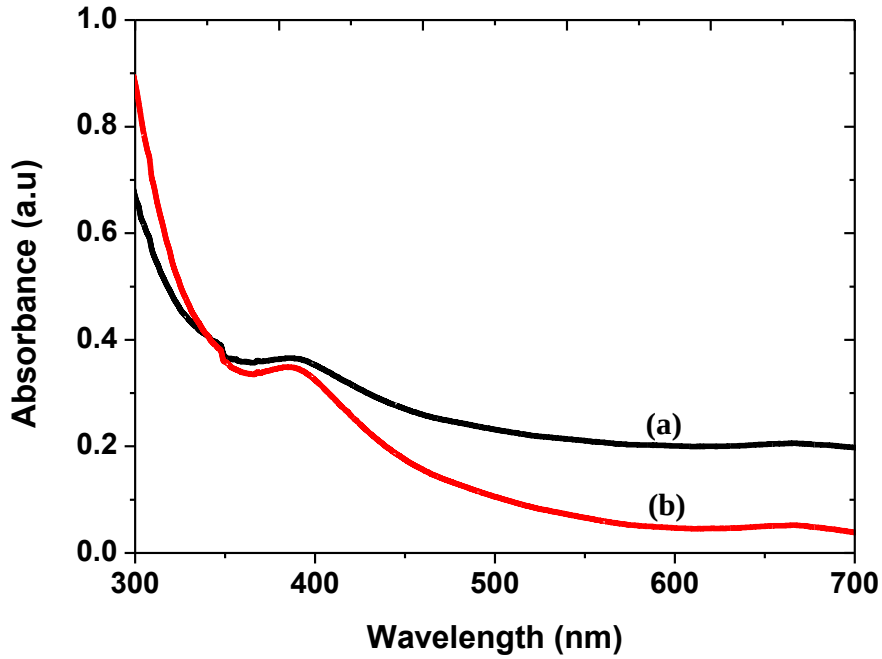

Figure 5-12: Absorption spectra of Ni_3Se_2 synthesized in OLA at 200 °C after (a) 10 min and (b) 30 min.

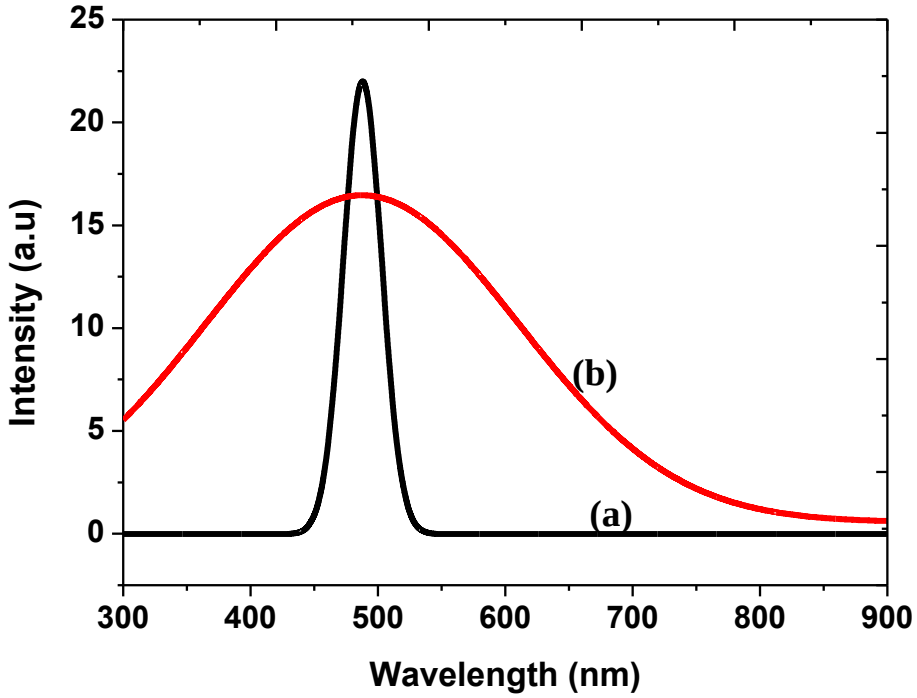

Figure 5-13: Emission spectra of Ni_3Se_2 synthesized in OLA at 200 °C after (a) 10 min and (b) 30 min.

5.3.2.1.2 Properties of nanostructures obtained at 220 °C

Fig. 5-14 shows the XRD patterns of the as-prepared Ni_3Se_2 nanocrystals synthesized at 220 °C indicating a pure phase compound as the peaks were indexed according to the standard of card JCP2.2CA:00-085-0754. The peaks were strong and narrow which indicated good crystallinity of both samples obtained after 10 min (Fig. 5-14a) and 30 min (Fig. 5-14b). There was a slight shift in the peak positions for the two samples associated with the nanorods undergoing stress then breaking at longer reaction times. The peaks marked with (*) are associated with Ni_3Se_2. However they match the standard diffraction pattern of card JCP2.2CA:00-019-0841.

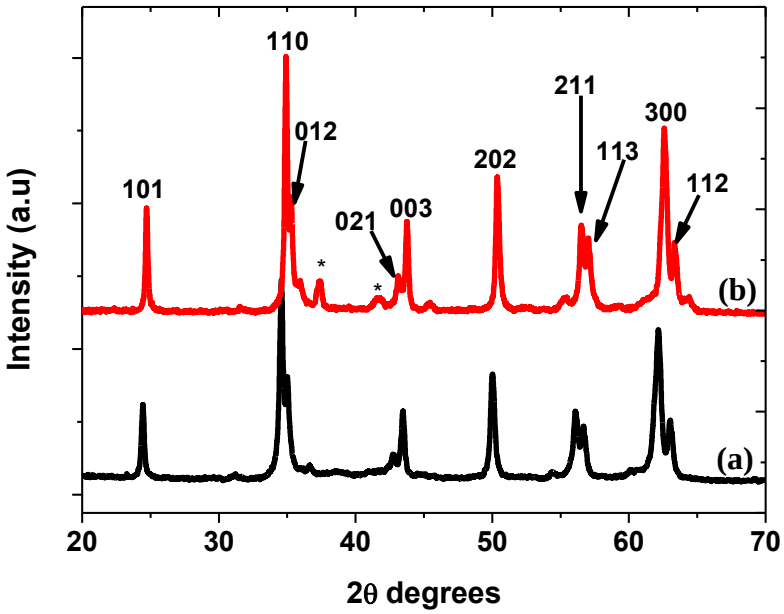

Figure 5-14: : XRD spectra of Ni_3Se_2 synthesized in OLA at 220° C for (a) 10 min and (b) 30 min.

The TEM images showed that both the samples contained nanorods of Ni_3Se_2. At lower reaction times (10 min), the sample consisted of nanorods and rectangular shaped particles as portrayed in Fig. 5-15a. The nanorods increased in size with increased reaction time to 30

min (Fig. 5-15b). They were seen to increase in length and still exhibit the polydispersity with the rectangular-like nanostructures also observed. The formation of nanorods at 220 °C was attributed to an increase in monomer concentration as a result of the slightly higher reaction temperature. The higher temperature increased the monomer diffusion rate thereby favouring a kinetic controlled growth; which subsequently favoured the anisotropic growth. The polydispersity was also associated with the high temperature used during synthesis [17].

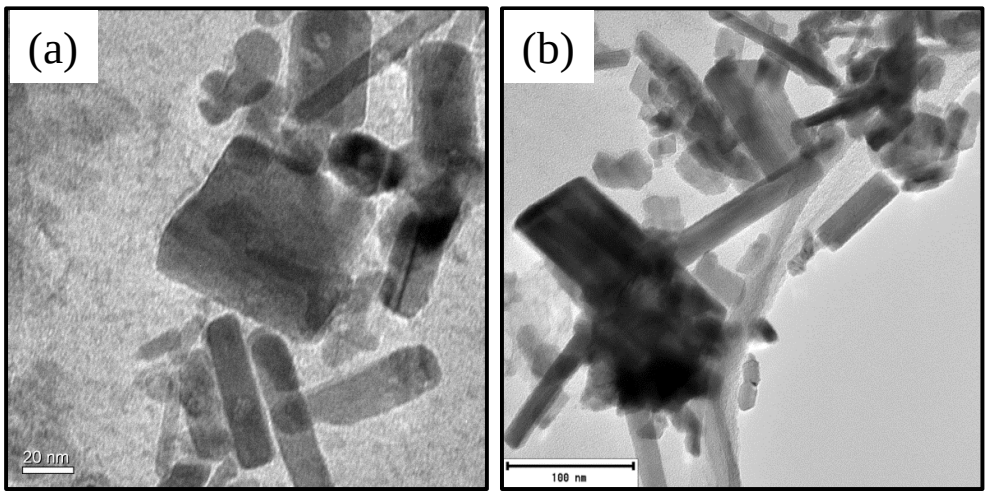

Figure 5-15: TEM images of Ni_3Se_2 synthesized in OLA at 220 °C after a) 10 min and b) 30 min.

The optical properties were determined by analysing their absorption and emission spectra. The absorption spectra presented in Fig. 5-16 revealed that the as-prepared nanoparticles exhibited multiple excitonic peaks. From Fig. 5-16a it was evident that the 10 min sample had its first, second and third excitonic peaks at 324 nm, 373 nm and 457 nm respectively. The 30 min samples had its peaks positioned at 317 nm and 368 nm; after which the nanoparticles continued to absorb into the longer wavelengths. As was observed in the TEM image in Fig. 5-15b, the nanoparticle population contained different shapes and sizes of the nanorods and the rectangular-like nanostructures. The non-uniform population resulted in a continuous absorption into the longer wavelength as shown in Fig. 5-16b. Despite this, the

nanoparticles showed good quantum confinement. The emission spectra portrayed in Fig. 5-17 were red shifted from the excitonic peaks. The 10 min samples as shown in Fig. 5-17a had their emission maximum wavelength positioned at 427 nm, 486 nm and 538 nm for the first second and third excitonic peaks respectively. Similarly, the 30 min sample (Fig. 5-17b) also had its first and second emission peaks at 427 nm and 486 nm respectively. Two other emission peaks were exhibited by the 30 min sample at 536 nm and 598 nm. This confirmed that the continuous absorption in the longer wavelengths occurred as a result of an uneven population caused the emissions at these wavelength positions.

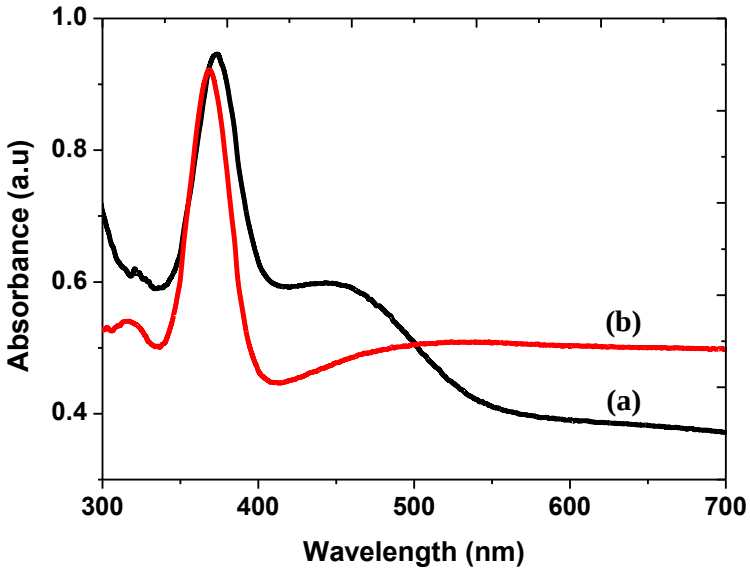

Figure 5-16: The absorption spectra of the Ni_3Se_2 fabricated in OLA at 220 °C for (a) 10 min and (b) 30 min.

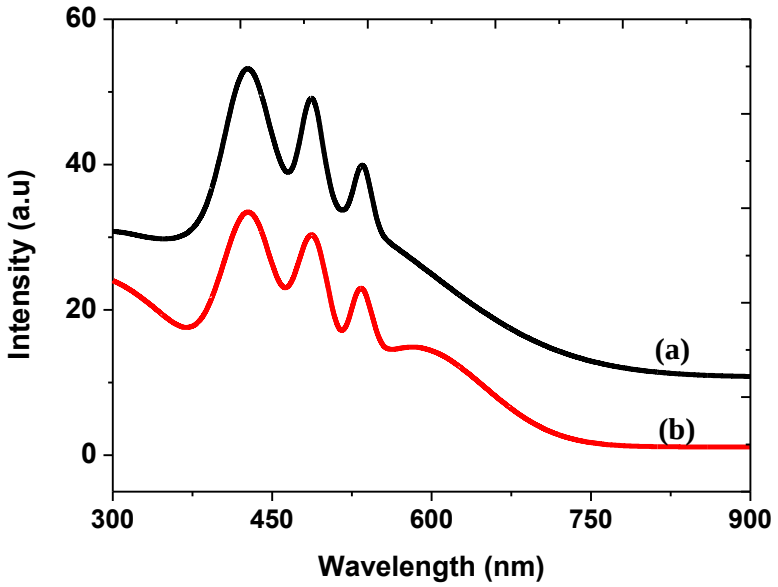

Figure 5-17: The emission spectra of the Ni_3Se_2 fabricated in OLA at 220 °C for a) 10 min and b) 30 min.

The hot injection method involved the use of TOP to disperse the metal precursor. As discussed in chapter 2, ligands/surfactants can manipulate the thermodynamics and the kinetics of shape evolution through their binding process to the surface of the nanoparticle and by being part of the monomer in the solution. Presumably in this case, TOP was part of the monomer in the solution since the starting materials were TOPSe and TOP-$NiCl_2$; and it might have bonded to specific facets during synthesis. As such, despite increasing the temperature and using HDA and OLA as surfactants, Ni_3Se_2 was the stoichiometry obtained in all reaction setups. Therefore, it is in order to conclude that the presence of TOP in the reaction mixture determined the stoichiometry while other factors such as HDA and OLA controlled the shape of the nanocrystals.

5.3.3 Synthesis of nickel selenide nanostructures via direct heating method (without TOP)

5.3.3.1 Synthesis of NiSe at mole ratio 1:1

At mole ratio (Ni/Se) 1:1, the influence of reaction temperature on the products was investigated. The structural properties were then studied using TEM, XRD and SEM, while the optical properties were analysed using UV and PL spectra. The two temperatures used were 180°C and 200 °C.

Fig. 5-18 shows the XRD patterns of samples fabricated at (a) 180° C and (b) 200° C for 30 min at mole ratio 1:1. The 180° C sample gave a pattern (Fig. 5-18a) that matched to the diffraction pattern of monoclinic Ni_3Se_4 (wilkmanite, syn), JCP2.2CA:01-089-2020 with lattice parameters a = 12.15, b = 3.633, c = 10.45, a/b = 3.34 and c/b = 2.87641 of space group C2/m (12). The diffraction peaks were intense and sharp portraying that the Ni_3Se_4 nanostructures had relatively good crystallinity. On increasing the temperature to 200° C, both cubic $NiSe_2$ and monoclinic Ni_3Se_4 were obtained, with Ni_3Se_4 dominating (Fig. 5-18b). Cubic $NiSe_2$ (penroseite, syn) peaks correspond to a diffraction pattern of card number JCP2.2CA:00-011-0552 (marked by *) while the monoclinic Ni_3Se_4 was indexed to card number JCP2.2CA:01-089-2020. Orthorhombic $NiSe_2$ has been reported to occur almost exclusively as an alteration product of monoclinic Ni_3Se_4 while Ni_3Se_4 is also an alteration product of β-NiSe as a result of reduced nickel content [6]. In addition, cubic $NiSe_2$ is known to be the most thermodynamically stable phase of $NiSe_2$. Therefore, at 200 °C there was a likelihood of monoclinic Ni_3Se_4 transforming to $NiSe_2$; hence resulting in the presence of $NiSe_2$ diffraction peaks. In addition, the peaks located at values 2Θ = 38°, 53° and 59° are shared by both monoclinic Ni_3Se_4 and cubic $NiSe_2$ as illustrated in the appendix by the XRD pattern. The nanoparticles obtained at 180 °C exhibited sharper and more intense peaks

compared to those obtained at 200 °C indicating that they are relatively bigger in size and that they are more crystalline.

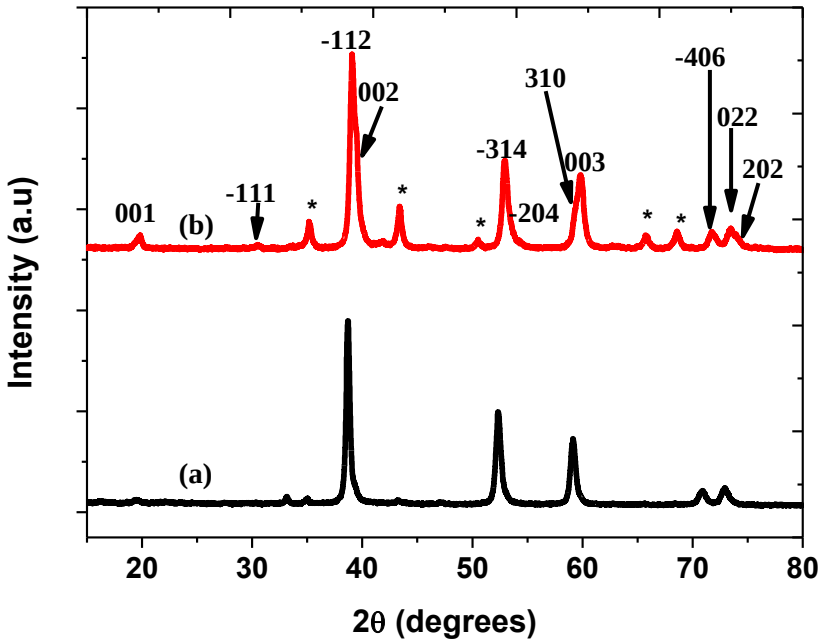

Figure 5-18: XRD patterns of nickel selenide nanoparticles synthesized at mole ratio (Ni/Se) 1:1 for 30 min at a) 180° C and b) 200° C. The matched indices are for the monoclinic Ni_3Se_4 while the (*) represent the cubic $NiSe_2$ peaks.

SEM was employed to investigate the morphology of the as-prepared nickel selenide nanoparticles. Fig. 5-19a show the SEM images of nanoparticles obtained at 180° C demonstrating that the products consisted of a large quantity of spherical nanoparticles that agglomerated to form clusters. The agglomeration was reduced when the reaction temperature was increased to 200° C as portrayed in Fig. 5-19b. In addition, the particle sizes appeared smaller for samples obtained at 200° C compared to the ones obtained at 180° C. This was in agreement with the slightly broader pattern observed during XRD analysis. The difference in sizes exhibited in the two samples were due to the fact that at relatively high

temperature (200 °C), more NiSe nuclei were formed before the growth process, thus more spheres of smaller diameters were formed.

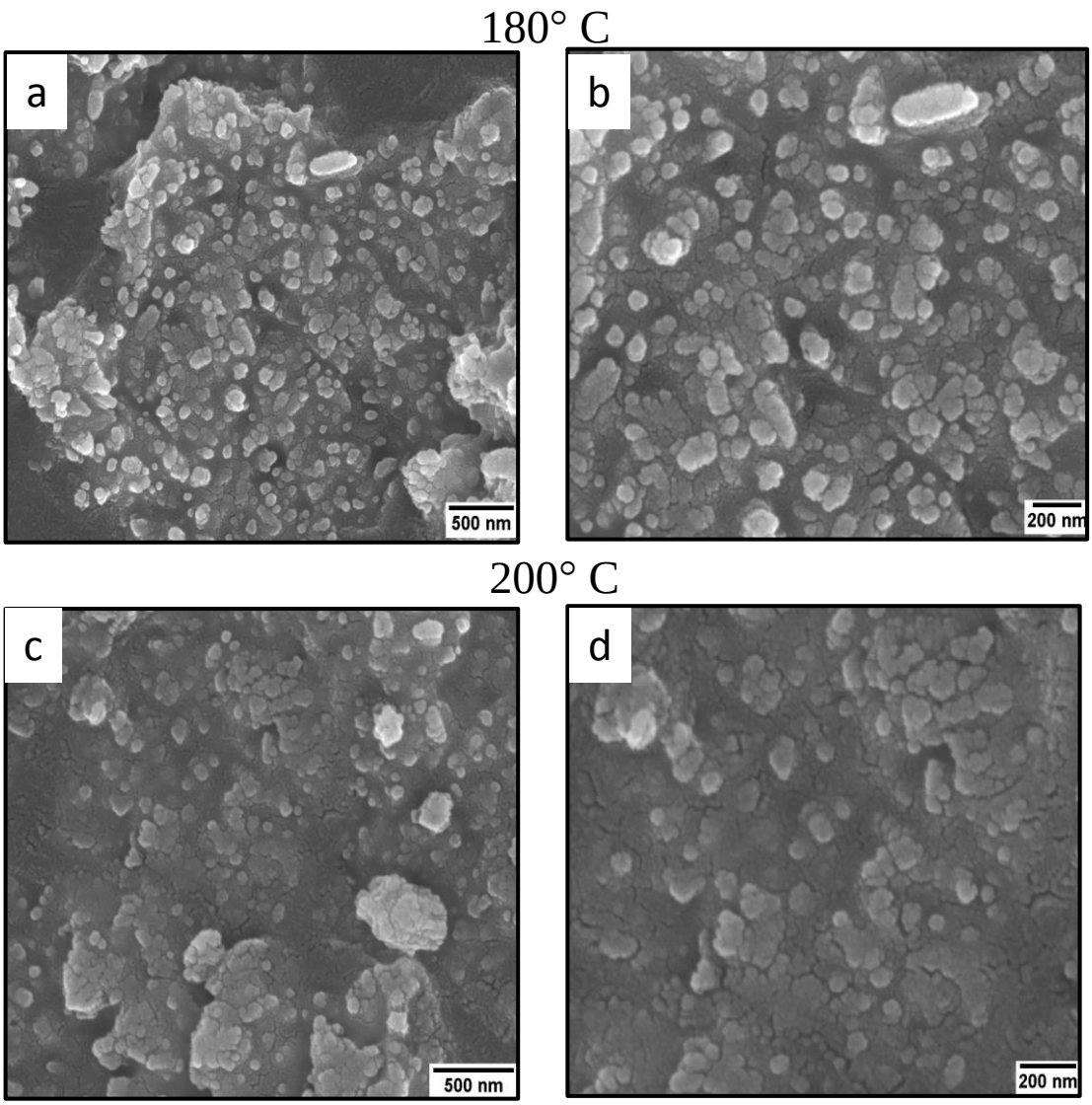

Figure 5-19: SEM micrographs of nanoparticles synthesized at mole ratio 1:1 for 30 min 180 °C with (b) being the higher showing the nanoparticles at higher magnification than a) and 200 °C with (d) representing the nanoparticles at higher magnification than (c).

Fig. 5-20 illustrates the absorption spectra of the as-obtained nanoparticles. The Ni_3Se_4 nanoparticles synthesized at 180 °C had an excitonic peak at 398 nm as shown in spectrum

(a). The 200 °C sample however depicted three excitonic peaks which were attributed to the existence of different phases in the sample. The peaks were positioned at 324 nm, 398 nm and 610 nm as shown in spectrum (b). The emission spectrum in Fig. 5-21 showed that the emissions were red shifted compared to their absorption spectrum. The 180 °C sample had its emission band centred at 408 nm as shown in spectrum (a). The Gaussian curve was narrow thus indicating that the particle population was nearly uniform and the Stokes shift was 81. The 200 °C sample exhibited three emission peaks positioned at 364 nm, 410 nm and 682 nm (Fig. 5-21b) with Stokes shifts of 40, 10 and 72 respectively. The emission band at 410 nm which is associated with the strongest excitonic peak at 398 nm was ascribed to near-band-gap emission resulting could have resulted from electrone hole recombination while the other weaker emissions were linked to possible defects with the nanoparticles [24]. Nanoparticles produced at both temperatures generally exhibited a good quantum confinement.

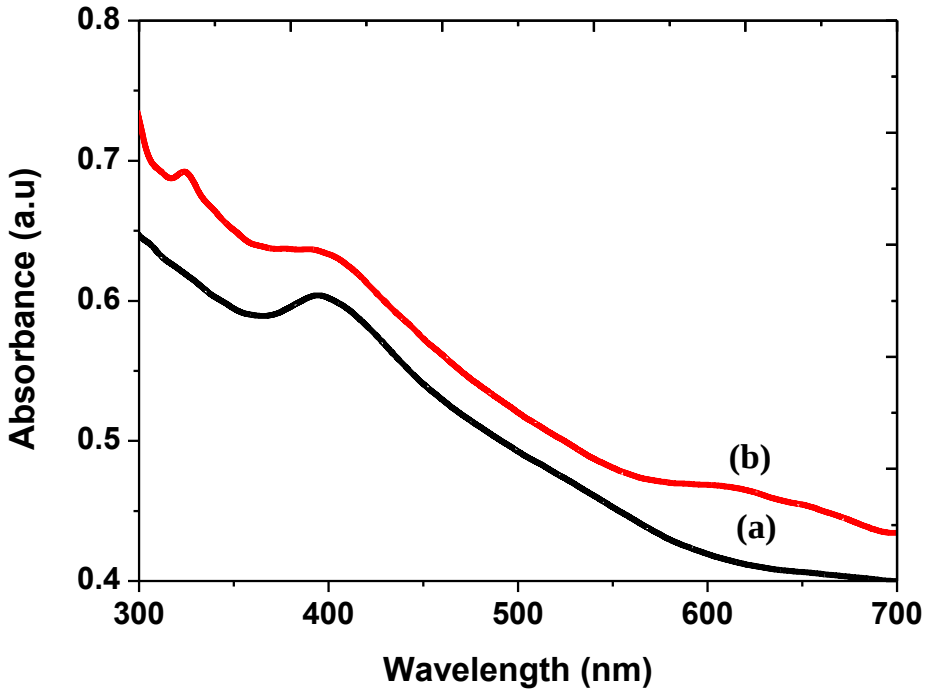

Figure 5-20: Absorption spectra of nanoparticles synthesized at mole ratio 1:1 for 30 min at (a) 180° C and (b) 200° C.

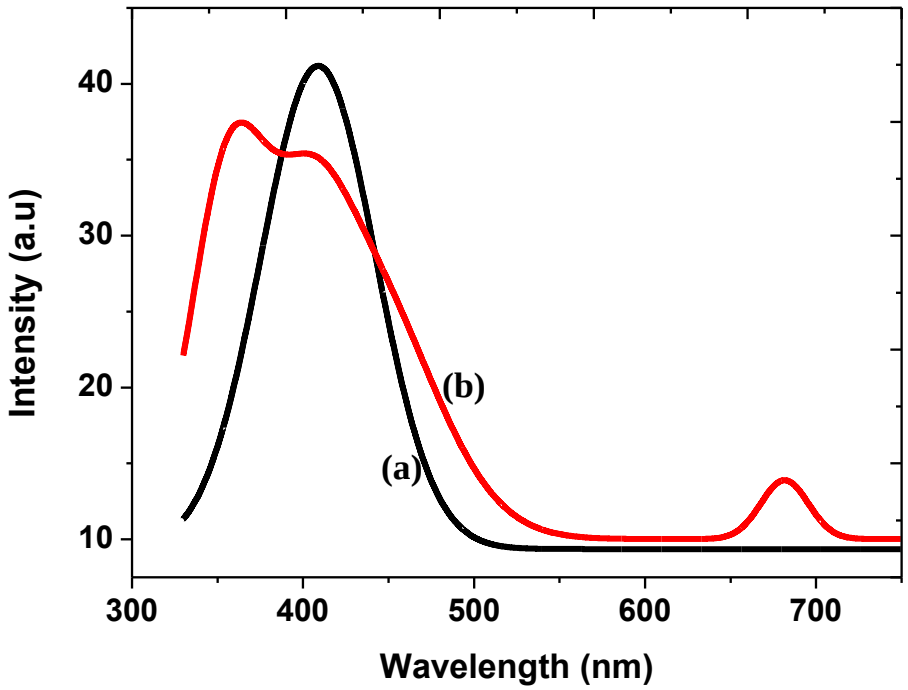

Figure 5-21: Emission spectra of nanoparticles synthesized at mole ratio 1:1 for 30 min at (a) 180° C and (b) 200° C.

5.3.3.1 Synthesis of Nickel Selenide at mole ratio 1:2.

In this section, the amount of selenium precursor used was doubled so that the reaction system could contain more selenium. The effect of this on the processed nanocrystals at different temperatures and reaction time were studied.

The XRD patterns of the samples obtained at (a) 180 °C, (b) 200 °C and (c) 220 °C are shown in Fig. 5-22. The controlled experiments over different reaction temperatures demonstrated the phase evolution of $NiSe_2$ from the orthorhombic phase to the cubic phase with the more thermodynamically stable phase forming at higher temperatures. At lower reaction temperatures (180 °C), the diffraction peaks predominantly matched the orthorhombic $NiSe_2$ (kullerudite) phase which was in agreement with the diffraction pattern of card JCP2.2CA:00-018-0886. This belonged to the space group Pnnm(58) with lattice

constants a = 4.89 Å, b = 5.96 Å and c = 3.67 Å; a/b = 0.82047 and c/b = 0.61577. However other peaks marked with * were also observed and they corresponded to those of the cubic $NiSe_2$ (penroseite, syn) phase of space group Pa-3 (205) with lattice parameter a = 5.9604 Å according to card JCP2.2CA:00-011-0552. The mixture of the orthorhombic and the cubic phase are clearly demonstrated in appendix A4. Increasing the temperature to 200 °C saw the reduction of peaks associated with the orthorhombic phase exhibited by the peaks labelled (101), (120), (210), (211) and (031) while the characteristic peaks of cubic phase became more intense as portrayed by the peaks labelled (200), (220), (221), (311), (230) and (321). However, the sample still comprised of both the phases. Upon further heating to 220 °C, only pure cubic $NiSe_2$ was obtained. Therefore it was deduced that in the synthesis of $NiSe_2$, at lower reaction temperatures resulted in the formation of orthorhombic $NiSe_2$ which gradually transformed into thermodynamically stable cubic $NiSe_2$ at higher reaction temperatures. This observation was in agreement with those reported by Yuan et al. [17].

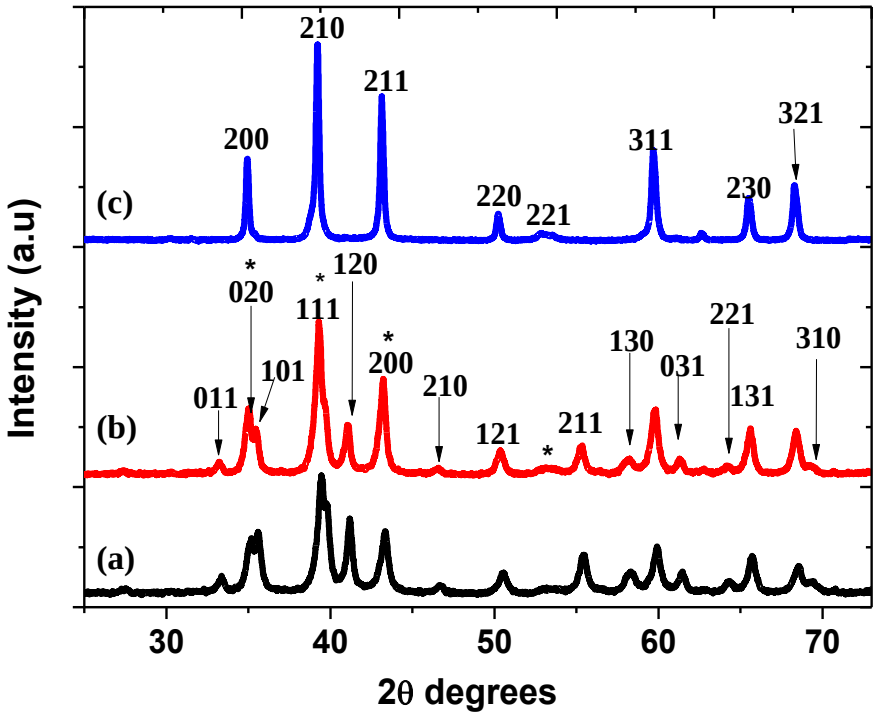

Figure 5-22: XRD patterns of $NiSe_2$ obtained at mole ratio 1:2 after 30 min showing phase evolution from orthorhombic $NiSe_2$ to thermodynamically stable cubic $NiSe_2$ at (a) 180 °C, (b) 200 °C and c) 220 °C.

SEM and TEM images were used to study the morphologies of the as-obtained particles. Fig. 5-23 (a) and (b) show the SEM images of the products obtained at 180 °C indicating that it comprised primarily of smaller spherical nanoparticles which subsequently aggregated together and formed clusters and elongations that joined the clusters together. The tips of the elongations that did not join the clusters were seen to contain a nanosphere. The elongations diminished with increase in reaction temperature to 200° C (Fig. 5-23 (c) and (d)) and the agglomeration was reduced as a result of different nucleation growth processes originating from the temperature change [25, 26]. More spherical nanoparticles are formed at this temperature though the sample was still polydispersed. Further increase of the temperature to 220° C resulted in particles with even bigger sizes as depicted in the TEM images of $NiSe_2$

(Fig. 5-23 (c) and (d)). For thermodynamic stability, the smaller spheres combined through an Ostwald ripening process to form the bigger spheres. The sizes of the spheres ranged from 50 nm to 150 nm.

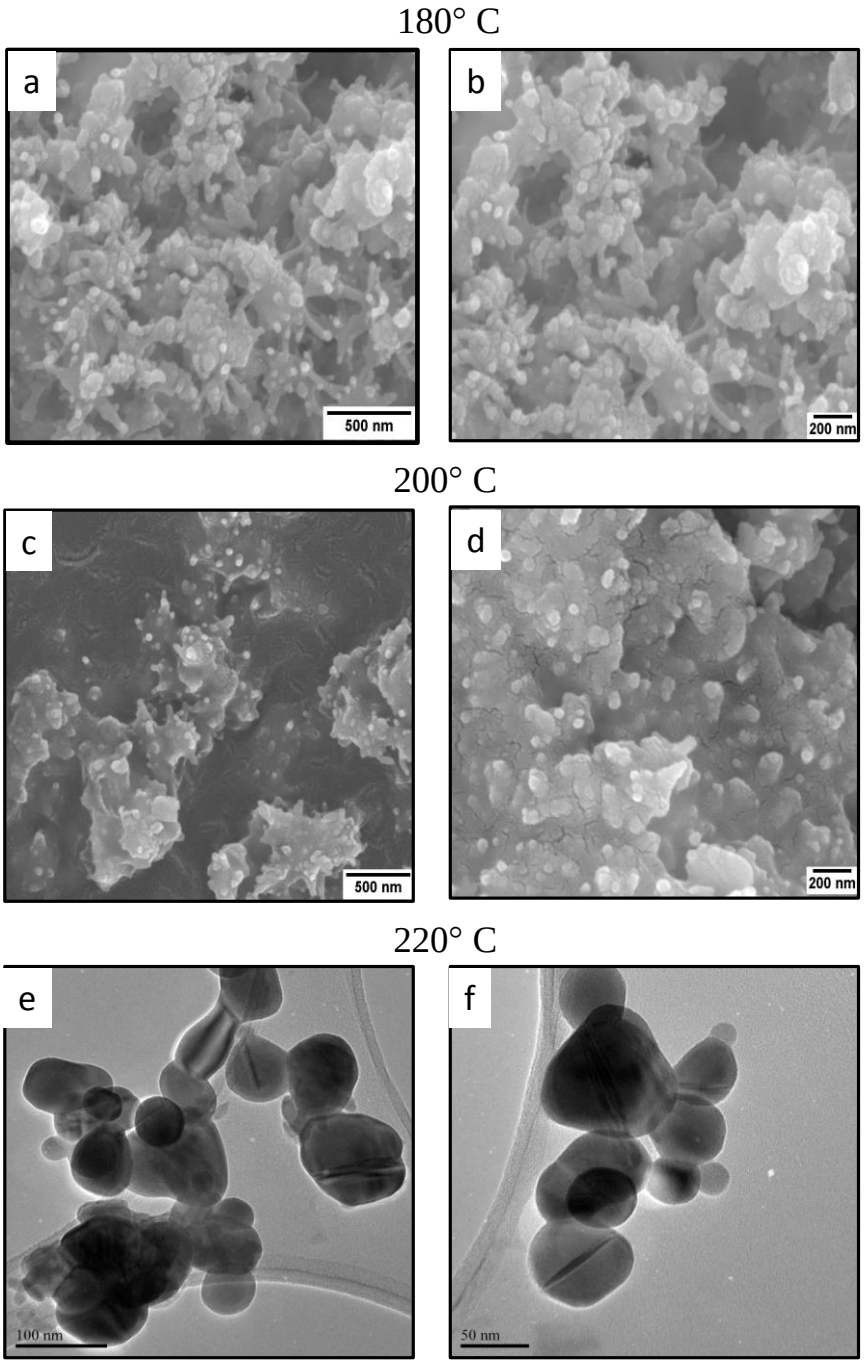

Figure 5-23: (a) and (b) are the SEM images of the $NiSe_2$ nanoparticles fabricated at 180 °C and 200 °C respectively while (c) are the TEM images of the particles fabricated at 220 °C. All these were obtained at a mole ratio 1:2 for a period of 30 min.

The position of the excitonic peak was observed to red shift with increasing synthesis temperature. In particular, the 180 °C, 200 °C and 220 °C samples had their peaks at 450 nm, 475 nm and 489 nm as depicted in Fig. 5-24 (a), (b) and (c) respectively. This implied that particle sizes increased with increasing reaction temperature which is in agreement with the observations made from the SEM micrographs. The XRD suggested that a mixture of the orthorhombic and cubic phases of $NiSe_2$ in both the 180 °C and 200 °C samples had formed. This may have contributed to the broad excitonic peak exhibited by these samples. The possible causes of a broad excitonic absorption and emission spectrum reported in literature include polydispersity in nanocrystals size and sub-bandgap transitions involving defect states or capping molecules or impurity phase overlapping with the excitonic transition thus blurring the absorption spectrum [27]. Therefore these factors might have caused the broad excitonic peak exhibited by the as-prepared samples; however, they are still a subject for further investigations with regards to the obtained nanocrystals. The nanoparticles obtained in this section emitted at longer wavelengths compared to their excitonic peaks in the absorption spectra. Specifically the 180 °C, 200 °C and 220 °C samples had their maximum emissions centred at 531 nm, 567 nm and 579 nm as shown in Fig. 5-25(a), (b) and (c) respectively. This resulted in a Stokes shift of 81, 92 and 90 for the 180 °C, 200 °C and 220 °C samples. The Stokes shift values confirmed that the nanoparticles were well passivated. The nanoparticles produced broad Gaussian distribution curve suggesting polydispersity in the samples. The mixed phases in the 180 °C and 200 °C samples may have also contributed to the broadness of the curve. Despite the possible polydispersity of the samples population, the nanoparticles exhibited a good quantum confinement as their excitonic wavelengths were shorter than the bulk band gap which is about 620 nm.

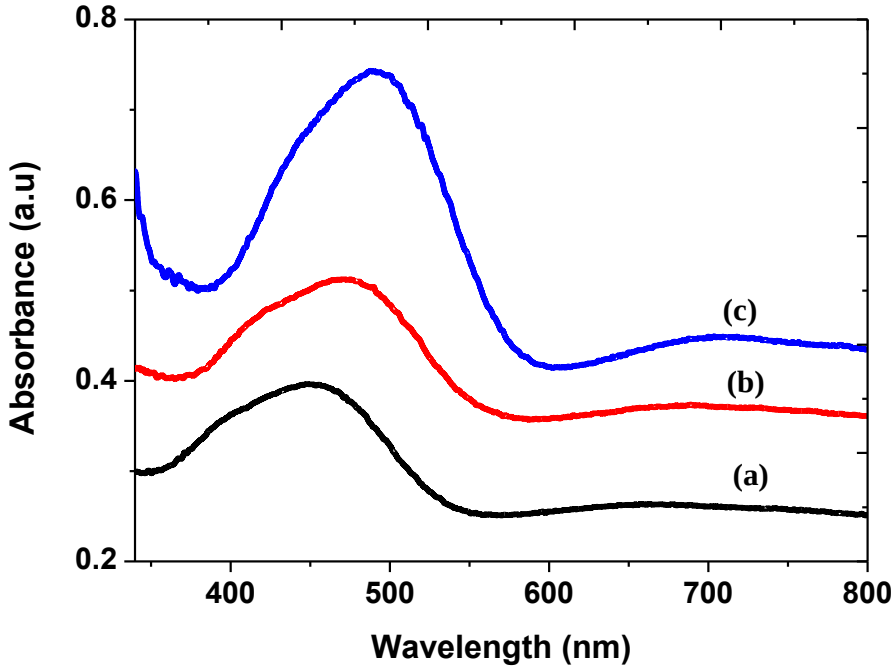

Figure 5-24: Absorption spectra of $NiSe_2$ nanoparticles obtained in a mole ratio 1:2 at reaction temperatures (a) 180 °C, (b) 200 °C and (c) 220 °C for duration of 30 min in oleylamine as the coordinating solvent.

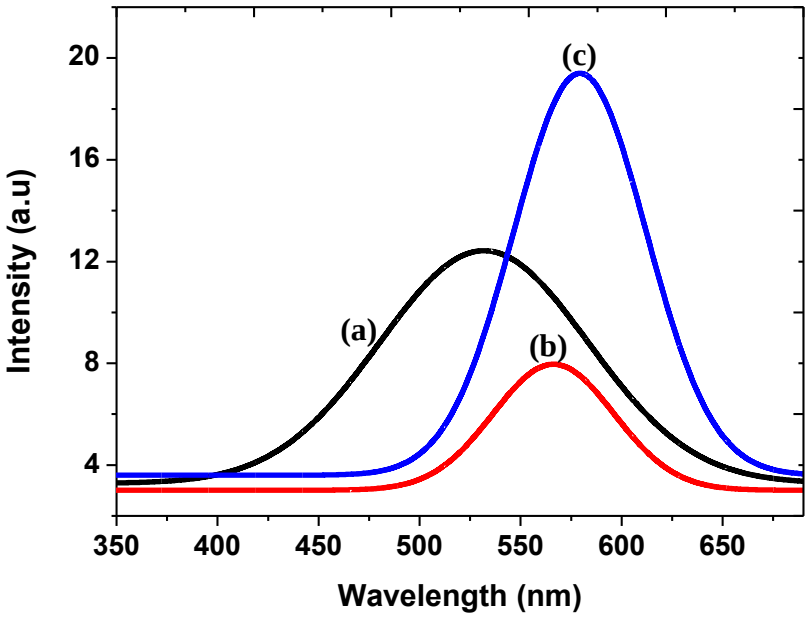

Figure 5-25: Emission spectra of $NiSe_2$ nanoparticles obtained in a mole ratio 1:2 at reaction temperatures (a) 180 °C, (b) 200 °C and (c) 220 °C for duration of 30 min in OLA as the coordinating solvent.

5.3.4 Effect of different coordinating solvents on the structural properties of nickel selenide nanoparticles

Different coordinating solvents including OLA, ODA, OLA/OA and HDA were used in the preparation of the nickel selenide series and their effect on the structural properties of the nanoparticles were investigated.

XRD analysis was used to identify the crystal phases of the as-prepared samples in the different solvents. The first case involved dispersion of metal precursors in TOP before injecting them to the hot solvent and the outcomes are presented in Fig. 5-26. Despite the use of the various solvents including ODA, HDA and OLA, the presence of TOP in the reaction mixture favoured the formation of rhombohedral Ni_3Se_2 whose peaks were indexed according to the card number JCP2.2CA:00-085-0754 and the lattice parameters were a = 6.03382 Å and c = 7.25102 Å with a space group of R32 (155); and their spectra are illustrated in Fig. 5-

26a spectrum w – y respectively. Instead of TOP, oleic acid was used as a co-surfactant to OLA. This resulted in the synthesis of a pure phase of monoclinic Ni_3Se_4 (Fig. 5-26a spectrum z) with diffraction pattern that matched that of monoclinic Ni_3Se_4 (wilkmanite, syn) from card number JCP2.2CA:01-089-2020; with lattice parameters a = 12.15 Å, b = 3.633 Å, c = 10.45 Å, a/b = 3.34 and c/b = 2.87641 of space group C2/m (12). To further explore the effects of the solvents without the TOP, the nanoparticles were prepared in ODA, HDA, OA and OLA; and the results are presented in Fig. 26b. According to spectrum w, the synthesis in ODA produced orthorhombic NiSe. The peaks were indexed according to card JCP2.2CA:00-029-0935 with lattice parameters a = 3.437 Å, b = 11.86 Å and c = 17.06 Å. Other peaks marked with (*) were noted and they were associated with impurities in the sample. The HDA produced samples that exhibited the same pattern as HDA/TOP as shown in spectrum x; and matched to rhombohedral Ni_3Se_2. Spectrum y resulted from samples synthesized in OA and they were matched to monoclinic Ni_3Se_4. The peaks were similar to those exhibited by the OLA/OA sample in spectrum z of Fig. 26a with a slight deviation in the peak position which was attributed to the presence of OLA in one of the samples. Finally, the use OLA resulted in the synthesis of a mixed phase of monoclinic Ni_3Se_4 (Fig. 5-26b) with diffraction patterns that were indexed to monoclinic Ni_3Se_4 (wilkmanite, syn) from card number JCP2.2CA:01-089-2020 and lattice parameters a = 12.15, b = 3.633, c = 10.45, a/b = 3.34 and c/b = 2.87641 of space group C2/m (12). The other peaks marked with (#) were associated with the NiSe phase.

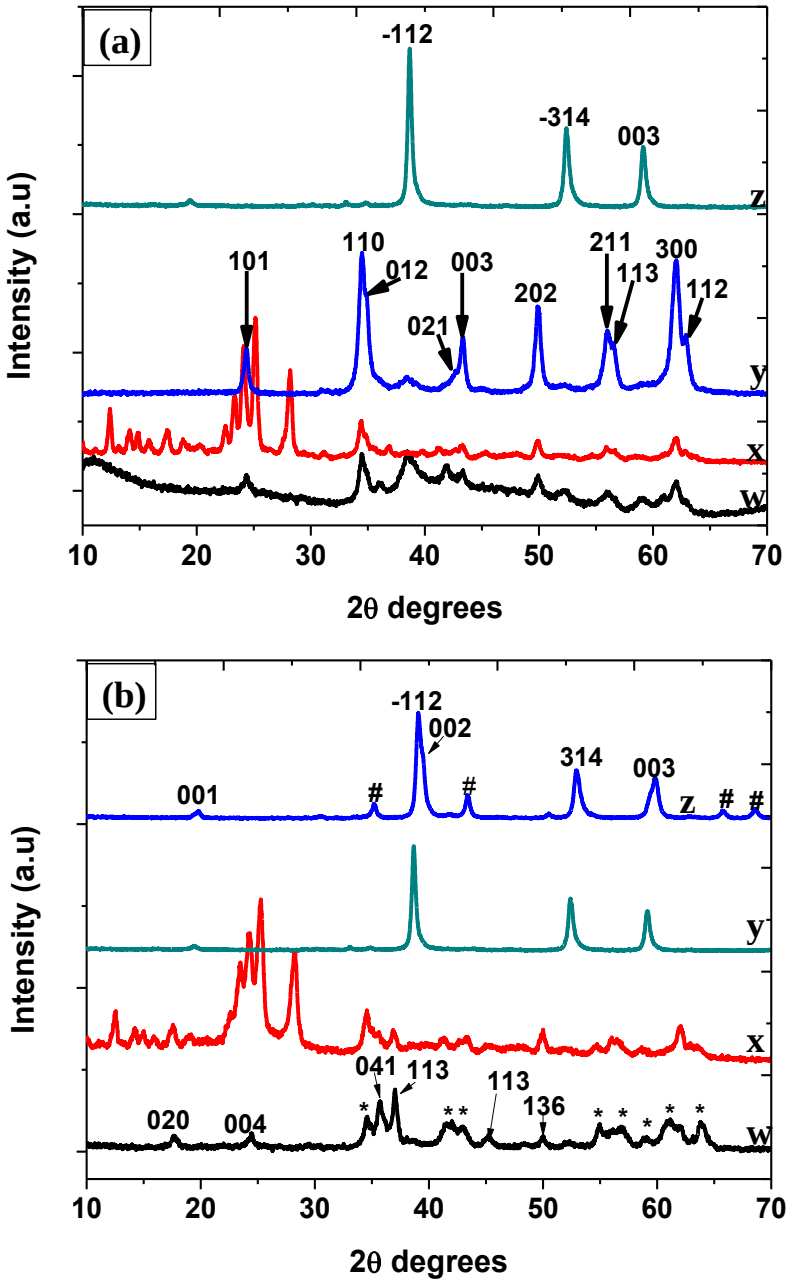

Figure 5-26: The XRD patterns of nanoparticles synthesized at 200 °C for 30 min in different solvents. In (a), spectra w, x, y and z represent nanoparticles obtained in; ODA/TOP, HDA/TOP, OLA/TOP and OLA/OA respectively. (b) Spectra w, x, y and z are obtained from nanoparticles synthesized in; ODA, HDA, OA and OLA respectively. The (*) in spectrum w are associated with impurities in the sample while the (#) in spectrum are ascribed to NiSe phase within the sample. Spectrum x in both (a) and (b) have the same indices as they were matched using the same card numbers.

TEM and SEM analyses were used to study the morphologies of the as-synthesized nanoparticles and the micrographs are portrayed in Fig. 5-27. Using metal precursors dispersed in TOP, HDA produced nearly monodispersed Ni_3Se_2 quantum dots of average size of 7 nm (Fig. 5-27a); ODA resulted in fibre-like nanostructures that aggregated into spheres as depicted in the TEM and SEM images shown in Fig. 5-27 (b) and (c) respectively while OLA produced rectangular-like nanostructures as shown in Fig. 5-27d. Using the solvents alone without TOP, HDA produced sample with mixed morphology as shown in Fig. 5-27e. The sample consisted of nanorods and cuboids. Samples synthesized in OLA comprised of spherical nanoparticles as displayed in Fig. 5-27f; while oleic acid resulted in agglomerated quantum dots as shown in Fig. 5-27g. ODA as a solvent gave a polydispersed sample comprising of nanorods, quantum dots and nanocubes as illustrated by Fig. 5-27h. Most of the shapes were associated to impurities to as portrayed by the XRD. A mixture of OLA and oleic acid in the ratio of 1:1 yielded spherical nanoparticles as demonstrated by Fig. 5-27i.

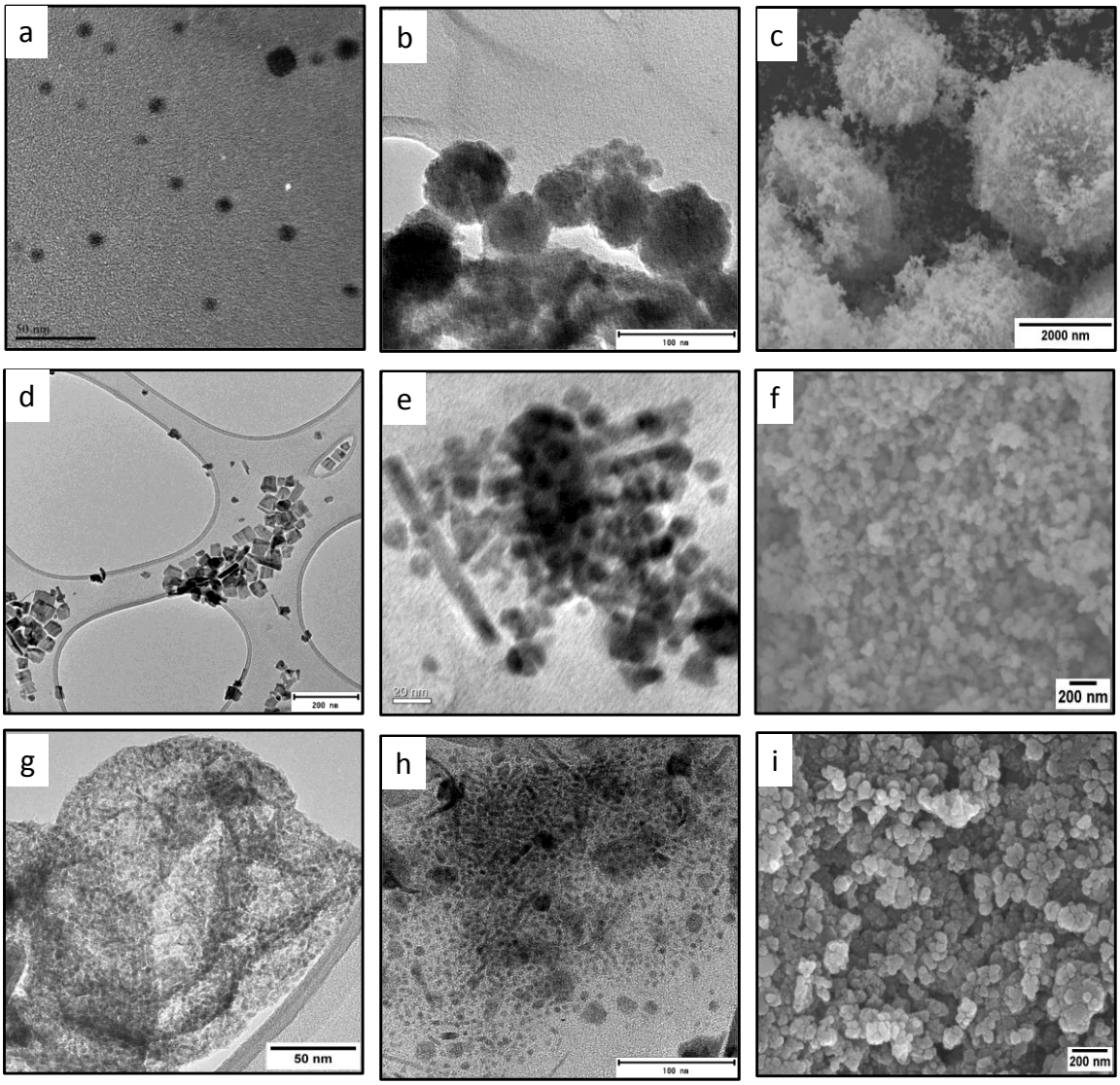

Figure 5-27: (a) TEM image of nanoparticles obtained in HDA/TOP; (b) TEM images of products obtained in ODA/TOP while (c) is the SEM image of same; (d) is the TEM image of NPs in OLA/TOP; (e) TEM images of NPs synthesized in HAD; (f) SEM image of NPs in OLA; (g) TEM image of NPs in OA; (h) TEM image of NPs in ODA and (i) SEM image of NPs in OLA/OA.

Based on the findings above, TOP was established to play a very significant role in the formation process of nickel selenide nanoparticles. Primarily, the metal precursors were dispersed in TOP to obtain TOP-$NiCl_2$ and TOP-Se, which were later injected into the hot solvent. It was assumed that at the initial stages of the nanoparticle formation, TOP bonded to the metal precursors in such a way that it controlled the nucleation process and even

determined the monomer activities. As a result, despite using different coordinating solvents together with TOP, the preferred stoichiometry obtained was rhombohedral Ni_3Se_2. HDA, ODA and OLA were responsible for the shape and crystallinity control [28-30]. The absence of TOP in the reaction mixture comprising of HDA or OLA or ODA yielded other stoichiometries. This further confirmed the role of TOP in the formation of the nickel selenide. TOP also aided in the control of the particle population. For example, HDA alone without TOP resulted in the formation of both nanorods and quantum dots within the same sample while HDA/TOP gave a nearly monodispersed sample comprising of only dots. OLA, ODA and HDA acted as electron donors at elevated temperatures. They exhibited similar basicity and affinity to metals through their NH_2 functional group. However the difference in the alkyl chain length which presents different levels of steric hindrances to the nuclei of the nanoparticle; and the existence of a double bond in the OLA chain are responsible for the significant differences in the morphology and the crystallinity of the resultant nanoparticles. This therefore ascribes to the difference morphologies of nickel selenide obtained when these solvents were used [31, 32]. The mixed morphology and the impurities in the sample obtained in ODA were associated with the difficulty of Ni^{2+} to withdraw electrons from ODA. From literature, the ability of metal ions to withdraw electrons from ODA is in the order $Zn^{2+} < Co^{2+} < Ni^{2+} < Ag^{+} < Pd^{2+} < Pt^{4+} < Au^{3+}$. Any metal ion below Ni^{2+} is unable to extract electrons from ODA thus are susceptible to forming the metal oxide [32].

5.4 Conclusions

In this part of the thesis, several stoichiometries of Ni-Se systems with different morphologies have been synthesized by simply varying the reaction conditions. Specifically, the morphology of nanocrystals was systematically controlled by varying the surfactant and the reaction temperature. It was also demonstrated that phase transformation was dependent on the reaction temperature and surfactant employed. For instance, monoclinic Ni_3Se_4 was

transformed to cubic $NiSe_2$. Similarly the presence of TOP in the reaction mixture preferentially led to the formation of rhombohedral Ni_3Se_2. An increase in selenium to a ratio of $NiCl_2$:Se 1:2 in the reaction mixture resulted in the formation of pure $NiSe_2$ unlike the 1:1 ratio that gave mixed phases. Based on optical and structural studies of nickel selenide series we demonstrated that the properties of these nanostructures were dependent on their stoichiometries. This was in agreement with most reports in literature [8-16]. The use of the hot injection and direct heating both produced well passivated nickel selenide nanocrystals based on the values generated from the Stokes shift. Therefore, a direct heating method which is less cumbersome and high yields was shown to be a better prospect for large scale production of colloidal nanoparticles in general.

References

[1] N. Moloto, M. Moloto, N. Coville, S.S. Ray, Optical and structural characterization of nickel selenide nanoparticles synthesized by simple methods, Journal of Crystal Growth, 311 (2009) 3924-3932.

[2] A. Panneerselvam, M.A. Malik, M. Afzaal, P. O'Brien, M. Helliwell, The chemical vapor deposition of nickel phosphide or selenide thin films from a single precursor, Journal of the American Chemical Society, 130 (2008) 2420-2421.

[3] A. Sobhani, F. Davar, M. Salavati-Niasari, Synthesis and characterization of hexagonal nano-sized nickel selenide by simple hydrothermal method assisted by CTAB, Applied Surface Science, 257 (2011) 7982-7987.

[4] W. Maneeprakorn, C.Q. Nguyen, M.A. Malik, P. O'Brien, J. Raftery, Synthesis of the nickel selenophosphinates [Ni (Se 2 PR 2) 2](R= i Pr, t Bu and Ph) and their use as single source precursors for the deposition of nickel phosphide or nickel selenide nanoparticles, Dalton Transactions, (2009) 2103-2108.

[5] C. Campos, J. de Lima, T. Grandi, K. Machado, P. Pizani, R. Hinrichs, Structural, thermal and optical studies of Ni 3 Se 2 compound produced by mechanical alloying, Solid state ionics, 168 (2004) 205-210.

[6] Y. Vuorelainen, A. Huhma, A. Häkli, Sederholmite, wilkmanite, kullerudite, mäkinenite and trüstedtite, five new nickel selenide minerals, Comptes Rendus de la Société Géologique de Finlande, 36 (1964) 113-125.

[7] Z. Zhuang, Q. Peng, J. Zhuang, X. Wang, Y. Li, Controlled hydrothermal synthesis and structural characterization of a nickel selenide series, Chemistry–A European Journal, 12 (2006) 211-217.

[8] A.P. Alivisatos, Semiconductor clusters, nanocrystals, and quantum dots, Science, 271 (1996) 933.

[9] J. Honig, J. Spalek, Electronic properties of NiS2-x Se x single crystals: from magnetic Mott-Hubbard insulators to normal metals, Chemistry of materials, 10 (1998) 2910-2929.

[10] A. Matsuura, H. Watanabe, C. Kim, S. Doniach, Z.-X. Shen, T. Thio, J. Bennett, Metal-insulator transition in NiS 2− x Se x and the local impurity self-consistent approximation model, Physical Review B, 58 (1998) 3690.

[11] M.A. El-Sayed, Small is different: shape-, size-, and composition-dependent properties of some colloidal semiconductor nanocrystals, Accounts of chemical research, 37 (2004) 326-333.

[12] M.A. El-Sayed, Some interesting properties of metals confined in time and nanometer space of different shapes, Accounts of chemical research, 34 (2001) 257-264.

[13] J.Z. Zhang, Ultrafast studies of electron dynamics in semiconductor and metal colloidal nanoparticles: Effects of size and surface, Accounts of chemical research, 30 (1997) 423-429.

[14] R. Cowburn, Property variation with shape in magnetic nanoelements, Journal of Physics D: Applied Physics, 33 (2000) R1.

[15] Y. Xia, B. Gates, Y. Yin, Y. Lu, Monodispersed colloidal spheres: old materials with new applications, Advanced Materials, 12 (2000) 693-713.

[16] Y. Xia, P. Yang, Y. Sun, Y. Wu, B. Mayers, B. Gates, Y. Yin, F. Kim, H. Yan, One-dimensional nanostructures: synthesis, characterization, and applications, Advanced materials, 15 (2003) 353-389.

[17] B. Yuan, W. Luan, S.-t. Tu, One-step solvothermal synthesis of nickel selenide series: Composition and morphology control, CrystEngComm, 14 (2012) 2145-2151.

[18] M.-Z. Xue, Z.-W. Fu, Lithium electrochemistry of NiSe 2: a new kind of storage energy material, Electrochemistry communications, 8 (2006) 1855-1862.

[19] A. Zhao, L. Xu, T. Luo, Y. Qian, Synthesis of nickel selenide nanocables and nanotubes, Chemistry Letters, 34 (2005) 1136-1137.

[20] C.-T. Lee, J.-D. Peng, C.-T. Li, Y.-L. Tsai, R. Vittal, K.-C. Ho, Ni 3 Se 4 hollow architectures as catalytic materials for the counter electrodes of dye-sensitized solar cells, Nano Energy, 10 (2014) 201-211.

[21] Z.-H. Han, S.-H. Yu, Y.-P. Li, H.-Q. Zhao, F.-Q. Li, Y. Xie, Y.-T. Qian, Convenient solvothermal synthesis and phase control of nickel selenides with different morphologies, Chemistry of materials, 11 (1999) 2302-2304.

[22] Q. Lu, J. Hu, K. Tang, B. Deng, Y. Qian, G. Zhou, X. Liu, A simple synthetic method for MSe 2 (M= Fe, Co or Ni) nanocrystallites at low temperature, Materials chemistry and physics, 69 (2001) 278-280.

[23] X. Liu, G. Qiu, J. Wang, Y. Li, Formation of hollow submicrometer spheres of nickel selenides, Chemistry letters, 33 (2004) 852-853.

[24] W. Cao, H. Gai, B. Zhu, Y. Wu, C. Zhang, Morphology-controlled synthesis and characterization of urchin-like CdS and nanowire, Applied Physics A, 108 (2012) 451-456.

[25] S. Yu, C. Wang, J. Yu, W. Shi, R. Deng, H. Zhang, Precursor induced synthesis of hierarchical nanostructured ZnO, Nanotechnology, 17 (2006) 3607.

[26] S. Xiong, B. Xi, C. Wang, D. Xu, X. Feng, Z. Zhu, Y. Qian, Tunable synthesis of various wurtzite ZnS architectural structures and their photocatalytic properties, Advanced Functional Materials, 17 (2007) 2728-2738.

[27] W.J. Mir, A. Swarnkar, R. Sharma, A. Katti, K. Adarsh, A. Nag, Origin of Unusual Excitonic Absorption and Emission from Colloidal Ag2S Nanocrystals: Ultrafast Photophysics and Solar Cell, The journal of physical chemistry letters, 6 (2015) 3915-3922.

[28] E. Groeneveld, Synthesis and optical spectroscopy of (hetero)-nanocrystals: An exciting interplay between Chemistry and Physics, (2012).

[29] Y. Wang, J. He, C. Liu, W.H. Chong, H. Chen, Thermodynamics versus kinetics in nanosynthesis, Angewandte Chemie International Edition, 54 (2015) 2022-2051.

[30] J.B. Schlenoff, M. Li, H. Ly, Stability and self-exchange in alkanethiol monolayers, Journal of the American Chemical Society, 117 (1995) 12528-12536.

[31] S. Mourdikoudis, L.M. Liz-Marzán, Oleylamine in nanoparticle synthesis, Chemistry of Materials, 25 (2013) 1465-1476.

[32] D. Wang, Y. Li, Effective octadecylamine system for nanocrystal synthesis, Inorganic chemistry, 50 (2011) 5196-5202.

Chapter 6 : Application of Nickel Selenide nanocrystals as counter electrodes in dye sensitized solar cells (DSSCs).

6.1 Background

In an attempt to reduce our dependence on fossil fuel as one of the major sources of energy, researches have embarked on a journey to find ways to exploit the renewable and sustainable energy options. This is with the aim of increasing energy sources to cater for the swelling world population that possess a very sharp and quick increase in demand for energy especially in this era of technology; while alienating the overconsumption of fossil fuels. In addition, renewable sources are considered to be environmentally clean unlike fossil fuels whose combustion results in greenhouse gases thus resulting in ecological problems [1-6]. There exist several sources of renewable energy sources including solar energy, geothermal energy, hydropower and hydrogen energy [3, 7-10] among others. These renewable sources not only need to be converted to more useful forms but also the energy produced needs to be stored to ensure sustainability. Subsequently energy conversion and storage (ECS) devices need to be cost effective, efficient and environmentally friendly [11]. Typical ECS devices include fuel cells, solar cells, photo – electrochemical water splitting cells, batteries (especially Li-ion batteries), and supercapacitors [5, 6, 12-35].

The energy conversion and storage field is also a major beneficiary of nanoscience and the performance of the ECS devices has been reported to rely strongly on the properties of the nanostructures [11, 36]. Conventionally, transition metal chalcogenide nanostructures, due to their interesting electronic and optical properties, have attracted tremendous attention in the field of energy just to mention a few [37, 38]. Specifically, Ni-Se binary systems have been subject of research for applications as ECS materials due to their stable nature in air[39], high metallic conductivity[23, 40, 41] and excellent catalytic activities [10, 42]. The multiphasic nickel selenide nanostructures have illustrated good catalytic activities in hydrogen evolution

reaction (HER) and oxygen evolution reaction (OER), water splitting processes and in DSSCs as counter electrodes. In particular, Ni_3Se_2 has been reported as a highly efficient catalyst for oxygen evolution reactions [38]. In addition, Ni_3Se_4 [39], $NiSe_2$ [42], composites containing NiSe-Ni_3Se_2/graphene [36] and $Co_{0.85}Se/Ni_{0.85}Se$ [43] have been exploited as electrocatalysts in DSSCs with conversion efficiencies of about 8 %. In fact based on the comparatively high catalytic activities experienced with the nickel selenides, they are promising substitutes for the Pt-based electrocatalyst which are costly due to the high cost of the noble metal platinum. A DSSC usually contains a photoanode comprising TiO_2 nanocrystals sensitized by dye molecules, an electrolyte with a redox couple of iodide/triiodide (I^-/I_3^-) and a counter electrode. The function of the counter electrode is to transfer electrons arriving from the external circuit to the electrolyte and also catalyses the reduction of I_3^- to I^-. Therefore, a CE should be highly conductive, have a high catalytic activity and should be both chemical and electrochemically stable. Pt is the most commonly used catalytic material. However Pt is a noble metal with a low abundance ratio and high cost. In addition, there are chances that it may corrode the iodide solution. These factors prevent it from being used in large scale manufacturing of DSSCs. As a result, a low cost electrode with high electrochemical activity and chemical stability is an important requirement to enhance practical application of DSSCs [44-54]. In this chapter, we investigate both the catalytic and the electronic properties of the as-prepared nickel selenide series presented in the previous chapter. The nanoparticles with different stoichiometries were used as counter electrodes in DSSCs and their I-V characteristics were studied to elucidate the effect of the different phases on catalytic activity. The use of a very thin layer of Pt of about 40 nm to form a layer of Ni_xSe_y – Pt was prompted by the failure of the Ni_xSe_y nanocrystals to extract current on their own; as depicted in appendix A5. The Pt aided the

movement of electrons within the inter-particle distance created by the coordinating solvent during synthesis.

6.2 Experimental procedures

6.2.1 Chemicals and materials

Nickel selenide crystals (synthesis and characterization was reported on in chapter 5), degassed TiO_2 nanoparticles, acetic acid, distilled water, sunlight liquid soap as an alternative to hydroxypropyl cellulose, iodine (synthetic grade), guanidine thiocyanate, lithium iodide, 1-butyl-3-methyl-imidazolium iodide, dye N–179, 4-tertbutylpyridine, ethanol, chloroform, toluene, acetone, isopropanol, hexane, deionized water and FTO were purchased from Sigma Aldrich.

6.3 Fabrication and assembly of the DSSC device

6.3.1 Cleaning of the substrates

FTO conducting glasses were cleaned in a detergent solution in an ultrasonic bath for 15 min then rinsed with deionized water, acetone, and isopropanol/ethanol sequentially. The substrates were then dried in a nitrogen stream.

6.3.2 Preparation of TiO_2 paste

The procedure described in literature was adopted for this project [55]. Typically 1 g of commercially available/ degassed TiO_2 powder was mixed with 12 mL distilled water and 0.5 mL acetylacetone with constant 24 h stirring. The mixture was later dried at 60 °C followed by grinding to a fine powder. This initial stage was carried out to prevent re-aggregation of the TiO_2 nanoparticles. The subsequent stage involved the mixing of 5% (w/v) ethanolic solution of hydroxypropyl cellulose with a dispersion of the pretreated TiO_2 powder in water

with constant stirring for 12 hours using a magnetic stirrer. The solution was heated afterwards at 70 °C with constant stirring to evaporate ethanol slowly. The volume of the hydroxypropyl cellulose (HPC) solution was changed to achieve the concentration of HPC in the pastes up to 70% (TiO_2 w/w).

6.3.3 Fabrication of the photoanode

The nanocrystalline TiO_2 paste was printed on a clean FTO substrate via a doctor blade technique after which the films were annealed at 350 °C for 30 min. The aim of the heat treatment was to remove all the residual organic components/chemicals from the TiO_2 surface as well as to get an improved contact with the TiO_2 aggregates, and between the TiO_2 and dye molecules. The thickness and the active area of the TiO_2 films were approximately 200 nm and 0.25 cm^2 respectively. For sensitization, the TiO_2 films were immersed in a dye solution (3.0×10^{-4} M mixture of the ruthenizer 535-bisTBA (N-719) in methanol) for 5 s then left to dry for 12 h. All this were done at room temperature.

6.3.4 Preparation of the counter electrode

The entire process was conducted in a fume hood under ambient atmosphere. To prepare the counter electrode, a thin layer of Pt (50 nm) was first sputter coated to a clean FTO substrate. Meanwhile 5 mg of the as-prepared nickel selenide nanocrystals were dissolved in 1 mL of toluene via ultra – sonication for 30 min. Next, clean FTO-Pt substrates were dipped by hand into the dilute solution of NCs and slowly removed from the solution, then left to dry. Once dry, the substrate was then dipped into a beaker containing 0.01 M EDT in anhydrous acetonitrile for 5 s and quickly removed and then allowed to dry before repeating the dipping sequence which was done three times. The substrates were rotated 90° after each treatment in EDT to ensure film uniformity. Careful dip-coating results in the addition of less than a

monolayer of NCs with each step, yielding smooth films across several square centimetres. This entire process of ligand exchange was adapted from Law et al. [56] as for the standard Pt-CE was prepared by sputtering a film of platinum, with a thickness of 30 nm on the FTO substrate. For the preliminary studies, the procedure was repeated without dipping the substrate with Ni_xSe_y – Pt into EDT; thus no EDT treatment was conducted in these set of experiments.

6.3.5 Device assembly

Finally, the DSSC device was assembled according to the following method. The photoanode was placed face up on a flat surface, and the Ni_xSe_y – Pt – coated counter electrode was placed on top of the photoanode. These two opposing glass plates were offset from one another so that the entire photoanode was covered by the counter electrode. The redox electrolyte solution (I^-/I_3^-), composed of 0.6 M methylhexylimidazolium iodide, 0.1 M iodine, 0.5 M tert-butylpyridine, and 0.1 M lithium iodide in 3-methoxypropionitrile, was placed at the edges of the plates, and the liquid was drawn into the space between the electrodes via capillary action. An epoxy adhesive was utilized to hold/seal the electrodes together. Accordingly, we fabricated the $NiSe_2$-Pt, Ni_3Se_4-Pt, Ni_3Se_2-Pt and Pt (as a reference device) counter electrode-based DSSCs. Scheme 6-1 shows the schematic illustration of the device assembly.

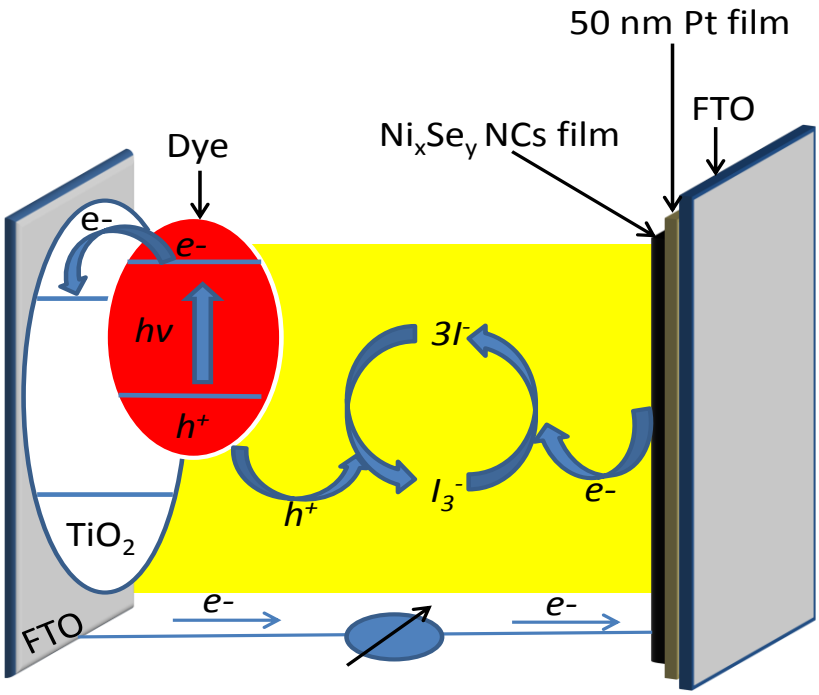

Scheme 6-1: Schematic illustration of the assembled DSSC device.

6.4 Characterization techniques

6.4.1 Structural characterization

The morphology of the nanoparticle based CE film was determined by scanning electron microscopy. The morphologies of the films were determined by the scanning electron microscopy carried out on a FEI Nova Nanolab 600 SEM microscopes operated at an acceleration voltage of 30 kV.

The phase purity, crystallinity and preferred crystal orientation of the products were examined by using XRD on a Bruker MeasSrv (D2-205530)/D2-205530 diffractometer using secondary graphite monochromated CoKα radiation (λ 1.78897 Å) at 30 kV/30 mA. Measurements were taken using a glancing angle of incidence detector at an angle of 2°, for 2θ values over 10 - 90° in steps of 0.026° with a step time of 37 s and at a temperature of 25 °C.

6.4.2 BET measurements

The BET surface areas were obtained from adsorption data in a relative pressure range from 0.05 to 0.30. The total pore volumes were calculated from the amount of N_2 vapor adsorbed at a relative pressure of 0.99. The pore size distributions were evaluated from the desorption branches of the isotherms using the Barrett–Joyner–Halenda (BJH) method. The micropore area and volume were calculated using the t-plot data.

6.4.3 Photovoltaic measurements

The photovoltaic test for the DSSCs with an active area of 0.25 cm^2 was carried out by measuring the photocurrent–voltage (J–V) characteristic curves using a HP 4141B source measure unit (SMU). All the measurements were carried out in ambient atmosphere at room temperature. The incident light intensity was controlled at 70 mW cm^{-2} (AM 1.5G).

6.5 Results and Discussion

In this section, different nickel selenide stoichiometries synthesized in the previous chapter were used to fabricate counter electrodes for the DSSCs. Fig. 6-1 illustrates the XRD patterns of Ni_3Se_2, $NiSe_2$ and Ni_3Se_4 that were specifically employed. Spectra (a) and (b) in Fig. 6-1 present pure phases of rhombohedral Ni_3Se_2 (card number JCP2.2CA:00-085-0754) and monoclinic Ni_3Se_4 (card number JCP2.2CA:01-089-2020) respectively. Spectrum (c), though presenting a single $NiSe_2$ stoichiometry, contained both the orthorhombic (the indexed planes) matching those from card JCP2.2CA:00-018-0886 and cubic phases (shown by the #) matching those from card JCP2.2CA:00-011-0552. The peaks marked (*) are shared planes between the orthorhombic and the cubic phase. As seen from the figure in appendix A4, the 2 theta values from the XRD spectrum for the orthorhombic and the cubic phase of $NiSe_2$ are very close thus; it is a challenge to confidently index it to a single phase.

The counter electrode material is associated with the catalytic reduction of I_3^- to I^- and the catalytic activity is related to the total surface area of the catalyst. Therefore, the Bruanauer–Emmett–Teller (BET) surface area and the total pore volume of Ni_xSe_y were calculated for 1 g of each stoichiometry and the results summarized in Table 6-1. Specifically, the surface area and the total pore volume of $NiSe_2$ were estimated to be 68.5 m^2/g and 0.32 cm^3/g, in contrast to those of Ni_3Se_4 (21.5 m^2/g and 0.11 cm^3/g) and Ni_3Se_2 (15.9 m^2/g and 0.09 cm^3/g). The different stoichiometries exhibited a difference in the surface area and the pore size distribution, thus adsorption of the electrolyte. Subsequently, this impacted on the photoelectric performance of the DSSC due to varied catalytic activity and electrochemical properties of each stoichiometry.

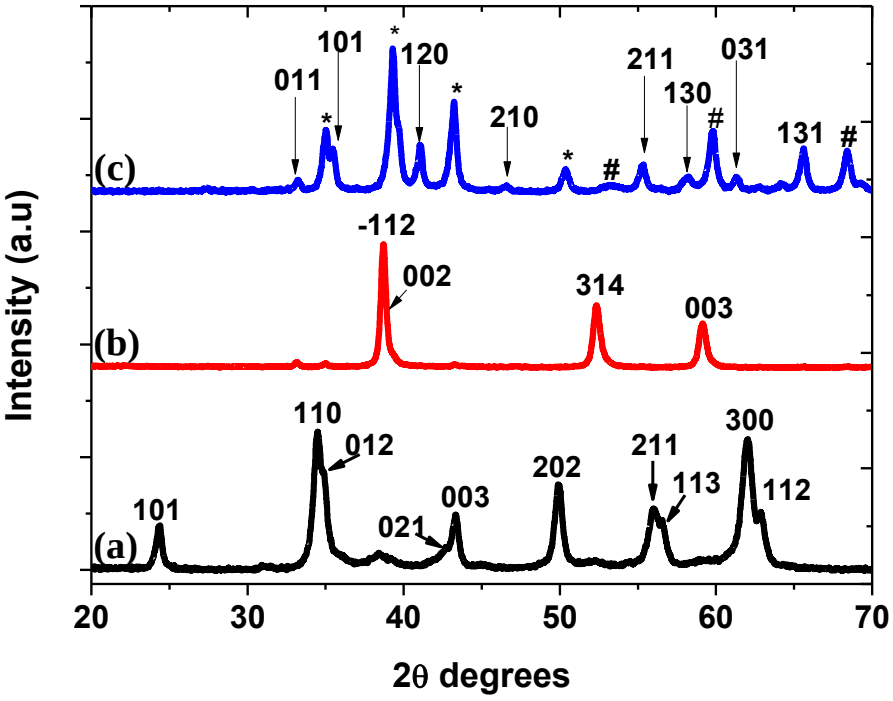

Figure 6-1: XRD patterns showing the stoichiometries of nickel selenide nanostructures used for the device fabrication; (a) Ni_3Se_2, (b) Ni_3Se_4 and (c) $NiSe_2$. The peaks marked (*)

represent planes for both orthorhombic and cubic $NiSe_2$ phase and (#) presenting the planes for the cubic phase.

Table 6-1: Summary of the BET surface area of different stoichiometries of different nickel selenide nanostructures used in the fabrication of the counter electrodes.

Polymorph	BET Surface area m^2/g	Pore Volume cm^3/g
Ni_3Se_2	15.9	0.09
Ni_3Se_4	21.5	0.11
$NiSe_2$	68.5	0.32

Preliminary studies on the photovoltaic performances of the as-prepared Ni_3Se_2 and Ni_3Se_4 nanocrystals before surface treatment with EDT were demonstrated and the results are presented by the *J-V* characteristic curves illustrated in Fig. 6-2. The devices performed dismally recording low parameters such as PCE=0.05 %, Jsc=0.79 mA cm^{-2}, Voc=0.34 V and FF=20 % for the Ni_3Se_4-Pt CE based device while the Ni_3Se_2-Pt CE based device produced a PCE of 0.0005 %, Jsc=0.0078, Voc=0.33 V and FF=21 %. One important observation from these results was that the catalytic activity of the nickel selenide series was dependent on the stoichiometry of the materials; as such Ni_3Se_4 performed better than Ni_3Se_2. However, as shown in Fig. 6-2b, the fill factors of the devices were poor and the current extracted was also very small and finally the power conversion of the devices was very low. These low performances of the devices was attributed to the long hydrocarbon organic layer on the surface on the nanocrystals which are assumed to have resulted in high resistance

causing low mobility of electrons in the devices and reducing the catalytic activity of the nanocrystals towards the reduction of I_3^-.

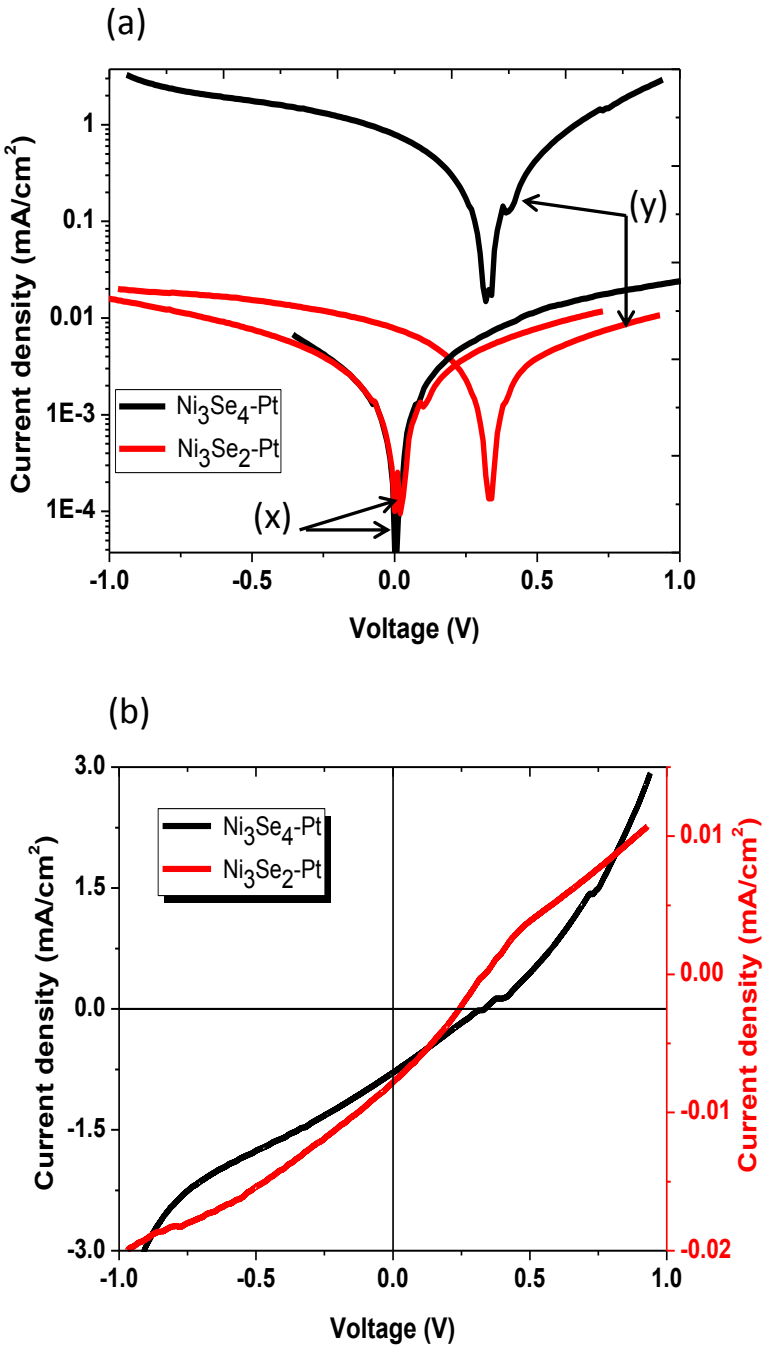

Figure 6-2: J-V characteristics curves of untreated Ni_3Se_4 and Ni_3Se_2 nanocrystals; (a) is the log curve of current density showing the dark current (represented by [x]) and current generated under illumination (represented by [y]) while (b) is the J-V curves showing the quality of the FF.

In the case of this study, oleylamine, which is a long hydrocarbon molecule, was employed during synthesis of nickel selenide nanocrystals as a coordinating ligand. Just like any other hydrocarbon with coordinating head-group, oleylamine's function was to sterically stabilize the NCs in nonpolar, hydrophobic solvents as well as play a key role in the self-assembly of ordered NC arrays or superlattices [57-59]. However, the presence of such a bulky capping molecule creates an insulating barrier around each NC and blocks the access of molecular species to the NC surface, which is disadvantageous for electronic and catalytic applications [56, 60].

In order to address this problem, the surfaces of the as-synthesized nanocrystals were modified via ligand exchange process. Typically the original long chain ligand (oleylamine) was replaced with a shorter chain ethanedithiol (EDT) in order to expose the nanocrystal surface to the electrolyte. This was achieved by dipping the FTO-Pt-Ni_xSe_y film into 0.01 M EDT in anhydrous acetonitrile for 5 s then baked at about 70 °C on a hot plate. The final film surfaces were analysed by SEM and the resulted are portrayed in Fig. 6-3. The nanoparticles were seen to be well distributed and nicely packed. The compactness was attributed to a reduced inter-particle spacing that resulted from the exchange of long hydrocarbon molecules with the much shorter one which has stronger surface binding properties. The resulting smaller clusters enables strong electronic coupling between neighbouring NCs, thereby yielding highly conductive NC films [59].

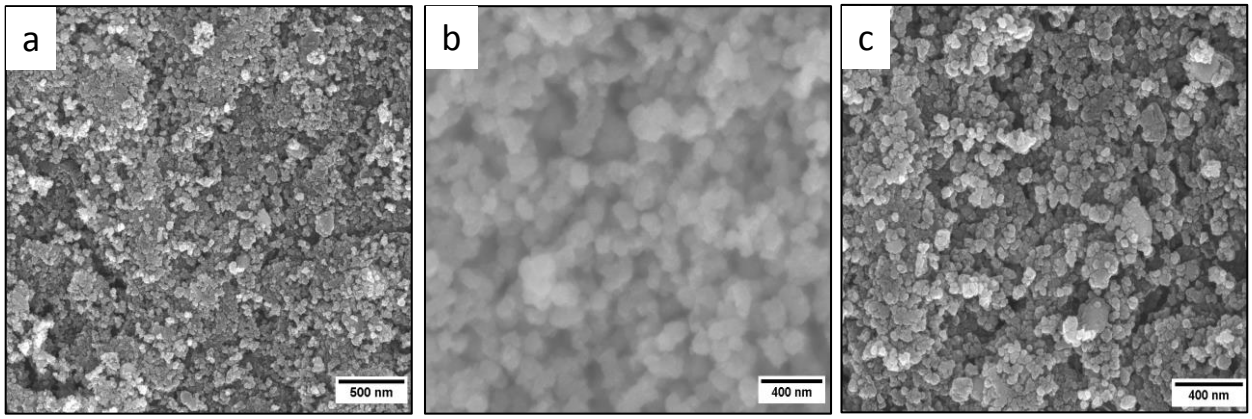

Figure 6-3: SEM images (a) Ni_3Se_2, (b) Ni_3Se_4 and (c) $NiSe_2$ respectively.

Figure 6-4 compares the photovoltaic performance of N719-sensitized solar cells assembled with various cathodes treated with EDT including $NiSe_2$-Pt, Ni_3Se_2-Pt, Ni_3Se_4-Pt and conventional Pt/FTO CEs, and the corresponding photovoltaic performance parameters are summarized in Table 6-2. It is noteworthy to mention that these devices performed better than the ones with untreated Ni_xSe_y nanocrystals. The DSSC with $NiSe_2$-Pt-loaded CE yielded a PCE of 0.16 % (Jsc = 1.53 mA cm^{-2}, Voc = 0.42 mV and FF = 24.9 %), while the DSSC with Ni_3Se_2-Pt-loaded CE produced a PCE of 0.11 % (Jsc = 0.48 mA cm^{-2}, Voc = 0.66 V, FF = 34.7 %) and Ni_3Se_4-Pt-loaded generated a PCE of 0.15 % (Jsc = 0.68 mA cm^{-2}, Voc = 0.68 V, FF = 33.9 %). For reference, the Pt-coated CE-based DSSC was also measured under the same condition, giving a PCE of 0.13 % (Jsc = 0.53 mA cm^{-2}, Voc = 0.53 V, FF = 46 %). From these parameters, it was evident that addition of nickel selenide nanocrystals to the Pt-coated CE had an effect on the performance of the device. For example, the short circuit current density, Jsc, increased in the order of Ni_3Se_2 < Pt < Ni_3Se_4-Pt < $NiSe_2$-Pt, and PCE increased in the same order. Also, it was evident that stoichiometry of nickel selenide played a significant role in the electro-catalytic reduction of I_3^-. $NiSe_2$ CE produced the highest Jsc followed by Ni_3Se_4 then Ni_3Se_2. The lowest Voc recorded was that of the $NiSe_2$-Pt device. This was attributed to the fact that the sample used contained both the cubic and

orthorhombic $NiSe_2$. In addition to the above observations, the fill factor was seen to reduce upon incorporation of nickel selenide nanocrystals onto the Pt-coated CE.

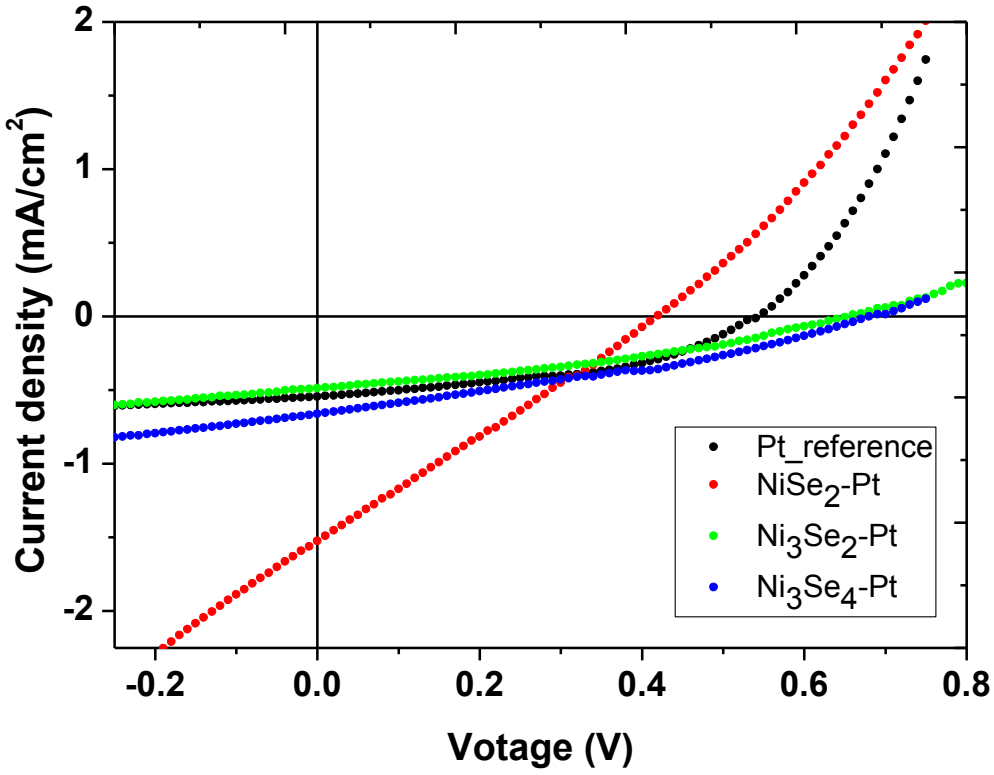

Figure 6-4: Photocurrent density-voltage characteristics of DSSCs with Ni_xSe_y-Pt and Pt CEs at AM1.5G illumination (100 mW cm^{-2}).

Table 6-2: Photovoltaic performance parameters of DSSCs with Ni_xSe_y-Pt and Pt CEs measured at AM1.5G illumination (100 mW cm^{-2}).

Device	Jsc (mA/cm^2)	V_{oc} (V)	Rs ($\Omega\ cm^2$)	FF (%)	PCE (%)
Pt-reference	0.53±0.12	0.53± 0.02	418	46.3±1.2	0.13±0.01
$NiSe_2$-Pt	1.53±0.16	0.42± 0.02	250	24.90±1.1	0.16±0.02
Ni_3Se_2-Pt	0.48±0.13	0.66± 0.01	742	34.70±1.4	0.11±0.01
Ni_3Se_4-Pt	0.65±0.10	0.68± 0.01	850	33.90±1.0	0.15±0.01

Examining the data however, and comparing them to the ones reported in literature (table 6-3 summarizes some of the reports) [39, 42, 43]; one cannot overlook the fact that the devices exhibited low photovoltages as well as low PCE. This suggested that the devices response and the extracted currents were being suppressed thus not allowing for the full potential of the DSSC to be utilized. The most likely candidate mechanism suppressing the cell's performance is the low mobility of electrons within the device. Electron injections to the conduction band of the TiO_2 as well as dye regeneration by the electrolyte are fast occurring processes. Therefore any scenario that leads to slow mobility of electrons will enhance recombination losses thus resulting in poor performance of the device. It is noteworthy to mention that these results are from un-optimized devices and the aim was to demonstrate that nickel selenide nanocrystals can be used as CEs. Therefore, our primitive way of assembling/designing the device may be one of the reasons to account for the suppressed performance of the devices. Firstly, the formation of the nanostructured TiO_2 layer is greatly affected by TiO_2 suspension procedures as well as the annealing temperature [61]. As such, most reports use commercialized TiO_2 paste to fabricate the anode, while in this case we made the paste from scratch. During the making of the paste, instead of using hydroxypropyl cellulose, we used an equivalent which was sunlight liquid soap. The resultant film had

cracks as shown in Fig. 6-5. Another reason for the cracks on the surface of the TiO_2 was attributed the annealing temperature used which was 300 °C. Research has found that sintering TiO_2 film at temperatures lower than 450 °C resulted in TiO_2 layer degradation by fast cracks after a short period of time when the cell exposed to direct sunlight. Moreover temperature below 450 resulted in cells that generated unnoticeable electric current [61]. (Dye sensitized solar cells-working principles, challenges and opportunities). The cracks in the anode could have been responsible for parasitic resistances, more specifically the series resistance as well enhance recombination.



Figure 6-5: An image showing the cracked TiO_2 surface after exposing it air for 10 min.

Table 6-3: A summary of photovoltaic performance parameters of various Ni-Se CE from literature.

Authors	Material on CE	Method of NPs synthesis	**J**sc (mA/cm^2)	V_{oc} (V)	FF (%)	PCE (%)	Rs ($\Omega\ cm^2$)
Gong et al. [42]	Pt	Film deposition	15.26	731	72.10	8.04	2.50
Gong et al. [42]	$NiSe_2$	Hydrothermal	15.94	734.00	74.30	8.69	2.57
Lee et al. [39]	Ni_3Se_4	Hydrothermal	16.27	746.00	69.00	8.31	10.25
Gong et al. [43]	$Ni_{0.85}Se$	In situ directly on the substrate	15.63	739.00	72.00	8.32	1.80

The fill factor is a parameter which reflects on the maximum power output of the DSSC device and it is dependent on parasitic resistances such as series resistance [62]. The series resistance reduces the fill factor and thus the efficiency of solar cell by dissipating power in the resistances. The origination of series resistance may be from (i) the movement of electrons through porous structured semiconductor and the diffusion of ions through the electrolyte, (ii) the contact resistance at the interface between the semiconductor and the transparent conductive film, and (iii) the resistance of the top and rear metal contacts. All these narrow down to the geometry of the device. The devices herein exhibited an apparent low fill factor, leading to their poor performances compared to the ones in literature; considering they are of the same materials. This was as a result of the high series resistances exhibited by the devices. Specifically, $NiSe_2$-Pt-, Pt-, Ni_3Se_4-Pt- and Ni_3Se_2-Pt- CE based devices recorded Rs with values of 418, 250, 742 and 850 $\Omega\ cm^2$ respectively. In addition to the above causes to resistance, the nickel selenide nanoparticles used for the fabrication of the

counter electrode were organically capped. The organic ligand might have hindered the free movement of the electrons thus increasing the resistance within the device.

Apart from resistive effect, the low fill factor in the nickel selenide DSSCs likely implies that there exist serious charge recombination for those injected conduction band electrons at the semiconductor and/or at the interface between the semiconductor and the electrolyte solution. The type of dye and the constituents of the electrolyte have been proven experimentally as some of the factors that affect charge recombination. Also from literature [63-65], a criterion using a comparison between the photocurrent and the space charge limited current measured under current injection has been established to determine whether charge recombination and space charge effects are dominant. Therefore, a log-log curve (Fig. 6-6b) of the dark current-voltage characteristic of the standard Pt device was used to verify the possibility of space charge and recombination as the limiting factor in these devices. As the V^2 asymptote shows, for applied bias between ~1 and 10 volts the device is in the space charge regime [66] and we note that for ~1V bias the current density is about 0.01 mA/cm^2. This observation along with the fact that the current levels shown in Fig. 6-6a is about 0.01 mA/cm^2 clearly indicate that the photo-current levels shown in Fig. 6-6a are indeed limited by recombination and probably also by space charge effects [66] and thus not much current is extracted.

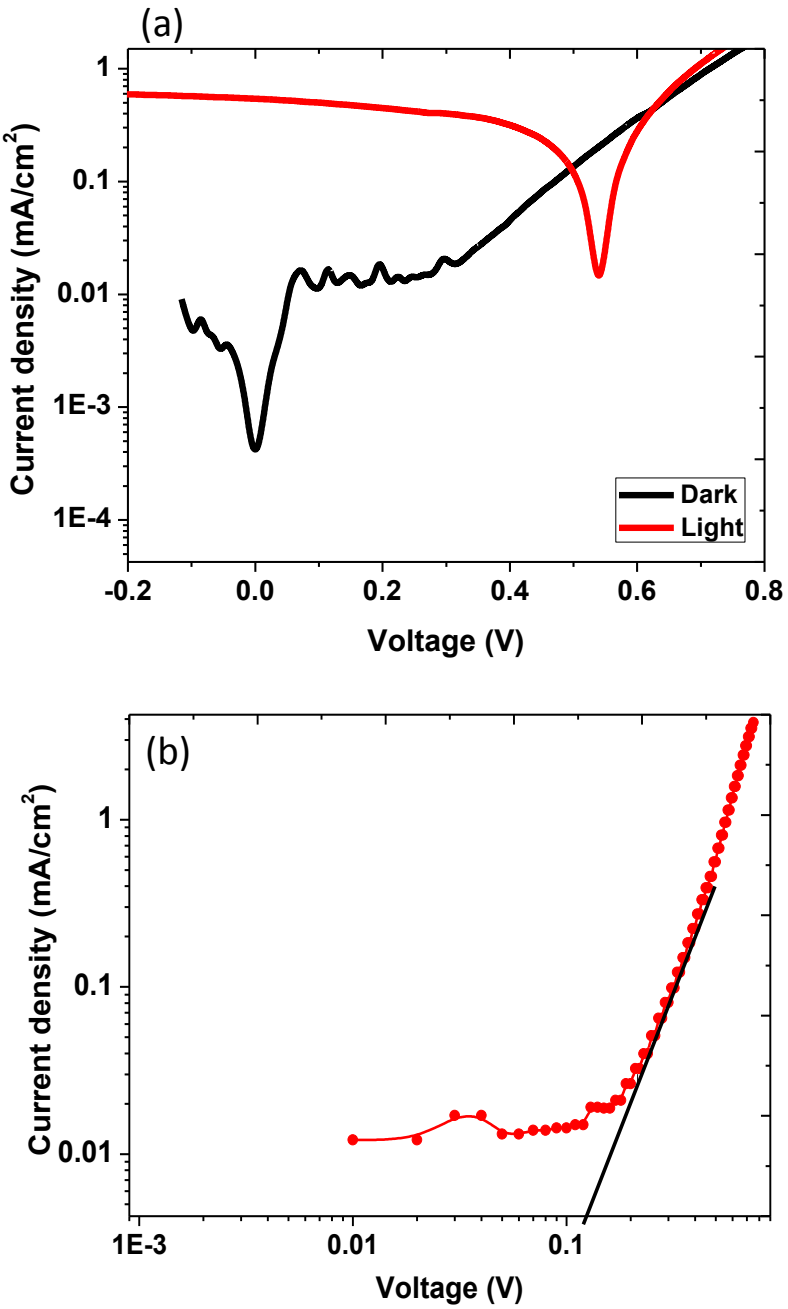

Figure 6-6: (a) Current-voltage characteristics of the reference Pt device and (b) Log-log curve of the dark current-voltage characteristic of the Pt device.

6.6 Conclusion

In summary, the experimental results demonstrated the potential application Ni_xSe_y nanocrystals synthesized in organic solvent as CE material in DSSC. The three stoichiometries selected as research objects exhibited different electrocatalytic activities in the reduction of I_3^- thus producing different performance parameters. DSSC with $NiSe_2$-Pt CE displayed a high PCE and Jsc comparable to that of those based on Ni_3Se_2-Pt, Ni_3Se_4 and Pt alone, though with the lowest FF. This finding paves the way for preparing cheap and highly efficient counter electrodes for DSSCs. We believe that future work involving the improvement on; photoanode fabrication (such as reducing the amount of cracks of TiO_2 film), electrolyte constituents, improving on the ligand exchange process and synthesizing single stoichiometry on Ni_xSe_y will result in higher conversion efficiencies and to some extent, obtain a Pt-free CE using these nanocrystals.

References

[1] N.H. Afgan, M.G. Carvalho, Multi-criteria assessment of new and renewable energy power plants, Energy, 27 (2002) 739-755.

[2] b.g. FF conserve energy future, stay green., causes and solutions to the global energy crisis-conserve energy.

[3] N. Panwar, S. Kaushik, S. Kothari, Role of renewable energy sources in environmental protection: a review, Renewable and Sustainable Energy Reviews, 15 (2011) 1513-1524.

[4] M. Winter, R.J. Brodd, What are batteries, fuel cells, and supercapacitors?, Chemical reviews, 104 (2004) 4245-4270.

[5] A.S. Arico, P. Bruce, B. Scrosati, J.-M. Tarascon, W. Van Schalkwijk, Nanostructured materials for advanced energy conversion and storage devices, Nature materials, 4 (2005) 366-377.

[6] A. Kudo, Y. Miseki, Heterogeneous photocatalyst materials for water splitting, Chemical Society Reviews, 38 (2009) 253-278.

[7] K. Winemiller, P. McIntyre, L. Castello, E. Fluet-Chouinard, T. Giarrizzo, S. Nam, I. Baird, W. Darwall, N. Lujan, I. Harrison, Balancing hydropower and biodiversity in the Amazon, Congo, and Mekong, Science, 351 (2016) 128-129.

[8] I.B. Fridleifsson, Geothermal energy for the benefit of the people, Renewable and Sustainable Energy Reviews, 5 (2001) 299-312.

[9] A. Kaufman, Hydrogen power cell, in, Google Patents, 1994.

[10] M.-R. Gao, Z.-Y. Lin, T.-T. Zhuang, J. Jiang, Y.-F. Xu, Y.-R. Zheng, S.-H. Yu, Mixed-solution synthesis of sea urchin-like NiSe nanofiber assemblies as economical Pt-free catalysts for electrochemical H 2 production, Journal of Materials Chemistry, 22 (2012) 13662-13668.

[11] M.-R. Gao, Y.-F. Xu, J. Jiang, S.-H. Yu, Nanostructured metal chalcogenides: synthesis, modification, and applications in energy conversion and storage devices, Chemical Society Reviews, 42 (2013) 2986-3017.

[12] M.G. Walter, E.L. Warren, J.R. McKone, S.W. Boettcher, Q. Mi, E.A. Santori, N.S. Lewis, Solar water splitting cells, Chemical Reviews, 110 (2010) 6446-6473.

[13] M. Grätzel, Photoelectrochemical cells, Nature, 414 (2001) 338-344.

[14] Y.-J. Wang, D.P. Wilkinson, J. Zhang, Noncarbon support materials for polymer electrolyte membrane fuel cell electrocatalysts, Chemical Reviews, 111 (2011) 7625-7651.

[15] R.R. Adzic, J. Zhang, K. Sasaki, M.B. Vukmirovic, M. Shao, J. Wang, A.U. Nilekar, M. Mavrikakis, J. Valerio, F. Uribe, Platinum monolayer fuel cell electrocatalysts, Topics in Catalysis, 46 (2007) 249-262.

[16] N.G. Sahoo, Y. Pan, L. Li, S.H. Chan, Graphene-Based Materials for Energy Conversion, Advanced Materials, 24 (2012) 4203-4210.

[17] C. Koenigsmann, S.S. Wong, One-dimensional noble metal electrocatalysts: a promising structural paradigm for direct methanol fuel cells, Energy & Environmental Science, 4 (2011) 1161-1176.

[18] A.A. Gewirth, M.S. Thorum, Electroreduction of dioxygen for fuel-cell applications: materials and challenges, Inorganic Chemistry, 49 (2010) 3557-3566.

[19] S.E. Habas, H.A. Platt, M.F. Van Hest, D.S. Ginley, Low-cost inorganic solar cells: from ink to printed device, Chemical Reviews, 110 (2010) 6571-6594.

[20] P.V. Kamat, K. Tvrdy, D.R. Baker, J.G. Radich, Beyond photovoltaics: semiconductor nanoarchitectures for liquid-junction solar cells, Chemical Reviews, 110 (2010) 6664-6688.

[21] G. Zhang, S. Finefrock, D. Liang, G.G. Yadav, H. Yang, H. Fang, Y. Wu, Semiconductor nanostructure-based photovoltaic solar cells, Nanoscale, 3 (2011) 2430-2443.

[22] A. Kubacka, M. Fernandez-Garcia, G. Colon, Advanced nanoarchitectures for solar photocatalytic applications, Chemical Reviews, 112 (2011) 1555-1614.

[23] M.-Z. Xue, Z.-W. Fu, Lithium electrochemistry of NiSe 2: a new kind of storage energy material, Electrochemistry Communications, 8 (2006) 1855-1862.

[24] J.-M. Tarascon, M. Armand, Issues and challenges facing rechargeable lithium batteries, Nature, 414 (2001) 359-367.

[25] M. Armand, J.-M. Tarascon, Building better batteries, Nature, 451 (2008) 652-657.

[26] M.S. Whittingham, Lithium batteries and cathode materials, Chemical Reviews, 104 (2004) 4271-4302.

[27] P.G. Bruce, B. Scrosati, J.M. Tarascon, Nanomaterials for rechargeable lithium batteries, Angewandte Chemie International Edition, 47 (2008) 2930-2946.

[28] M.G. Kim, J. Cho, Reversible and High-Capacity Nanostructured Electrode Materials for Li-Ion Batteries, Advanced Functional Materials, 19 (2009) 1497-1514.

[29] J. Liu, X.W. Liu, Two-Dimensional Nanoarchitectures for Lithium Storage, Advanced Materials, 24 (2012) 4097-4111.

[30] Y. Huang, J. Liang, Y. Chen, An overview of the applications of graphene-based materials in supercapacitors, Small, 8 (2012) 1805-1834.

[31] A. Ghosh, Y.H. Lee, Carbon-based electrochemical capacitors, ChemSusChem, 5 (2012) 480-499.

[32] G. Wang, L. Zhang, J. Zhang, A review of electrode materials for electrochemical supercapacitors, Chemical Society Reviews, 41 (2012) 797-828.

[33] L.L. Zhang, X. Zhao, Carbon-based materials as supercapacitor electrodes, Chemical Society Reviews, 38 (2009) 2520-2531.

[34] M.D. Stoller, R.S. Ruoff, Best practice methods for determining an electrode material's performance for ultracapacitors, Energy & Environmental Science, 3 (2010) 1294-1301.

[35] P. Simon, Y. Gogotsi, Materials for electrochemical capacitors, Nature Materials, 7 (2008) 845-854.

[36] X. Zhang, M. Zhen, J. Bai, S. Jin, L. Liu, Efficient NiSe-Ni3Se2/Graphene Electrocatalyst in Dye-Sensitized Solar Cells: the Role of Hollow Hybrid Nanostructure, ACS Applied Materials & Interfaces, (2016).

[37] H. Yuan, H. Wang, Y. Cui, Two-dimensional layered chalcogenides: from rational synthesis to property control via orbital occupation and electron filling, Accounts of Chemical Research, 48 (2015) 81-90.

[38] A. Swesi, J. Masud, M. Nath, Nickel selenide as a high-efficiency catalyst for oxygen evolution reaction, Energy & Environmental Science, 9 (2016) 1771-1782.

[39] C.-T. Lee, J.-D. Peng, C.-T. Li, Y.-L. Tsai, R. Vittal, K.-C. Ho, Ni 3 Se 4 hollow architectures as catalytic materials for the counter electrodes of dye-sensitized solar cells, Nano Energy, 10 (2014) 201-211.

[40] S. Ogawa, Magnetic properties of 3d transition-metal dichalcogenides with the pyrite structure, Journal of Applied Physics, 50 (1979) 2308-2311.

[41] J. Honig, J. Spalek, Electronic properties of NiS_{2-x} Se x single crystals: from magnetic Mott-Hubbard insulators to normal metals, Chemistry of Materials, 10 (1998) 2910-2929.

[42] F. Gong, X. Xu, Z. Li, G. Zhou, Z.-S. Wang, $NiSe_2$ as an efficient electrocatalyst for a Pt-free counter electrode of dye-sensitized solar cells, Chemical Communications, 49 (2013) 1437-1439.

[43] F. Gong, H. Wang, X. Xu, G. Zhou, Z.-S. Wang, In situ growth of Co0. 85Se and Ni0. 85Se on conductive substrates as high-performance counter electrodes for dye-sensitized solar cells, Journal of the American Chemical Society, 134 (2012) 10953-10958.

[44] B. O'regan, M. Grfitzeli, A low-cost, high-efficiency solar cell based on dye-sensitized, Nature, 353 (1991) 737-740.

[45] I. Chung, B. Lee, J. He, R.P. Chang, M.G. Kanatzidis, All-solid-state dye-sensitized solar cells with high efficiency, Nature, 485 (2012) 486-489.

[46] E.J. Crossland, N. Noel, V. Sivaram, T. Leijtens, J.A. Alexander-Webber, H.J. Snaith, Mesoporous TiO2 single crystals delivering enhanced mobility and optoelectronic device performance, Nature, 495 (2013) 215-219.

[47] H. Sun, D. Qin, S. Huang, X. Guo, D. Li, Y. Luo, Q. Meng, Dye-sensitized solar cells with NiS counter electrodes electrodeposited by a potential reversal technique, Energy & Environmental Science, 4 (2011) 2630-2637.

[48] Y. Luo, D. Li, Q. Meng, Towards Optimization of Materials for Dye-Sensitized Solar Cells, Advanced Materials, 21 (2009) 4647-4651.

[49] E. Olsen, G. Hagen, S.E. Lindquist, Dissolution of platinum in methoxy propionitrile containing LiI/I 2, Solar Energy Materials and Solar Cells, 63 (2000) 267-273.

[50] N. Papageorgiou, W. Maier, M. Grätzel, An iodine/triiodide reduction electrocatalyst for aqueous and organic media, Journal of the Electrochemical Society, 144 (1997) 876-884.

[51] N. Papageorgiou, Counter-electrode function in nanocrystalline photoelectrochemical cell configurations, Coordination Chemistry Reviews, 248 (2004) 1421-1446.

[52] A. Kay, M. Grätzel, Low cost photovoltaic modules based on dye sensitized nanocrystalline titanium dioxide and carbon powder, Solar Energy Materials and Solar Cells, 44 (1996) 99-117.

[53] T.N. Murakami, S. Ito, Q. Wang, M.K. Nazeeruddin, T. Bessho, I. Cesar, P. Liska, R. Humphry-Baker, P. Comte, P. Péchy, Highly efficient dye-sensitized solar cells based on carbon black counter electrodes, Journal of the Electrochemical Society, 153 (2006) A2255-A2261.

[54] Y. Duan, Q. Tang, B. He, R. Li, L. Yu, Transparent nickel selenide alloy counter electrodes for bifacial dye-sensitized solar cells exceeding 10% efficiency, Nanoscale, 6 (2014) 12601-12608.

[55] S. Sarker, N.C.D. Nath, M. Rahman, S.-S. Lim, A. Ahammad, W.-Y. Choi, J.-J. Lee, Tio2 Paste Formulation for Crack-Free Mesoporous Nanocrystalline Film of Dye-Sensitized Solar Cells, Journal of Nanoscience and Nanotechnology, 12 (2012) 5361-5366.

[56] M. Law, J.M. Luther, Q. Song, B.K. Hughes, C.L. Perkins, A.J. Nozik, Structural, optical, and electrical properties of PbSe nanocrystal solids treated thermally or with simple amines, Journal of the American Chemical Society, 130 (2008) 5974-5985.

[57] J. Park, J. Joo, S.G. Kwon, Y. Jang, T. Hyeon, Synthesis of monodisperse spherical nanocrystals, Angewandte Chemie International Edition, 46 (2007) 4630-4660.

[58] D.V. Talapin, J.-S. Lee, M.V. Kovalenko, E.V. Shevchenko, Prospects of colloidal nanocrystals for electronic and optoelectronic applications, Chemical reviews, 110 (2009) 389-458.

[59] A. Dong, X. Ye, J. Chen, Y. Kang, T. Gordon, J.M. Kikkawa, C.B. Murray, A generalized ligand-exchange strategy enabling sequential surface functionalization of colloidal nanocrystals, Journal of the American Chemical Society, 133 (2010) 998-1006.

[60] Y. Kang, C.B. Murray, Synthesis and electrocatalytic properties of cubic Mn− Pt nanocrystals (nanocubes), Journal of the American Chemical Society, 132 (2010) 7568-7569.

[61] K.E. Jasim, Dye sensitized solar cells-working principles, challenges and opportunities, A chapter in Solar Cells/Book, 2 (2011).

[62] Q. Zhang, T.P. Chou, B. Russo, S.A. Jenekhe, G. Cao, Polydisperse Aggregates of ZnO Nanocrystallites: A Method for Energy-Conversion-Efficiency Enhancement in Dye-Sensitized Solar Cells, Advanced Functional Materials, 18 (2008) 1654-1660.

[63] N. Tessler, N. Rappaport, Excitation density dependence of photocurrent efficiency in low mobility semiconductors, Journal of Applied Physics, 96 (2004) 1083-1087.

[64] N. Tessler, N. Rappaport, Loss of photocurrent efficiency in low mobility semiconductors: Analytic approach to space charge effects, Applied Physics Letters, 89 (2006) 013504.

[65] N. Rappaport, O. Solomesch, N. Tessler, The interplay between space charge and recombination in conjugated polymer/molecule photocells, Journal of Applied Physics, 98 (2005) 033714.

[66] N. Yaacobi-Gross, Colloidal Semiconductor Nanocrystals Based Solar Cells, Technion-Israel Institute of Technology, Faculty of Electrical Engineering, 2012.

Chapter 7 : Conclusion and Future work.

7.1 Conclusion

In this thesis, the colloidal syntheses of indium selenide and nickel selenide nanostructures have been broadly explored. Systematic controls of growth parameters during synthesis have been demonstrated to have effect on the physical, morphological, optical, electronic and catalytic properties of the as-prepared nanostructures. Unique strategies to obtain highly uniform and monodisperse morphologies in a highly reproducible manner were developed, and a general understanding of their facet/phase distribution with respect to metal precursor concentration was demonstrated. In addition simple DSSCs and sensor devices were developed in order to assess their potential application in photovoltaics and chemical sensors.

A direct heating method was used obtain nanostructures for In_xSe_y and their properties investigated. This was achieved by thermal decomposition of $InCl_3$ and selenium powder in oleylamine, a coordinating solvent that has been reported to promote lateral growth while truncating the vertical growth. The studies showed/revealed that the polymorphs of In_xSe_y with layered crystal structure experienced a band structure modification when reduced to a monolayer thus resulting in luminescence properties. A small contamination of the reaction system with a co-surfactant was seen to result in shape and phase transformation if the nanostructure. Further, the sensing ability of the nanostructures to different VOCs shed light on the use of non-metal oxide chalcogenide as chemiresistive sensors, a field that has been dominated by metal oxide nanostructures. Also the electrical characterization of different dimensional nanostructures established that different morphologies of InSe nanostructures interacted differently with the analyte gas. In particular, InSe nanoparticles, which showed better performance than 2-D nanostructures, could allow for interesting future developments. Based on the strength of their gas responses, as shown in chapter 4, one can conclude that metal selenides are potentially suitable materials for chemoresistive sensors.

Systematic control of different stoichiometries of Ni-Se systems with different morphological optical and properties has been demonstrated. This was achieved by variation of reaction conditions including synthetic method, reaction temperature, reaction time, concentration of precursors and coordinating solvent. Both the hot injection and the direct heating method produced good quantum confined and well passivated nanostructures. In literature, indeed the hot injection method produces high quality colloidal nanostructures, but with a compromised yield and this limits large scale production of nanostructures by this method. Therefore based on the outcome of the studies herein, a direct heating method whose yield was relatively good could be a potential alternative for large quantity production nanostructures.

The catalytic activity of nickel selenide nanostructures was demonstrated. This was done by incorporating the nanostructures together with a thin layer of platinum as CEs in DSSCs. The work revealed that different polymorphs of nickel selenide resulted in different power conversion efficiencies; thus indicating that the catalytic activity was dependent on the stoichiometry of the Ni-Se system. A special attention was given to the role of the organic capping layer that covers the NCs. It was found that by means of ligand exchange the catalytic properties of NCs could be improved, offering another design tool for the device engineer. At its essence, this research emphasized the importance of comprehensive approach to the understanding of the reciprocal relations between the NC core and its capping layer.

7.2 Future work

Our results have so far established a controlled hot injection and direct heating approach to synthesize different kind of In_xSe_y and Ni_xSe_y nanostructures. The potential electronic applications of these nanostructures to sensors were also demonstrated. Given these considerations, we seek to extend the follow-up work on the basis on this thesis as follows:

- A theoretical/simulation framework to understand the band structure modification concept when the three layered InSe crystal structure is reduced to a monolayer
- To investigate the effect of other coordinating solvents on the shape and phase transformation of indium selenide nanostructures
- To carry out additional investigations on the sensing ability of metal selenides to other vapours and the establishment of the sensing mechanism since the selenides do not possess an oxygen backbone.
- It would be interesting to investigate the performance of the sensors at temperatures above 100 °C.
- Optimization of the DSSC fabrication method is recommended to an extent that the Pt is replaced completely with Ni-Se nanostructures. Precisely, using the correct chemical instead of the sunlight liquid soap to make the paste and annealing the TiO_2 anode at 450 °C are important consideration. In addition, the roughness and thickness of the electrodes should be monitored to achieve an improved PCE.
- To further evaluate the catalytic activities of the Ni_xSe_y electrodes, electrochemical impedance spectroscopy (EIS) measurements and IPCE measurements are recommended.
- Electrochemical studies to probe the extent of electrochemical behaviour of various Ni-Se catalysts.

- Optimization of the dye inclusion in TiO_2, that is studying the temperature and the duration of exposure of the TiO_2 to the dye.

Appendix

Chapter 3

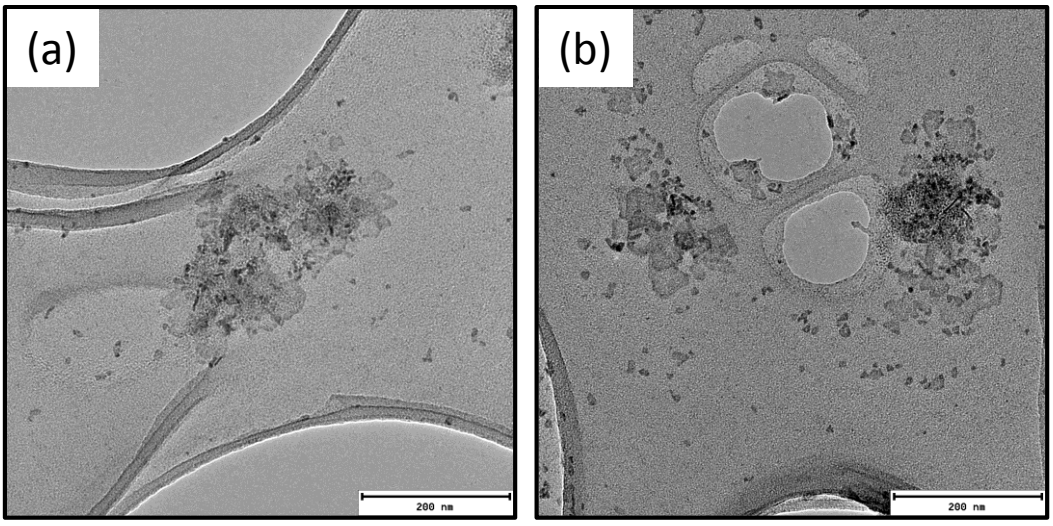

Appendix A1: TEM images illustrating the coalescence of the nuclei into 2D – like InSe nanostructures

Thickness measurements

Digital micrograph technique was used to analyze TEM images of the nanosheets in order to approximate their thickness. This analysis works on the principle that the intensity of the electron beam varies depending on the region it strikes on the copper grid covered with a thin layer of holey carbon. The intensity of the beam decreases as it strikes the carbon layer and further reduces on interaction with the sample placed on the carbon layer. This decrease is attributed to the thickness of the carbon layer on the copper grid as well as the properties of the sample, in this case, the thickness of the nanosheets. The thickness of the carbon layer on the copper grid is 7.5 nm (value as per the supplier). This thickness is represented by the difference in the intensity counts of the beam between the vacuum region and the carbon layer. The additional decrease in the beam intensity is as a result of the nanosheet thickness on the carbon. Therefore, a relationship was created using the difference the vacuum and the carbon layer regions and the vacuum and the sample region to approximate the thickness of

the nanosheets (equation 1). Typically, to analyse the image, a region of interest was selected on the image to include the vacuum, the carbon layer and the sample on the carbon layer sections using rectangles as depicted on the images on Appendix A2 (a), (b) and (c). Varying intensities in pixel counts were recorded for the three different sections on each image and are also shown in Appendix A2.

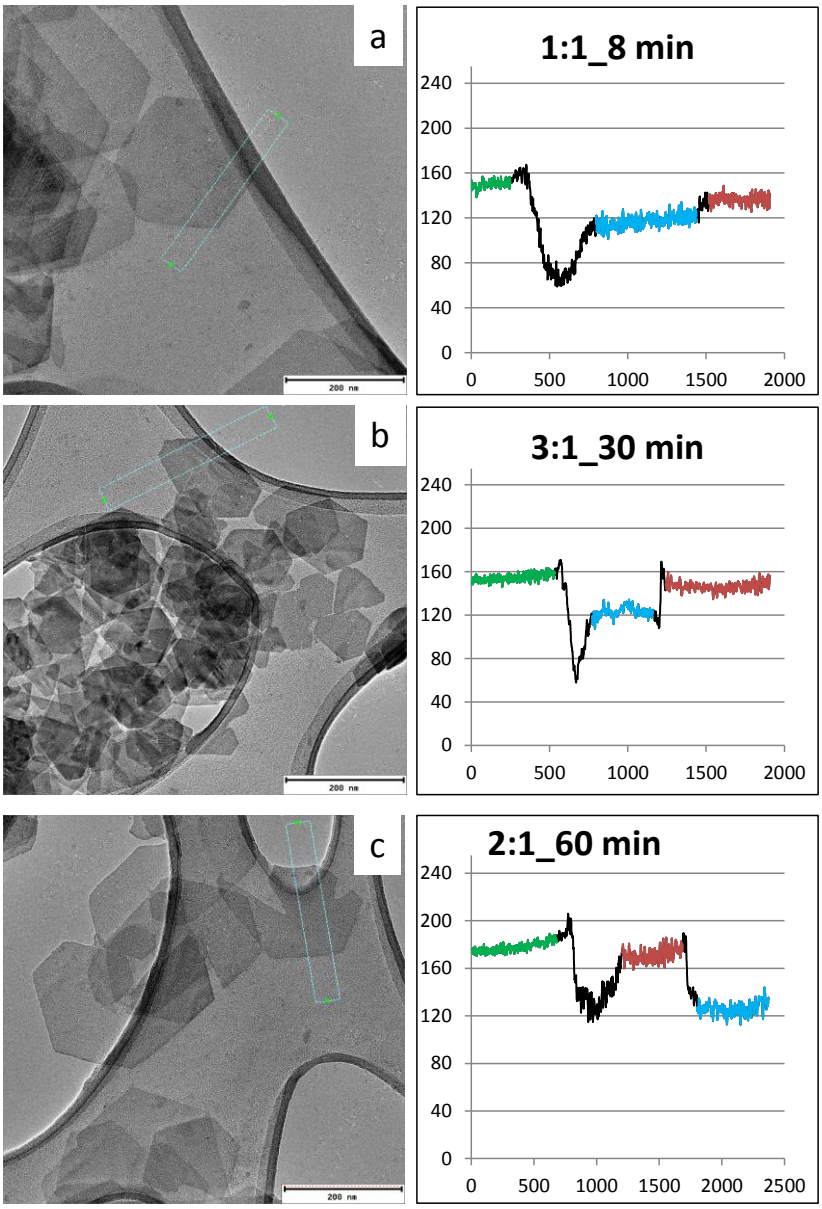

Appendix A2: Intensity profiles obtained from the TEM images of InSe nanosheets synthesized at a) 1:1, 8 min, b) 3:1, 30 min and c) 2:1, 60 min using the digital micrograph technique. The rectangles on the TEM images indicate the regions of interest that were

analysed. The green, blue and red sections on the intensity profiles are a representation of the intensity counts at the vacuum, the carbon layer and the sample on the carbon layer regions.

$$\mathrm{Ct} = (V - C) \quad \ldots\ldots\ldots\

Table A1 summarizes the values obtained from the intensity graphs that aided in the approximation of the thicknesses of the nanosheets.

Image	V (cts)	C (cts)	S (cts)	C_t (cts)	C_t (nm)	Ns_t (cts)	Ns_t (nm)
a	149.815	136.464	117.235	13.351	7.5	32.580	18.30
b	154.521	146.319	122.916	8.201	7.5	31.604	28.90
c	177.815	171.559	126.370	6.256	7.5	51.445	61.67

Chapter 5

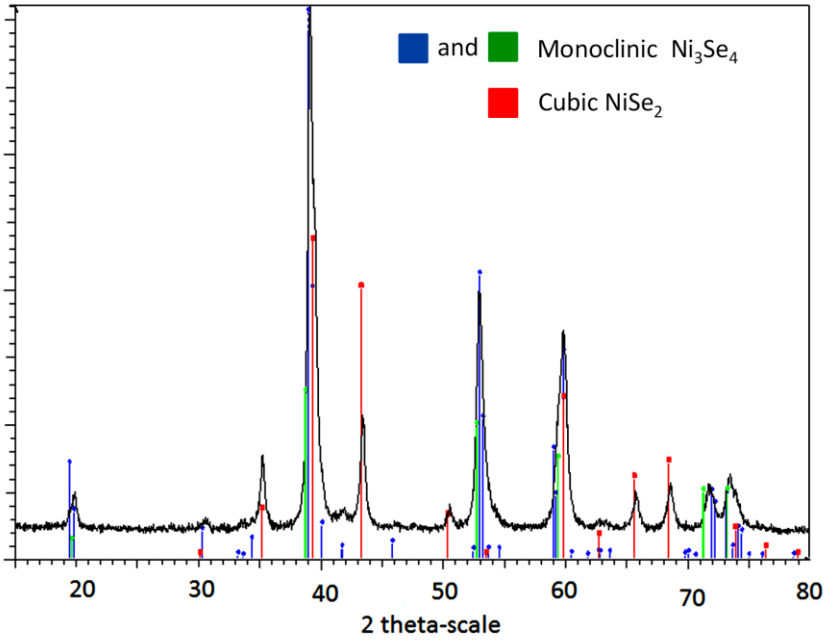

Appendix A3: XRD pattern showing a mixture of phases within the same sample. The blue and the green indices matched the cards for the monoclinic Ni_3Se_4 and for the sake of this study, the one was selected. The red indices corresponded to the cubic $NiSe_2$.

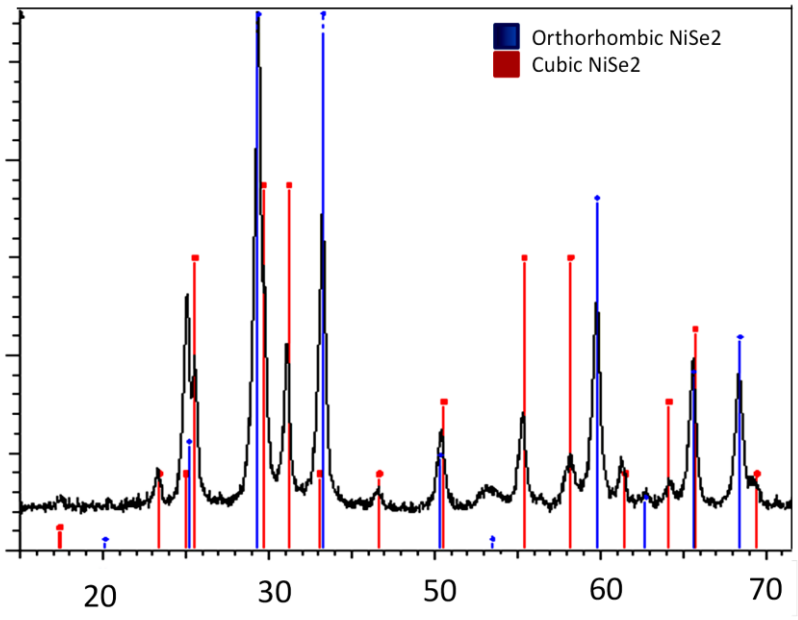

Appendix A4: XRD pattern illustrating the existence of both the orthorhombic and cubic NiSe2 within the same sample represented by the blue and the red indices respectively.

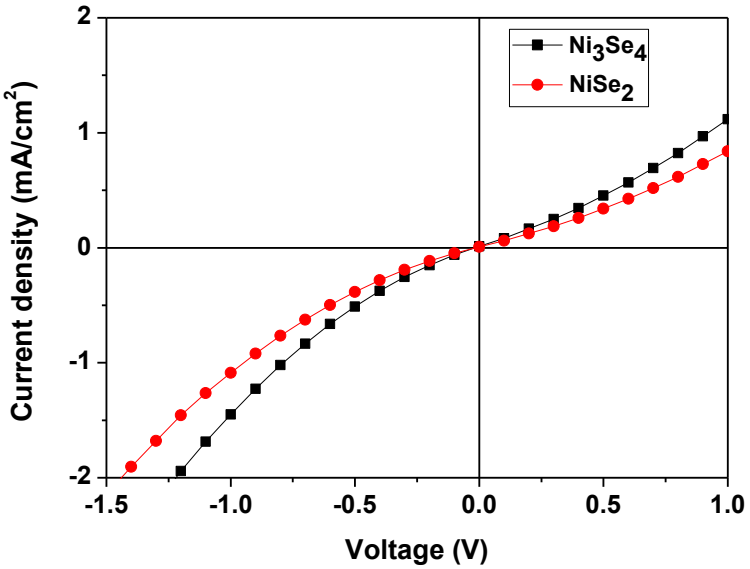

Appendix A5: Photocurrent density-voltage characteristics of DSSCs with nickel selenide nanocrystals CEs.